LHCb 实验上五夸克态的寻找和 CP 破坏的研究

（申请清华大学工学博士学位论文）

培 养 单 位：工 程 物 理 系

学　　　科：核 科 学 与 技 术

研　究　生：刘　雪　淞

指 导 教 师：陈　少　敏　教　授

二〇一九年十二月

Search for pentaquark state and measurement of *CP* violation with the LHCb detector

Dissertation Submitted to

Tsinghua University

in partial fulfillment of the requirement

for the degree of

Doctor of Philosophy

in

Nuclear Science and Technology

by

LIU Xuesong

Dissertation Supervisor : Professor CHEN Shaomin

December, 2019

关于学位论文使用授权的说明

本人完全了解清华大学有关保留、使用学位论文的规定，即：

清华大学拥有在著作权法规定范围内学位论文的使用权，其中包括：(1) 已获学位的研究生必须按学校规定提交学位论文，学校可以采用影印、缩印或其他复制手段保存研究生上交的学位论文；(2) 为教学和科研目的，学校可以将公开的学位论文作为资料在图书馆、资料室等场所供校内师生阅读，或在校园网上供校内师生浏览部分内容；(3) 根据《中华人民共和国学位条例暂行实施办法》，向国家图书馆报送可以公开的学位论文。

本人保证遵守上述规定。

（保密的论文在解密后应遵守此规定）

作者签名：刘雪松　　　　导师签名：陈力军

日　　期：2019.12.13　　　　日　　期：2019.12.13

摘　要

检验标准模型并寻找其外的新物理，解释自然界正反物质的不对称性是粒子物理学研究的前沿。大型强子对撞机（LHC）上的 LHCb 实验在 TeV 质心能量区间采集了海量的质子-质子（pp）对撞数据，为以上前沿研究提供了可能。本论文基于该实验对 J/ψ 粒子探测的优势，开展了奇异隐粲五夸克态的寻找，为低能非微扰量子色动力学的理论研究提供实验支撑；同时测量了电荷共轭-宇称（CP）破坏相角 ϕ_s，为寻找标准模型外的新物理提供实验依据。论文的主要工作有：

1. 分析了积分亮度为 3 fb^{-1}，质心系能量在 7 TeV 和 8 TeV 的 pp 对撞数据（Run-I），首次观测到 $\Xi_b^- \to J/\psi \Lambda K^-$ 衰变，并对 $\mathcal{B}(\Xi_b^- \to J/\psi \Lambda K^-)/\mathcal{B}(\Lambda_b^0 \to J/\psi \Lambda)$ 相对衰变道分支比进行测量，考虑到 Λ_b^0 和 Ξ_b^- 产生的相对碎裂函数的影响，得到 $0.0419 \pm 0.0029(\text{stat.}) \pm 0.0015(\text{syst.})$。该衰变道是寻找理论预言的 $udsc\bar{c}$ 五夸克态的理想途径。同时我们还给出 Λ_b^0 与 Ξ_b^- 质量差异的测量结果 $M(\Xi_b^-) - M(\Lambda_b^0) = 177.08 \pm 0.47(\text{stat.}) \pm 0.16(\text{syst.})\ \text{MeV}/c^2$，该结果是目前国际上最好的测量之一。
2. 研究了两个含 J/ψ 末态的不同 B_s^0 衰变道，开展了 CP 破坏的研究，并对 ϕ_s 相角进行了测量。基于 Run-I 数据，首次在 $J/\psi K^+K^-$，K^+K^- 不变质量高于 $\phi(1020)$ 介子质量的衰变道中测量 ϕ_s，得到 $0.119 \pm 0.107(\text{stat.}) \pm 0.034(\text{syst.})$ rad，与使用 Run-I 数据在 $J/\psi\phi(1020)$ 衰变道测量的结果一致；由于 B_s^0 产额随 pp 对撞质心系能量增加，因此我们同时还分析了积分亮度 1.9 fb^{-1}，质心系能量 13 TeV 的 pp 对撞数据（Run-II），在 $J/\psi\pi^+\pi^-$ 衰变道中测量 ϕ_s，得到 $-0.057 \pm 0.060(\text{stat.}) \pm 0.011(\text{syst.})$ rad，也与 Run-I 数据同样衰变道已发表的测量结果吻合。两个衰变道的测量结果在一个标准偏差范围内均与标准模型预言的 ϕ_s 值 $-0.0368^{+0.0096}_{-0.0068}$ rad 一致。

关键词： 标准模型；五夸克态；CP 破缺；LHCb 实验

Abstract

Testing the standard model (SM) of particle physics and searching for new physics beyond it, explaining the asymmetry between matter and antimatter in the universe is the frontier of particle physics researches. The LHCb experiment at the Large Hadron Collider (LHC) has collected a large number of proton-proton (*pp*) collision data at the TeV energy scale, provided the possibility for the relative frontier researches. Based on the advantages of J/ψ particle detection in this experiment,we searched the strangeness hidden-charm pentaquark state, which provides experimental support for the theoretical study of low-energy non-perturbative quantum chromodynamics. We also measured the charge conjugation and parity (CP) destruction, which provides an experimental basis for the search for new physics outside the SM. The main work described in this dissertation is as follows:

1. We observed the $\Xi_b^- \to J/\psi \Lambda K^-$ decay for the first time by analysing a data sample corresponding to an integrated luminosity of 3 fb^{-1} at 7 TeV and 8 TeV *pp* collision energy (Run-I). Taking into account the effect of the relative fragmentation fraction between Λ_b^0 and Ξ_b^-, the relative branching ratio of $\mathcal{B}(\Xi_b^- \to J/\psi \Lambda K^-)/\mathcal{B}(\Lambda_b^0 \to J/\psi \Lambda)$ is measured to be $0.0419 \pm 0.0029(\text{stat.}) \pm 0.0015(\text{syst.})$. This decay channel is an ideal channel for searching the predicted $udsc\bar{c}$ pentaquark state. The mass difference between the Λ_b^0 and Ξ_b^- baryons is also determined, which is $M(\Xi_b^-) - M(\Lambda_b^0) = 177.08 \pm 0.47(\text{stat}) \pm 0.16(\text{syst})\ \text{MeV}/c^2$. This measurement gives one of the best results on this parameter in the world.
2. We analysed two different B_s^0 decay channels containing J/ψ final states that could be used in the searches of CP violation. Using the LHC Run-I data, a measurement of CP-violating phase ϕ_s is first time performed in the $m(K^+K^-)$ higher than $\phi(1020)$ region of $B_s^0 \to J/\psi K^+K^-$ decay channel. ϕ_s is measured to be $0.119 \pm 0.107(\text{stat}) \pm 0.034(\text{syst})$ rad, which is consistent with result obtained in $B_s^0 \to J/\psi\phi(1020)$ channel. As the B_s^0 production cross-section increases with the colliding energy, another data set of $B_s^0 \to J/\psi\pi^+\pi^-$ decay channel corresponding to an integrated luminosity of 1.9 fb^{-1} at 13 TeV *pp* collision energy (Run-II) is used to measurement ϕ_s, this results in $\phi_s = -0.057 \pm 0.060(\text{stat}) \pm 0.011(\text{syst})$ rad, which is consistent with Run-I result from the same decay channel. Both of the

measurements are in line with the SM calculations of $\phi_s = -0.0368^{+0.0096}_{-0.0068}$ rad in one standard deviation.

Key Words: Standard Model; Pentaquark; *CP* violation; LHCb experiment

Contents

Chapter 1 Introduction 1
1.1 The Standard Model 1
1.2 Quark Model 3
1.3 CP violation 7
1.3.1 CKM matrix 7
1.3.2 The unitarity triangle 8
1.3.3 Neutral mesons mixing 9
1.3.4 Classification of CP violation 12
1.4 Advantages of using $b \to J/\psi X$ decays for SM probing 14
Chapter 2 The LHCb experiment 16
2.1 The Large Hadron Collider 16
2.2 The LHCb detector 19
2.2.1 LHCb tracking system 20
2.2.2 LHCb particle identification system 26
2.2.3 LHCb trigger 30
2.3 Flavour tagging algorithms 35
2.3.1 Tagging algorithms 36
2.3.2 Flavour tagging performance 37
2.3.3 Combination and calibration of flavour tagging algorithms 38
Chapter 3 First observation of $\Xi_b^- \to J/\psi \Lambda K^-$ 40
3.1 Introduction 40
3.2 Analysis strategy 40
3.3 Dataset and selection requirement 41
3.3.1 Data and simulated samples 41
3.3.2 Selection 41
3.4 Signal yields extraction 49
3.4.1 Background studies 49
3.4.2 Fit model 51
3.4.3 Fit results 52
3.4.4 Significance 52

3.5 Efficiency 53
3.5.1 Geometrical acceptance 54
3.5.2 Reconstruction and preselection efficiency 55
3.5.3 Trigger efficiency 55
3.5.4 BDTG selection efficiency 55
3.5.5 PID selection efficiency 55
3.5.6 Relative efficiency 56
3.6 Systematic uncertainties 56
3.6.1 Signal model 56
3.6.2 Background model 57
3.6.3 BDTG selection efficiency 58
3.6.4 PID efficiency 59
3.6.5 Tracking efficiency 59
3.6.6 Resonances in $\Xi_b^- \to J/\psi \Lambda K^-$ 60
3.6.7 b-baryon kinematics 60
3.6.8 Ξ_b^- and Λ_b^0 lifetime 61
3.6.9 MC statistics 63
3.6.10 Fixed resolution ratio 63
3.6.11 Trigger efficiency 63
3.7 Determination of the mass difference 63
3.8 Search for Pentaquark states 65
3.9 Results 66
Chapter 4 Measurement of CP-violating phase ϕ_s in $B_s^0 \to J/\psi\ K^+K^-$ decays in the mass region above the $\phi(1020)$ 67
4.1 Introduction 67
4.2 Analysis strategy 67
4.3 Dataset and selection requirement 70
4.4 Signal yields extraction 72
4.5 Flavour tagging calibration 76
4.6 Detector effects 77
4.6.1 Decay-time resolution 77
4.6.2 Decay-time efficiency 79
4.6.3 Angular and m_{KK} efficiency 84
4.7 Fit validation and results 85

4.7.1 Likelihood construction 85
4.7.2 Validation of fitter 87
4.7.3 Fit results 88
4.8 Systematic uncertainties 90
4.8.1 Resonance modelling 90
4.8.2 Efficiency of m_{KK} and angles 92
4.8.3 Decay time 93
4.8.4 Background modelling 94
4.8.5 Fit bias 94
4.8.6 Flavour tagging and production asymmetry 94
4.8.7 *sWeights* 94
4.8.8 B_c^+ contribution 95
4.9 Results 95
Chapter 5 Measurement of CP-violating phase ϕ_s with $B_s^0 \to J/\psi\, \pi^+\pi^-$ 96
5.1 Introduction 96
5.2 Analysis strategy 96
5.3 Dataset and selection requirement 98
5.4 Signal yields extraction 103
5.4.1 Backgrounds 103
5.4.2 Fits to B_s^0 mass distribution 103
5.4.3 Background subtraction 104
5.5 Flavour tagging calibration 108
5.5.1 Calibration of the OS tagger 108
5.5.2 Calibration of the SS tagger 111
5.5.3 Tagging performance 116
5.6 Detector effects 118
5.6.1 Decay-time resolution 118
5.6.2 Decay-time acceptance 120
5.6.3 Angular and $m_{\pi\pi}$ 123
5.7 Fit validation and results 125
5.7.1 Toy study 125
5.7.2 Fit to $B_s^0 \to J/\psi\, \pi^+\pi^-$ simulated samples 126
5.7.3 Fit results 128
5.8 Systematic uncertainties 129

5.8.1 Resonances modelling 130
5.8.2 Resonant masses and widths 132
5.8.3 Efficiency of $m_{\pi\pi}$ and angles 132
5.8.4 Decay-time efficiency 132
5.8.5 B^0 lifetime 133
5.8.6 Decay-time resolution 133
5.8.7 Background modelling 133
5.8.8 Calibration of flavour tagging 133
5.8.9 Production asymmetry 133
5.8.10 Fix of Δm_s and Γ_L 134
5.8.11 B_c^+contribution 134
5.9 Results 134
Chapter 6 Summary and prospects 135
Bibliography 138
Acknowledgments 145
声　明 146
Appendix A Time-dependent amplitude analysis 147
Resume and publications 152

Chapter 1 Introduction

In this chapter, the theoretical framework of the Standard Model (SM) of particle physics[1-4] is described. Detailed overviews of two key components in the SM, the Quark Model[5-6] and the *CP* violation[7-8], are given. Finally, advantages of using $b \to J/\psi X$ decays as a probe to test the SM are presented.

1.1 The Standard Model

Knowledge of particle physics can give us the answers to two oldest and most profound questions : what the world consists of and how they interact. Nowadays, our comprehension of nature can be summarised as the SM of particle physics. It is a spontaneously broken non-abelian, Yang-Mills quantum field theory, based on the ganga symmetry group $SU(3)_C \otimes SU(2)_L \otimes U(1)_Y$, in which particles are produced and destroyed with field and the dynamics are described by a Lagrange function. The $SU(3)_C$ symmetry results of interaction via the strong force where the subscript C denotes the colour charge, while the $SU(2)_L \otimes U(1)_Y$ symmetry give rise to the electroweak interactions where the subscript Y represents the weak hypercharge and L means that the $SU(2)_L$ part only affects on left-hands fields.

The fundamental particles in the SM are categorised into three groups: fermions, ganga bosons and the Higgs boson. All matter is formed by twelve fermions, six quarks and six leptons, which have half-integer spin. Forces between the fermions are mediated by ganga bosons which have integer spin. The masses of all these particles arise due to the couplings to the Higgs field. These couplings are mediated by the Higgs boson. A graphical representation of all fundamental particles is presented in Fig. 1.1.

Both quarks and leptons are classified into three families, where each family comprises a duplet of two particles:

$$\text{quarks} \quad \begin{pmatrix} u \\ d \end{pmatrix}, \quad \begin{pmatrix} c \\ s \end{pmatrix}, \quad \begin{pmatrix} t \\ b \end{pmatrix};$$

$$\text{leptons} \quad \begin{pmatrix} e^- \\ \nu_e \end{pmatrix}, \quad \begin{pmatrix} \mu^- \\ \nu_\mu \end{pmatrix}, \quad \begin{pmatrix} \tau^- \\ \nu_\tau \end{pmatrix}.$$

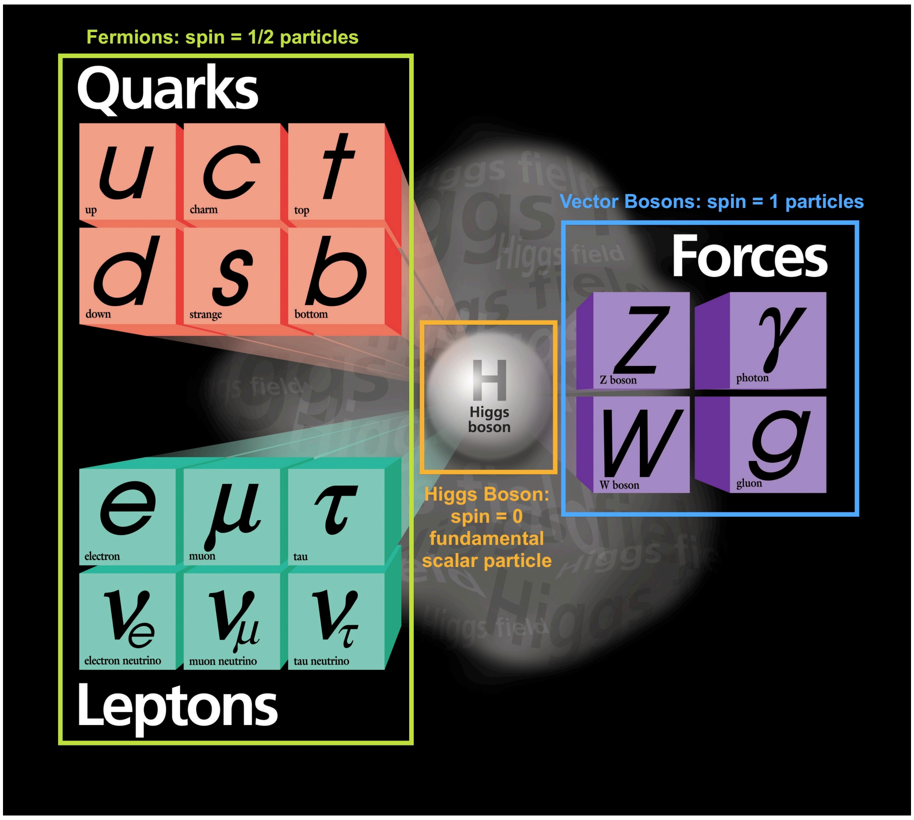

Figure 1.1 Schematic representation of the SM of particle physics, detailing the constituent and force mediating particles.

Quarks are further divided into two types: the *up-type* quarks up (u), charm (c) and top (t), having charge $+\frac{2}{3}$, and the *down-type* quarks down (d), strange (s) and bottom/beauty(b), which have charge $-\frac{1}{3}$. They are massive and carry colour charge, weak isospin and electric charge, so they can interact via the electromagnetic, weak and strong interaction. Leptons includes three charged, massive particles: electron (e^-), muon (μ^-) and tau (τ^-) which interact via the electromagnetic and weak interactions, and three neutral, (nearly) massless particles, called neutrinos: ν_e, ν_μ and ν_τ, which only experience weak interactions.

The ganga bosons are classified into three types depending on the interaction they get involved. The force-carrier particle of electromagnetic interaction is the photon (γ) which couples to the electric charge. The weak force is mediated by the uncharged, massive Z boson and charged, massive $W^\pm$ bosons which couple to all twelve fermions. The associated particles for strong interaction are the eight massless gluons (g) which couple to colour charge. Gluonic self-coupling are also allowed in the SM. The Higgs boson (H), which is discovered in 2012[9-10] by LHC, is associated to the Higgs field and interacts with all massive particles.

The SM is a very successful theory which accurately describes, predicts and explains almost all of the observed results in particle physics accelerator experiments. However, the absent of a description of the fourth fundamental force, gravity, the non-zero masses of neutrinos, the dark matter and the matter-antimatter asymmetry indicate that the SM is not a complete description of the universe. There must be a more complex laws of physics behind the SM theory. The measurements presented in this dissertation are part of the experiment efforts to test and extend our understanding of the SM.

1.2 Quark Model

The major breakthrough in our understanding of the spectrum of hadrons was the Quark Model raised by Murray Gell-Mann[5] and George Zweig[6] independently in 1964. Hadrons are composed of three fundamental quarks (u, d, s) and their anti-quark ($\bar{u}, \bar{d}, \bar{s}$) with baryon number $B = \frac{1}{3}$. Mesons are a combination of $q\bar{q}$ ($B = 0$) while baryons are made up of qqq ($B = 1$). This model can well described the pseudoscalar meson, vector meson octets, baryon octets and baryon decuplets which observed at that time based on the group $SU(3)$, as shown in Fig. 1.2. A more complex structures with integer charges $B = 0$ or $B = 1$ could exist with quark components $qq\bar{q}\bar{q}$ (tetraquark) or $qqqq\bar{q}$ (pentaquark). However, no candidates with multiquark constituents are observed at that time.

Quantum Chromodynamics (QCD)[11-14] is the underly theory describing the strong interaction between quarks which could be used to explain the inner structure of hadron. QCD theory was proposed in 1973 and has two main properties: 1) asymptotic freedom: hadron is viewed as a 'sea' of free gluons and quark-antiquark pairs and 2) colour confinement: colour charged particles cannot be isolated therefore clumps together to a colour singlet. QCD theory has been well studied and tested in high energy regime through precisely perturbative calculation. Except for the conventional hadrons, the existence of more complex structure, *e.g.* the multiquark states ($qq\bar{q}\bar{q}$, $qqqq\bar{q}$), the hybird states (qqg) and glueballs (ggg) are also allowed since the development of QCD theory. These states provide a chance to explore the complicated non-perturbative behaviours of QCD theory in low energy regime.

The multiquark states can be classified into tetraquarks ($qq\bar{q}\bar{q}$), pentaquarks ($qqqq\bar{q}$) and dibaryon ($qqqqqq$) etc. The theory framework of tetraquark states was first proposed in 1976[15-16] and soon expand upon to pentaquarks in 1978[17-18]. Since 2003, a series of charmonium-like/bottomonium-like XYZ tetraquark states have been observed in high

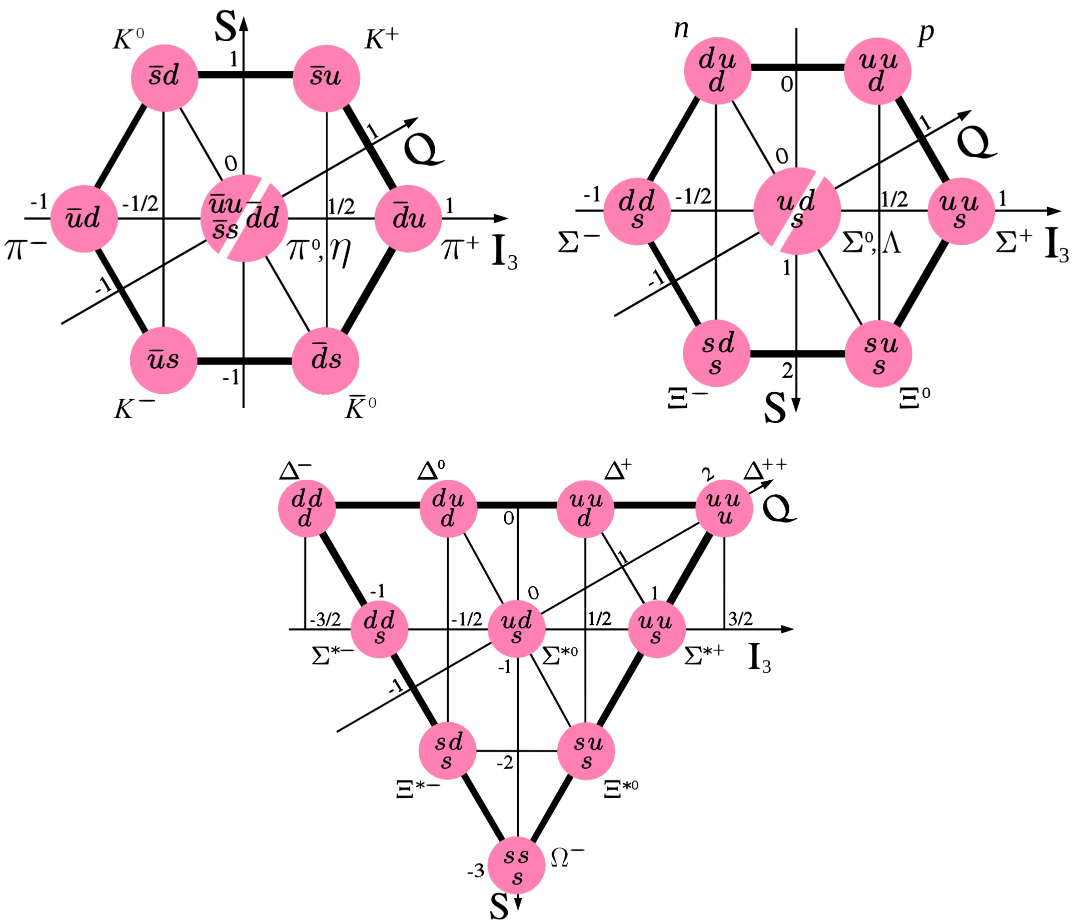

Figure 1.2 Schematic representation of meson octets (top left), baryon octets (top right) and baryon decuplets (bottom).

energy experiments[19-29]. However, the observation of pentaquark states $uudd\bar{s}$ reported by LEP collaboration in 2003[30] was not confirmed by subsequently more advanced experiments[31].

In 2015, the LHCb collaboration reported observation of two exotic states, $P_c^+(4380)$ and $P_c^+(4450)$, in the mass spectrum of $J/\psi p$ of $\Lambda_b^0 \to J/\psi p K^-$ decay, with a significance of 9σ and 12σ, respectively[32]. Their minimal quark contents are $c\bar{c}uud$ which are good candidates of hidden-charm pentaquarks.

An amplitude analysis of the three-body final-state was performed, the masses and

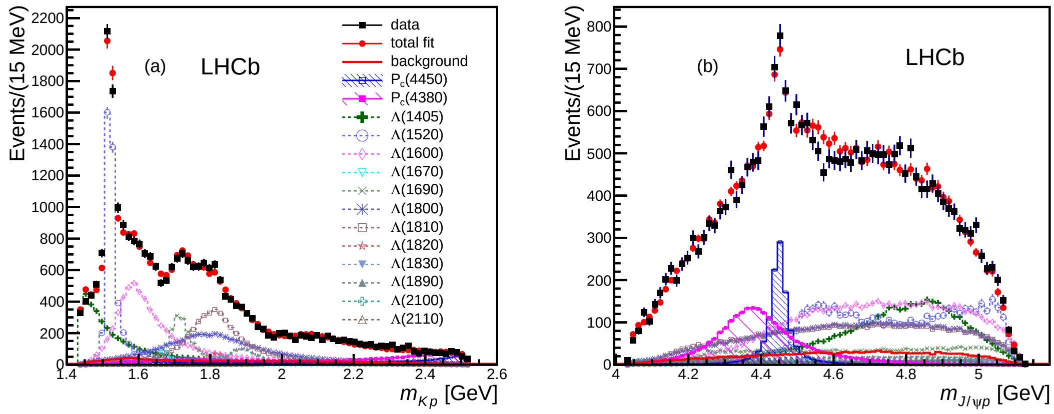

Figure 1.3 The invariant mass spectrum of $K^- p$ (left) and $J/\psi p$ (right) of $\Lambda_b^0 \to J/\psi p K^-$ decays. The background has been subtracted. Figures taken from Ref.[32].

widths of the two P_c^+ states are measured to be①

$$\begin{aligned}
M_{P_c(4380)^+} &= 4380 \pm 8 \pm 29 \text{ MeV}, \\
\Gamma_{P_c(4380)^+} &= 205 \pm 18 \pm 86 \text{ MeV}, \\
M_{P_c(4450)^+} &= 4449.8 \pm 1.7 \pm 2.5 \text{ MeV}, \\
\Gamma_{P_c(4450)^+} &= 39 \pm 5 \pm 19 \text{ MeV},
\end{aligned} \tag{1-1}$$

Different fit models are used to interpret the structure of the spectrum. The best fit results in spin-parities J^P $(\frac{3}{2}^-, \frac{5}{2}^+)$ for $P_c^+(4380)$ and $P_c^+(4450)$, respectively. $(\frac{3}{2}^+. \frac{5}{2}^-)$ and $(\frac{5}{2}^+, \frac{3}{2}^-)$ are also found in other acceptable fits. The best fit projection of invariant mass spectrum of $K^- p$ and $J/\psi p$ are shown in Fig. 1.3. The Dalitz plot and decay angular distributions for this fit are shown in Fig. 1.4.

The fraction of the two P_c^+ states are found to be $(8.4 \pm 0.7 \pm 4.2)\%$ and $(4.1 \pm 0.5 \pm 1.1)\%$. The overall branching fractions of $\Lambda_b^0 \to J/\psi p K^-$ was measured by LHCb[33] as

$$\mathcal{B}(\Lambda_b^0 \to J/\psi p K^-) = (3.04 \pm 0.04 \pm 0.06 \pm 0.33^{+0.43}_{-0.27}) \times 10^{-4}, \tag{1-2}$$

which leads to the product branching fractions of the $P_c(4380)^+$ and $P_c(4450)^+$

$$\begin{aligned}
\mathcal{B}(\Lambda_b^0 \to J/\psi p K^-) \times \mathcal{B}(P_c(4380)^+ \to J/\psi p) &= (2.56 \pm 0.22 \pm 1.28^{+0.46}_{-0.36}) \times 10^{-5} \\
\mathcal{B}(\Lambda_b^0 \to J/\psi p K^-) \times \mathcal{B}(P_c(4450)^+ \to J/\psi p) &= (1.25 \pm 0.15 \pm 0.33^{+0.22}_{-0.18}) \times 10^{-5}
\end{aligned} \tag{1-3}$$

The observation of the two pentaquarks states have inspired theorist's extensive interests in revealing their underlying structure and nature. Several theoretical model were

① The natural units are used in this dissertation where $\hbar = c = 1$.

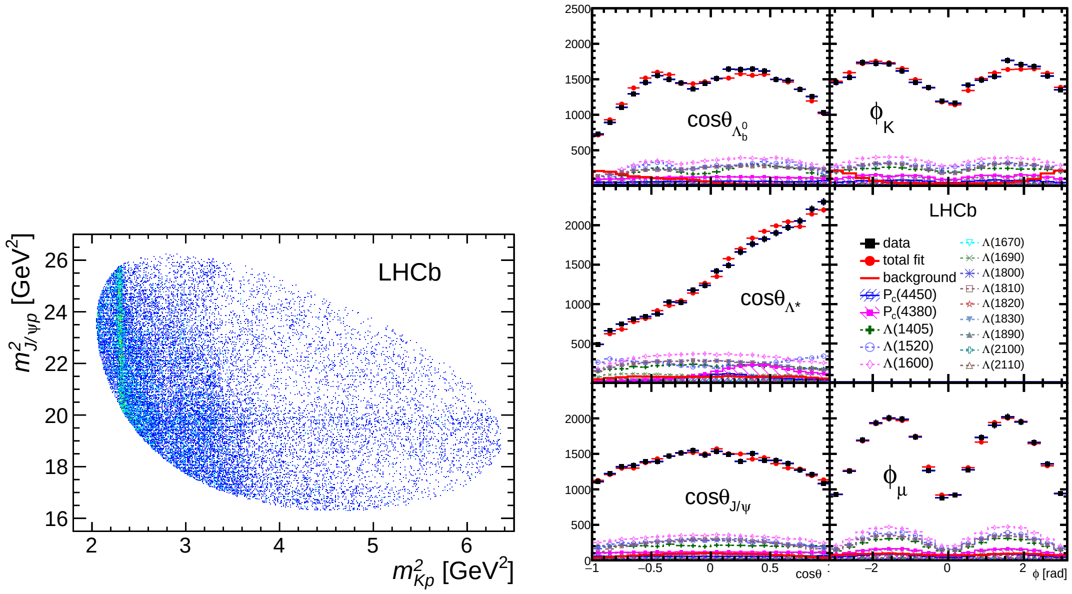

Figure 1.4 The Dalitz plot of K^-p and $J/\psi p$ invariant masses-squared (left). Various decay angular distributions for the best fit with two P_c^+ states (right). Figures taken from Ref.[32]

proposed, three well-known theories are molecular scheme[34-44], diquark model[45-51], and non-resonant kinematical effects[52-54].

According to molecular scheme, the pentaquarks are composed of one meson and one baryon which are loosely bounded. The observed two P_c^+ can be viewed as a system of one open-charm and one open-charm baryon, *e.g.* $\Lambda_c \bar{D}^*$, $\Sigma_c \bar{D}^*$, $\Sigma_c^* \bar{D}$, $\Sigma_c^* \bar{D}^*$, χ_c and one proton, $\psi(2S)$ and one proton etc. They interact via Goldstone Boson exchange interaction and Van der Waals interaction.

The diquark model interprets the P_c states as compact pentaquarks, where five quarks are tightly bounded together. The two P_c^+ states are further constructed as diquark-diquark-antiquark or diquark-triquark. They interact through colour magnetic interaction.

Furthermore, a non-resonant interpretation of pentaquarks is also exist. They explain the resonance structure as a kinematic effects of rescattering processes.

However, the current experimental results can not ruled out any of these models. Searching for new P_c states with similar quark contents can lead us to a deeper understanding of the physics nature of pentaquarks①.

① From a updated result that reconstructed almost ten times more signal decays of $\Lambda_b^0 \to J/\psi p K^-$, a new narrow pentaquark structure $P_c(4312)^+$ is observed. In addition, the $P_c(4450)^+$ peak is found to be a combination of two narrow pentaquark states $P_c(4440)^+$ and $P_c(4457)^+$ [55]

1.3 *CP* violation

1.3.1 CKM matrix

In the SM, the flavour of quark can change through weak interaction by absorb or mediate $W^{\pm}$ boson, which can be expressed as a Lagrangian density

$$\mathcal{L}_W = -\frac{g}{\sqrt{2}}\{W_u^+ \left(\bar{u}, \bar{c}, \bar{t}\right) \gamma^{\mu} \frac{1-\gamma^5}{2} V_{\text{CKM}} \begin{pmatrix} d \\ s \\ b \end{pmatrix} \} + h.c., \quad (1\text{-}4)$$

where g is a coupling constant, γ^{μ} are Dirac matrices and V_{CKM}, known as the Cabibbo-Kobayashi-Maskawa (CKM) matrix[56-57], couples the flavour eigenstates d, s and b to the mass eigenstates $d^{'}$, $s^{'}$ and $b^{'}$:

$$\begin{pmatrix} d^{'} \\ s^{'} \\ b^{'} \end{pmatrix} = \begin{pmatrix} V_{ud} & V_{us} & V_{ub} \\ V_{cd} & V_{cs} & V_{cb} \\ V_{td} & V_{ts} & V_{tb} \end{pmatrix} \begin{pmatrix} d \\ s \\ b \end{pmatrix} \quad (1\text{-}5)$$

The CKM matrix is unitary, so it can be written in terms of four independent physical parameters. A standard parametrisation of the CKM matrix[58] gives

$$V_{\text{CKM}} = \begin{pmatrix} c_{12}s_{13} & s_{12}c_{13} & s_{13}e^{-i\delta} \\ -s_{12}c_{23} - c_{12}s_{23}s_{13}e^{-i\delta} & c_{12}s_{23} - s_{12}s_{23}s_{13}e^{-i\delta} & s_{23}c_{13} \\ s_{12}s_{23} - c_{12}c_{23}s_{13}e^{-i\delta} & -c_{12}s_{23} - s_{12}c_{23}s_{13}e^{-i\delta} & c_{23}c_{12} \end{pmatrix} \quad (1\text{-}6)$$

where $c_{ij} = \cos\theta_{ij}$, $s_{ij} = \sin\theta_{ij}$. The θ_{ij} parameters are three real mixing angles and δ is the KM phase.

Another, useful parametrisation is given by Wolfenstein[59]. By defining the parameters λ, A, ρ and η with

$$\begin{aligned} s_{12} =& \ \lambda, \\ s_{23} =& \ A\lambda^2, \\ s_{13}e^{i\delta} =& \ A\lambda^3(\rho + i\eta). \end{aligned} \quad (1\text{-}7)$$

The CKM matrix can be rewritten with the following definitions

$$V_{\text{CKM}} \simeq \begin{pmatrix} 1 - \frac{1}{2}\lambda^2 & \lambda & A\lambda^3(\rho - i\eta) \\ -\lambda & 1 - \frac{1}{2}\lambda^2 & A\lambda^2 \\ A\lambda^3(1-\rho-i\eta) & -A\lambda^2 & 1 \end{pmatrix} + \mathcal{O}(\lambda^4) \quad (1\text{-}8)$$

This parametrisation indicates that inter-generational mixing of quarks is much more suppressed than mixing occurring within a given generation.

1.3.2 The unitarity triangle

The unitarity condition of the CKM matrix gives the constraints:

$$\sum_i = V_{ij}V_{ik}^* = \delta_{jk}, \quad \sum_j V_{ij}V_{kj}^* = \delta_{ik}. \tag{1-9}$$

which can be expressed as six scalar equations

$$V_{ud}V_{ub}^* + V_{cd}V_{cb}^* + V_{td}V_{tb}^* = 0, \tag{1-10}$$

$$V_{us}V_{ub}^* + V_{cs}V_{cb}^* + V_{ts}V_{tb}^* = 0, \tag{1-11}$$

$$V_{ud}V_{us}^* + V_{cd}V_{cs}^* + V_{td}V_{ts}^* = 0, \tag{1-12}$$

$$V_{ud}V_{cd}^* + V_{us}V_{cs}^* + V_{ub}V_{cb}^* = 0, \tag{1-13}$$

$$V_{ud}V_{td}^* + V_{us}V_{ts}^* + V_{ub}V_{tb}^* = 0, \tag{1-14}$$

$$V_{cd}V_{td}^* + V_{cs}V_{ts}^* + V_{cb}V_{tb}^* = 0. \tag{1-15}$$

Each of these equations requires the sum of three complex quantities to vanish, so can be geometrically represents in the complex plane as a triangle, namely ”the unitarity triangle”.

Eq. (1-10) and Eq. (1-11) are particularly relevant for the b-hadron phenomenology, the angles of the unitarity triangle are defined by

$$\alpha = \arg\left(-\frac{V_{td}V_{tb}^*}{V_{ud}V_{ub}^*}\right), \tag{1-16}$$

$$\beta = \arg\left(-\frac{V_{cd}V_{cb}^*}{V_{td}V_{tb}^*}\right), \tag{1-17}$$

$$\gamma = \arg\left(-\frac{V_{ud}V_{ub}^*}{V_{cd}V_{cb}^*}\right), \tag{1-18}$$

$$\beta_s = \arg\left(-\frac{V_{ts}V_{tb}^*}{V_{cs}V_{cb}^*}\right). \tag{1-19}$$

As shown in Fig. 1.5, the left triangle, defined by Eq. (1-10) can be studied using B^0, B_s^0 and $B^{\pm}$ decays; the right triangle, defined by Eq. (1-11) can be measured from analyses of B_s^0 mesons. Experimental measurements of these angles can overconstrained the triangles and test the unitarity of the matrix. A non-closing triangle would be a clear sign of physics beyond the SM.

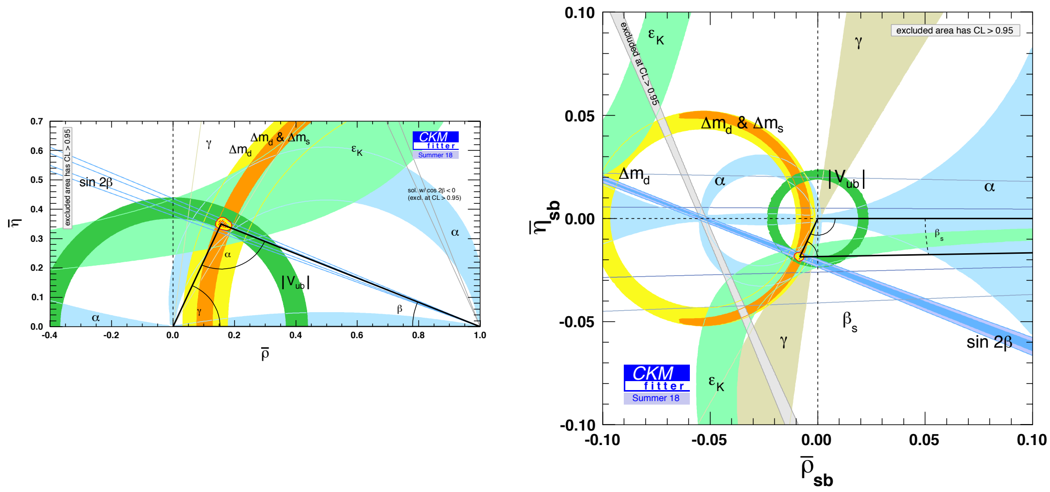

Figure 1.5 Schematic representation of two of the six unitarity conditions of the CKM matrix, superimposed with the current experimental constraints. Figures taken from Ref.[60].

The complex phase of CKM matrix δ is the only-known source of CP-violating phenomena in the SM, and it is proportional to the Jarlskog invariant J[61], where $\frac{1}{2}|J|$ is the size of the six unitarity triangles. The empirical value of J is several orders of magnitude smaller than the observed matter-antimatter asymmetry in the universe according to the baryogenesis model[62], which indicates the existence of contribution of CP violation beyond the SM. Thus, high precision measurements of the unitarity triangles are crucial to constrain these New Physics (NP) scenarios.

1.3.3 Neutral mesons mixing

The process of neutral meson changing to its anti-meson, or vice verse, is the neutral mesons mixing[8,58]. Using $|P^0\rangle$ and $|\bar{P}^0\rangle$ to denote neutral meson and its anti-meson, the time evolution of a neutral meson system can be generally written as

$$|\Phi(t)\rangle = a(t)|P^0\rangle + b(t)|\bar{P}^0\rangle + \sum_i c_i(t)|f_i\rangle, \tag{1-20}$$

where $|f_i\rangle$ are all the possible final states with $c_i(0) = 0$ as initial condition.

Using Weisskopf-Wigner approximation, the Schroedinger equation for $|\Phi(t)\rangle$ can be described in terms of a 2×2 effective non-Hermitian Hamiltonian matrix $\mathcal{H}$:

$$i\partial_t \begin{pmatrix} a(t) \\ b(t) \end{pmatrix} = \mathcal{H} \begin{pmatrix} a(t) \\ b(t) \end{pmatrix} = \begin{pmatrix} H_{11} & H_{12} \\ H_{21} & H_{22} \end{pmatrix} \begin{pmatrix} a(t) \\ b(t) \end{pmatrix} \tag{1-21}$$

The $\mathcal{H}$ matrix can be rewritten as the sum of two hermitian matrices M and Γ:

$$\mathcal{H} = M - \frac{i}{2}\Gamma = \begin{pmatrix} M_{11} & M_{12} \\ M_{21} & M_{22} \end{pmatrix} - \frac{i}{2} \begin{pmatrix} \Gamma_{11} & \Gamma_{12} \\ \Gamma_{21} & \Gamma_{22}. \end{pmatrix} \tag{1-22}$$

The mass eigenstates $|P_{L,H}\rangle$ (L and H stand for Light and Heavy, respectively) are linear combination of $|P^0\rangle$ and $|\bar{P}^0\rangle$:

$$|P_L\rangle = p|P^0\rangle + q|\bar{P}^0\rangle, \tag{1-23}$$

$$|P_H\rangle = p|P^0\rangle - q|\bar{P}^0\rangle, \tag{1-24}$$

where p and q are constrained to fulfil $|p|^2 + |q|^2 = 1$ and are given by

$$\frac{q}{p} = \frac{M_{12}^* - \frac{i}{2}\Gamma_{12}^*}{M_{12} - \frac{i}{2}\Gamma_{12}} = \frac{\Delta m - \frac{i}{2}\Delta\Gamma}{2(m_{12} - \frac{i}{2}\Gamma_{12})}, \tag{1-25}$$

where $\Delta m = m_H - m_L$ and $\Delta\Gamma = \Gamma_L - \Gamma_H$ are the differences of the masses and decay widths of flavour eigenstates. The sign convention for $\Delta\Gamma$ is chosen to have a positive experimental value for the B_s^0 system. The corresponding eigenvalues are:

$$\lambda_{L,H} = m_{L,H} - \frac{i}{2}\Gamma_{L,H}. \tag{1-26}$$

After diagonalising the Schroedinger equation can be rewritten as

$$i\partial_t \begin{pmatrix} P_L \\ P_H \end{pmatrix} = \begin{pmatrix} \lambda_L & 0 \\ 0 & \lambda_H \end{pmatrix} \begin{pmatrix} P_L \\ P_H \end{pmatrix}. \tag{1-27}$$

Using the mass eigenvalues and mass eigenstates from Eq.(1-23, 1-24, 1-26), the Schroedinger equation can be easily solved and leads to the time evolution of the mass eigenstates with simple exponential function $P_{L,H}(t) = e^{-i\lambda_{L,H}t}P_{L,H}$. Inverting Eq. (1-23, 1-24), the time evolution for the flavour eigenstates follows:

$$|P^0(t)\rangle = g_+|P_t^0\rangle + \frac{q}{p}g_-(t)|\bar{P}^0\rangle, \tag{1-28}$$

$$|\bar{P}^0(t)\rangle = g_+|\bar{P}_t^0\rangle + \frac{p}{q}g_-(t)|P^0\rangle, \tag{1-29}$$

where

$$g_{\pm}(t) = \frac{1}{2}\left(e^{-im_H t - \frac{1}{2}\Gamma_H t} \pm e^{-im_L t - \frac{1}{2}\Gamma_L t}\right), \tag{1-30}$$

where $m \equiv \frac{m_H+m_L}{2}$, $\Gamma \equiv \frac{\Gamma_H+\Gamma_L}{2}$ are the average masses and decay widths of flavour eigenstates.

The probabilities that a state initially produced as P^0 or $\bar{P}^0$ becomes a P^0 or $\bar{P}^0$ at time t are

$$|\langle P^0|P^t|\rangle|^2 = |g_+(t)|^2 = \frac{e^{-\Gamma t}}{2}\left(\cosh\frac{\Delta\Gamma t}{2} + \cos\Delta mt\right), \tag{1-31}$$

$$|\langle \bar{P}^0|P^t|\rangle|^2 = |\frac{q}{p}|^2|g_-(t)|^2 = |\frac{q}{p}|^2\frac{e^{-\Gamma t}}{2}\left(\cosh\frac{\Delta\Gamma t}{2} - \cos\Delta mt\right), \tag{1-32}$$

$$|\langle P^0|\bar{P}^t|\rangle|^2 = |\frac{p}{q}|^2|g_-(t)|^2 = |\frac{p}{q}|^2\frac{e^{-\Gamma t}}{2}\left(\cosh\frac{\Delta\Gamma t}{2} - \cos\Delta mt\right), \tag{1-33}$$

$$|\langle \bar{P}^0|\bar{P}^t|\rangle|^2 = |g_+(t)|^2 = \frac{e^{-\Gamma t}}{2}\left(\cosh\frac{\Delta\Gamma t}{2} + \cos\Delta mt\right). \tag{1-34}$$

The amplitudes of a neutral meson decay into a final state f can be expressed using the effective Hamiltonian $\mathcal{H}$:

$$\begin{aligned} A_f &= \langle f|\mathcal{H}|P^0\rangle, & \bar{A}_f &= \langle f|\mathcal{H}|\bar{P}^0\rangle, \\ A_{\bar{f}} &= \langle \bar{f}|\mathcal{H}|P^0\rangle, & \bar{A}_{\bar{f}} &= \langle \bar{f}|\mathcal{H}|\bar{P}^0\rangle, \end{aligned} \tag{1-35}$$

After defining the parameters

$$\lambda_f = \frac{q}{p}\frac{\bar{A}_f}{A_f}, \qquad \lambda_{\bar{f}} = \frac{q}{p}\frac{\bar{A}_{\bar{f}}}{A_{\bar{f}}} \tag{1-36}$$

The time-dependent decay rates can be written as

$$\begin{aligned} \Gamma(|\Phi(t)\rangle_{B\to f}) &= |g_+(t)A_f - \tfrac{q}{p}g_-t\bar{A}_f|^2 \\ &= \mathcal{N}_f|A_f|^2e^{-\Gamma t}\{\tfrac{1+|\lambda_f|^2}{2}\cosh\tfrac{\Delta\Gamma t}{2} + \tfrac{1-|\lambda_f|^2}{2}\cos(\Delta mt) \\ &-\mathcal{R}e(\lambda)_f\sinh\tfrac{\Delta\Gamma t}{2} - \mathcal{I}m(\lambda)_f\sinh(\Delta mt)\}. \end{aligned} \tag{1-37}$$

where $\mathcal{N}_f$ is a time-dependent normalisation factor. Similarly one can write

$$\begin{aligned} \Gamma(|\Phi(t)\rangle_{\bar{B}\to f}) &= \mathcal{N}_f|A_f|^2|\tfrac{p}{q}|^2e^{-\Gamma t}\{\tfrac{1+|\lambda_f|^2}{2}\cosh\tfrac{\Delta\Gamma t}{2} - \tfrac{1-|\lambda_f|^2}{2}\cos(\Delta mt) \\ &-\mathcal{R}e(\lambda)_f\sinh\tfrac{\Delta\Gamma t}{2} + \mathcal{I}m(\lambda)_f\sinh(\Delta mt)\}. \end{aligned} \tag{1-38}$$

The decay rates to the CP-conjugate final state $\bar{f}$ are obtained analogously, with $\mathcal{N}_f = \mathcal{N}_{\bar{f}}$ and the substitutions $A_f \to A_{\bar{f}}$ and $\bar{A}_f \to \bar{A}_{\bar{f}}$ in Eq.(1-37, 1-38)

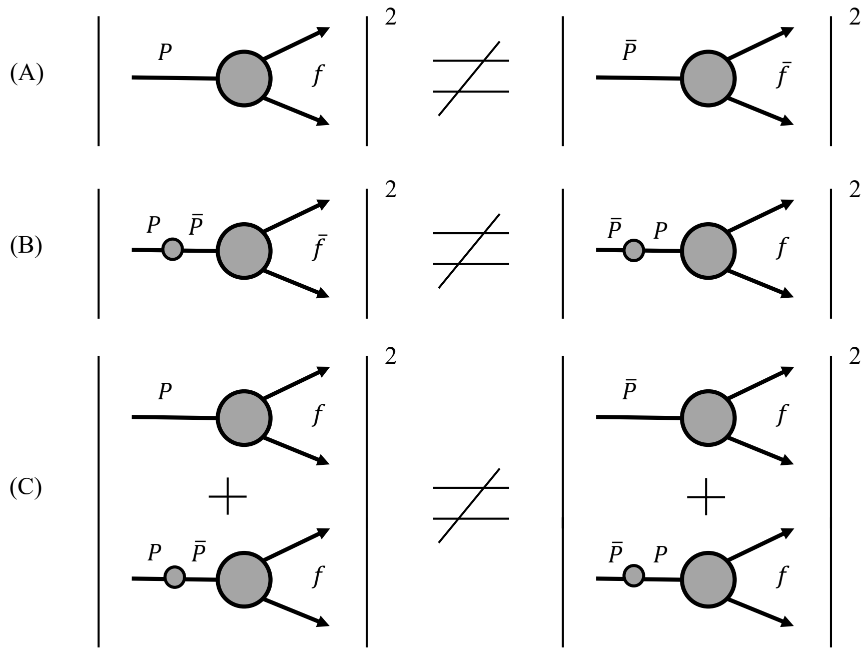

Figure 1.6 Schematic representation of *CP* violation in decays (A), mixing (B) and interference between mixing and decay (C).

1.3.4 Classification of *CP* violation

The *CP* symmetry relates particles with their anti-particles. If *CP* is conserved, one must have

$$\Gamma(A \to B) = \Gamma(\bar{A} \to \bar{B}), \tag{1-39}$$

with A and B representing any possible initial and final states. The only way to find *CP* violation is to look for decays where the equality presented in Eq. (1-39) does not hold. It is not easy to observe *CP* violation, since the deviations is very small.

In general, *CP* violation can be classified into three types: *CP* violation in decays, *CP* violation in mixing and *CP* violation in the interference between mixing and decay. They are briefly sketched in Fig. 1.6 and described in the following paragraphs.

1.3.4.1 *CP* violation in decays

CP violation in decays, also called *direct CP* violation, occurs when the decay rate for $P \to f$ is different from that of the *CP*-conjugated process $\bar{P} \to \bar{f}$:

$$|\frac{\bar{A}_{\bar{f}}}{A_f}| = |\frac{\sum_i \mathcal{A}_i e^{-i\phi_i} e^{i\delta_i}}{\sum_i \mathcal{A}_i e^{i\phi_i} e^{i\delta_i}}| \neq 1 \tag{1-40}$$

where ϕ and δ are the weak phase and strong phase, respectively. ϕ origins from weak interaction, thus with flip sign under *CP* conjugation; δ origins from intermediate state which is *CP* converged.

For decays of charged particles, *e.g.* B^+ and D^+, the *direct CP* violation is the only source of *CP* violation, the following asymmetry between final states can be measured to determine the direct *CP* violation experimentally:

$$\mathcal{A}_{f^\pm} = \frac{\Gamma(P^- \to f^-) - \Gamma(P^+ \to f^+)}{\Gamma(P^- \to f^-) + \Gamma(P^+ \to f^+)} = \frac{|\bar{A}_{f^-}/\mathcal{A}_{f^+}|^2 - 1}{|\bar{A}_{f^-}/\mathcal{A}_{f^+}|^2 + 1} \tag{1-41}$$

1.3.4.2 *CP* violation in mixing

CP violation in mixing is also known as *indirect CP* violation, happens when the decay amplitudes of $P^0 \to \bar{P}^0 \to \bar{f}$ and its conjugation process $\bar{P}^0 \to P^0 \to f$ are different. These two oscillation probabilities are given by Eq. (1-32, 1-33), thus they are identical unless:

$$|\frac{q}{p}| \neq 1. \tag{1-42}$$

Experimentally, this *CP* violation can be searched in flavour-specific, semileptonic decays of neutral mesons by comparing the oscillation rates with:

$$\mathcal{A}_{\mathrm{SL}}(t) = \frac{\partial_t\Gamma(\bar{P}^0(t) \to l^+X^-) - \partial_t\Gamma(P^0(t) \to l^-X^+)}{\partial_t\Gamma(\bar{P}^0(t) \to l^+X^-) + \partial_t\Gamma(P^0(t) \to l^-X^+)} = \frac{1 - |\frac{q}{p}|^4}{1 + |\frac{q}{p}|^4} \tag{1-43}$$

1.3.4.3 *CP* violation in the interference between mixing and decay

This type of decay occurs when a neutral meson can decay directly to a given final state, $P^0 \to f$, or via mixing, $P^0 \to \bar{P}^0 \to f$, and the final state f is common to both P^0 and $\bar{P}^0$. This form of *CP* violation can be observed by measuring a non-zero value for the *CP* asymmetry parameter, which is given by

$$\mathcal{A}_{f_{\mathrm{CP}}} = \frac{\partial_t\Gamma(\bar{P}^0(t) \to f_{\mathrm{CP}}) - \partial_t\Gamma(P^0(t) \to f_{\mathrm{CP}})}{\partial_t\Gamma(\bar{P}^0(t) \to f_{\mathrm{CP}}) + \partial_t\Gamma(P^0(t) \to f_{\mathrm{CP}})}. \tag{1-44}$$

If the decay width between P^0 and $\bar{P}^0$, $\Delta\Gamma = 0$ and $\lambda_f = |\frac{q}{p}| = 1$(e.g.$B^0$), the above equation reduces to

$$\mathcal{A}_{f_{\mathrm{CP}}} = \mathcal{I}m(\lambda_f)\sin(\Delta m t). \tag{1-45}$$

For B_s^0 decays, the asymmetry parameter could be expressed as

$$\mathcal{A}_{f_{\rm CP}} = \eta_f \sin(\phi_s)\sin\Delta(m_s t) \tag{1-46}$$

where η_f is the CP eigenvalue of each of the final states and ϕ_s is the CP observables.

1.4 Advantages of using $b \to J/\psi X$ decays for SM probing

In the past few decades, many important experimental results have been observed in b-physics using $b \to J/\psi X$ decays. B_c^+ meson was first found by the CDF collaboration with semileptonic $B_c^+ \to J/\psi l^+ \nu$ decays in 1998 [63-64]. CP violation in B^0 meson system was observed in $B^0 \to J/\psi K_S^0$ decays by the Babar and Belle collaboration in 2001 [65-66]. Measurement of CP violation phase ϕ_s in B_s^0 meson system was first reported by the CDF and D0 collaboration at Tevatron in 2012 with $B_s^0 \to J/\psi\phi$ decays [67-68]. Two hidden-charm pentaquarks were observed in the mass spectrum of $J/\psi p$ using $\Lambda_b^0 \to J/\psi p K^-$ decays by the LHCb collaboration in 2015 [32].

J/ψ meson has a relatively narrow decay width with quark content $c\bar{c}$. The mass and decay width of J/ψ meson are precisely measured to be $M(J/\psi) = 3096.900 \pm 0.006$ MeV and $\Gamma(J/\psi) = 92.9 \pm 2.8$ KeV [58]. The lightest meson that has quark content c or $\bar{c}$ is the D meson, whose masses are around 1870 MeV. The mass of J/ψ meson is smaller than two D meson, thus it can decay only via $c\bar{c}$ annihilation. Experimentally, $J/\psi \to \mu^+\mu^-$ and $J/\psi \to e^+e^-$ are often used in the event reconstruction.

At the LHCb experiment, due to advantages of the muon tracking reconstruction system, the tracking reconstruction efficiency is great than 96% and momentum resolution $\frac{\Delta p}{p}$ varies from 0.5% at low momentum to 1.0% at 200 GeV [69-71]. In practice, a large fraction of background in $b \to J/\psi X$ can be suppressed with tight selection criteria on J/ψ mesons. The mass resolution is about 10 MeV [72] for $b \to J/\psi X$ decays with constraint on J/ψ meson mass which provide a good probe for studying b-physics in the SM.

Since the start of operation from 2010, many important analyses involving $b \to J/\psi X$ decays have been studied by the LHCb experiment. These results include newly found B_c^+ decays: $B_c^+ \to J/\psi\pi^+\pi^-\pi^+$ [73], $B_c^+ \to J/\psi D_s^{*+}$ [74], $B_c^+ \to J/\psi K^+$ [75] and $B_c^+ \to J/\psi K^+K^-\pi^+$ [76]; measurements of the CP-violating phase β in B^0 system using $B^0 \to J/\psi(\to \mu^+\mu^-)K_S^0$ [77] and $B^0 \to J/\psi(\to e^+e^-)K_S^0$ [78] decays, as well as measurements of CP-violating ϕ_s in B_s^0 system using $B_s^0 \to J/\psi\phi$ [79] and $B_s^0 \to J/\psi\pi^+\pi^-$ [80] decays with LHCb Run-I data.

In this dissertation, two categories of studies using $b \to J/\psi X$ ($J/\psi \to \mu^+\mu^-$) decays are performed: searching for hidden-charm strangeness pentaquark states in $\Xi_b^- \to J/\psi \Lambda K^-$ decays which can be a good test of the quark model and non-perturbative QCD theory; measurements of CP-violation phase ϕ_s in $B_s^0 \to J/\psi K^+ K^-$ and $B_s^0 \to J/\psi \pi^+ \pi^-$ decays which can be used to test the unitarity of the CKM matrix and constraint the NP scenario beyond SM.

Chapter 2 The LHCb experiment

The LHCb experiment[81] is one of the four major experiments at the Large Hadron Collider (LHC)[82]. It is designed focusing on the study of physics processes involving b- and c- quarks, to explore the asymmetry between matter and antimatter and to search for rare decays and rare particles. This chapter introduces the LHC and the main elements of the LHCb detector, including the tracking system, the particle identification system and triggers. Finally a short overview of the flavour tagging method used in LHCb is presented.

2.1 The Large Hadron Collider

The LHC, hosted by the European Organisation for Nuclear Research (CERN), is located at the France-Switzerland border. It is at present the world's largest and most powerful particle accelerator. It is a two-ring hadron accelerator and collider, installed inside a 26.7 km long tunnel, placed at a depth of about 100 m underground. The accelerator is designed to collide beams of protons up to a centre-of-mass energy of $\sqrt{s}$ =14 TeV, with a peak luminosity of 10^{34} cm$^2 s^{-1}$. Until now, the LHC has collided protons at $\sqrt{s}$ =7 TeV in 2011, $\sqrt{s}$ =8 TeV in 2012 and $\sqrt{s}$ =13 TeV in 2015-2018.

There are four main particle detectors at the LHC, where the beams are made to collide. The ATLAS (A Toroidal LHC ApparatuS)[83] and CMS (Compact Muon Solenoid) experiments[84] are two general-purpose detectors (GPDs) with cylindrical geometry around the beam line, which were designed to look for new particles at TeV scale and search for physics beyond the SM. The ALICE (A Large Ion Collider Experiment) experiment[85] is specially designed to collect heavy-ion collisions, studying the high energy density objects, and to understand the nature and properties of the quark-gluon plasma (QGP) state. Finally, the LHCb experiment is designed to study decays of hadrons containing bottom and charm quarks, with particular focus on precision measurement of *CP* violation, search for non-SM sources of *CP* violation and evidence of new physics in rare decays.

An overview of the LHC is given in Fig. 2.1. The proton accelerated chain begins with the extraction of protons from hydrogen gas where the electrons of the hydrogen atoms have been stripped off by an electric field. It is not possible to directly accelerate

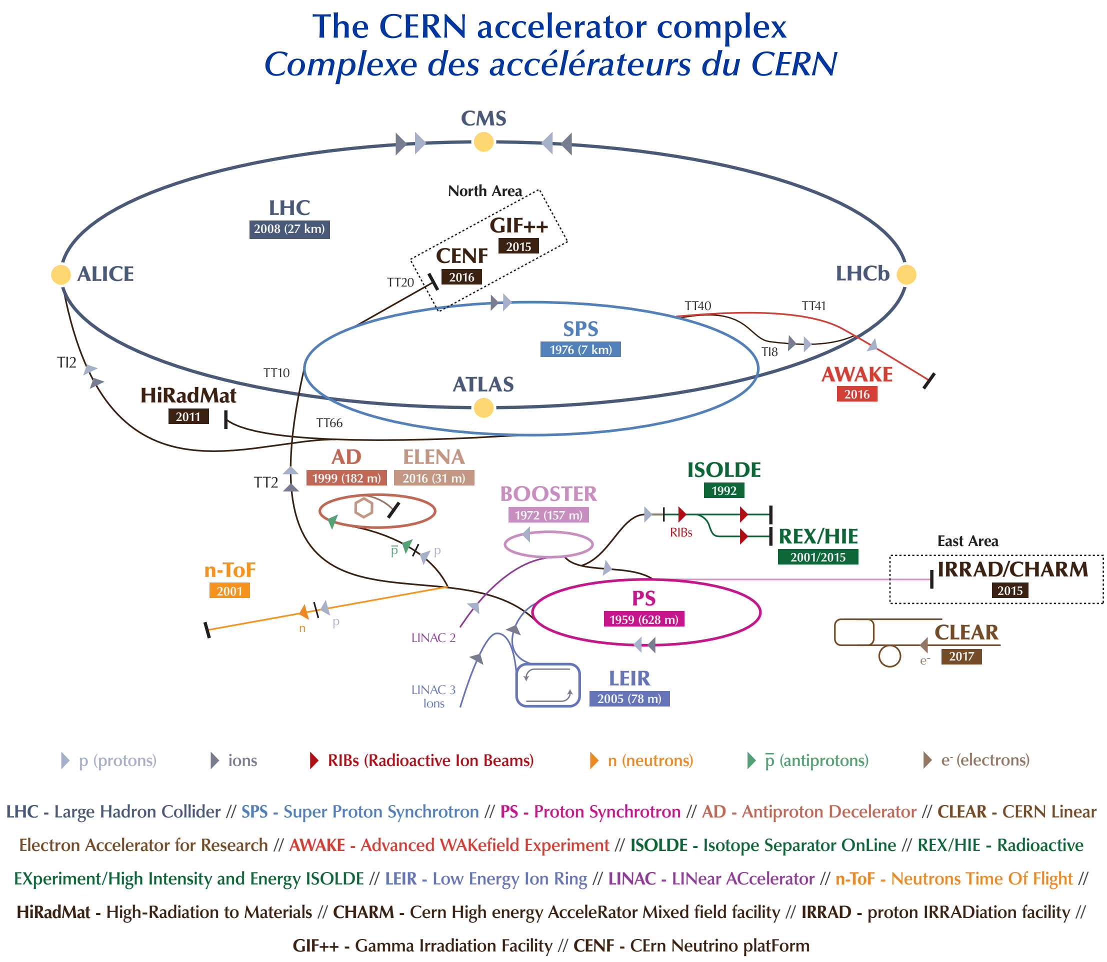

Figure 2.1 Schematic representation of the CERN accelerator complex and LHC injector chain. Figure taken from Ref.[86].

protons from their quasi-rest conditions up to the require energy, so the acceleration is taken in several steps. First, protons are injected into the linear particle accelerator, LINAC2, which accelerates the protons to the energy of 50 MeV. Then, the beam is injected into the Proton Synchrotron Booster (PSB), which accelerates the protons at energies up to 1.4 GeV, following by the Proton Synchrotron (PS), where it reaches energies of 25 GeV. The next step is the Super Proton Synchrotron (SPS), where it is accelerated to 450 GeV. After SPS, the protons are finally transferred to the two beam pipes of the LHC with the beams circulating in opposite directions to each other.

The proton beams inside the LHC ring are not continuously distributed but are arranged in bunches. Each bunch contains $O\,(10^{11})$ protons and is separated in time by about 25 ns, corresponding to a crossing frequency of 40 MHz. The collision rate of

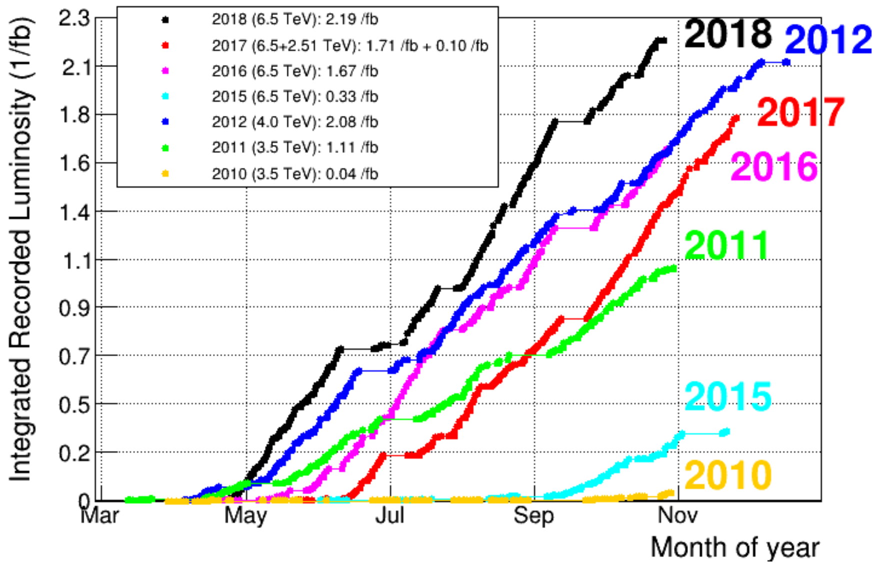

Figure 2.2 Integrated luminosity recorded by LHCb as a function of the month of the year, divided by years of data taking. Figure taken from Ref.[87].

protons is defined by the luminosity of the beam, $\mathcal{L}$, which is parametrised as

$$\mathcal{L} = F\frac{N_b^2 n_b \gamma_r f_{\text{rev}}}{4\pi\epsilon_n\beta^*}, \tag{2-1}$$

where F is the luminosity reduction factor resulting from the beam crossing angle, N_b is the number of particles per bunch, n_b is the number of proton bunches per beam, γ_r is the Lorentz factor, f_{rev} is the revolution frequency, ϵ_n is the normalised transverse beam emittance and $\beta^*$is transverse size of the beams at the collision point. The total number of bunches and bunch scheme in the beam, depending on the physics of interests, vary over experiments. The two high luminosity experiments, ATLAS and CMS, collected data at a maximum instantaneous luminosity of 2.06×10^{34} cm$^{-2}s^{-1}$. The LHCb, requiring a low beam intensities, recorded data at a peak luminosity of 4×10^{32} cm$^{-2}s^{-1}$.

The LHC has performed very well during Run-I (2010-2012) and Run-II (2015-2018) data-taking period, allowing the LHCb experiment to collect more than 9 fb^{-1} of integrated luminosity as shown in Fig. 2.2, with an efficiency over 90%. This unprecedented sample of charm and beauty hadrons allows the LHCb collaboration to perform high-precision measurements and to improve results from the BaBar, Belle and CDF collaborations.

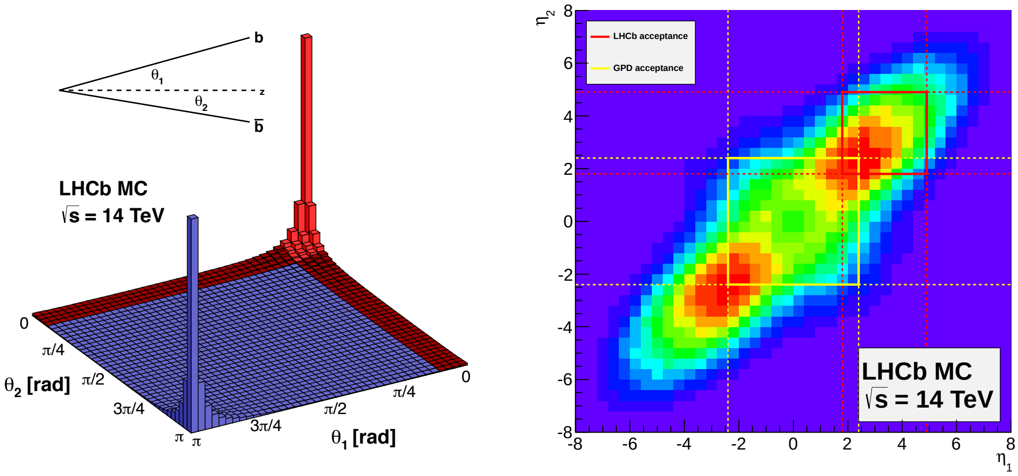

Figure 2.3 Production angles of $b\bar{b}$ pair with respect to the beam direction (left). Pseudorapidity of $b\bar{b}$ produced in a pp collision at $\sqrt{s}$=14 TeV generated using Pythia 8 [89] (right). The solid lines show the acceptance of LHCb (red) compared to the general purpose detectors (yellow). Figure taken from Ref. [91].

2.2 The LHCb detector

The LHCb detector is a signal-arm forward spectrometer designed to take advantage of the large $b\bar{b}$ production cross-section at the LHC. The $b\bar{b}$ production cross-section σ is $\sim$ 295 μb at 7 TeV and $\sim$ 560 μb at 13 TeV [88] at the LHC. The production cross-section of $c\bar{c}$ quark pairs is $\sim 20{\times}\sigma(pp \to b\bar{b}X)$. At high centre of mass energies, the b and c quarks are produced strongly boosted along the beam-line. Thus, they are produced prominently in the forward or backward region as shown in Fig. 2.3. To take advantage of this peculiarity, as well as considering the spatial limitation, the LHCb detector is designed as a forward spectrometer covering the range of pseudorapidity in $2 < \eta < 5$. The angular acceptance of the LHCb detector is 10-300 mrad in the magnet bending plane and up to 250 mrad in the vertical plane. 24% of the $b\bar{b}$ quark pairs can drop into the LHCb acceptance. Comparing with the GPDs, LHCb covers a different complementary geometry region which allows us to explore the physics in the forward region.

A schematic representation of the LHCb detector and the position of each subdetector in the LHCb cavern are shown in Fig. 2.4. A right-handed Cartesian coordinate system is used with origin located at the nominal interaction point. The z-axis is aligned with the beam-line direction and the y-axis points vertically upwards.

To perform a high quality flavour physics measurement at LHCb, two main requirements are considered: First, the ability to reconstruct the trajectory of the decay

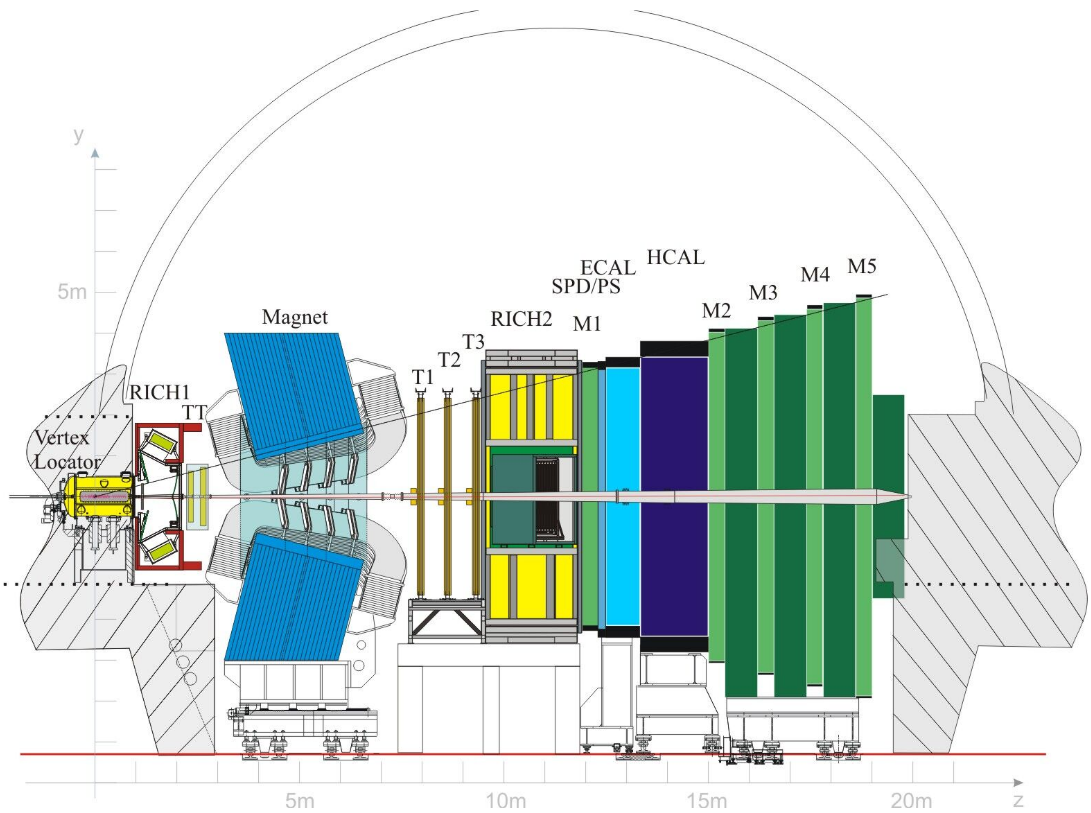

Figure 2.4 An overview of the LHCb detector[92]. The z axis indicates the direction of the beam line.

hadrons and well separate the primary pp collision vertex (PV) from the secondary b-hadron decay vertex (SV). Second, the capability of distinguish between topological similar decays that only differ by final state particles. The detector tracking and particle identification systems and how they fulfil these requirements are discussed in the following sections.

2.2.1 LHCb tracking system

The LHCb tracking system consists of the Vertex Locator (VELO) and a series of tracking stations located both up (TT) and downstream (T1-T3) of the detector dipole magnet. Both VELO and TT use silicon micro-strip technology. The T-station (T1-T3) makes use of two different technologies, due to the different occupancies in the inner and outer regions of the detector. The central part, referred to as Inner Tracker (IT), uses a silicon strip similar as that used by TT. The outside region, referred to as Outer Tracker (OT), consists of straw-drift tubes.

An illustration of the position of each tracking subdetector and the different reconstructed track types are illustrated in Fig. 2.5. Not all charged particles have hits in all the tracking subdetectors. At the PV and SV, particles with large transverse momentum

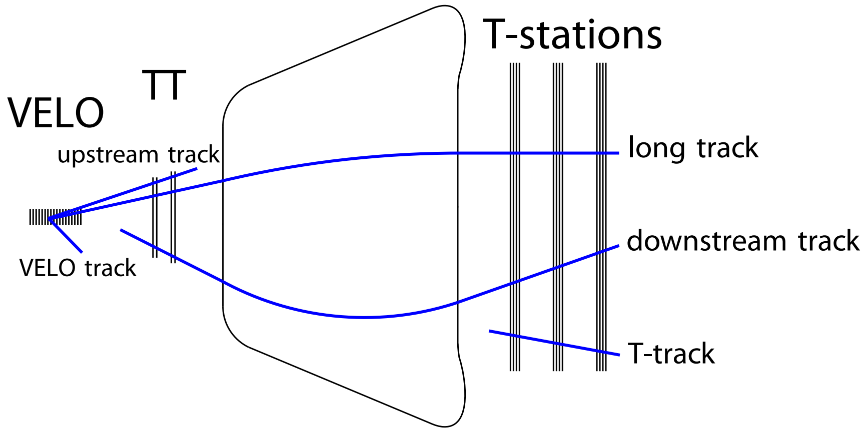

Figure 2.5 Schematic of tracking components with different types of track definitions[71].

or produced in backward direction will fly out of the LHCb acceptance and leave hits only in VELO, referred to as *VELO* tracks. These tracks could be used for vertex reconstruction studies but not used in the further physics analysis. Low momentum particles in the forward region can have hits in both VELO and TT but failed to hit the T-station, referred to as *upstream* tracks. Long-lived particles like Λ and K_S^0 are often produced outside VELO, the decay products of them only leave hits in the downstream tracking stations, referred to as *downstream* tracks. Tracks traverse all the tracking systems called *long* tracks and tracks have hits only in T-station are named as *T* tracks. The most useful track types for physics analyses are *long* and *downstream* tracks.

2.2.1.1 Vertex locator

The VELO is designed to perform precise measurements of the track coordinates near the interaction region. For decays of b and c hadrons, it is crucial to reconstruct the production and decay vertices and measure the impact parameter (IP), defined as the distance of closest approach between the PV of the event and the track.

The VELO is composed of 2×21 modules of silicon micro-strip sensors placed between -0.2 < z < 0.8 m around the beam line and 8 mm from its axis. An overview is given in Fig. 2.6. Each semicircular module is composed of two sensors, one with strips in the radial direction (R sensors) and the other with strips in the azimuthal direction (Φ sensors), as shown in Fig. 2.7. The two modules in each station are slightly overlapping to ensure a full Φ coverage. Together with the station position in z-axis, a 3-dimensional measurement of a track point is performed. Four additional modules, installed only R sensors, were placed upstream of the interaction point, referred to as the VETO stations.

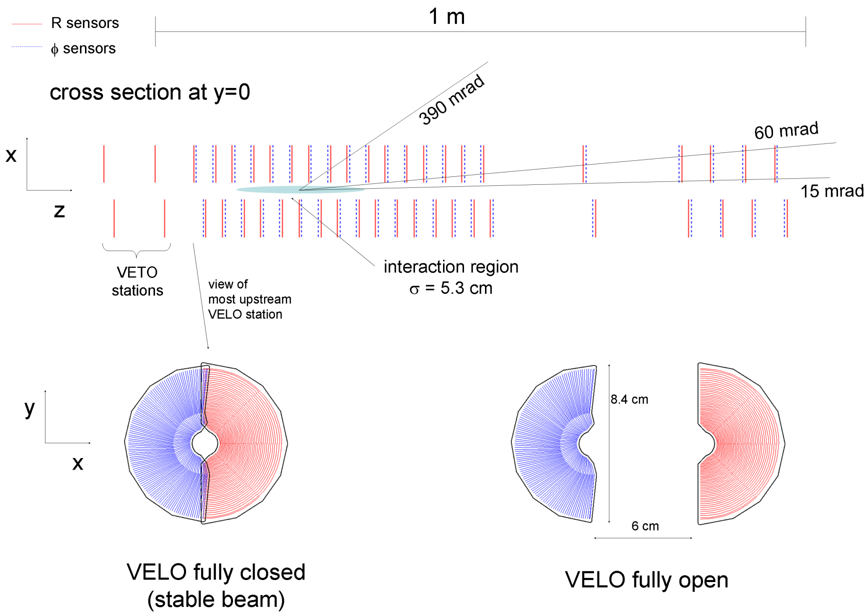

Figure 2.6 Layout of the VELO detector[92].

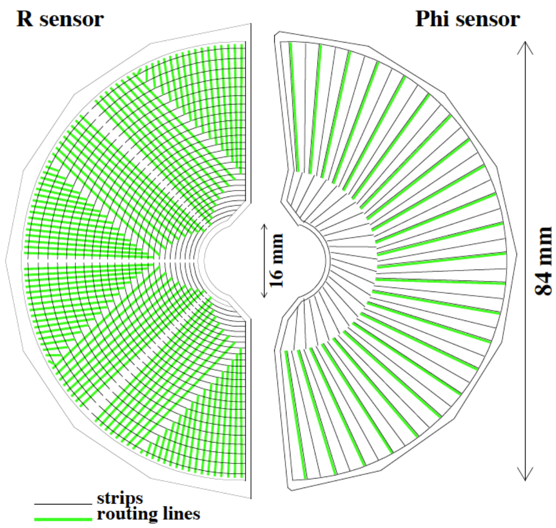

Figure 2.7 Geometry of the R (left) and Φ (right) sensors of the silicon modules composing the VELO[93].

They were initially designed to study the multiple pp collisions but used for luminosity measurement now. During the injection of protons into the LHC, the beam position is not stable and might damage the VELO. Therefore, the VELO is designed as retractable, the stations are fully closed only during data-taking period when stable beam has reached. The open and close configurations are also given in Fig. 2.6.

The performance of VELO detector have been analysed using the data collected in

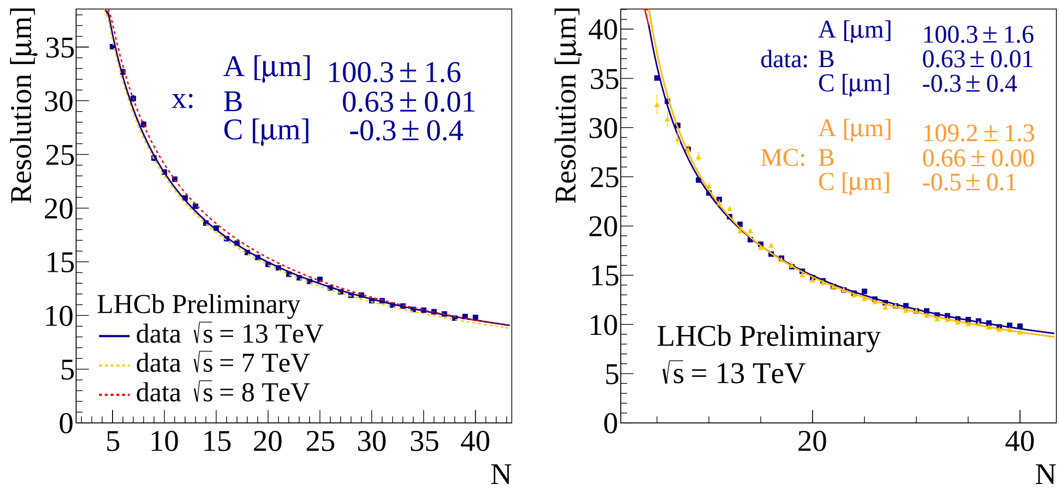

Figure 2.8 VELO PV resolution for events with one PV as a function of the number of tracks in the x direction in data (left) and MC (right).

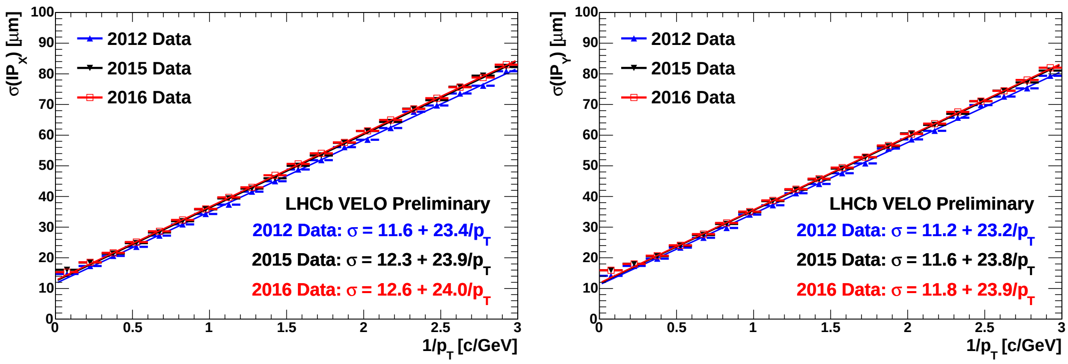

Figure 2.9 VELO IP resolution for events with one PV as a function of $1/p_{\mathrm{T}}$ in both the x (left) and y (right) direction in 2012 data (blue), 2015 data (black) and 2016 data (red).

Run 1. Well PV resolutions and IP resolutions can effectively reject background events which are very close to the PV. The PV resolution and IP resolution of the VELO are shown in Fig. 2.8 and Fig. 2.9.

2.2.1.2 Dipole magnet

A warm dipole magnet is placed between the TT and T-station to deflect charged particles allowing the measurement of the particles momentum. It is composed of two separate saddle-shaped aluminium coils, as illustrated in Fig. 2.10. The magnetic field is oriented in the y direction and covers a range of ± 250 mrad vertically and ± 300 mrad horizontally which can deflect the charged particles in the x-z plane with a bending power of 4 Tm. To achieve the maximum momenta precision and resolution, the integrated

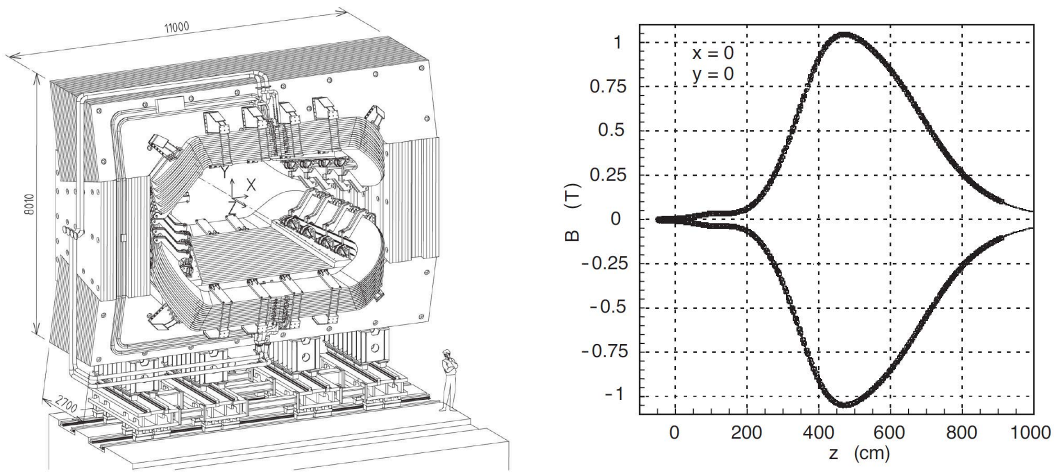

Figure 2.10 A schematic representation of the magnet (left). Magnetic field as a function of z-position, at x=0 cm and y=0 cm (right). Figures taken from Ref.[92]

magnetic field must have a precision on the order of 10^{-4}. This precision was achieved using arrays of Hall probes, with which the components of the field were measured in a fine grid spanning from the interaction point to the RICH2 detector.

During the data-taking period, the polarity of the magnet is reversed several times such that a same size of data samples are collected for each magnet. This allows the cancellation of any left-right detector asymmetry which may appears in the *CP* violation measurements.

2.2.1.3 Silicon tracker

The Silicon Tracker (ST) consists of two subdetectors, the Tracker Turicensis (TT) and the Inner Tracker (IT), positioned upstream and downstream of the magnet, respectively. The TT covers the full acceptance of the detector, while the IT covers a 120 cm wide and 40 cm high cross-shaped area in the centre of the three downstream tracking stations. Both TT and IT are composed of four layers of silicon microstrip sensors with a pitch of 183 μm and 198 μm between the strips. The layers are placed in an $(x-u-v-x)$ arrangement, in which the first and last layers are oriented vertically, and the second and the third layers are rotated by a stereo angel of -5° and +5°, respectively.

Each TT layer is composed of modules holding 14 sensors each. The central modules are divided into two halves, placed above and below the beam pipe. Each of the half modules is organised into two or three readout sectors. The readout sensors are bonded together in a group of one, two, three or four as a sector, depending on the density of particle flux. An overview of the third layer are shown in Fig. 2.11. The TT is especially

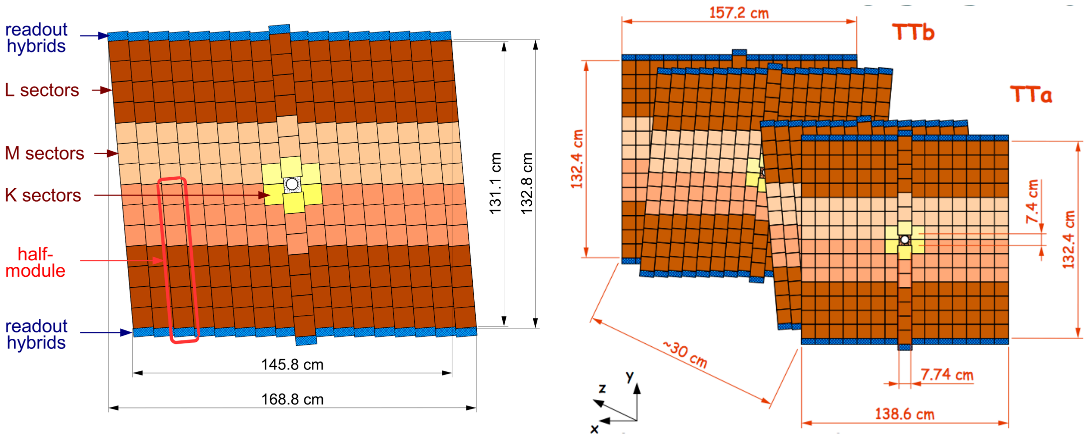

Figure 2.11 Layout of the third TT detection layer (left). Schematic view of the TT detector (right). Figures taken from Ref.[92].

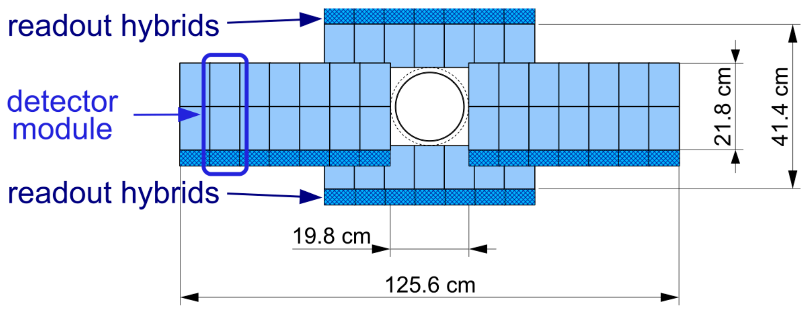

Figure 2.12 Layout of a second IT station detection layer[92].

useful in reconstructing long lived particles such as K_S^0 and Λ hadrons that are not detected by the VELO, as well as low momentum tracks which will be bent out of the acceptance by the magnet.

The three IT stations share the same four-layer layout as TT. Each IT layer has 7 silicon modules. The modules are arranged in four detector boxes, on the two sides of the beam and on its top and bottom as shown in Fig. 2.12. The top and bottom boxes have one readout sensor while the side modules have two. The IT tracker helps in reconstructing tracks which have passed through the magnetic field and lie near the beam axis.

2.2.1.4 Outer tracker

The outer region of the T-stations is referred as the Outer Tracker (OT). A schematic view of the OT is presented in Fig. 2.13. It is a drift detector which consists of three gas-tight straw-tube stations, positioned at T1, T2 and T3. It covers the rest of the acceptance which are not taken by the IT. Each station is built out of four layers, arranged in the same stereo layout as the ST. Each module contains two staggered layers of 64'

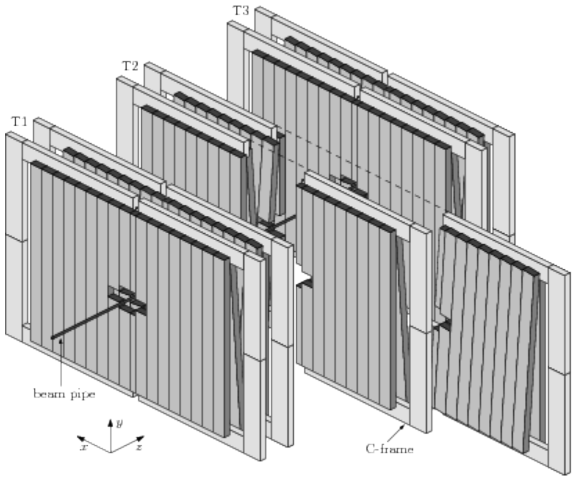

Figure 2.13 An overview of the OT stations [94].

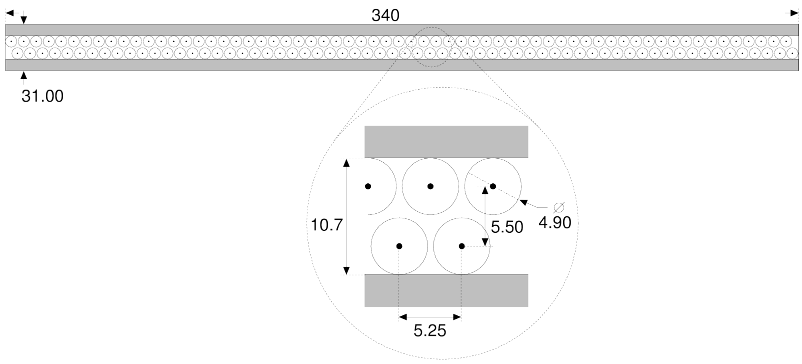

Figure 2.14 A cross section view of a straw-tubes module [92].

straw' drift-tubes with an inner diameter of 4.9 mm, as shown in Fig. 2.14. A gas mixture of 70% Argon, 28.5% CO_2 and 1.5% O_2 is used to guarantee a drift time below 50 ns and resulting a spatial resolution of 200 μm.

2.2.2 LHCb particle identification system

Particle identification (PID) is performed combining information from two Ring-Imaging Cherenkov (RICH) detectors, the calorimeter system and the muon system. In each event, mass hypotheses are assigned to every particle, and the relative likelihood is calculated via multivariate likelihood classifiers combining information from the PID subdetectors. The classifiers are trained to compare the various particle hypotheses against the pion hypothesis. One can then estimate whether a reconstructed track belongs more likely to a kaon or pion based on the difference between the log-likelihood of the kaon and pion hypotheses, respectively. The particle identification efficiency of this classifier varies depending on the track momentum.

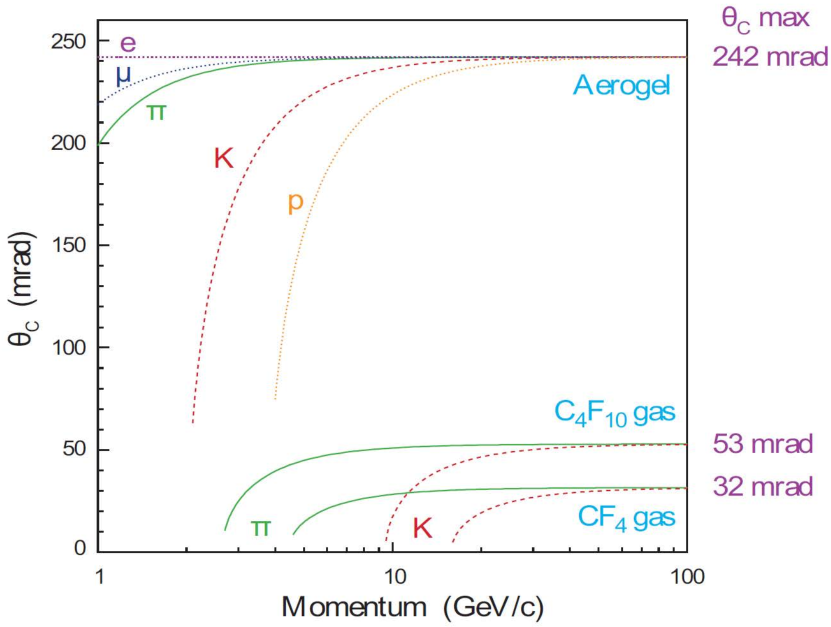

Figure 2.15 Reconstructed Cherenkov angle as a function of the track momentum[92]..

In LHCb, PID information is further refined by the use of a neural network combining the output of the PID classifiers and information from the other subdetectors. The output of the neural network is a variable taking values between 0 and 1, that can be interpreted as the absolutely probability of a particle to be of a certain species.

2.2.2.1 RICH

LHCb has two RICH detectors. These detectors can measure the Cherenkov radiation emitted by charged particles traversing a medium faster than the speed of light in that medium. The emission angle Cherenkov radiation is given by

$$\cos\theta_C = \frac{1}{n\beta} \tag{2-2}$$

where θ_C is the angle between the direction of the emitted light and the trajectory of the particle, n is the refractive index of the medium and β is the particle velocity in units of c. Knowing n and measuring $\cos\theta_C$ can give us the results on the speed of the particle, combing this information with the momentum measurement given by the track system, the mass of the particle can be determined. Then Cherenkov angle dependence on the particle momentum is shown in Fig. 2.15.

Both RICH detector record Cherenkov light by means of a system of two mirrors that deflect photons outside of LHCb acceptance. Hybrid Photon Detectors (HPD) are

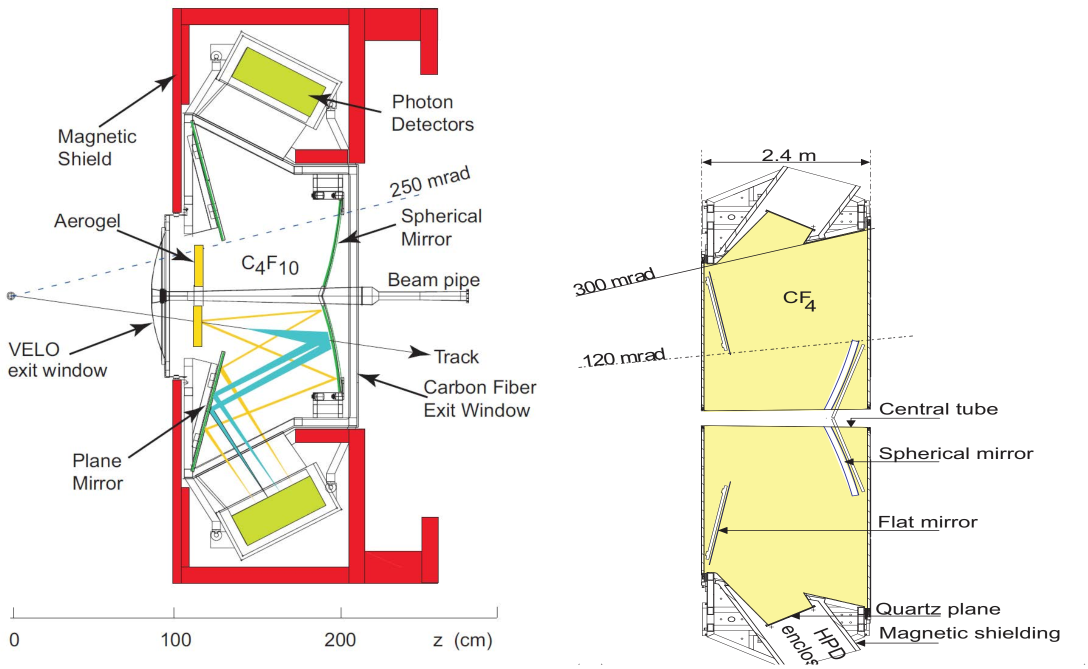

Figure 2.16 Side view of RICH1 (left) and RICH2 (right) detectors [92].

employed to read out the signal. The first RICH detector, as illustrated in Fig. 2.16, is located between the VELO and the TT. It uses a C_4F_{10} radiator, covering the momentum range of $1 < p < 60$ GeV. RICH2 is situated downstream of the T-stations and covers the momentum range $15 < p < 100$ GeV using CF_4 as radiator. RICH2 covers only a central region ($\eta < 3$) of the LHCb acceptance, where high momentum particles are most abundant.

2.2.2.2 Calorimeters

The calorimeter system is composed of four subdetectors, as shown in Fig. 2.17. A Scintillating Pad Detector (SPD), consisting of fine-granularity scintillator pads, is followed by a 15 mm thick lead absorber plane and by another scintillating pad detector with Pre-Shower function (PS). The aim of the SPD layers is to help distinguishing between calorimeter charge deposits initiated by charged and neutral particles. The electromagnetic showering process then initiates in the PS, which has the same function of the ECAL, but provided much finer granularity. The radiation length X_0, defined as the mean distance over which a high-energy electron reduces its energy by a factor $1/e$, losing energy by bremsstrahlung, of SPS and PS combined amount to 2.5 X_0

The ECAL, built as a sampling calorimeter, has a length of 25 X_0 in order to fully contain the whole electromagnetic shower. It is composed of 66 alternating layers of

2 mm thick lead and 4 mm thick scintillator tiles. The latter are wrapped in reflecting Tyvek paper with the purpose of increasing the light collection efficiency. Wavelength shifting fibres collect the light generated in the scintillator and guide it to Multi-Anode Photomultiplier Tubes (MAPMT). The same readout technology is shared by the SPD, PS and ECAL, but in the ECAL 64 fibres are read out together by a single photomultiplier.

The HCAL is also made of alternating layers of scintillating tiles and absorbing material for a length of 19.7 cm, but the tiles oriented paralleled to the beam pipe. The readout technology uses wavelength shifting fibres and PMTs, which are placed at the downstream end of the HCAL.

The energy resolution of the calorimeters has an energy dependence measured to be

$$\begin{aligned} \frac{\sigma_E/}{E} &\simeq \frac{9\%}{\sqrt{E}\mathrm{GeV}} \oplus 0.8\% \qquad \text{for the ECAL and} \\ \frac{\sigma_E/}{E} &\simeq \frac{69\%}{\sqrt{E}\mathrm{GeV}} \oplus 10\% \qquad \text{for the HCAL.} \end{aligned} \tag{2-3}$$

where first term accounts for stochastic effects in the development of the shower, and the second one is due to the intrinsic resolution of the detector.

The addition of the preceding SPD/PS layer largely improves the PID performance of the calorimeter system. Electrons are separated from hadrons with an efficiency of 92% and a misidentification rate of hadrons as electrons of 4.5%.

2.2.2.3 Muon stations

The muon system is composed of five Multi-Wire Proportional Chamber (MWPC) detectors (M1-M5). The first one, M1, aimed at improving the transverse momentum resolution for use in the trigger, is located in front of the calorimeter system. The other four stations, M2-M5, are placed downstream of the HCAL and interleaved by 80 cm thick layers of iron, acting as absorber stopping all particles except muons and neutrinos. A side view of the muon system is presented in Fig. 2.18.

The muon stations have finer granularity in the region closest to the beam pipe, and are composed of MWPC. The innermost part of M1 uses triple-GEM (Gas Electron Multiplier) detectors, which are more suited to cope with the higher occupancy of that region.

The identification of muons is implemented in two ways. One provides information used by the likelihood classifier. The other one is a binary classifier based on a minimum number of hits in the muon stations depending on the track momentum. Both classifiers

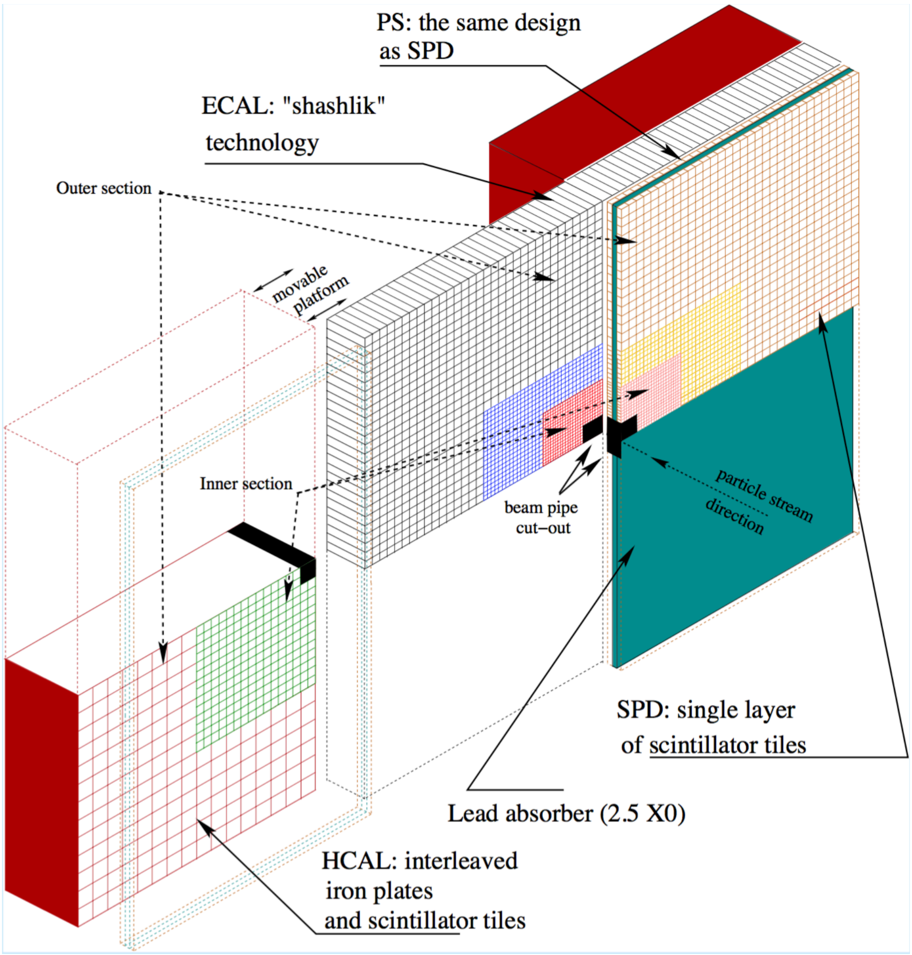

Figure 2.17 An overview of the calorimeter system[92].

have a very high identification efficiency as well as a tight background rejection.

2.2.3 LHCb trigger

A good trigger system is fundamental in every high energy physics experiments in order to only save the events of interesting while reject most of the background. At the nominal instantaneous luminosity of $2{\times}10^{32}$ cm$^{-2}s^{-1}$, the rate of events containing at least one pp interactions is roughly 10 MHz which is way too large to be stored. The LHCb detector can only be read out at a rate of 1 MHz and data is only saved to disk at a rate between 2-5 kHz in Run 1 and up to 12 kHz in Run 2. The LHCb trigger consists of two levels: the Level-0 (L0) hardware trigger which uses custom electronics synchronised with the LHC clock and the High Level Trigger (HLT) software trigger which runs asynchronously from the LHC clock. The general flow of information through the trigger systems for 2011, 2012, 2015 (where 2015 is representative of all Run 2) are shown in Fig. 2.19.

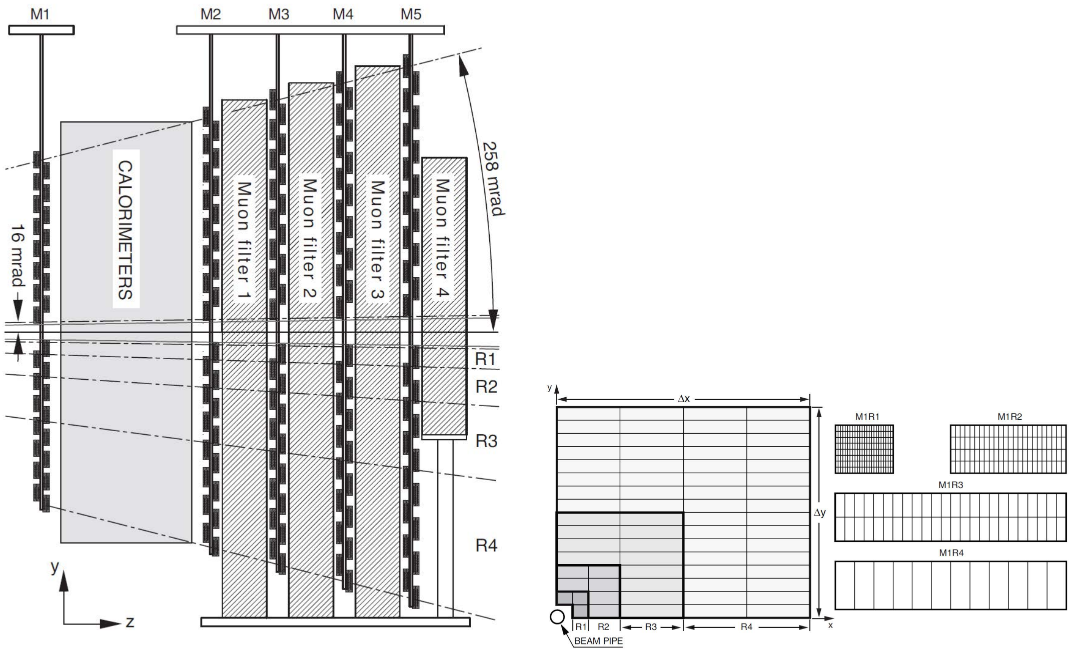

Figure 2.18 Side view (left) and front view (right) of the muon system[92].

In LHCb offline analysis, all the trigger decisions can be associated with the offline reconstructed signal candidates and hence can be classified into three categories with respect to that candidates: 'Trigger on Signal' (TOS), 'Trigger Independently of Signal' (TIS) and 'Trigger on Both' (TOB). TOS candidates are those triggered by the final state particles of the signal candidate under study, regardless of the remaining tracks in the event. TIS candidates are those triggered by the tracks of other particles presents in the same event instead of the signal. TOB candidates are those triggered both by the final state particles of the signal candidate and the tracks in the rest of the events.

2.2.3.1 Hardware trigger

The L0 hardware trigger consists of two independent parts: the calorimeter trigger and the muon trigger. The information from these two triggers is used to decide whether or not to pass the full event to the HLT. It helps to reduce the rate from the maximum bunch crossing rate of 40 MHz to 1 MHz.

The calorimeter trigger identifies high transverse energy E_{T} electrons, photons and hadrons. It forms clusters by adding the E_{T} of 2×2 cells in the ECAL and HCAL, and selects the clusters with the highest E_{T}. An L0 Electron candidates is the highest E_{T} ECAL cluster with 1 or 2 PS cells hit in front of the ECAL cluster and at least one SPD cells corresponding to the PS cells. An L0 Photon candidates has the same requirements

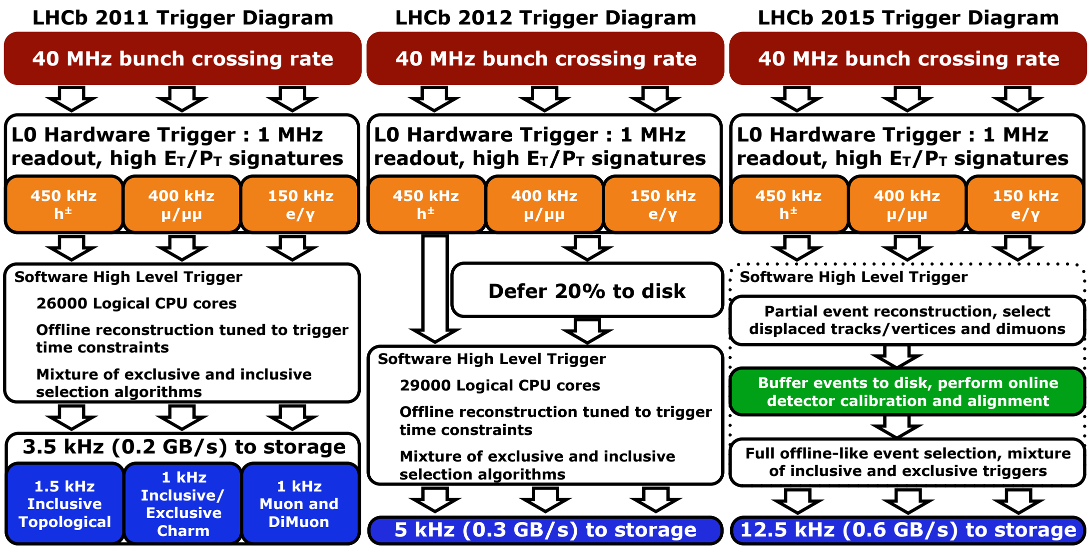

Figure 2.19 Trigger schemes in 2011 condition (left), 2012 condition (middle) and Run 2 (right)[92].

Table 2.1 The L0 thresholds for the different trigger lines used to take the majority of the data in 2011 and 2012.

L0 trigger	E_T or p_T threshold 2011	2012	SPD threshold
Electron	> 2.5 GeV	> 3.0 GeV	< 600
Photon	> 2.5 GeV	> 3.0 GeV	< 600
Hadron	> 3.5 GeV	> 3.7 GeV	< 600
Muon	> 1.48 GeV	> 1.76 GeV	< 600
Dimuon	$> (1.3)^2$ GeV	$> (1.6)^{2}$ GeV	< 600

as for a electron candidate, but without hit in the SPD cells. An L0 Hadron candidates is the highest E_T HCAL cluster.

The muon trigger uses information provided by the five muon stations to look for muon tracks with large p_T. The trigger is fired if at least one muon candidate has a p_T greater than the a given threshold (L0 Muon) or the product of the two largest p_T of muon candidates is larger than a given threshold (L0 Dimuon).

A typical minimum E_T or p_T values and number of SPD hits threshold are given in Table. 2.1 and Table. 2.2.

2.2.3.2 Software trigger

The HLT trigger consists of two stages, HLT1 and HLT2, which are carried out by C++ applications running on an approximately 52,000 logical CPU cores (~29,000 in Run

Table 2.2 The L0 thresholds for the different trigger lines used to take the majority of the data in 2015-2017.

L0 trigger	E_T or p_T threshold			SPD threshold
	2015	2016	2017	
Electron	> 2.7 GeV	> 2.4 GeV	> 2.11 GeV	< 450
Photon	> 2.7 GeV	> 2.78 GeV	> 2.47 GeV	< 450
Hadron	> 3.6 GeV	> 3.7 GeV	> 3.46 GeV	< 450
Muon	> 2.8 GeV	> 1.8 GeV	> 1.35 GeV	< 450
Dimuon	$> (1.69)^2$ GeV	$> (2.25)^2$ GeV	$> (1.69)^2$ GeV	< 450

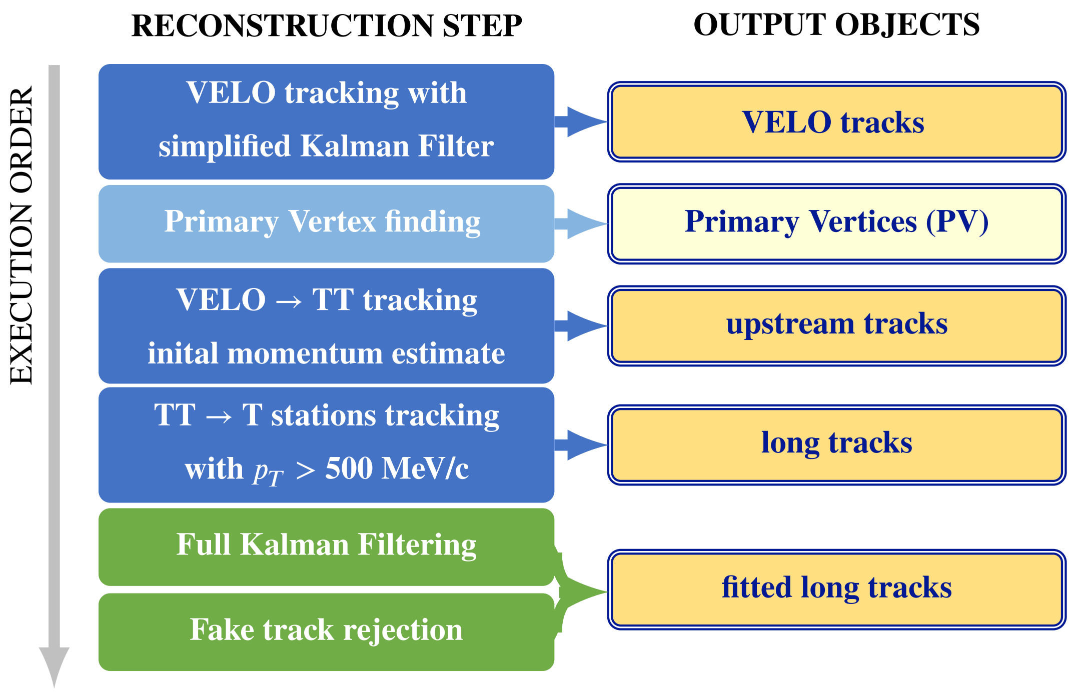

Figure 2.20 Sketch of the HLT1 track and vertex reconstruction[95].

1) computing farm.

The HLT1 stage performed a partial event reconstruction mainly in three steps: reconstructing the tracks in VELO, extrapolating the tracks to the TT stations to build upstream tracks, and extending them to the T stations to produce long tracks. A Kalman fit is performed on the long tracks to reject the fake trajectories. The positions of PVs are determined with the fitted VELO tracks. The algorithm used in HLT1 to reconstruct the long tracks and the primary vertices is shown in Fig. 2.20. The tracks are selected requiring a minimal p and p_T, have a good track χ^2 fit quality and larger than a given threshold on the IP.

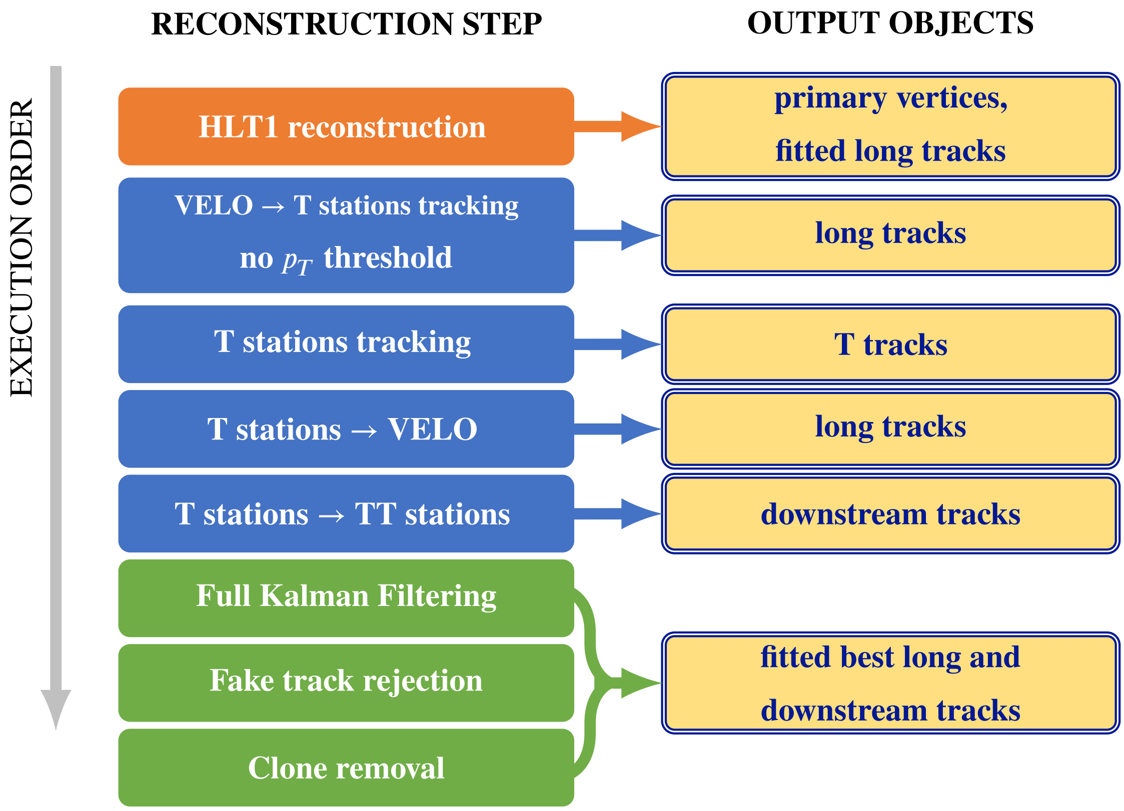

Figure 2.21 Sketch of the HLT2 track and vertex reconstruction sequence[95].

After passing from HLT1 to HLT2, the rate of events has been reduced to about 150 kHz, where a full event reconstruction can be carried out. The HLT2 track reconstruction uses the full information collected by the sub detector, performing additional steps of the pattern recognition that can not be done in HLT1. The algorithm and sequences used for HLT2 track and vertex reconstruction is shown in Fig. 2.21. At this stage, not only tracks but also the particle identification information are available. Many different trigger selections are carried out which are motivated by the requirement for different physics analyses.

2.2.3.3 Data processing and simulation

The data samples saved after HLT stages are still very huge, it is necessary to further processed to obtain a smaller sample for performing physics analyses. The LHCb data flow is shown in Fig. 2.22. The data samples after the trigger selection are reconstructed with Brunel. Then further filter using DaVinci referred to as Stripping. Users can use DaVinci to read the information saved in DST or MDST format after Stripping.

To produce simulation samples for direct comparison with the real collision data,

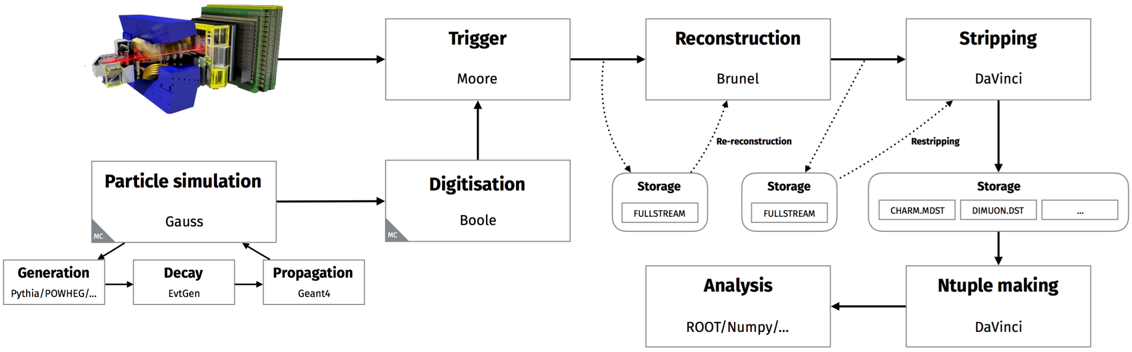

Figure 2.22 The data flow and the associated applications at LHCb.

a similar sequence is used. The particle simulation is divided into three steps: First, the fragmentation and hadronisation in pp collisions are generated with a specific LHCb configuration[96] of PYTHIA[89]. Then, the actual decay of the hadronic particles are modelled with EVTGEN[97] package except for the radiation from the final state particles which is described by PHOTOS[98]. Finally, the detector response of the interaction between detector material and a simulation of the data collection process is handled by GEANT4[99]. Gauss is used to mediate and propagate data from generation to propagation stage and Boole is used to digitise the data by modelling the response of the LHCb sub-detectors. The output samples are transferred to Moore and stripped by the normal trigger, reconstruction and stripping selections.

2.3 Flavour tagging algorithms

The identification of the flavour at production time of a neutral B meson, *i.e.*, whether the meson contains a b or a $\bar{b}$ quark at production, is a key element for any time-dependent analysis aiming at the measurement of oscillations and CP asymmetries. For CP violation related analyses using decays of $B_s^0 \to J/\psi\pi^+\pi^-$ and $B_s^0 \to J/\psi K^+K^-$, the flavour tagging is very important due to two reasons: 1) neutral B_s^0 meson oscillate, so the flavour at the production time might differ from the flavour at the decay time; 2) The final states can be produced by the decay of both B_s^0 and $\overline{B}_s^0$ mesons. The flavour of the B meson can not be obtained from the charge of the final state, even if there is no oscillations.

At LHCb experiment, techniques to infer the initial flavour of a reconstructed candidate, flavour tagging algorithms, are developed. A schematic representation of the taggers that can be used for tagging B mesons is shown in Fig. 2.23.

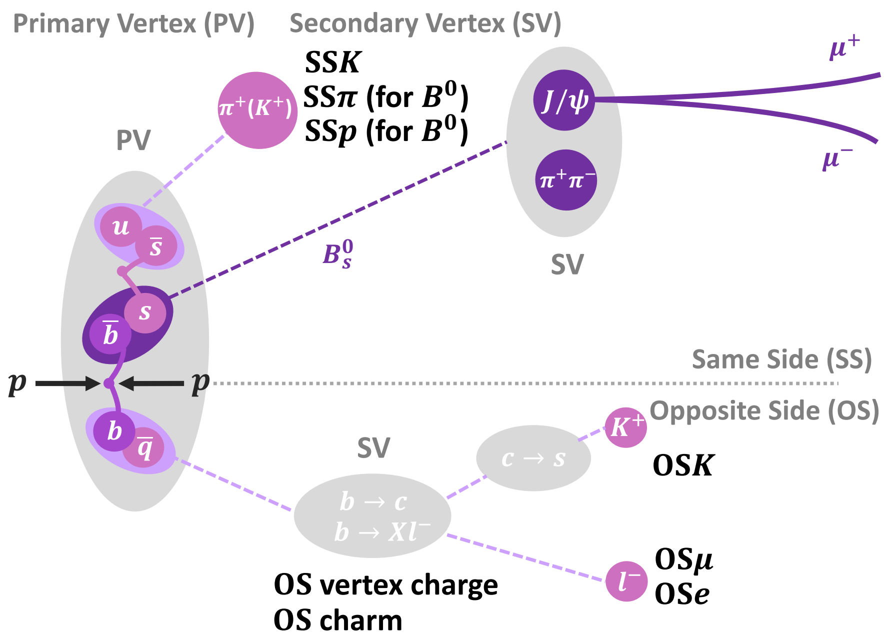

Figure 2.23 Schematic overview of flavour tagging algorithms used in LHCb .

2.3.1 Tagging algorithms

As shown in Fig. 2.23, the tagging algorithms can be categorised into two classes: opposite side (OS) and same side (SS) algorithms. The OS algorithms exploit the predomiant production process of the second B mesons via $b\bar{b}$ pair production[100]. By partially reconstruct the decay products of the other b hadron produced as muons, electrons, kaons and D-mesons associated with the reconstructed signal B meson, the initial flavour of the signal B meson is inferred. Furthermore, charged tracks with originate from a secondary vertex, which is displaced from the PV, are used to make a decision on the production flavour of the signal B meson. Since the hadronisation and the decay of the OS b-hadron is independent of the signal B meson, these algorithms can be used for both B^0 and B_s^0. In contrast, the SS algorithms infer the production flavour of the signal B meson by selecting charged particle candidates that have a high chance of being remnants of the hadronisation process of the signal B meson[101-102]. As the companion quark of the b-quark is different for B^0 and B_s^0 mesons, different algorithms are used to deduce the initial flavour of the signal B meson. For B^0 $(\bar{b}d)$ meson, the free $\bar{d}$ quark is produced which can hadronise to a π^+ or $\bar{p}$. For B_s^0 $(\bar{b}s)$, the hadronisation of the free $\bar{s}$ quark can hadronise to a K^+. The charge of these co-produced particles are used to infer the initial flavour of the B meson.

For each reconstructed candidate, a decision q whether a B candidate was initially produced as a B or a $\overline{B}$ meson and a probability-estimate (mistag) η of being wrong with this decision is provided by each flavour tagging algorithms. The flavour tag takes the values $q = +1$ for an initial B_s^0, $q = -1$ for an initial $\overline{B}_s^0$ and $q = 0$ when no tag could be assigned. The mistag probability η is defined in a range $[0, 0.5]$ and is based on the output of multivariate classifiers, which are trained on datasets on flavour-specific decays, and combine several kinematic and geometric information on the tagging particles.

2.3.2 Flavour tagging performance

The prediction of the flavour tagging algorithms is not perfect. Among N reconstructed candidates only $N^{'}$ candidates get a tag q and mistag η assigned, N_U are untagged. The $N^{'}$ can be further divide into N_R (correctly tagged candidates) and N_W (wrongly tagged candidates). The tagging efficiency can be defined as

$$\epsilon_{\text{tag}} = \frac{N_R + N_W}{N_R + N_W + N_U} \tag{2-4}$$

and the mistag probability is

$$\omega = \frac{N_W}{N_W + N_R} \tag{2-5}$$

Therefore, in an analysis using flavour tagging to infer the initial B flavour, the number $N_{B_s^0}(t)(N_{\overline{B}_s^0}(t))$ of measured initial B_s^0 ($\overline{B}_s^0$) candidates are

$$\begin{aligned} N_{B_s^0}(t) &= (1-\omega)N^{\text{true}}_{B_s^0}(t) + \omega N^{\text{true}}_{\overline{B}_s^0}(t) \\ N_{\overline{B}_s^0}(t) &= \omega N^{\text{true}}_{B_s^0}(t) + (1-\omega)N^{\text{true}}_{\overline{B}_s^0}(t) \end{aligned} \tag{2-6}$$

where$N^{\text{true}}_{B_s^0}(t)$ and $N^{\text{true}}_{\overline{B}_s^0}(t)$ denotes the true number of initial B_s^0 and $\overline{B}_s^0$ candidates. These quantities need to be transferred further into measurement of CP-asymmetries such as

$$A_{CP}(t) = \frac{N^{\text{true}}_{B}(t) - N^{\text{true}}_{\overline{B}_s^0}(t)}{N^{\text{true}}_{B}(t) + N^{\text{true}}_{\overline{B}_s^0}(t)} \tag{2-7}$$

The true number of initial B_s^0 and $\overline{B}_s^0$ mesons need to be replaced by the observed yields which lead to

$$A^{\text{meas}}_{CP}(t) = \frac{N_{B_s^0}(t) - N_{\overline{B}_s^0}(t)}{N_{B_s^0}(t) + N_{\overline{B}_s^0}(t)} = (1-2\omega)A^{\text{theo}}_{CP}(t) = DA^{\text{theo}}_{CP}(t) \tag{2-8}$$

where the quantity $D = 1 - 2\omega$ is known as average dilution. If $\omega = 0$(perfect tagger), then $D = 1$ and no asymmetry dilution occurs. If $\omega = 0.5$ (random tagger), then $D = 0$, then it is no possible to measure the asymmetry anymore.

The quantity that can be interpreted as the figure of merit to optimise a tagging algorithm is the effective tagging efficiency, also called tagging power

$$\epsilon_{\text{eff}} = \epsilon_{\text{tag}}(1-2\omega)^2 = \epsilon_{\text{tag}} D^2 \tag{2-9}$$

Assuming that ϵ_{eff} is known without uncertainty, then the statistical uncertainty on the physical asymmetry is given by

$$\sigma_{A_{CP}^{\text{theo}}} = \frac{\sqrt{1-A_{CP}^{\text{meas}}}}{\sqrt{N\epsilon_{\text{tag}}}(1-2\omega)} = \frac{\sqrt{1-A_{CP}^{\text{meas}}}}{\sqrt{N\epsilon_{\text{eff}}}} \tag{2-10}$$

Then we can conclude, the greater the tagging power, the smaller the resulting statistical uncertainty on the CP asymmetry.

Rather than using an average mistag ω, the mistag η estimated with various tagging algorithms are used. η are calibrated via a function $\omega(\eta)$ in order to return the true mistag probability, given a pre-event tagging power:

$$\epsilon_{\text{eff}} = \frac{1}{N}\sum_{i=1}^{N} D_i^2 = \frac{1}{N}\sum_{i=1}^{N}(1-2\omega(\eta_i))^2 \tag{2-11}$$

2.3.3 Combination and calibration of flavour tagging algorithms

To improve the overall performance of the flavour tagging, the individual algorithms are combined to form one single tag decision and mistag for the OS (q_{OS} and η_{OS}) and a tag decision and mistag for the SS (q_{SS} and η_{SS}). This is done by calculating the combined probability, that a B candidate contains a b quark

$$P(b) = \frac{p(b)}{p(b)+p(\bar{b})}, \; P(\bar{b}) = 1 - P(b) \tag{2-12}$$

The probabilities $p(b)$ and $p(\bar{b})$ are defined as

$$\begin{aligned} p(b) &= \Pi_i(\tfrac{1+q_i}{2} - q_i(1-\eta_i)) \\ p(\bar{b}) &= \Pi_i(1 - \tfrac{-q_i}{2} + q_i(1-\eta_i)) \end{aligned} \tag{2-13}$$

where $q_i(\eta_i)$ are the tag decision (mistag estimates) of the individual tagging algorithms. If $P(\bar{b}) > P(b)$, the combined tagging decision $q = +1$ and the final mistag probability $\eta = 1 - P(\bar{1})$. Otherwise if $P(\bar{b}) < P(b)$, the combined tagging decision and the mistag probability are $q = -1$ and $\eta = 1 - P(b)$.

The output of the flavour tagging algorithms is the result of training multivariate classifiers using datasets of flavour-specific B decays. This output is transformed into a mistag estimate η. However, the training and validation samples are usually different from the signal channel used in a CP-violation measurement. This differences are caused by different trigger and selection criteria and can influence the distribution that are used in the multivariate classifier. Thus, the mistag must be calibrated on a dedicated flavour specific decay which shows at best kinematically similar distributions compared to the signal decay.

A common choice for the calibration function is a linear function

$$\omega(\eta) = p_0 + p_1(\eta - \langle\eta\rangle) \tag{2-14}$$

The use of the arithmetic mean $\langle\eta\rangle$ of the η distribution aims at a decorrelation of p_0 and p_1. A perfect calibration of the taggers would result ini $p_0 = \langle\eta\rangle$ and $p_1 = 1$.

The performance of the tagger can depend on the initial B flavour. If the interaction rates of the charged decay products with the detector material depend on the charge, the mistags will also depend on the flavour of the initial B meson. Such asymmetry yields in an additional dilution factor, which needs to be understood and properly described. So different calibration parameters for B and $\overline{B}$ are used

$$\begin{aligned} \omega^{B_s^0}(\eta) &= p_0^{B_s^0} + p_1^{B_s^0}(\eta - \langle\eta\rangle) \\ \omega^{\overline{B}_s^0}(\eta) &= p_0^{\overline{B}_s^0} + p_1^{\overline{B}_s^0}(\eta - \langle\eta\rangle) \end{aligned} \tag{2-15}$$

Equivalently, we can parametrise the calibration parameters p_i with $(i = 0, 1)$ as

$$p_i^{B_s^0} = p_i + \frac{\Delta p_i}{2},\ p_i^{\overline{B}_s^0} = p_i - \frac{\Delta p_i}{2} \tag{2-16}$$

The calibration function are determined in each analysis using an unbinned maximum-likelihood method with the flavour-specific calibration samples. For the OS taggers, this is most often done using charged decay modes, as the charge of the final state particles allows to directly infer the production flavour. For the SS taggers, a decay mode with the same initial B flavour is needed, as these taggers highly depend on the hadronisation process.

Chapter 3 First observation of $\Xi_b^- \to J/\psi \Lambda K^-$

3.1 Introduction

The existence of multi-quark hadrons including tetraquarks and pentaquarks was hypothesised by Murray Gell-Mann[5] and George Zweig[6] independently in their proposals of the quark model. With experimental progress, dozens of charmonium-like/bottomonium-like tretaquarks were observed by several particle physics experimental collaborations[19-29]. Meanwhile, many experiments made efforts on searching for pentaquarks. However, no undisputed candidates were found until the LHCb collaboration reported the observation of two exotic states $P_c(4380)^+$ and $P_c(4450)^+$ in the$J/\psi p$ invariant mass spectrum of the $\Lambda_b^0 \to J/\psi p K^-$ decay[32]. The minimal quark content of these two states is $uudc\bar{c}$. By replacing one u quark with an s quark in the pentaquark content, a strangeness hidden-charm pentaquark ($udsc\bar{c}$) is formed and could be searched in the $J/\psi \Lambda$ mass spectrum of the $\Xi_b^- \to J/\psi \Lambda K^-$ decay[103]. Examples of Feynman diagrams contributing to the $\Xi_b^- \to J/\psi \Lambda K^-$ decay are shown in Fig. 3.1.

3.2 Analysis strategy

In this analysis, the $\Xi_b^- \to J/\psi \Lambda K^-$ decay is searched using pp collisions data collected by the LHCb experiment during LHC Run-I data-taking period. The $\Lambda_b^0 \to J/\psi \Lambda$ decay is used as a reference channel. The main challenge in this analysis is to reconstructed Λ baryon associated with J/ψ meson. By using the reference channel, systematic effects in the Λ baryon reconstruction are expected to cancel largely. The branching fraction of the $\Xi_b^- \to J/\psi \Lambda K^-$ decay with respect to that of the $\Lambda_b^0 \to J/\psi \Lambda$ decay, multiplied by the relative fragmentation fraction between $f_{\Xi_b^-}$ and $f_{\Lambda_b^0}$, is defined as

$$R \equiv \frac{f_{\Xi_b^-}}{f_{\Lambda_b^0}} \frac{\mathcal{B}(\Xi_b^- \to J/\psi \Lambda K^-)}{\mathcal{B}(\Lambda_b^0 \to J/\psi \Lambda)}, \tag{3-1}$$

where $\mathcal{B}$ represents the branching fraction of the corresponding b-baryon decay. Practically, the ratio is determined by

$$R = \frac{N(\Xi_b^- \to J/\psi \Lambda K^-)}{N(\Lambda_b^0 \to J/\psi \Lambda)} \frac{\epsilon(\Lambda_b^0 \to J/\psi \Lambda)}{\epsilon(\Xi_b^- \to J/\psi \Lambda K^-)}, \tag{3-2}$$

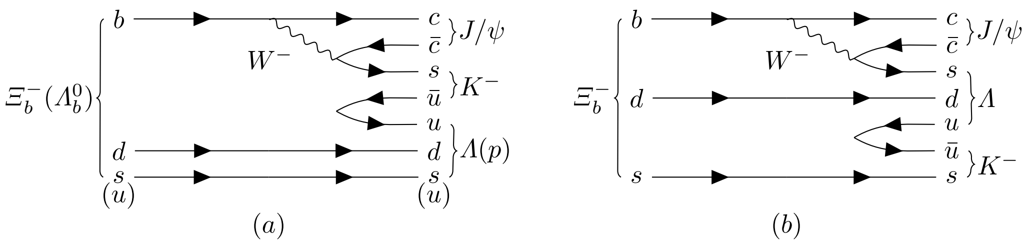

Figure 3.1 Examples of Feynman diagrams of $\Xi_b^- \to J/\psi \Lambda K^-$ and $\Lambda_b^0 \to J/\psi p K^-$ decays. Diagram (a) contributes to both Ξ_b and Λ_b^0 decays, diagram (b) contributes only to the Ξ_b decay.

Table 3.1 Simulation samples used in this analysis. PHSP indicates the simulation is generated with the phase space model. More details on the generator model can be found at Ref.[97].

Decay channel	Production type	Events	Model	Utilisation
$\Xi_b^- \to J/\psi \Lambda K^-$	Full	5.15×10^6	PHSP	Signal study
$\Lambda_b^0 \to J/\psi \Lambda$	Full	1.57×10^6	PHSP	Control channel
$\Lambda_b^0 \to \psi(2S) \Lambda$	Generator level	0.75×10^6	PHSP	Background modelling
$\Xi_b^- \to J/\psi \Sigma^0 K^-$	Generator level	0.75×10^6	PHSP	Background modelling

which means it could be accessed by measuring the numbers (N) of signal reconstructed from the two decays and the relative efficiency (ϵ) between the Λ_b^0 and Ξ_b^- decays. The mass difference $\delta M \equiv M(\Xi_b^-) - M(\Lambda_b^0)$ is also determined with a simultaneous fit to the same datasets.

3.3 Dataset and selection requirement

3.3.1 Data and simulated samples

The results described in this chapter are obtained by analysing datasets with a centre-of-mass energies of $\sqrt{s}$ =7 TeV and 8 TeV collected in 2011 and 2012, they correspond to integrated luminosities of $1.0\,\mathrm{fb}^{-1}$ and $2.0\ \mathrm{fb}^{-1}$, respectively. The decay channels, types , generated events, model and utilisation of simulated samples used in this analysis are listed in Table 3.1.

3.3.2 Selection

The selection of candidates is performed in a sequence of steps. An offline selection is applied after triggers, followed by a multivariate classifier (MVA) based on a Gradient Boosted Decision Tree (BDTG)[104]. Then the PID requirement on the kaons is optimised simultaneously with BDTG selection to maximise the signal significance. After which, the multiple candidates contribution is studied.

3.3.2.1 Preselection requirement

Online selection is based on muon triggers with TOS decision as listed in Table 3.2. A full reconstruction of the decay chain is performed offline, the selection criteria is given in Table 3.3. The $\Xi_b^- \to J/\psi \Lambda K^-$ and $\Lambda_b^0 \to J/\psi \Lambda$ are reconstructed using the decays $J/\psi \to \mu^+\mu^-$ and $\Lambda \to p\pi^-$. In the offline selection, the J/ψ candidates are formed from two oppositely charged tracks with $p_{\mathrm{T}} > 500$ MeV, identified by the muon system (`IsMuon`), as well as the likelihood calculated by the Cherenkov detectors that each track is a muon with respect to a pion hypothesis, $\mathrm{DLL}_{\mu\pi} > 0$[105]. The di-muon pairs are selected with the fit quality of the di-muon decay vertices less than 20 and have an invariant mass $m(\mu^+\mu^-) - m(J/\psi) \in (-48, +43)$ MeV. The Λ candidates are reconstructed by combining candidate p and π^- tracks. Given the long lifetime of the Λ baryon, it can be reconstructed either from a pair of tracks that include segments in the VELO, called *long* tracks (LL Λ candidates), or from a pair of tracks reconstructed using only the tracking stations located downstream of the VELO, called *downstream* tracks (DD Λ candidates). The p and π^- tracks are required to satisfy $\chi^2_{\mathrm{IP}} > 9$, where χ^2_{IP} is defined as the difference in the χ^2 of the vertex fit for a given PV reconstructed with and without the considered particle. The invariant mass of the $p\pi^-$ pair is required to be within $\pm 4\,(6)$ MeV of the known Λ mass[58] for the LL (DD) Λ candidates. For the LL Λ candidates, both proton and pion must satisfy $p_{\mathrm{T}} > 250$ MeV, and pass loose PID criteria based on information provided by the RICH detectors. For the DD Λ candidates, the decay vertex must not be reconstructed in the first half of the VELO, so the final-state particles can be reconstructed as *downstream* tracks. In order to suppress the contribution from mis-identified background from $K_S^0 \to \pi^+\pi^-$ decays, the reconstructed mass for the LL (DD) Λ candidate under the $\pi^+\pi^-$ hypothesis is required to be more than 4 (10) MeV away from the known K_S^0 mass[58]. All final state tracks are required to have good-quality vertices, $\chi^2_{\mathrm{vtx}}/\mathrm{ndf} > 3$. The probability of hadron tracks are reconstructed using fake tracks is less than 0.3 (1.0) for the LL (DD) samples. The bachelor kaon candidate using for reconstructed Ξ_b^- baryon should satisfy $p_{\mathrm{T}} > 250$ MeV and $\chi^2_{\mathrm{IP}} > 9$. Each reconstructed b-baryon candidate is required to satisfy $\chi^2_{\mathrm{IP}} < 25$. The decay vertices of b candidates must also have a good fit χ^2 and a separation of at least 1.5 mm from the PV. The angle between the b-baryon momentum and the vector from the

Table 3.2 Trigger lines used for selected $B_s^0 \to J/\psi \pi^+ \pi^-$ candidates. More details on the trigger lines can be found in Ref.[107].

Trigger level	Trigger line
L0	`Jpsi_L0MuonDecision_TOS` or `Jpsi_L0DimuonDecision_TOS`
HLT1	`Jpsi_HLT1DiMuonHighMassDecision_TOS` or `Jpsi_HLT1TrackMuonDecision_TOS` or `Jpsi_HLT1TrackAllL0Decision_TOS`
HLT2	`Jpsi_HLLT2DiMuonDetachedJPsiDecision_TOS`

associated PV to the decay vertex, θ , must satisfy $\cos\theta > 0.999$. For both b baryons fiducial cuts of $p_{\mathrm{T}} < 25$ GeV and rapidity in the range $2.0 < y < 4.5$ are required to have a well-defined kinematic region in which the measurement is performed. There are only 0.2% events outside the fiducial kinematic region. A kinematic fit (DecayTreeFitter, DTF)[106] is applied to the Ξ_b^- and Λ_b^0 candidates. The fit is performed using a Kalman fitter which conducts progressive refitting of the full decay tree for a given mass hypothesis of the daughter particles together with selected vertex constrains. The invariant mass resolution of the particles in the decay has been significantly improved by the fit.

3.3.2.2 Multivariate analysis

Candidates satisfying the preselection requirements are filtered using a multivariate analyser based on a BDTG technique to further suppress the combinatorial background. For Ξ_b^- decays, fifteen variables are used in BDTG algorithm: the minimum $\mathrm{DLL}_{\mu\pi}$ of the μ^+ and μ^-; the minimum χ^2_{IP} of the μ^+ and μ^-; p_{T} and χ^2_{IP} of the proton; p_{T} and χ^2_{IP} of the pion; χ^2_{IP}, flight distance χ^2 and vertex χ^2 of the Λ; p_{T} of J/ψ ; DTF fit χ^2, pointing angle and decay time of the Ξ_b^-; and p_{T}, χ^2_{IP} of the bachelor Kaon. For the normalisation channel, the variables for the bachelor K^- are excluded in the BDTG algorithm. BDTG is trained with a simulated $\Xi_b^- \to J/\psi \Lambda K^-$ sample for the signal, and data candidates in upper sideband with $5944 < m(J/\psi \Lambda K) < 6094$ MeV are used to model the background. The low mass sideband is not used to avoid potential partial reconstructed background which has similar behaviour as the signal. Signal and background distributions for all the training variables for Ξ_b^- decays are shown in Fig. 3.2 and Fig. 3.3. All of these variables has discrimination power to separate signals and backgrounds. The distributions of the BDTG classifier for signal and background for Ξ_b^- decays and Λ_b^0 decays are shown in

Table 3.3 Preselection requirement applied for the two decays $\Lambda_b^0 \to J/\psi\Lambda$ and $\Xi_b^- \to J/\psi\Lambda K^-$. The selection for the bachelor K^- is not used for the Λ_b^0 decays. When different value is used between LL and DD Λ, the number before the brackets corresponds to LL and that in the brackets corresponds to DD.

#	Selection variables	Requirement
1	All tracks χ^2/ndf	< 3
2	Hadron ghost probability	$< 0.3\,(1.0)$
	J/ψ selection	
3	Muon DLL($\mu - \pi$)	> 0
4	Muon p_{T}	$> 500\,\mathrm{MeV}$
5	Muon `IsMuon`	true
6	J/ψ vertex χ^2	< 20
7	$m(\mu^+\mu^-) - m(J/\psi)$	$(-48, 43)\,\mathrm{MeV}$
8	Trigger TOS	(see text)
	Λ selection	
9	Hadron p_{T}	$> 250\,(0)\,\mathrm{MeV}$
10	Hadron χ^2_{IP}	$> 9\,(4)$
11	proton $\mathrm{DLL}_{p\pi}$	$> -5\,(-1000)$
12	pion $\mathrm{DLL}_{\pi K}$	$> -10\,(-1000)$
13	vertex χ^2	$< 30\,(25)$
14	mass window	$(1112(1110), 1120(1122))\,\mathrm{MeV}$
15	K_s^0 veto window	$\pm 4\,(10)\,\mathrm{MeV}$
16	z_{vertex} (DD only)	$> 500\,\mathrm{mm}$
	Bachelor K^- selection	
17	p_{T}	$> 250\,\mathrm{MeV}$
18	χ^2_{IP}	> 9
19	ProbNNk	> 0.1
	B baryon selection	
20	χ^2_{IP}	< 25
21	χ^2_{vtx}/ndf	< 10
22	flight distance (FD)	$> 1.5\,\mathrm{mm}$
23	pointing, $\cos\theta_p$	> 0.999
24	fiducial cut, p_{T}	$< 25\,\mathrm{GeV}$
25	fiducial cut, y	$(2.0, 4.5)$

Fig. 3.4 and Fig. 3.5. There is no visible overtraining for all the cases.

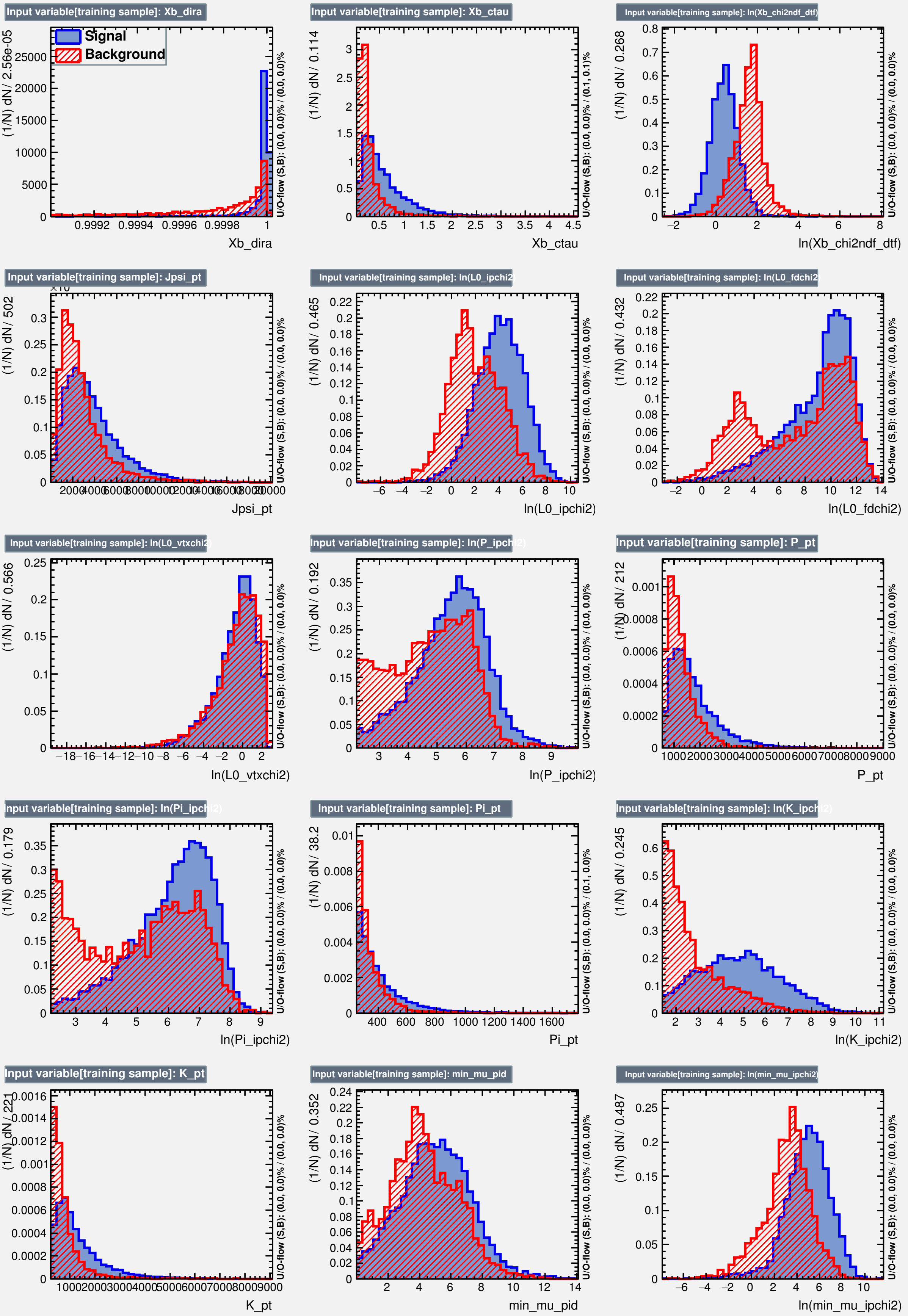

Figure 3.2 Distributions of variables used in BDTG for LL Ξ_b^- decays.

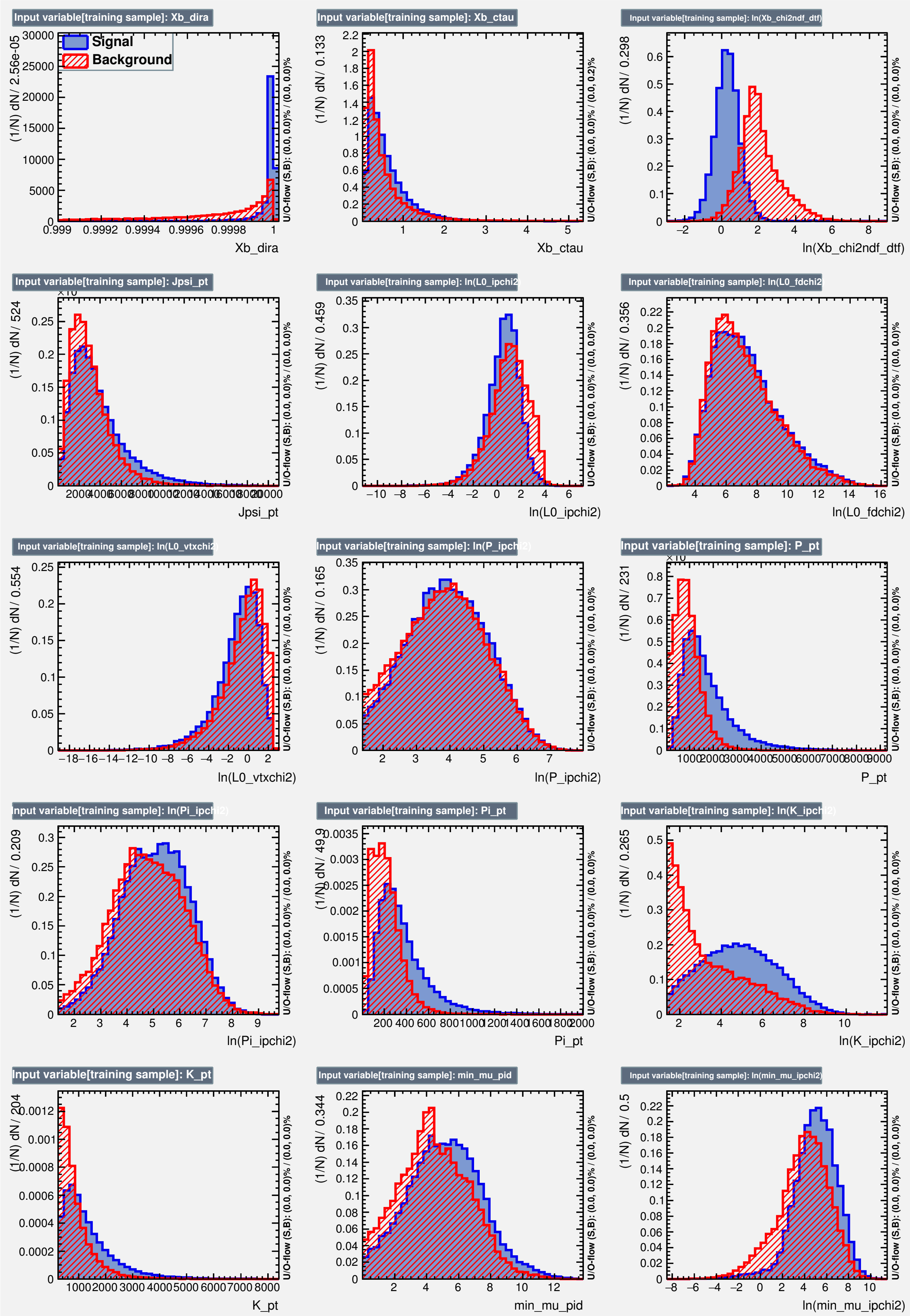

Figure 3.3 Distributions of variables used in BDTG for DD Ξ_b^- decays.

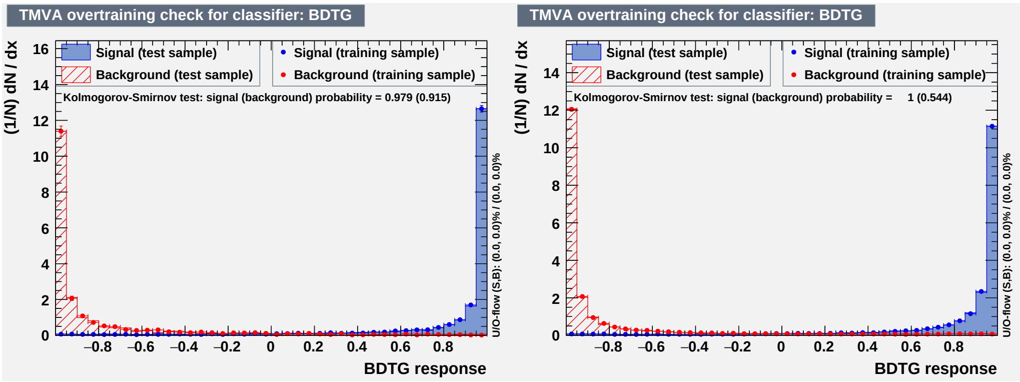

Figure 3.4 BDTG distributions for the signal and background for the Ξ_b^- decays in (left) LL and (right) DD types.

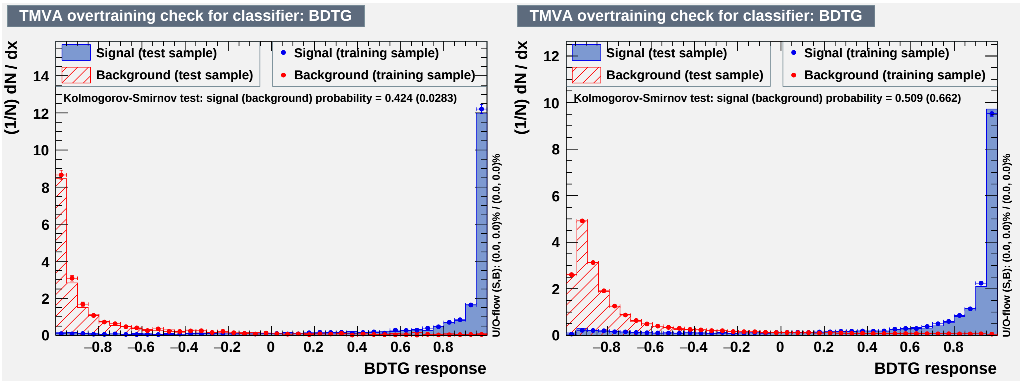

Figure 3.5 BDTG distributions for the signal and background for the Λ_b^0 decays in (left) LL and (right) DD types.

3.3.2.3 Particle identification

The PID information of K (`ProbNNk`) is not well described in the simulation. To correct it, the `ProbNNk` in simulation is resampled using the binned `ProbNNk` probability density functions of dedicated calibration samples of $D^0 \to K^-\pi^+$ in bins of p_K, η_K and `nTracks` (number of well reconstructed tracks in one event). Such procedure is done separately for 2011 and 2012 data using the standard script in the `PIDCalib` package[108]. Possible effects due to the chosen of ($p_{\rm T}$, η, `nTracks`)-binning are evaluated in the systematic uncertainties in Sec.3.6.4.

3.3.2.4 Selection optimisation

The optimal requirement on the BDTG response and the PID variable, `ProbNNk` of K, is determined simultaneously by maximising the signal significance, $S/\sqrt{S+B}$, where S (B) is the expected signal (background) yields in $\pm 2.5\sigma$ mass window around the known Ξ_b^- mass[58]. The signal yield is determined as the product of an initial signal

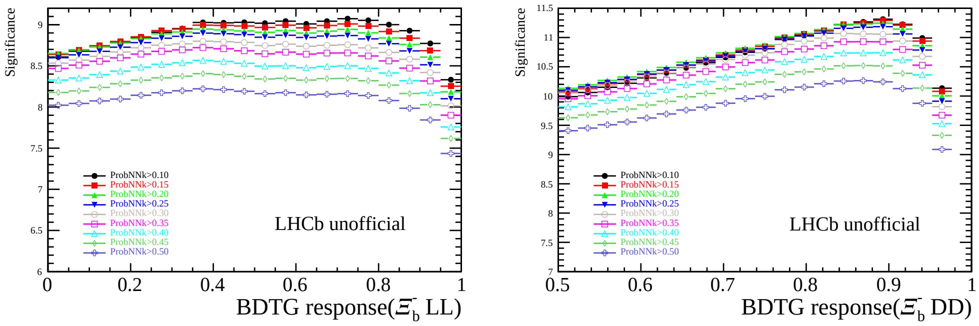

Figure 3.6 BDTG optimisation for the Ξ_b^- decays in (left) LL and (right) DD types.

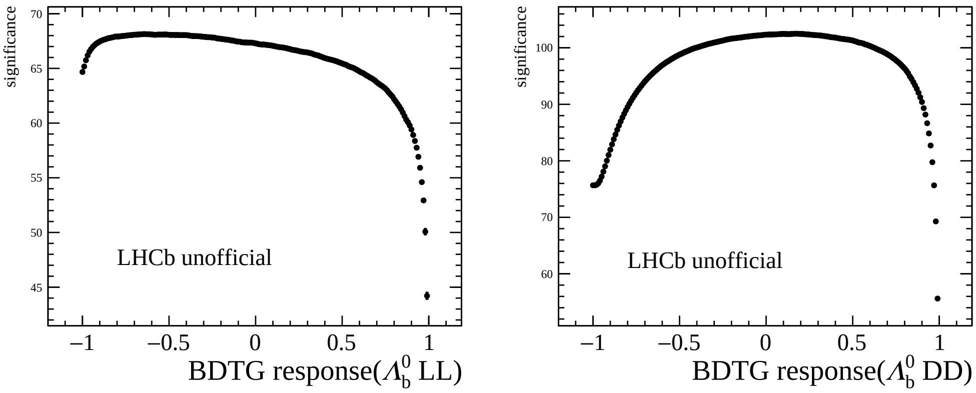

Figure 3.7 BDTG optimisation for the Λ_b^0 decays in (left) LL and (right) DD types.

yield from the data at BDTG $>$ 0 and the relative BDTG efficiencies with respect to the initial working point which obtained from the simulation. The background yield is estimated using candidates in the upper sideband range $(+150, +350)$ MeV of data and extrapolated to the signal region. The estimated significance distributions for LL and DD types are shown in Fig. 3.6. Based on these distributions, the working points are chosen to be BDTG > 0.5 (BDTG > 0.9) and `ProbNNk` > 0.15 which has a signal efficiency of 90% (70%) and a background rejection rate of 97% (99%) for LL (DD) samples.

For the control channel, the BDTG response is studied using the same procedure. The significances as a function of BDTG working point for the two Λ_b^0 types are shown in Fig. 3.7. The working points are chosen as BDTG > 0 for both types.

3.3.2.5 Multiple candidates

The contribution of multiple candidates are checked by comparing the fraction of multiple candidates in fit region and 2σ mass region. The results are listed in Table 3.4. The fraction are consistent with each other and very small, so the multiple candidates are

Table 3.4 Fractions of multiple candidates.

Channel	Fit region	2 σ mass region
Ξ_b^-	0.31%	0.61%
Λ_b^0	0.30%	0.22%

kept in data samples.

3.4 Signal yields extraction

3.4.1 Background studies

The veto of K_S^0 meson in the preselection eliminates the background source from any B meson that decay to $J/\psi K_S^0 X$, where X denotes null or any number of particles. Candidates from other b-baryon decays, which can be reconstructed as the decay of interest if their decay products are misidentified or not fully reconstructed, are considered. A study of possible backgrounds shows that there are two physics background sources. One background is $\Lambda_b^0 \to \psi(2S)(\to J/\psi\pi^+\pi^-)\Lambda$ decay, where one of the pions is misidentified as a kaon and the other is not reconstructed. The other background is from $\Xi_b \to J/\psi\Sigma^0(\to \Lambda\gamma)K^+$ channel, where γ is not reconstructed.

3.4.1.1 Study of $\Lambda_b^0 \to \psi(2S)\Lambda$

The expected shape of misidentified $\Lambda_b^0 \to \psi(2S)\Lambda$ candidates is studied using simulation with same selection requirements as applied to the data sample. The mass distribution of the misidentified $\Lambda_b^0 \to \psi(2S)\Lambda$ candidates is shown in Fig. 3.8. This misidentification causes both a smearing and a shift of the mass peak, due to the change of mass in hypothesis for the misidentified track.

The branching ratio of $\Lambda_b^0 \to \psi(2S)\Lambda$ has not been measured before. To have a rough estimation, we assume the relative branching fractions are the same for Λ_b^0 and B^+ decays:

$$\frac{B(\Lambda_b^0 \to \psi(2S)\Lambda)}{B(\Lambda_b^0 \to J/\psi\Lambda)} = \frac{B(B^+ \to \psi(2S)K^+)}{B(B^+ \to J/\psi K^+)}. \tag{3-3}$$

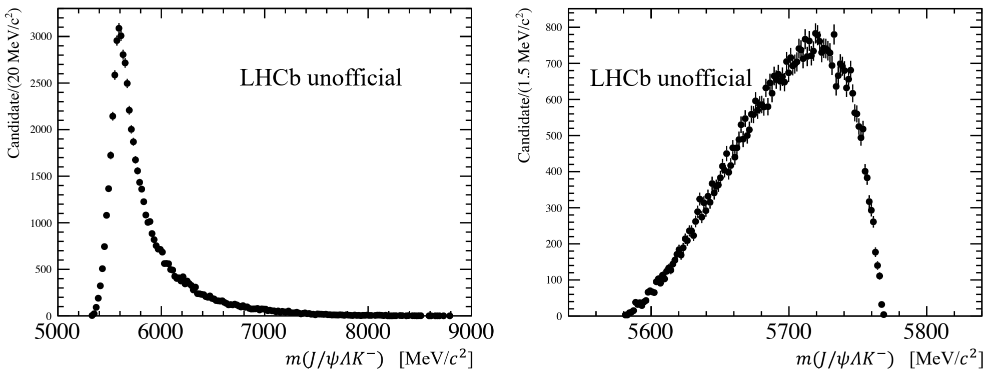

Figure 3.8 Invariant mass distribution of simulated mis-reconstructed $\Lambda_b^0 \to \psi(2S)\Lambda$ candidates (left) and $\Xi_b^- \to J/\psi\Sigma^0 K^-$ candidates (right).

Thus, the misidentified $\Lambda_b^0 \to \psi(2S)\Lambda$ yield is estimated as:

$$
\begin{aligned}
N(\Lambda_b^0 \to \psi(2S)\Lambda) = & \frac{B(B^+ \to \psi(2S)K^+)B(\psi(2S) \to J/\psi\pi^+\pi^-)}{B(B^+ \to J/\psi K^+)} \times \\
& \frac{\epsilon^{tot}_{\Lambda_b^0 \to \psi(2S)\Lambda}}{\epsilon^{tot}_{\Lambda_b^0 \to J/\psi\Lambda}} \times N(\Lambda_b^0 \to J/\psi\Lambda),
\end{aligned}
\tag{3-4}
$$

where $B(B^+ \to \psi(2S)K^+) = (6.26 \pm 0.24) \times 10^{-4}$, $B(\psi(2S) \to J/\psi\pi^+\pi^-) = (34.46 \pm 0.30)\%$, $B(B^+ \to J/\psi K^+) = (1.026 \pm 0.031) \times 10^{-3}$ [58], $\epsilon^{tot}_{\Lambda_b^0 \to \psi(2S)\Lambda}$ is estimated with the official fully simulated samples as $(5.560 \pm 0.495) \times 10^{-5}$ ($(1.111 \pm 0.070) \times 10^{-4}$) for LL(DD) samples, $\epsilon^{tot}_{\Lambda_b^0 \to J/\psi\Lambda}$ and $N(\Lambda_b^0 \to J/\psi\Lambda)$ are described in Sec .3.4.3 and Sec. 3.5. The predicted number of $\Lambda_b^0 \to \psi(2S)\Lambda$ events misidentified as $\Xi_b^- \to J/\psi\Lambda K^-$ decays is 10.3 ± 1.1 (15.6 ± 1.3) for LL (DD) samples in the fit region. The contribution is very small and has a similar shape as the combinatorial background, so it is not treated as a separate component in the invariant mass fits.

3.4.1.2 Study of $\Xi_b^- \to J/\psi\Sigma^0 K^-$

The decay of $\Xi_b^- \to J/\psi\Sigma^0 K^-$ has same final-state particles as the signal channel and can't be suppressed with preselection cuts or BDTG. It can generate a bump in the low mass sideband region as shown in Fig. 3.8, so it is included in the final invariant mass fit.

3.4.2 Fit model

The signal yields of $\Xi_b^- \to J/\psi \Lambda K^-$ and $\Lambda_b^0 \to J/\psi \Lambda$ are extracted using unbinned extended maximum-likelihood fits to the distributions of invariant mass (m). The likelihood in the signal channel can be expressed as:

$$\mathcal{L} = \frac{e^{-(N_{\rm S}+N_{\rm comb}+N_{\rm phsbg})}}{N!} \times \prod_{i=1}^{N} [N_{\rm S} P_{\rm S}(m_i) + N_{\rm comb} P_{\rm comb}(m_i) + N_{\rm phyb} P_{\rm phyb}(m_i)], \quad (3\text{-}5)$$

where N is the total number of events, N_k ($P_k(m)$) is the yield (probability density function) for the category k as signal (S), combinatorial (comb) or physics background (phyb) respectively. For the normalisation channel, no obvious physics background are found. The likelihood has only two constituents: the signal and the combinatorial background.

The signal component is described by a Hypatia function[109], defined as

$$\mathcal{F}(m, \mu, \sigma, \lambda, \zeta, a_1, n_1, a_2, n_2) \propto \begin{cases} G(m, \mu, \sigma, \lambda, \zeta), & -a_1 < \frac{m-\mu}{\sigma} < a_2; \\ \frac{G(\mu - a_1\sigma, \mu, \sigma, \lambda, \zeta)}{\left(1 - mR_1^{-1}\right)^{n_1}}, & -a_1 > \frac{m-\mu}{\sigma}; \\ \frac{G(\mu - a_2\sigma, \mu, \sigma, \lambda, \zeta)}{\left(1 - mR_2^{-1}\right)^{n_2}}, & a_2 < \frac{m-\mu}{\sigma}, \end{cases} \quad (3\text{-}6)$$

with

$$R_i = n_i \frac{G(\mu - a_i\sigma, \mu, \sigma, \lambda, \zeta)}{G'(\mu - a_i\sigma, \mu, \sigma, \lambda, \zeta)} - a_i\sigma, \quad (3\text{-}7)$$

where $G(\mu - a_i\sigma, \mu, \sigma, \lambda, \zeta)$ is the generalised hyperbolic function

$$G(\mu - a_i\sigma, \mu, \sigma, \lambda, \zeta) = \left((x-\mu)^2 + A_\lambda^2(\zeta)\sigma^2\right)^{\frac{1}{2}\lambda - \frac{1}{4}} K_{\lambda - \frac{1}{2}} \left(\zeta \sqrt{1 + \left(\frac{m-\mu}{A_\lambda(\zeta)\sigma}\right)^2}\right). \quad (3\text{-}8)$$

The quantities $K_\lambda(\zeta)$ are the cylindrical harmonics, parametrise by

$$A_\lambda^2(\zeta) = \frac{\zeta K_\lambda(\zeta)}{K_{\lambda+1}(\zeta)}. \quad (3\text{-}9)$$

This parametrisation describes a distribution with a Gaussian core which has a mean μ and a width σ. The parameter λ and ζ are further degrees of freedom to model the shape of the peak while the parameter a_i and n_i describe power-law tails to both sides of the distribution. This model can effectively takes into account the event-by-event variation of mass for radiative tails. The shape parameters are obtained from the simulated sample with full selection. The expected width in signal Ξ_b^- channel is calculated as $\sigma_{\Xi_b}^{\rm Data} =$

$\sigma^{\rm MC}_{\Xi_b} \times \sigma^{\rm Data}_{\Lambda_b^0}/\sigma^{\rm MC}_{\Lambda_b^0}$, using the simulation value calibrated by the width ratio between data and simulation from the Λ_b^0 control channel. The other parameters are free in the fit.

The combinatorial background is modelled by an exponential function. This arises due to the the random combination of tracks that fake the signal candidate. The exponential slope is let floating independently for LL and DD samples.

The partially reconstructed background are those modes that decay into the same final states as the signal mode but with an extra particle in the final state that has not been reconstructed. It peaks at the low-mass sideband region as studied in Sec. 3.4.1.2. The shape of this background is extracted from the generator level simulation of $\Xi_b^- \to J/\psi \Sigma^0 K^-$ decay, using kernel density estimation[110] implemented as `RooKeysPdf` in RooFit[111]. And it has been convolved with a Gaussian function with a resolution of 7.3 MeV, which is the mass resolution in the data. The yield is a free parameter in the fit.

3.4.3 Fit results

Fits performed on the Ξ_b^- and Λ_b^0 decays are illustrated in Fig. 3.9. The numbers of signal yields obtained from the fits are $N(\Xi_b^- \to J/\psi \Lambda K^-) = 99 \pm 12$ (209 ± 17), $N(\Lambda_b^0 \to J/\psi \Lambda) = 4838 \pm 72$ (12499 ± 125) for LL (DD) samples. The ratio is calculated to be:

$$\frac{N(\Xi_b^- \to J/\psi \Lambda K^-)}{N(\Lambda_b^0 \to J/\psi \Lambda)} = 0.0204 \pm 0.0025(\text{stat.}) \ \ (\text{LL});$$
$$\frac{N(\Xi_b^- \to J/\psi \Lambda K^-)}{N(\Lambda_b^0 \to J/\psi \Lambda)} = 0.0167 \pm 0.0014(\text{stat.}) \ \ (\text{DD}).$$

The background yields of $\Xi_b^- \to J/\psi \Sigma^0 K^-$ are 72 ± 25 (LL) and 221 ± 35 (DD) which are well consistent with the expected ratio 2.9.

The performance of DTF mass variable is checked by fitting the signal yields of the mass variable without J/ψ and Λ masses constrained to the known value and b-baryon candidates pointing back to PV. The ratios of mass resolutions are 2.48 (LL) and 2.39 (DD) for Ξ_b^- samples which suggested that the DTF gives a 60% improvement on the measurement resolution.

3.4.4 Significance

A fit to the combined LL and DD samples is used to estimate the statistical significance of the signal. The significance is determined by $\sqrt{-2\Delta\ln\mathcal{L}}$, where $\Delta\ln\mathcal{L}$ is the change in log-likelihood between the nominal fit and a fit in which the relevant

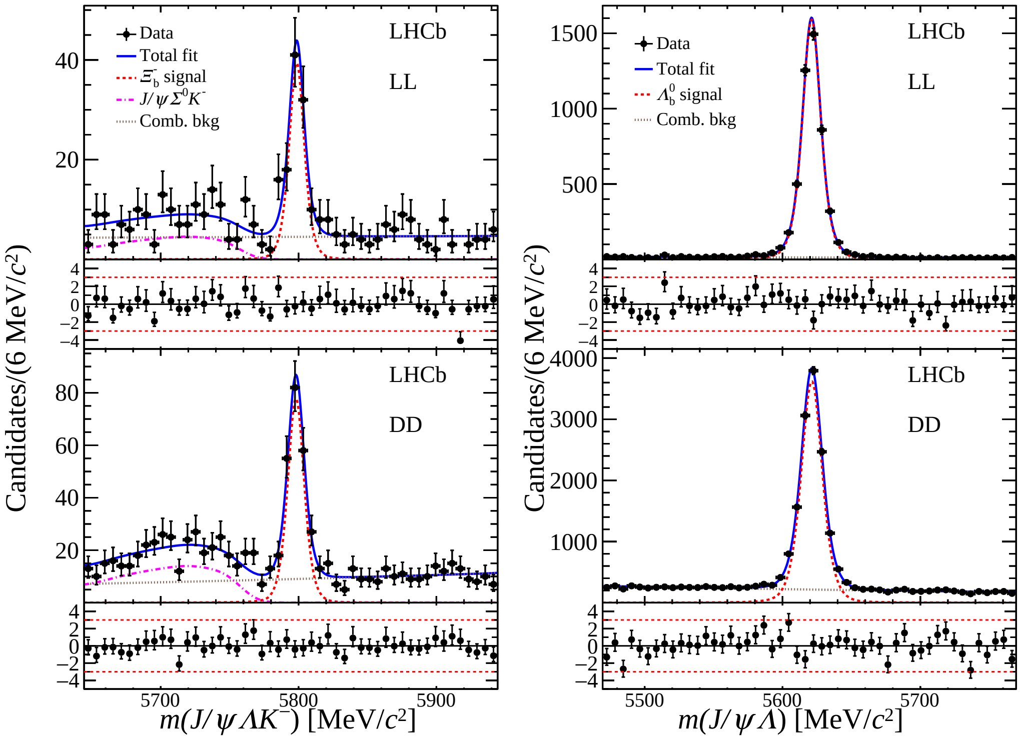

Figure 3.9 Fits to $J/\psi \Lambda K^+$ (left) and $J/\psi \Lambda$ (right) mass distributions using (top) LL and (bottom) DD Λ types. The black points with error represent the data. The solid blue lines show the full fit. The dashed red lines are the signal components. The dot-dashed purple lines gives the $\Xi_b^- \to J/\psi \Sigma^0 K^-$ background. The dotted black lines represent the combinatorial background.

signal yield is fixed to zero. Evidence for the $\Xi_b^- \to J/\psi \Lambda K^-$ decay is found at a level of approximately 21 σ.

3.5 Efficiency

The total efficiency is calculated as a product of the efficiencies of the intermediate steps:

$$\epsilon_{\text{tot}} = \epsilon_{\text{acc|fiducial}} \cdot \epsilon_{\text{rec\&sel|acc}} \cdot \epsilon_{\text{trig|sel}} \cdot \epsilon_{\text{BDTG|trig}} \cdot \epsilon_{\text{PID}_\text{K}\text{|BDTG}}. \tag{3-10}$$

Each efficiency is calculated from the samples with the cuts of the previous steps applied. All efficiencies are obtained using simulated samples, except the PID efficiency, which is obtained using a data-driven method. For the control channel $\Lambda_b^0 \to J/\psi \Lambda$, $\epsilon_{\text{PID}_\text{K}\text{|BDTG}} = 1$. All the quoted uncertainties are statistical. For the reconstruction and stripping efficiency, the trigger efficiency and the selection efficiency, their uncertainties are obtained using

Table 3.5 Absolute efficiency values for $\Xi_b^- \to J/\psi \Lambda K^-$ decays. Errors shown are statistical only.

Efficiency	Value(LL)	Value(DD)
Acceptance	0.7996±0.0009	
Reconstruction and preselection	0.0048±0.0000	0.0189±0.0001
Trigger	0.7704±0.0028	0.7659±0.0014
BDTG	0.8934±0.0024	0.6932±0.0018
PID	0.9476±0.0018	0.9546±0.0010
Total	0.0025±0.0000	0.0077±0.0000

Table 3.6 Absolute efficiency values for $\Lambda_b^0 \to J/\psi \Lambda$ decays. Errors shown are statistical only.

Efficiency	Value(LL)	Value(DD)
Acceptance	0.8271±0.0009	
Reconstruction and preselection	0.0083±0.0001	0.0282±0.0001
Trigger	0.7481±0.0041	0.7460±0.0022
BDTG	0.9297±0.0028	0.9407±0.0014
Total	0.0048±0.0001	0.0163±0.0001

the binomial formula,

$$\sigma(\epsilon) = \sqrt{\frac{\epsilon(1-\epsilon)}{N}}, \tag{3-11}$$

where N is the total number of events before the cut is applied. The summary of efficiencies is listed in Table 3.5 and Table 3.6 for $\Xi_b^- \to J/\psi \Lambda K^-$ and $\Lambda_b^0 \to J/\psi \Lambda$, respectively.

3.5.1 Geometrical acceptance

The geometrical acceptance requires all final state particles in $\Xi_b^- \to J/\psi \Lambda K^-$ ($\Lambda_b^0 \to J/\psi \Lambda$) decays, except for the daughters of Λ decays, to be within a polar angle θ from 10 to 400 mrad. It is studied with 0.75M generator level simulated events for both $\Xi_b^- \to J/\psi \Lambda K^-$ and $\Lambda_b^0 \to J/\psi \Lambda$ decays generated without the daughter in LHCb acceptance requirement. Then the requirement is applied to the simulation, and the acceptance efficiency is calculated as $\epsilon_{\text{acc|fiducial}} = N_{\text{acc}}/N_{\text{GL}}$, where N_{acc} is the number of events after the LHCb acceptance and the fiducial cuts and N_{GL} is the number of events with only the requirement of the fiducial cuts.

3.5.2 Reconstruction and preselection efficiency

The reconstruction and preselection efficiency is defined as $\epsilon_{\text{rec\&sel|acc}} = N_{\text{rec\&sel}}/N_{\text{acc}}$, where $N_{\text{rec\&sel}}$ is the signal yield of the full simulation after preselection and N_{acc} is the corresponding number of generated events in the LHCb acceptance with the fiducial cuts.

For the reconstruction efficiency of LL or DD type, the denominator is the number of total generated Λ events, and the numerator is number of events with Λ reconstructed as LL or DD. The denominator is the same for LL and DD type, thus LL and DD give independent measurement for the branching fraction of $\Xi_b^- \to J/\psi \Lambda K^-$ decay. The resulting two measurements are then averaged.

3.5.3 Trigger efficiency

Trigger efficiency is calculated using the simulated sample, defined as $\epsilon_{\text{trig|sel}} = N_{\text{trig}}/N_{\text{rec\&sel}}$, where N_{trig} is the number of events passing the trigger after the preselection.

3.5.4 BDTG selection efficiency

The BDTG selection efficiency is defined as $\epsilon_{\text{BDTG|trig}} = N_{\text{BDTG}}/N_{\text{trig}}$, where N_{BDTG} is the number of signal after BDTG selection and trigger. As there is a slight but non-ignorable difference in Ξ_b^- (Λ_b^0) DTF fit χ^2 between data and simulation, this variable is smeared in the simulated sample to calculate the BDTG selection efficiency for both LL and DD samples of both b baryon decays.

3.5.5 PID selection efficiency

A data-driven method is used to obtain the PID efficiency for the bachelor kaon in $\Xi_b^- \to J/\psi \Lambda K^-$ decay. The PID selection is not directly applied to the original variable in the signal simulation. Instead, the `ProbNNk` variable of the kaon is resampled using the data distribution from the calibration sample of $D^0 \to K^-\pi^+$ decays in bins of (p_K, η_K, `nTracks`). The number of tracks (`nTracks`) in the simulation is also replaced by the distribution obtained in the data from the Λ_b^0 decays before applying the PID resampling, to have the correct `nTracks`.

Table 3.7 Relative efficiency of $\frac{\epsilon(\Lambda_b^0 \to J/\psi \Lambda)}{\epsilon(\Xi_b^- \to J/\psi \Lambda K^-)}$. Uncertainty reflects statistics of both samples.

Efficiency	Value(LL)	Value(DD)
Acceptance	1.0343±0.0017	
Reconstruction and preselection	1.7353±0.0200	1.4908±0.0091
Trigger	0.9710±0.0064	0.9740±0.0034
BDTG	1.0406±0.0042	1.3571±0.0040
PID	1.0553±0.0020	1.0475±0.0011
Total	1.9140±0.0270	2.1352±0.0168

3.5.6 Relative efficiency

The efficiency ratio between $\Lambda_b^0 \to J/\psi \Lambda$ and $\Xi_b^- \to J/\psi \Lambda K^-$ decays, $\frac{\epsilon(\Lambda_b^0 \to J/\psi \Lambda)}{\epsilon(\Xi_b^- \to J/\psi \Lambda K^-)}$, is shown in Table 3.7, in which most of the systematic uncertainties cancel out.

3.6 Systematic uncertainties

Sources of systematics uncertainty can potentially bias the determination of the relative branching fraction. The choice of control channel $\Lambda_b^0 \to J/\psi \Lambda$ reduces the size of possible systematic uncertainty. Nonetheless, some important factors remain and they are studied in details and described in this section.

Table 3.8 lists a summary of systematic uncertainties that come from the relative yield and efficiency. To take into account the differences between the simulation and data, correction factors are obtained for the relative efficiency. The uncertainties on the correction factors are given as the systematic estimation. Due to lack of statistics, a common correction factor and systematic uncertainties are obtained for DD and LL types.

3.6.1 Signal model

The Double-Sided Crystal Ball function[112] (DSCB) is taken as an alternative model to evaluated the systematics uncertainties. Toy MC is generated using fit results with the DSCB model. Fits to toy MC are performed using both DSCB model and default Hypatia model. The resulting $R_{\text{alternative}}/R_{\text{default}} - 1$ subjects to Gaussian distribution, whose mean value is taken as systematic uncertainty. The fit result is shown in Fig. 3.10, the uncertainty is 0.7% for the signal model.

Table 3.8 Summary of correction factors on $\epsilon(\Lambda_b^0 \to J/\psi\Lambda)/\epsilon(\Xi_b^- \to J/\psi\Lambda K^-)$ and systematic uncertainties both in unit of %.

Source	Correction factor(%)	Uncertainty (%)
Signal fit model		0.7
Background fit model		1.6
BDTG efficiency	-	0.1
PID efficiency	-	1.0
Tracking efficiency	101.70	1.2
Resonances in $\Xi_b^- \to J/\psi\Lambda K^-$	98.00	1.5
b-baryon kinematics	113.77	1.5
Λ_b^0 and Ξ_b^- lifetime	100.91	1.1
MC statistics	-	0.7
Fixed resolution ratio	-	0.6
Total	114.42	3.5

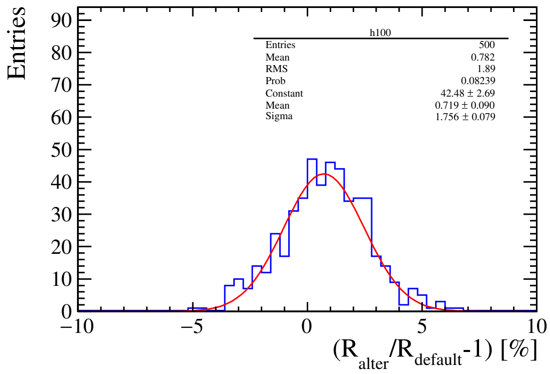

Figure 3.10 The fit result of $R_{alternative}/R_{default}$-1

3.6.2 Background model

The Chebyshev equation is used as an alternative model to study the systematic uncertainty due to the combinatorial background model. A similar strategy is used to study the systematics as reported in Sec. 3.6.1. The fit result of Gaussian function is given in Fig. 3.11. The resulting mean of $R_{\text{alternative}}/R_{\text{default}}$-1 is 1.6%.

The systematic uncertainty of the $\Xi_b^- \to J/\psi\Sigma^0 K^-$ background modelling is studies by using two alternative methods to described the background shape. Three methods are used in the fit: the MirrorBoth (default one, the input data is mirrored over the boundaries to minimise edge effects in distribution that do not fall to zero towards the edges), the NoMirror (without mirror option) and the MirrorBoth2 (estimate with a increased bandwidth scale factor). The larger differences in signal yields between the nominal fit and

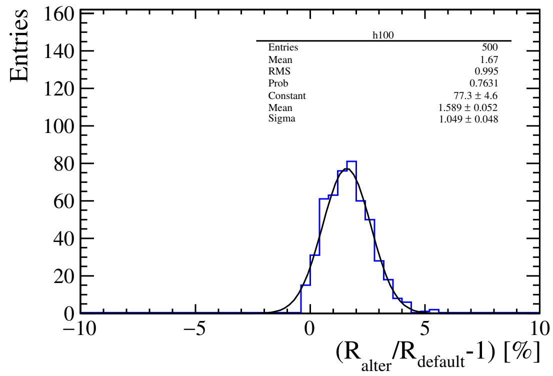

Figure 3.11 The fit results of $R_{alternative}/R_{default}$-1.

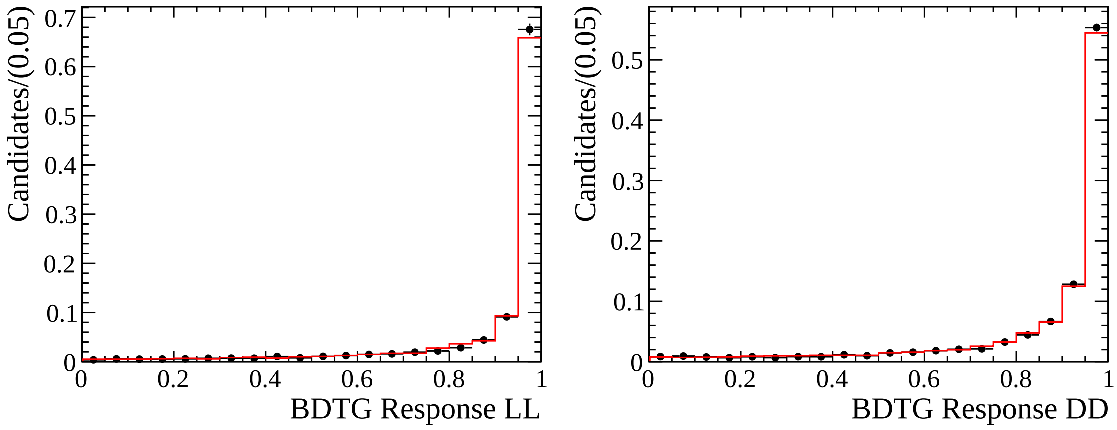

Figure 3.12 BDTG response for Λ_b^0 decays compared between the sWeighted data (points with error bars) and the signal MC (histogram) for LL (left) and DD (right) type.

alternative fit are taken as a systematic uncertainty, which are 0.14%(LL) and 0.46%(DD).

Two systematic uncertainties are added in quadrature, resulting in 1.6%.

3.6.3 BDTG selection efficiency

The BDTG responses of Λ_b^0 decays in data and simulation are shown Fig. 3.12. Good agreements are found both for LL and DD Λ. This gives confidence in the estimation of BDTG efficiency. In addition, the distributions of input variables for BDTG are checked. The variables are consistent, except that χ^2_{vtx} andχ^2_{IP} of Λ baryon in DD sample are not in good agreement. To take into account the impact of these differences, the simulated sample is smeared to match the data distributions. The change in efficiency is small and is taken as the systematic uncertainty.

Table 3.9 Binning strategies used in PID resampled

Default binning strategy	
$p(K)$ vin edges sequence (MeV)	(3000, 9300, 15600, 19000, 24400, 29800, 35200, 40600, 46000, 51400, 56800, 62200, 67600, 73000, 78400, 83800, 94600, 100000)
$\eta(K)$ bin edges sequence	(1.5, 2.375, 3.25, 4.125, 5)
nTrack bin edges sequence	(0, 50, 200, 300, 500)
New binning strategy	
$p(K)$ vin edges sequence (MeV)	(3000, 6150, 9300, 12450, 15600, 17300, 19000, 21700, 24400, 27100, 29800, 32500, 35200, 37900, 40600, 48700, 51400, 54100, 56800, 59500, 62200, 64900, 67600, 70300, 73000, 75700, 78400, 81100, 83800, 86500, 91900, 94600, 97300, 100000)
$\eta(K)$ bin edges sequence	(1.5, 1.9375, 2.375, 2.8125, 3.25, 3.6875, 4.125, 4.5625, 5)
nTrack bin edges sequence	(0, 25, 50, 125, 200, 250, 300, 400, 500)

3.6.4 PID efficiency

The systematic uncertainty of PID efficiency is estimated using `PIDCalib` package with a different binning strategy. The details of binning strategy are listed in Table 3.9. The changes in efficiency is taken as a systematic uncertainty. The statistics uncertainty of calibration data is 0.2%, the uncertainty due to the binning strategies is 1%, resulting a total systematic uncertainty 1%.

3.6.5 Tracking efficiency

An LHCb official tracking correction factor table is used to estimate the tracking efficiency. It is generated using information from the simulation and calibrated by data[113]. The uncertainty of the calibration is 0.4% per track. The uncertainty on the muons and Λ baryon daughters are fully cancel in the ratio. Additional systematic uncertainties are assigned to hadron due to insufficient knowledge of hadron interactions in the detector, which is 1.1% for kaons[33]. This is estimated by changing 10% of material budget in the detector. The total tracking efficiency related systematic uncertainty, adding the two contributions in quadrature, is 1.2%.

3.6.6 Resonances in $\Xi_b^- \to J/\psi \Lambda K^-$

Fig. 3.13 shows the Dalitz-plot (DP) distributions of $\Xi_b^- \to J/\psi \Lambda K^-$ decay using the ΛK^- and $J/\psi \Lambda$ invariant masses squared as axes, in background subtracted data sample and simulation. The simulation distribution reflects the relative efficiency as a function of the DP, showing a rather uniform efficiency.

To take into account the impact of the resonant structure in data sample, the data distribution across the DP is used to obtain an average efficiency, calculated as

$$\langle \epsilon \rangle = (\sum_i sw_i)/(\sum_i sw_i/\epsilon(\mathrm{DP}_i)), \tag{3-12}$$

where sw is an event-by-event *sWeight* obtained from fit to Ξ_b^- baryon invariant mass distribution, and $\epsilon(\mathrm{DP})$ is the efficiency as a function of DP distribution, determined as the DP distribution in simulated sample divided by the one in the generator level simulation. The index i sums over the data sample of $\Xi_b^- \to J/\psi \Lambda K^-$ decays. The systematic uncertainty is determined using toy MC. $\epsilon(\mathrm{DP}_i)$ is randomly sampled by a Gaussian random number with a width equal to the statistical uncertainty. All the bins are varied to obtain a new $\langle \epsilon \rangle$. Ensemble experiments are done to obtain a distribution of the $\langle \epsilon \rangle$. The width of the distribution divided by the central value of $\langle \epsilon \rangle$ is taken as the relative systematic uncertainty on $\langle \epsilon \rangle$. The PHSP efficiency is computed as the total number of reconstructed signal divided by the generated that to obtain the right plot in Fig. 3.13. The ratio between the average and PHSP efficiencies is taken as the correction factor.

The resonant structure in data samples can also affect the acceptance efficiency determined with generator level simulation. An event-by-event weight is assigned to generator level simulation. The weights are determined as the DP distribution of the background subtracted data divided by the distribution in signal simulation. The acceptance efficiency which takes into account the resonant structure is the ratio of the sums of weights after and before applying the acceptance selection. This results in an additional correction factor, which is multiplied to $\langle \epsilon \rangle$ to form an overall factor due to the resonant structure.

3.6.7 b-baryon kinematics

The simulated samples are reweighed to match the kinematic distributions in background subtracted data samples. The ratio between data and simulation distributions

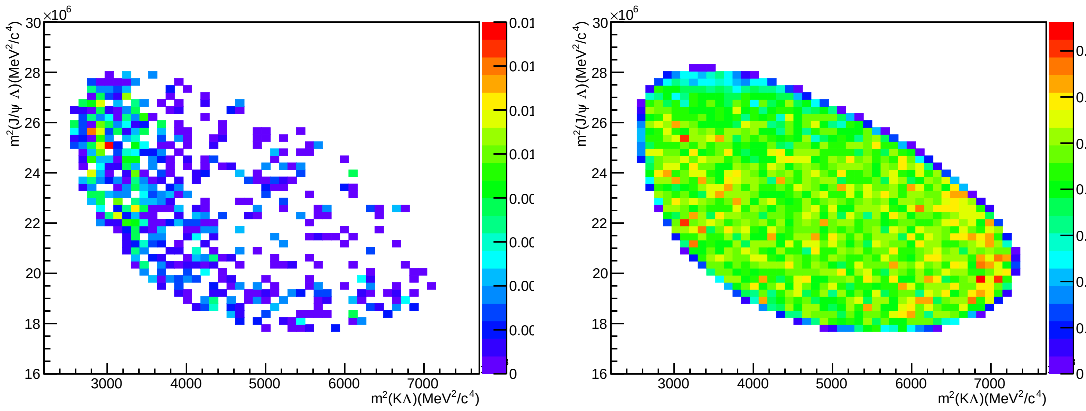

Figure 3.13 Dalitz-plot distributions of ($m^2(J/\psi\Lambda)$ vs. $m^2(K^-\Lambda)$) for data sample after background subtraction (left) and the simulated sample (right) in $\Xi_b^- \to J/\psi \Lambda K^-$ decays.

of transverse momentum and rapidity are taken as weights. The Ξ_b simulation is reweighed using the same weights extracted in Λ_b^0 samples due to lack of statistics. A new efficiency is obtained as sum of weights on the reconstruction level divided by sum of weights in generator level, recalculated for both signal and control modes, in the simulation. The ratio on the relative efficiency with and without the weighting procedure is the correction factor, which is $(114.42 \pm 1.5)\%$, where the uncertainties of the weights shown in Fig. 3.14 are used to obtain an uncertainty on the correction factor. Toy MC is used to evaluate the uncertainty. In each toy experiment, all the weights are varied randomly according to their errors, then the relative efficiency is evaluated. The ensemble toy tests result in a distribution of the relative efficiency, whose width is taken as uncertainty for the correction factor.

3.6.8 Ξ_b^- and Λ_b^0 lifetime

The MC inputs for the lifetimes are slightly different from the measured values. Therefore a correction factor and a systematic uncertainty due to the error of the measured lifetime for each b baryon need to be estimated. The Λ_b^0 and Ξ_b^- lifetime distributions in generator level simulated samples are shown in Fig. 3.15, fitted by an exponential function using the lifetimes for simulation generation: 1.426 ps and 1.568 ps, respectively. The Λ_b^0 and Ξ_b^- lifetime in simulated samples are checked to be consistent with the value measured by previous LHCb analysis, which is $\tau_0 = 1.468 \pm 0.009 \pm 0.008$ ps for Λ_b^0 baryon[114] and $\tau_0 = 1.57 \pm 0.04$ ps for Ξ_b^- baryon[58]. To estimate the impact of lifetimes, the simulated

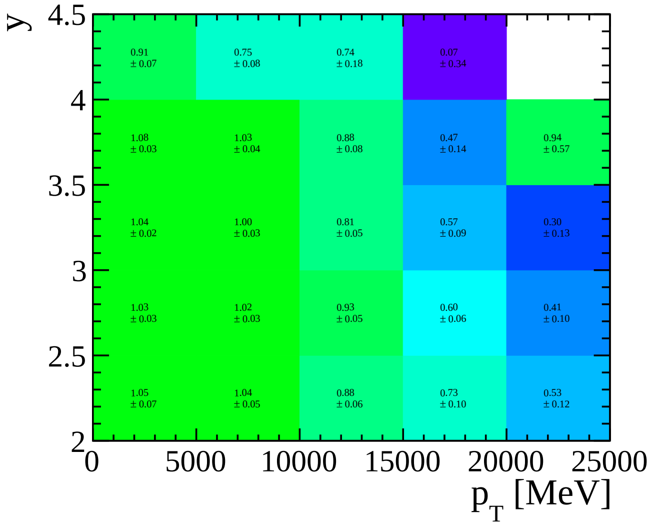

Figure 3.14 Relative yields between background-subtracted data and signal MC of $\Lambda_b^0 \to J/\psi \Lambda$ decays as function of p_T and y of the Λ_b^0 baryons.

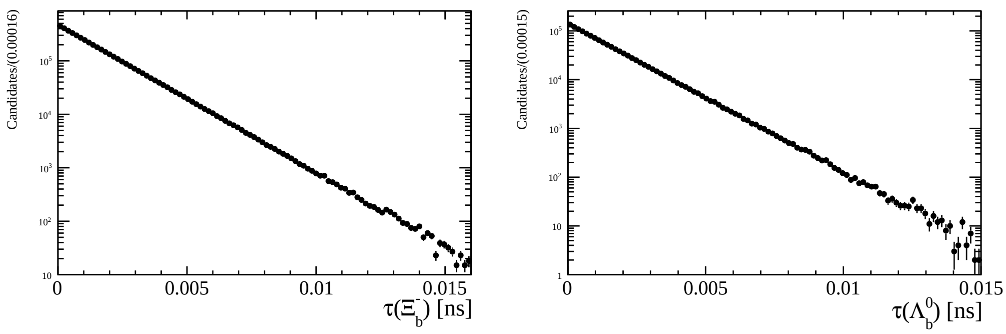

Figure 3.15 Distributions of lifetime of Ξ_b^- and Λ_b^0 in the MC sample at generator level.

samples are reweighed. The weight is defined as

$$w_\tau = e^{-t/\tau_0}/e^{-t/\tau_1}, \tag{3-13}$$

where τ_0 is the measured value in previous LHCb analysis and τ_1 is the value fitted from the generator level simulation. A new efficiency is calculated using simulated candidates with w_τ. The resulting efficiency divided by that without the weighting procedure, defined as a correction factor, is given in Table 3.8. To evaluate the systematic uncertainty, the central value of measured lifetime for each b baryon is varied by its error. The change on the relative efficiency is taken as the systematic uncertainty.

3.6.9 MC statistics

The limited statistics of the simulated samples used to estimate efficiencies is considered as a source of systematic uncertainty, which can be calculated as:

$$\frac{\sigma_\epsilon}{R} = \sqrt{\sum_{i=1}^{2}\left[\left(\frac{\partial \log R}{\partial \epsilon_i}\right)\right]^2 \sigma_{\epsilon_i}^2}, \tag{3-14}$$

where σ_ϵ stands for the uncertainty of R propagated from the efficiency uncertainties, and ϵ_i indicate the efficiencies of $\Lambda_b^0 \to J/\psi \Lambda$ and $\Xi_b^- \to J/\psi \Lambda K^-$ from the MC samples.

3.6.10 Fixed resolution ratio

The mass resolution of Ξ_b^- baryon is fixed using $\sigma_{\Xi_b}^{\rm Data} = \sigma_{\Xi_b}^{\rm MC} \times \sigma_{\Lambda_b^0}^{\rm Data}/\sigma_{\Lambda_b^0}^{\rm MC}$ in the default fit. Varying the mass resolution ratios of Ξ_b^- and Λ_b^0 mass peak in the fit results in an uncertainty of 0.6%.

3.6.11 Trigger efficiency

The comparison of distributions of momentum and transverse momentum of J/ψ in Λ_b^0 and Ξ_b^- channel is shown in Fig. 3.16 for the background subtracted data sample and MC sample. The variables in both of the two channels are in good agreement. The trigger selection is based on the kinematics of the dimuon pair, the systematic uncertainty caused by trigger selection cancels for ratios.

3.7 Determination of the mass difference

A simultaneous fit of the two samples is performed to measure the mass difference between the Ξ_b^- and Λ_b^0 candidate. The δM is required to be the same in LL and DD samples. The fit result is 177.08 ± 0.47(stat.) MeV and is consistent with the previous LHCb results[115]$\delta M = 178.36 \pm 0.46 \pm 0.16$ MeV using $\Xi_b^- \to \Lambda_c^0 \pi^-and\Lambda_b^0 \to \Lambda_c^+ \pi^-$.

Four sources of systematics are considered and listed in Table 3.10. The impact of momentum scale uncertainty of 0.03 MeV[116] is investigated by shifting the momenta of all final-state particles in simulated decays by this amount, leading to an uncertainty on δM 0.13 MeV. The correction for energy loss in the detector material is 0.06 MeV[115]. The above two sources are fully correlated with the previous measurement using $\Xi_b^- \to \Lambda_c^0 \pi^-and\Lambda_b^0 \to \Lambda_c^+ \pi^-$ decays[115]. The systematics come from the fitting models of signal and background are measured using alternative model and the results are 0.06 MeV

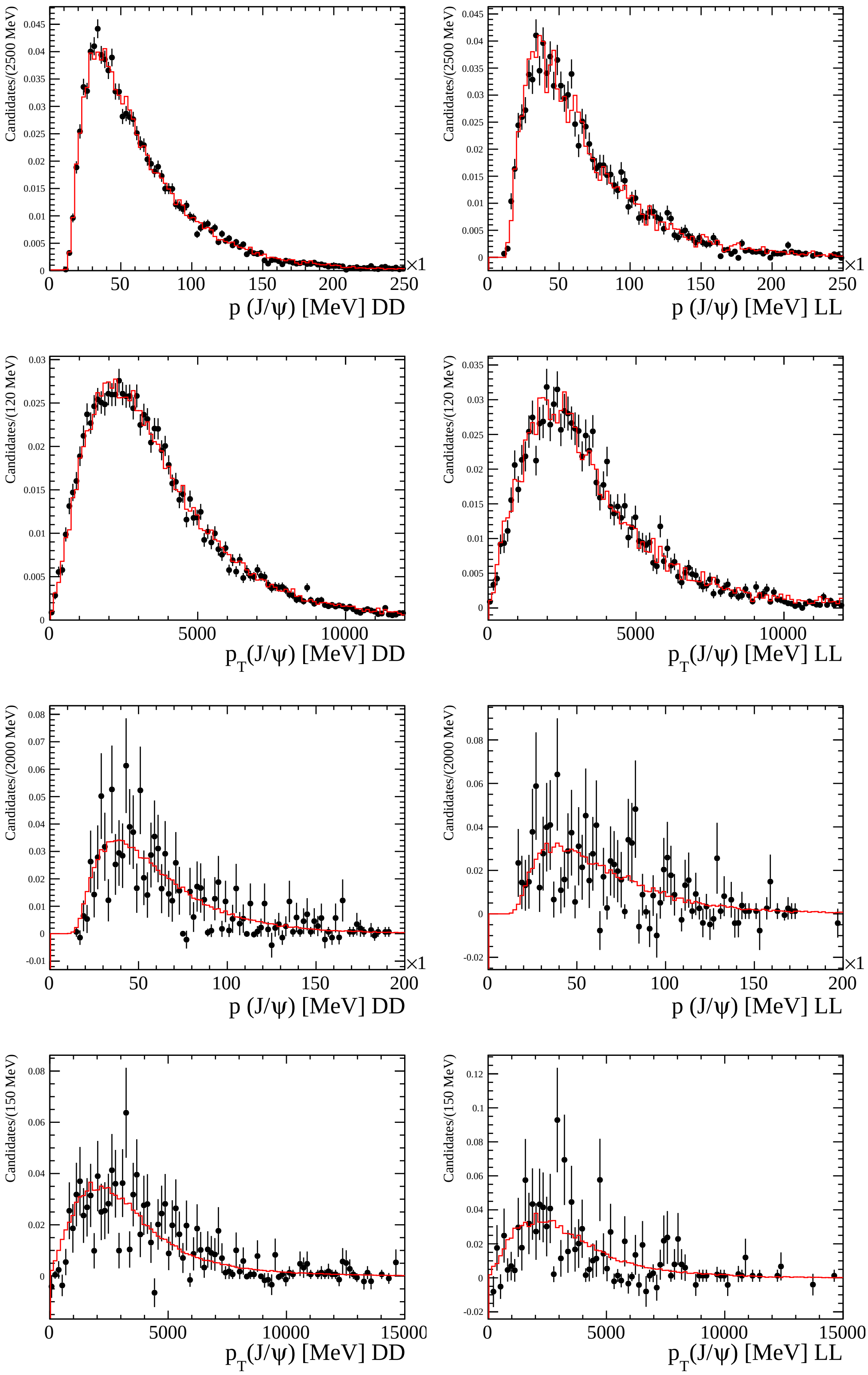

Figure 3.16 Distributions of p and p_T for J/ψ in $\Lambda_b^0 \to J/\psi \Lambda$ and $\Xi_b^- \to J/\psi \Lambda K^-$ decays, process from the data sample after background subtraction (points with error bars) and the simulation (histogram).

Table 3.10 Summary of systematic uncertainties on the $\delta M \equiv M(\Xi_b^-) - M(\Lambda_b^0)$ measurement.

Source	Value (MeV/c^2)
Signal fit model	0.06
Background fit model	0.02
Momentum scale	0.13
Energy loss	0.06
Total systematic	0.16

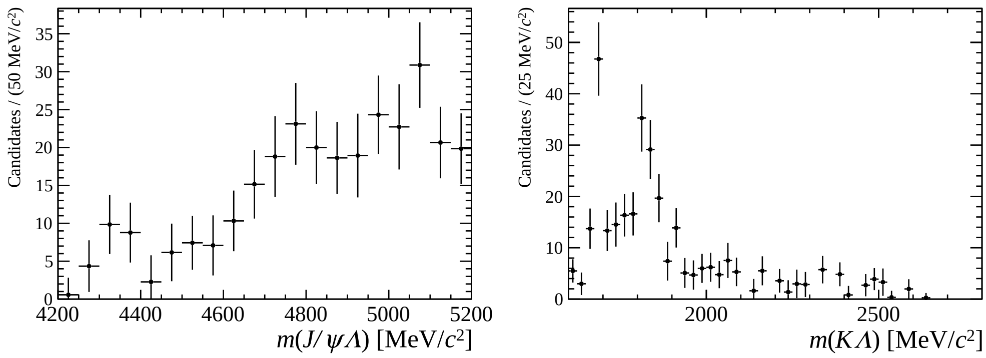

Figure 3.17 Distributions of $m(K\Lambda)$ (left) and $m(J/\psi\Lambda)$ (right) in background subtracted $\Xi_b^- \to J/\psi \Lambda K^-$ data sample.

and 0.02 MeV respectively. Adding all sources of uncertainty in quadrature leads to a systematic uncertainty in δM of 0.16 MeV.

The two results of δM measurement has been combined to obtain $\delta M = 177.73 \pm 0.33 \pm 0.14$ MeV, where the correlated systematic uncertainties have been included in the combination.

3.8 Search for Pentaquark states

The mass distributions of $m(K\Lambda)$ and $m(J/\psi\Lambda)$ in background subtracted $\Xi_b^- \to J/\psi \Lambda K^-$ sample are shown in Fig. 3.17. A cut of $m(K\Lambda) > 2.2$ GeV is applied to the data sample to subtract contributions from $\Xi(1690)$ and $\Xi(1820)$ states. The updated mass distribution of $m(J/\psi\Lambda)$ are shown in Fig. 3.18. Sign of pentaquark $usdc\bar{c}$ could be located at around 4.4 GeV. However, due to lack of statistics, a full amplitude analysis could not be performed.

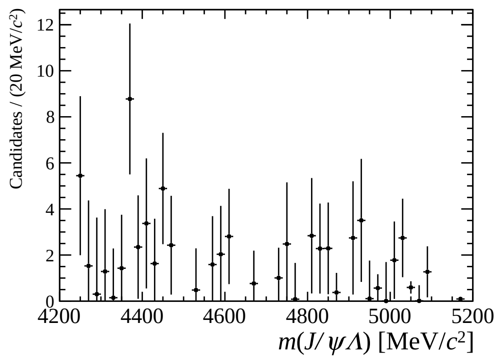

Figure 3.18 Distributions of $m(J/\psi\Lambda)$ with $m(K\Lambda) > 2.2$ GeV in background subtracted $\Xi_b^- \to J/\psi\Lambda K^-$ data sample .

3.9 Results

Using 3.0 fb^{-1} pp collisions data collected in 2011 and 2012, a search for $\Xi_b^- \to J/\psi\Lambda K^-$ decay channel has been performed. The mass difference between Ξ_b^- and Λ_b^0 baryons is also measured. Due to lack of statistics, the search for pentaquark state $usdc\bar{c}$ has not been performed.

The ratio of the branching fractions of $\Xi_b^- \to J/\psi\Lambda K^-$ with $\Lambda_b^0 \to J/\psi\Lambda$ is given by

$$R \equiv \frac{f_{\Xi_b^-}}{f_{\Lambda_b^0}} \frac{B(\Xi_b^- \to J/\psi\Lambda K^-)}{B(\Lambda_b^0 \to J/\psi\Lambda)} = 0.0419 \pm 0.0029(\text{stat.}) \pm 0.0015(\text{syst.}).$$

The mass difference between Ξ_b^- and Λ_b^0 baryon is determined as

$$\delta M = 178.08 \pm 0.47(\text{stat.}) \pm 0.16(\text{syst.})\ \text{MeV},$$

which is consistent with the previous LHCb results[116]. A combination of this value with the previous one leads to the most precise value of the mass difference:

$$\delta M = 177.73 \pm 0.33(\text{stat.}) \pm 0.14(\text{syst.})\ \text{MeV}. \tag{3-15}$$

Chapter 4 Measurement of CP-violating phase ϕ_s in $B_s^0 \to J/\psi\ K^+K^-$ decays in the mass region above the $\phi(1020)$

4.1 Introduction

The existence of phenomena beyond the SM could introduce sizeable effects on the CP-violating observables. The interference between B_s^0 meson decay amplitudes to CP eigenstates $J/\psi X$ directly or via mixing leads to a measurable CP-violating phase ϕ_s. Ignoring sub-leading corrections from penguin amplitudes[117], the phase ϕ_s in quark level $b \to c\bar{c}s$ transitions are predicted to be $-2\beta_s$. It can be determined indirectly via global fits to CKM matrix, which gives $2\beta_s = -0.0368^{+0.0096}_{-0.0068}$. However, many NP models[118-119] predict that the phase ϕ_s can be a large non-zero value if new physics processes contribute to the $B_s^0 - \overline{B}_s^0$ box diagram as illustrated in Fig. 4.1. Initial direct measurement of ϕ_s at Tevatron gave a large value which shows large discrepancy with the SM expectation[67], while LHCb results, determined using $B_s^0 \to J/\psi K^+K^-$ ($m_{KK} < 1.05$ GeV) and $B_s^0 \to J/\psi\pi^+\pi^-$ decays, are consistent with the SM value[79-80]. According to previous LHCb analysis[120], rich resonant spectrum is found in the $m_{KK} > 1.05$ GeV region of $B_s^0 \to J/\psi K^+K^-$ decays which could also be used in the ϕ_s determination.

4.2 Analysis strategy

In this analysis, the first measurement of ϕ_s using $B_s^0 \to J/\psi K^+K^-$ decays with m_{KK} above $\phi(1020)$ mass region is performed. A time-dependent amplitude analysis is used. The CP-violating phase ϕ_s is determined by simultaneously fit to the CP-even and CP-odd decay amplitudes for each contributing resonances.

The technique of time-dependent amplitude analysis for $B_s^0 \to J/\psi h^+h^-$ is first proposed in Ref.[121], where h stands for a pion or a kaon. The mathematical formula in Ref.[121], is used to reconstruct the fit function of signal decays. A short introduction of the method is included in App. A.

The decay amplitudes are defined as $\mathcal{A} \equiv A_f$ and $\overline{\mathcal{A}} \equiv \frac{q}{p}\overline{A}_f$, where A_f ($\overline{A}_f$) is the total amplitude of B_s^0 ($\overline{B}_s^0$) $\to J/\psi K^+K^-$ decays, which is the sum over the individual K^+K^- resonant transversity amplitude and a non-resonant amplitude, at time $t = 0$. The decay amplitudes $\mathcal{A}$ and $\overline{\mathcal{A}}$ can also be expressed as the sums of the individual B_s^0

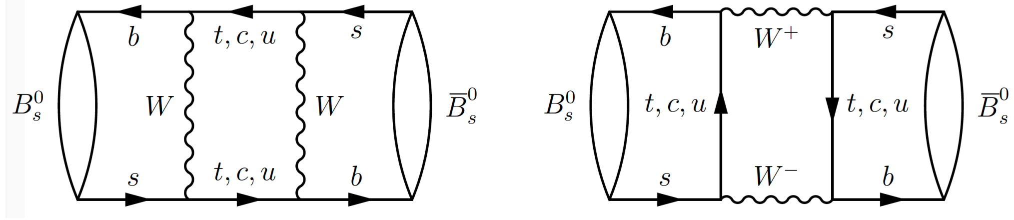

Figure 4.1 Feynman diagrams for $B_s^0 - \overline{B}_s^0$ mixing, within the SM.

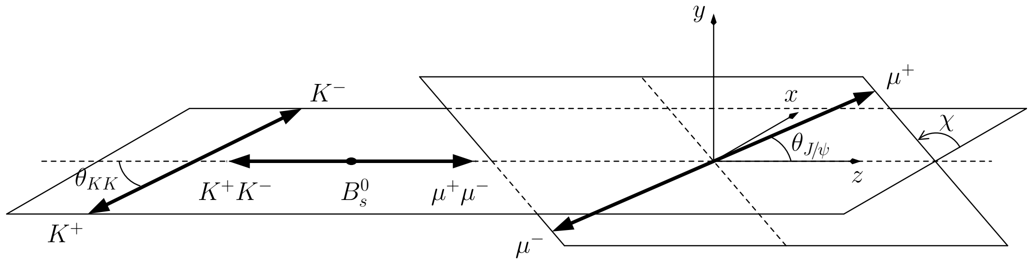

Figure 4.2 Definition of helicity angles.

amplitudes, $\mathcal{A} = \sum A_i$ and $\overline{\mathcal{A}} = \sum \lambda_i A_i = \sum \eta_i |\lambda_i| e^{-i\phi_s^i} A_i$, where $\lambda_i \equiv \frac{q}{p}\frac{\overline{A}_i}{A_i}$①. The CP-violating phase for each transversity state is given by $\phi_s^i \equiv -\arg(\eta_i \lambda_i)$[123], where η_i is the CP eigenvalue of the state. If CP violation in the decay is same for all amplitudes, then $\lambda \equiv \eta_i \lambda_i$ is common for all of these amplitudes.

The decay amplitude of $B_s^0 \to J/\psi K^+K^-$ decays could be expressed as a function of the K^+K^- invariant mass m_{KK} and the three angular variables $\Omega \equiv (\cos\theta_{KK}, \cos\theta_{J/\psi}, \chi)$, defined in the helicity basis, as illustrated in Fig. 4.2. θ_{KK} is the angle between K^+ direction in the K^+K^- rest frame with respect to the K^+K^- direction in the B_s^0 rest frame, $\theta_{J/\psi}$ is the angle between the μ^+ direction in the J/ψ rest frame with respect to the J/ψ direction in the B_s^0 rest frame and χ is the angle between the J/ψ and K^+K^- decay planes in the B_s^0 rest frame[121,123]. (These definitions are the same for B_s^0 and $\overline{B}_s^0$, namely, using μ^+ and K^+ to define the angles for both B_s^0 and $\overline{B}_s^0$ decays.)

The decay amplitude of $B_s^0 \to J/\psi K^+K^-$ via a two-body intermediate resonance $R(K^+K^-)$ and the J/ψ meson is given by

$$\mathcal{A}_R(m_{KK}) = \sqrt{2J_R+1}\sqrt{P_R P_B} F_B^{(L_B)} F_R^{(L_R)} A_R(m_{KK}) \left(\frac{P_B}{m_B}\right)^{L_B} \left(\frac{P_R}{m_0}\right)^{L_R}. \tag{4-2}$$

① The factor $|p/q|^2$ is related to the flavour-specific CP-violating asymmetry a_{sl}^s as

$$a_{sl}^s \equiv \frac{|p/q|^2 - |q/p|^2}{|p/q|^2 + |q/p|^2} \approx |p/q|^2 - 1. \tag{4-1}$$

LHCb measured $a_{sl}^s = (0.39 \pm 0.26 \pm 0.20)\%$[122], corresponding to $|p/q|^2 = 1.0039 \pm 0.0033$. Thus, $|p/q|^2 = 1$ is taken in this analysis.

Table 4.1 Breit-Wigner resonance parameters.

Resonance	Mass (MeV)	Width (MeV)	Source
$\phi(1020)$	1019.461 ± 0.019	4.266 ± 0.031	PDG[58]
$f_2(1270)$	1275.5 ± 0.8	186.7 ± 2.5	PDG[58]
$f_2'(1525)$	Varied in fits		
$\phi(1680)$	1689 ± 12	211 ± 24	Belle[126]
$f_2(1750)$	1737 ± 9	151 ± 33	Belle[127]
$f_2(1950)$	1980 ± 14	297 ± 13	Belle[127]

where $F_B^{(L_B)}$ and $F_R^{(L_R)}$ are the B_s^0 and R decay form factors; $P_B(P_R)$ is the J/ψ (either of the R resonance daughter's) momentum in the B_s^0 (R) rest frame;m_B is the B_s^0 mass, m_0 is the central mass of resonance R; J_R is spin of R; $L_B(L_R)$ is the orbital angular momentum between the B_s^0 meson (R resonance) 's daughters; $A_R(m_{KK})$ is the amplitude used to describe the mass line-shape of the resonance R.

According to previous LHCb publication[120] with 1 fb^{-1} pp collision data, a rich resonance structure is found in the K^+K^- mass spectrum. They are listed in Table 4.1 and described by Breit-Wigner amplitudes. The spin-0 f_0 resonances and non-resonance components are described in a model-independent way, by two cubic splines accounting for the real and imaginary parts of the amplitude as a function of m_{KK}.

The likelihood construction employed in this analysis were used in the measurement of CP-violating phase ϕ_s with $B_s^0 \to J/\psi\pi^+\pi^-$ decays[80]. An unbinned maximum likelihood fit is performed to the decay time t, m_{KK}, and the three helicity angles Ω, along with information on the initial flavour of the decaying hadron, *i.e.* whether it was produced as a B_s^0 or a $\overline{B}_s^0$ meson. The probability density function (PDF) used in the fit consists of only signal components that include detector resolution and acceptance effects, with background subtracted statistically using *sPlot* technique[124-125]. An event-by-event decay-time error and mistag probability are used in the decay-time resolution model and inclusion of flavour tagging.

Two different sets of fitting parameters $(\phi_s, |\lambda|, \Gamma_s, \Delta\Gamma_s)^{L,H}$ are used for the low (L) and the high (H) m_{KK} regions to get an independent measurement from the previous publication[79]. The log-likelihood is the sum of two constructed from L and H events. The shared parameters are Δm_s and all amplitudes and phases for the resonances.

Table 4.2 Simulated samples used in the analysis. PHSP indicates the simulation is generated with the phase space model. P2VV means the simulation is generated with pseudoscalar to two vector mesons mode where CP-violating time asymmetries including different lifetimes for the different mass eigenstates are allowed. SVV_HELAMP means that the generator is configured with scaler to two vector mesons model with amplitude given by helicity amplitude arguments, detail description of the generator models can be found at Ref.[97].

Decay channel	Production type	Events	Model	Utilisation
$B_s^0 \to J/\psi K^+K^-$	Full	7.0×10^6	PHSP	Signal study
$B_s^0 \to J/\psi\phi$	Full	20.0×10^6	P2VV	Signal study
$B_s^0 \to J/\psi\phi$	Full	20.0×10^6	P2VV,$\Delta\Gamma_G = 0$	Signal study
$\Lambda_b^0 \to J/\psi pK^-$	Full	8.0×10^6	PHSP	Background modelling
$B^0 \to J/\psi K^+\pi^-$	Full	8.0×10^6	PHSP	Background modelling
$B^0 \to J/\psi K^{*0}$	Full	8.0×10^6	SVV_HELAMP	Control channel

4.3 Dataset and selection requirement

The full LHCb Run-I dataset consisting of 1 fb^{-1} of pp collision data with a centre-of-mass energy of $\sqrt{s} = 7$ TeV taken in 2011 and 2 fb^{-1} of data with a centre-of-mass energy of $\sqrt{s} = 8$ TeV taken in 2012 is used in this analysis. The simulated samples listed in Table 4.2 are used with different purposes, as indicated in the table. To distinguish between the charged particles in the final states, a likelihood function assuming the respective particle to be a pion or kaon (proton, muon) is computed for every particle using information from the PID system. The difference between the two logarithmic likelihoods is calculated, which in the following is referred as DLL$_{K\pi}$, DLL$_{p\pi}$ and DLL$_{\mu\pi}$. The PID variables are not well described in the simulated samples, thus no PID selection is required in the simulation, instead an event-by-event PID weight calculating using a data-driven method in `PIDCalib` package[108] is assigned. This weight, estimated with kinematically-clean $D^{*+} \to D^0(\to K^-\pi^+)\pi^+$ and $\Lambda \to p\pi^-$ samples, is generated in bins of transverse momentum, pseudorapidity and `nTracks`. The two reflection background generated with the phase space models are weighted to take into account the decay amplitudes found in the data and PID efficiency obtained using the data-driven method.

The event selection is constituted of the trigger selection, followed by some preselection requirements and finally a BDTG[104] trained against combinatorial background. Trigger lines used in this analysis are listed in Table 4.3. The preselection requirements are given in Table 4.4. The $B_s^0 \to J/\psi K^+K^-$ candidates are reconstructed

Table 4.3 Trigger lines used for selected $B_s^0 \to J/\psi K^+K^-$ candidates. More details on the trigger lines can be found in Ref.[107].

Trigger level	Trigger line
HLT1	`Jpsi_Hlt1DimuonHighMassDecision_TOS` or `B_Hlt1TrackMuonDecision_TOS` or `B_Hlt1TwoTrackAllL0Decision_TOS`
HLT2	`Jpsi_Hlt2DimuonDetachedJpsiDecision_TOS`

with $J/\psi \to \mu^+\mu^-$ and two opposite-signed kaon tracks. The track fit χ^2 of all tracks must be less 3 and the fake track probability should be less than 0.2. The muon candidates should have p_{T} greater than 550 MeV, $\mathrm{DLL}_{\mu\pi} > 0$ and χ^2_{IP} larger than 4. The combined di-muon pairs need to fire the selection of vertex fit χ^2_{vtx} less than 16 and the invariant mass within the mass window $(-48, +43)$ around the known J/ψ mass[58]. The kaon candidates are chosen with p_{T} greater than 250 MeV, $\mathrm{DLL}_{K\pi} > 3$ or `ProbNNk`> 0.1. The sum p_{T} of two kaon tracks should be greater than 900 MeV and vertex fit χ^2_{vtx} of them should be no more than 16. The reconstructed B_s^0 candidates must have χ^2_{IP} less than 25, vertex fit χ^2_{vtx}/ndf less than 6, the pointing angle $\cos\theta_p$ greater than 0.999 and decay time larger than 0.2 ps. The next best χ^2_{IP} in the same events should pass $\chi^2_{\mathrm{IP}} > 50$.

Events satisfying this preselection are further filtered using a multivariate analyser based on a BDTG technique. The BDTG training variables are the minimum $\mathrm{DLL}_{\mu\pi}$ of the μ^+ and μ^- (mmPIDmu); the B_s^0 pointing angle, $\cos\theta_p$ (DIRA); B_s^0 vertex χ^2 log(BCHI2); p_{T} of the B_s^0 (BPT); B_s^0 χ^2_{IP} (LogBIPCHI2); p_{T} sum of the K^+ and K^- (SumPT). The training sample used for the signal is $B_s^0 \to J/\psi K^+K^-$ simulation. The background training sample is obtained using candidates in upper mass sideband $(+150, +250)$ region above the B_s^0 mass. $\Lambda_b^0 \to J/\psi p K^-$ and $B^0 \to J/\psi K^+\pi^-$ backgrounds due to incorrect particle identification are vetoed in order to improve the training performance. Signal and background distributions for each of the variables used in the BDTG are shown in Fig. 4.3. The BDTG output distributions are shown in Fig. 4.4.

A cut on the output value of the BDTG is used to reject combinatorial background. The optimisation procedure uses a figure of merit, defined as FOM$= \frac{S}{\sqrt{S+B}} \times \sqrt{\frac{S}{S+B}}$, where $S(B)$ are the number of expected signal and background events in the 2σ (± 15 MeV) region around the known B_s^0 mass[58]. The background yield B is estimated by scaling the event number in the low and high mass data sidebands from 85 to 135 MeV of the B_s^0 peak, in which the sidebands do not overlap with the fit region. The signal yield

Table 4.4 Preselection requirements for selected $B_s^0 \to J/\psi K^+K^-$ candidates.

#	Selection variables	Requirements
1	All tracks χ^2/ndf	< 3
2	Ghost track probability	< 0.2
	J/ψ selection	
3	Muon $\text{DLL}_{\mu\pi}$	> 0
4	Muon p_{T}	> 550 MeV
5	Muon χ^2_{IP}	> 4
6	J/ψ vertex χ^2_{vtx}	< 16
7	$m(\mu^+\mu^-) - m(J/\psi)$	$(-48, +43)$ MeV
	K selection	
8	Kaon p_{T}	> 250 MeV
9	Kaon PID	$\text{DLL}_{K\pi} > 3$ or `ProbNNk`> 0.1
10	Sum p_{T} of K^+K^-	> 900 MeV
11	K^+K^- vertex χ^2	< 16
	B_s^0 meson selection	
12	χ^2_{IP}	< 25
13	χ^2_{vtx}/ndf	< 6
14	Next best χ^2_{IP}	> 50
15	Pointing, $\cos\theta_p$	> 0.999
16	Decay time, t	> 0.2 ps

S is estimated by $S = N_{\text{tot}} - B$, where N_{tot} is total number of events in the 2σ mass window. The BDTG and PID selection are optimised simultaneously, resulting in best working point BDTG > 0.5, $\text{DLL}_{K\pi} > 6$ and $\text{DLL}_{Kp} > -10$. The BDTG cut has about 75% signal efficiency and rejects 95% of background.

Multiple candidates which have the same distributions as the combinatorial background is kept in the sample. It has an overall fraction of 1.1% in the fit region of $5300 < m(J/\psi K^+K^-) < 5450$ MeV, and 0.17% in ± 15 MeV around the B_s^0 mass peak.

4.4 Signal yields extraction

The signal yields of $B_s^0 \to J/\psi K^+K^-$ are determined separately for the events with m_{KK} less and greater than 1.05 GeV. Four components, the signal B_s^0, the combinatorial background, the misidentified $B^0 \to J/\psi K^+\pi^-$ and $\Lambda_b^0 \to J/\psi p K^-$ background are

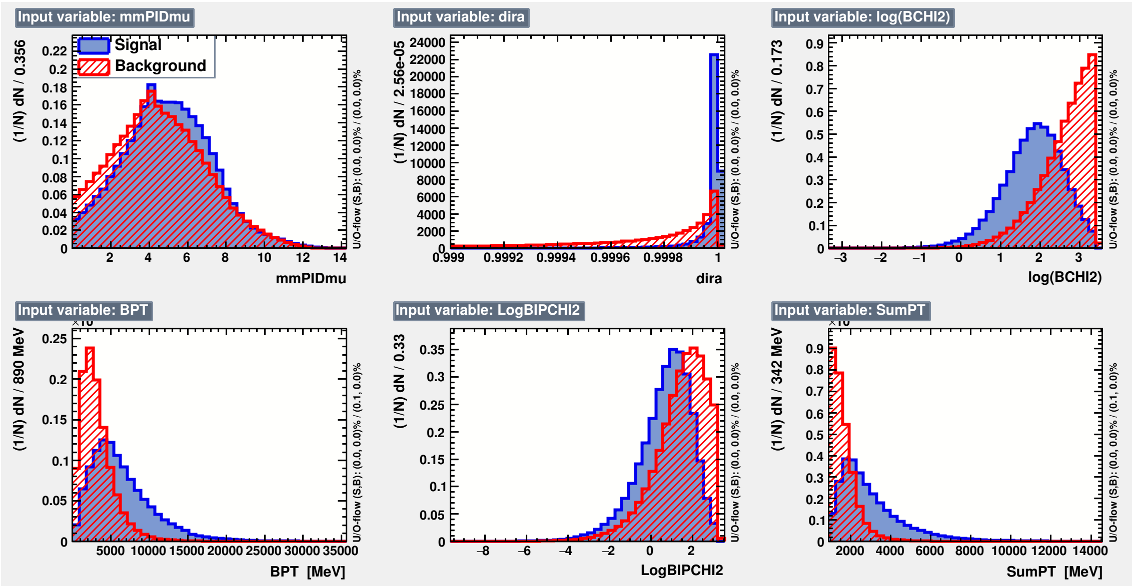

Figure 4.3 Distributions of variables used in BDTG. The darker shaded distributions are for signal.

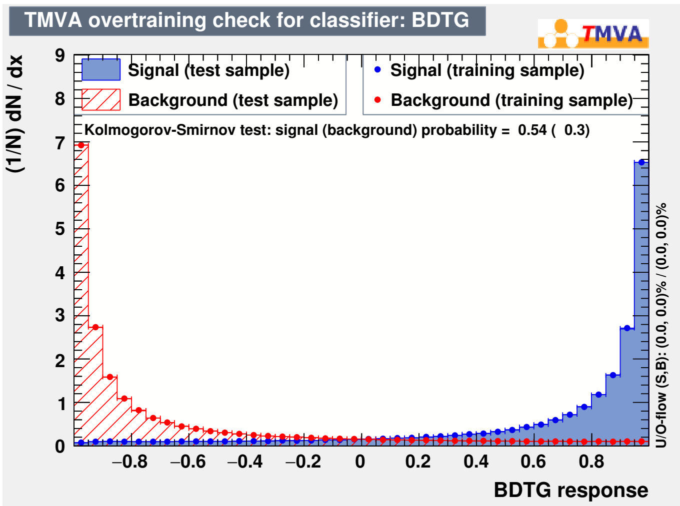

Figure 4.4 BDTG distributions for the signal and background.

considered.

The signal B_s^0 is parametrised by a Hypathia function[109] with shape parameters fixed to the values obtained from simulation while the combinatorial background is modelled with an exponential function. The B^0 background is modelled by sum of a bifurcated and a normal Gaussian while the Λ_b^0 background is described by a fourth-order polynomial. The shape parameters of the misidentified physics backgrounds are extracted from fits to the simulation, as shown in Fig. 4.5.

The yields of the misidentified physics backgrounds are estimated using candidates

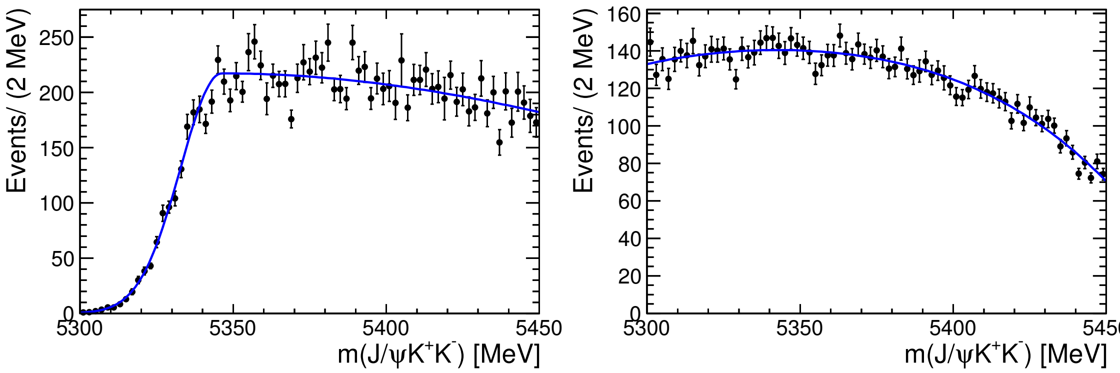

Figure 4.5 Simulated background $m(J/\psi K^+K^-)$ distributions from $B^0 \to J/\psi K^+\pi^-$ (left) and $\Lambda_b^0 \to J/\psi p K^-$ (right) decays with requirement of $m_{KK} > 1.05$ GeV. The B^0 reflection is modelled by sum of a bifurcated and a normal Gaussian while the Λ_b^0 by a fourth-order polynomial.

Table 4.5 Fitted yields in ± 15 MeV of the B_s^0 mass peak.

Source	$m_{KK} < 1.050$ GeV	$m_{KK} > 1.050$ GeV
signal	50527 ± 224	31112 ± 228
combinatorial background	114 ± 20	6143 ± 132
B^0 background	141 ± 19	2092 ± 105
Λ_b^0 background	189 ± 18	2311 ± 116

in the $m(J/\psi K^+K^-)$ sidebands. For B^0 background, the $J/\psi K^+K^-$ candidates in $m(J/\psi K^+K^-) \in (5450, 5614)$ MeV region are interpreted as $J/\psi K^\pm\pi^\mp$. The interpreted mass distribution is fitted with a double-Gaussian function for signal and a fourth-order polynomial function for background, as shown in Fig 4.6. The number of B^0 candidates extracted with the double-Gaussian function is 7117 ± 202. Using shape of the B^0 simulation and this yield, the number of B^0 background events in the (5300, 5450) MeV region is predicted to be 8715. A total uncertainty of 5% is assigned, 3% statistical and 4% systematic due to fake rates and simulation size used to predict the mass shape of the B^0 background. The same method is used to evaluate the Λ_b^0 yield in (5300, 5450) MeV region. In total, there are 8715 ± 435 B^0 candidates and 10752 ± 537 Λ_b^0 candidates left in the $m_{KK} > 1.05$ GeV region and 434 ± 65 B^0 candidates and 800 ± 100 Λ_b^0 candidates in the $m_{KK} < 1.05$ GeV region. These numbers are constrained in the fits to determine the B_s^0 yields. The fit results are shown in Fig. 4.7. The yields are 53440 ± 240 and 33200 ± 240 for the low and high m_{KK} intervals, respectively. Table 4.5 lists the yields for the B_s^0 signal and various backgrounds within the signal window ± 15 MeV.

The two misidentified backgrounds are correlated with m_{KK} and angular variables.

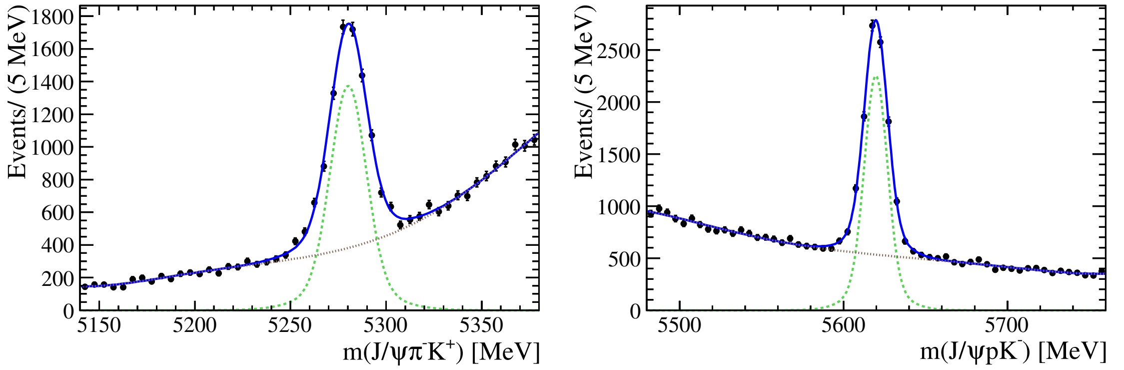

Figure 4.6 Invariant mass distributions for the sideband events resigned as different mass hypotheses as (left) $J/\psi\pi^-K^+$ and (right) $J/\psi pK^-$ with requirement of $m_{KK} > 1.05$ GeV. Fits are done by double-Gaussian as signal by (green) dashed line plus a fourth-order polynomial function for the background by (black) dotted lines, with (blue) solid line as total.

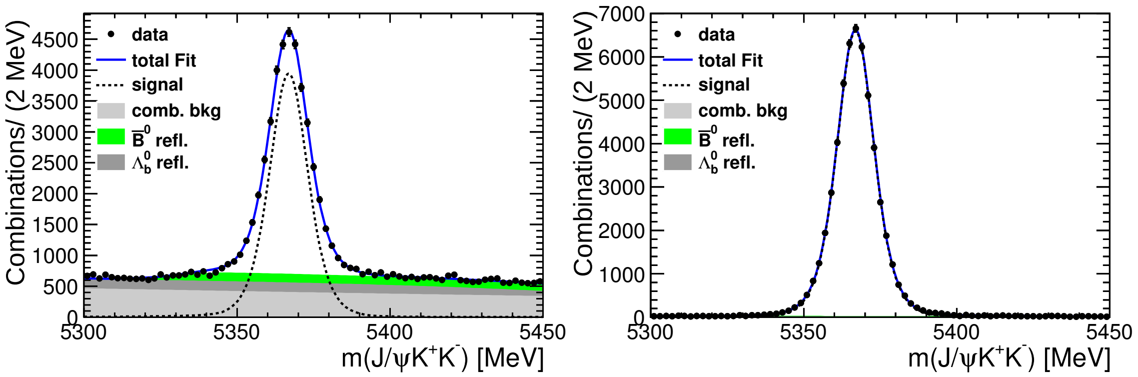

Figure 4.7 Fit to invariant mass spectrum of $J/\psi K^+K^-$ combination with $m_{KK} > 1.05$ GeV (left) and $m_{KK} > 1.05$ GeV (right) .

To subtract them, the B^0 and Λ_b^0 simulations are inserted into the data sample with negative weights, multiplied by the weights taking into account the decay amplitudes found in the data and the PID misidentification rates. The sum of the final weights is scaled to match the yields reported above in fit to data. A second mass fit is performed by including only the signal and combinatorial background to obtain *sWeight* using the *sPlot* technique[124]. The fits are performed in four equal bins of $|\cos\theta_{J/\psi}|$ and two bins of m_{KK} (separated at 1.05 GeV) for a total of eight fits. The signal resolution varies as function of $|\cos\theta_{J/\psi}|$ as reported in Ref.[79]. Overall fits to candidates in low and high m_{KK} regions are shown in Fig. 4.8. The signal parameters for radiative tails are fixed, and common for different $|\cos\theta_{J/\psi}|$ and the same m_{KK} bins. The signal yield and width, and background yield and parameters are freely varied and independent for each fit.

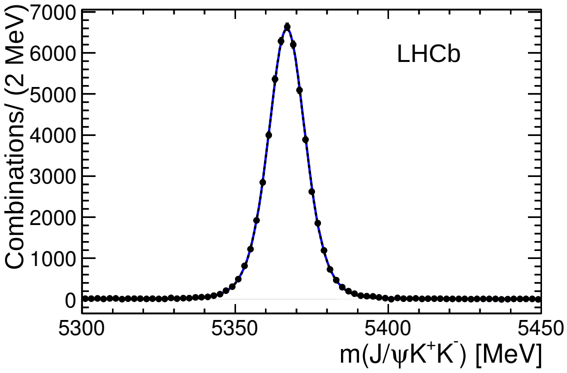

Figure 4.8 Fits to invariant mass distributions after subtraction of the two reflection backgrounds for $m_{KK} < 1.05$ GeV (left) and $m_{KK} > 1.05$ GeV (right). Dashed-lines show the signal and the darkened regions show the combinatorial background (it's hard to see in the left figure because the background is very small).

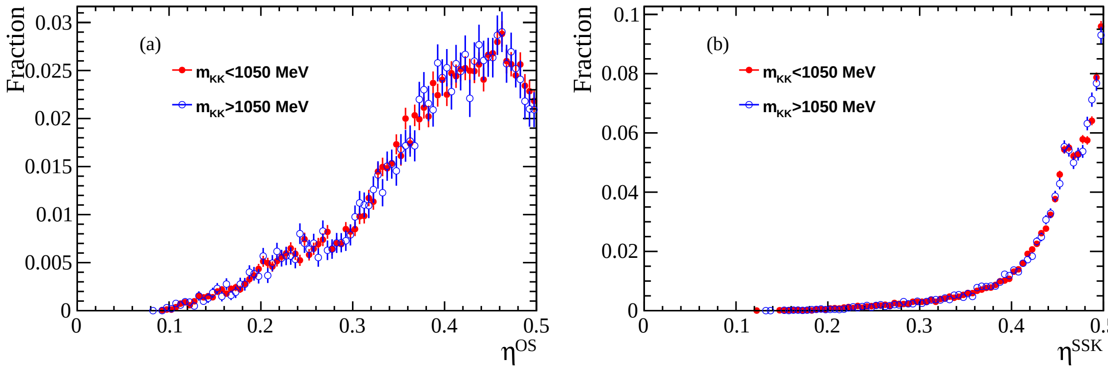

Figure 4.9 Estimated fractions of mistag probabilities from (a) the OS tagger, η^{OS}, and (b) the SSK tagger, η^{SSK}.

4.5 Flavour tagging calibration

Both OS and SS tagging algorithms are employed for this analysis. The combination of OS-electron, OS-muon, OS-vertex charge and OS-kaon algorithms is used as the nominal OS tagger. The neural network SS kaon tagger is used as the nominal SS tagger. The estimated-mistag-probability distributions of the tagged *sWeighted* events for the OS and SS taggers are show in Fig. 4.9.

The true mistag probability ω is calibrated using per-event mistag probability η in data, which is the output of a neural network based on information in the decay. A linear dependence is used to describe this relation

$$\begin{aligned} \omega(\eta) &= p_0 + \frac{\Delta p_0}{2} + (p_1 + \frac{\Delta p_1}{2}) \cdot (\eta - \langle\eta\rangle); \\ \bar{\omega}(\eta) &= p_0 - \frac{\Delta p_0}{2} + (p_1 - \frac{\Delta p_1}{2}) \cdot (\eta - \langle\eta\rangle), \end{aligned}$$

Table 4.6 Flavor tagging calibration parameters.

Par	OS	SSK
p_0	$0.3848 \pm 0.0019 \pm 0.0040$	$0.442 \pm 0.004 \pm 0.003$
p_1	$0.982 \pm 0.007 \pm 0.034$	$0.976 \pm 0.071 \pm 0.057$
$\langle\eta\rangle$	0.3786	0.437
Δp_0	$+0.0140 \pm 0.0012$	-0.0156 ± 0.0014
Δp_1	$+0.066 \pm 0.012$	$+0.007 \pm 0.022$

Table 4.7 Tagging information.

Category	$m_{KK} < 1.05$ GeV		$m_{KK} > 1.05$ GeV	
	ε_{tag} (%)	$\varepsilon_{tag}D^2$ (%)	ε_{tag} (%)	$\varepsilon_{tag}D^2$ (%)
OS only	13.14 ± 0.15	1.13	13.36 ± 0.23	1.15
SSK only	37.72 ± 0.21	0.93	37.35 ± 0.33	0.88
OS and SSK	17.80 ± 0.17	1.79	17.71 ± 0.26	1.76
Total	68.66 ± 0.20	3.83	68.42 ± 0.32	3.79

where $\omega(\eta)$ and $\bar{\omega}(\eta)$ are the calibrated probabilities for a mistag assignment for B_s^0 and $\overline{B}_s^0$ mesons, respectively. The calibration parameters p_0, p_1, Δp_0, Δp_1 and $\langle\eta\rangle$ (the mean mistag probability) are given in Table 4.6.

An effective tagging power of 3.83% and 3.79% for $m_{KK} < 1.05$ GeV and $m_{KK} > 1.05$ GeV regions are computed for the sample under study using the method described in Sec.2.3.3. Details of the tagging performance can be found in Table 4.7.

4.6 Detector effects

4.6.1 Decay-time resolution

The resolution of the B_s^0 decay-time measurement significantly affects the accuracy of the determination of ϕ_s, thus it has to be characterised and account for. The time resolution is determined using *fake* B_s^0 candidates which are reconstructed with two opposite-sign charged tracks associated to a prompt J/ψ candidate. These *fake* B_s^0 candidates are selected using the similar selection criteria for $J/\psi K^+K^-$ expect for the time bias trigger and selections. Explicitly, we use the selection in Table 4.4 except for the biased cuts # 14–16, and the final PID criteria, as for the B_s^0 signal.

This method has been validated using B_s^0 signal and inclusive J/ψ (reconstructed as *fake* B_s^0) simulations. The p_{T} distribution of *fake* B_s^0 from inclusive J/ψ sample is much softer than that of real B_s^0. Thus the *fake* B_s^0 sample is weighted according to the p_{T} ratio between the real and *fake* B_s^0 samples. The effective decay-time resolution is determined in B_s^0 simulation with three sets of selection: 1) the selection criteria used for *fake* B_s^0 data sample (time unbiased selection); 2) the selection criteria used in real B_s^0 data sample expect for the BDTG and detached selection (selection used to form the B_s^0 candidates); 3) the full selection criteria used in real B_s^0 data sample. The inclusive J/ψ sample is selected with option 1).

The decay-time resolution is non constant and varies with the decay time. Thus the decay-time resolution function used in the main fitter is constructed as a function of the estimated decay-time error, δ_t, computed per-event during the reconstructed process. A double-Gaussian function is used to describe this relation. The effective decay-time resolution σ_{eff} is extracted with binned fit to decay-time error δ_t distribution, calculated as

$$\sigma_{\mathrm{eff}} = \sqrt{(-2\ln(D_t))/\Delta m_s}, \tag{4-3}$$

where $D_t = \sum_i f_i e^{-(\sigma_i * \Delta m_s)^2/2}$ is the dilution due to time resolution, $\Delta m_s = 17.77$ ps^{-1} [58], f_i and σ_i are fraction and width of the i-th Gaussian, respectively.

The comparison of differences between decay-time error δ_t and effective decay-time resolutions in B_s^0 and inclusive J/ψ samples is shown in Fig. 4.10. The points are fitted by first order polynomial. The overall effective resolutions are 1) 42.9% fs; 2) 43.4 fs; 3) 41.5 fs in B_s^0 signal samples (corresponding to the selection criteria mentioned above). Results 1) and 2) are consistent within 1.2% while 2) and 3) are consistent within 4.4%. Thus, 5% uncertainty is assigned to the time resolution due to the calibration method.

For the data sample, a triple-Gaussian function is used due to the increase of statistics. The relation between the decay time and decay-time error is estimated with

$$T(t, \delta_t) = \sum_{i=1}^{3} f_i^T \frac{1}{\sqrt{2\pi} S_i \sigma_t} e^{\frac{-(t-\hat{t}-\mu_t)^2}{2(S_i\sigma_t)^2}}, \tag{4-4}$$

where $\sigma_t \equiv \delta_t + \sigma_t^0$, σ_t^0 is a constant accounting for underestimated decay-time error, $\hat{t}$ is the true decay time, μ_t is the bias on the time measurement, $f_1^T + f_2^T + f_3^T = 1$ are the fractions of each Gaussian function, and S_i is a constant scale factor for the ith Gaussian function.

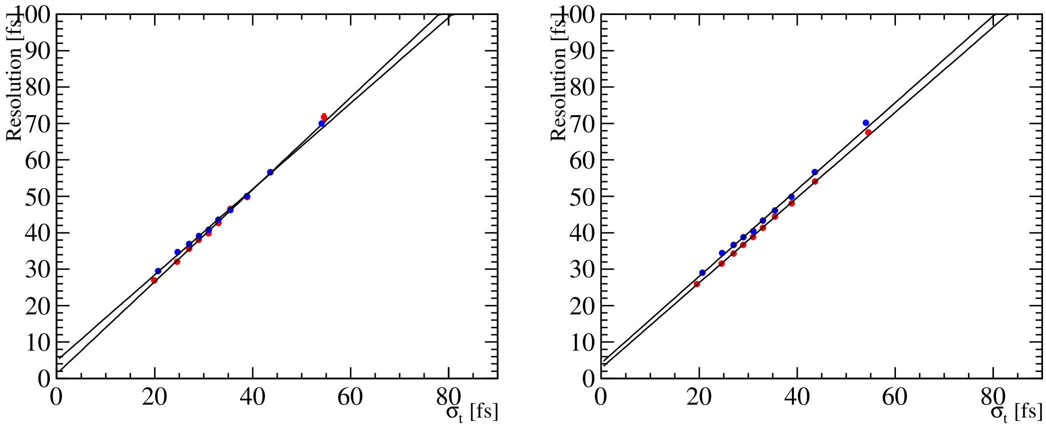

Figure 4.10 Calibration relation between predicted decay-time error δ_t vs effective decay-time resolution. Left plot shows the results from calibration sample (blue) and B_s^0 sample (red) with option 1), while right plot shows the B_s^0 sample (red) with additional detached and BDTG selections.

The calibration data sample is fitted with the time dependence given by

$$P^{\text{calib}}(t) = T(t-\hat{t}|\delta_t) \otimes [N_{\text{prompt}}\delta(\hat{t}) + N_{ll}(f_{sl}e^{-\hat{t}/\tau_s} + (1-f_{sl})e^{-\hat{t}/\tau_l})] + N_{\text{wpv}}G(t) \quad (4\text{-}5)$$

where N_{prompt} is the number of prompt J/ψ candidates, $N_{ll}(f_{sl}e^{-t/\tau_s} + (1-f_{sl})e^{-t/\tau_l})$ accounts for long-lived decays by two exponentials with free parameters lifetime τ_s, τ_l and fraction f_{sl}, and $G(t)$ is a wide gaussian corresponding to the wrong associated PV candidates, which doesn't dependent on δ_t.

The *sPlot* method is applied to the calibration data to remove the *fake* J/ψ background in the decay-time fit. Two single-sided Crystal Ball functions that share the same mean value but have different widths are used to describe the signal while a second-order polynomial function is used to described the combinatorial background. The fit to di-muon invariant mass is shown in Fig. 4.11. The calibration sample is weighted to match the p_{T} distribution in the B_s^0 data sample.

The parameters obtained in the fit to the decay-time resolution function are given in Table 4.8. The fit of decay-time distribution of the calibration sample is shown in Fig. 4.12. Taking into account the δ_t distribution of B_s^0 signal (see Fig. 4.13), the effective resolution is found to be 44.8 fs and 44.6 fs for low and high m_{KK} regions, respectively.

4.6.2 Decay-time efficiency

The selection and reconstruction efficiency is not constant as a function of the B_s^0 decay time due to displacement requirements made on signal tracks and a decay-time-dependent efficiency in the track reconstruction in the VELO[128]. The

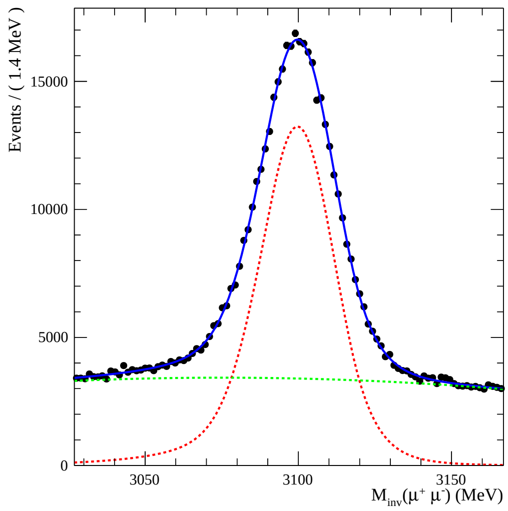

Figure 4.11 The projection plot of the fit to the J/ψ mass spectrum. The red dashed line corresponds to signal components, and the green dashed line corresponds to the combinatorial background component.

Table 4.8 Calibration parameters of decay-time resolution.

Parameters	overall
μ_t (ps)	$(-2.91 \pm 0.19) \times 10^{-3}$
σ_t^0 (ps)	$(4.52 \pm 0.55) \times 10^{-3}$
S_1	1.033 ± 0.023
S_2	1.751 ± 0.078
S_3	6.16 ± 0.51
f_2^T	0.239 ± 0.037
f_3^T	0.0078 ± 0.0014

decay-time efficiency for the B_s^0 signal is obtained using a control channel $B^0 \to J/\psi K^{*0}$, with $J/\psi \to \mu^+\mu^-$ and $K^{*0} \to K^+\pi^-$, which is kinematically similar to the signal decay.

The $B^0 \to J/\psi K^{*0}$ candidates are selected using a strategy similar to the one used for selecting $B_s^0 \to J/\psi K^+K^-$ signal candidates. A same selection criteria and BDTG algorithm are applied to the $B^0 \to J/\psi K^{*0}$ sample expect for the PID requirement $\mathrm{DLL}_{K\pi} > -6$ and $\mathrm{DLL}_{p\pi} > -10$ used to select the pion. Candidates within ±100 MeV mass window of the known K^* mass[58] are kept for the mass fit. The invariant mass distribution of the selected candidates is fitted by a Hypatia function for signal and an exponential function for background and shown in Fig. 4.14. The signal yield for B^0 is 301100 ± 800. An event-by-event *sWeight* is generated using the *sPlot* technique to

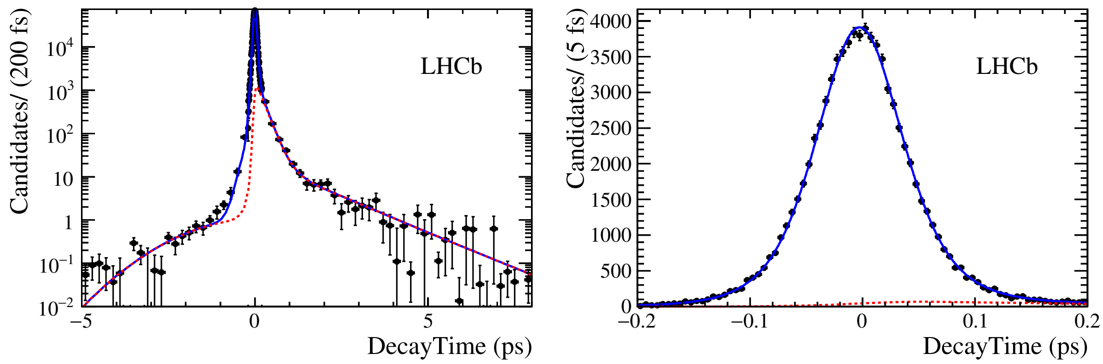

Figure 4.12 Decay-time distribution of $J/\psi K^+K^-$ calibration sample plotted in (left) whole fit region and (right) central region. The dashed (red) line shows the sum of long-lived and wrong PV components, and the solid curve the total.

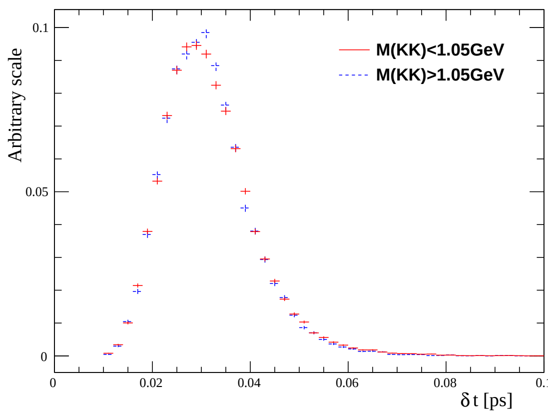

Figure 4.13 The comparison between the δ_t distributions for real $B_s^0 \to J/\psi K^+K^-$ candidates, with $m_{KK} > 1.05\,\text{GeV}$ or $m_{KK} < 1.05\,\text{GeV}$. *sWeight* is used to subtract the background. The similar distribution of σ_t leads to a similar average resolution.

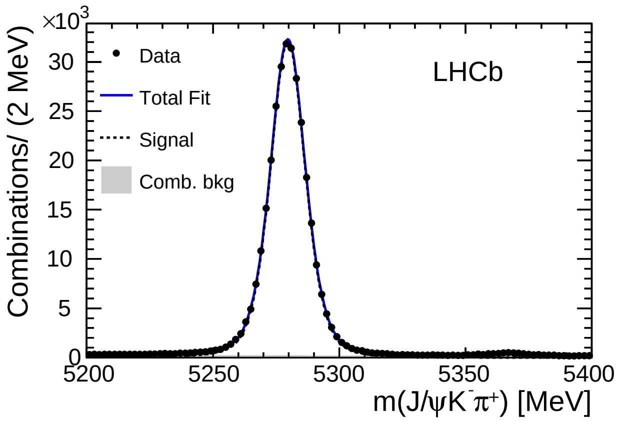

Figure 4.14 Mass distribution of $B^0 \to J/\psi K^{*0}$ candidates in data.

subtract the background.

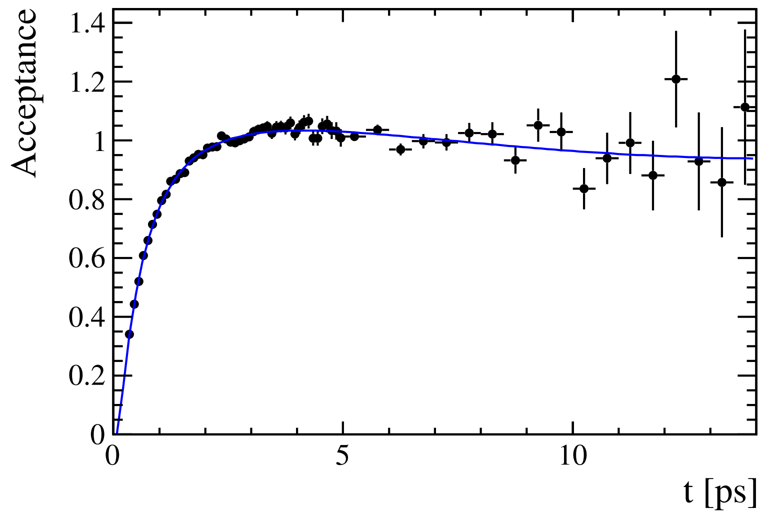

Figure 4.15 The decay-time efficiency of $B^0 \to J/\psi K^{*0}$. The data is obtained by *sWeighted* decay-time distribution divided by theoretical function with $\tau_{B^0} = 1.520\,ps$.

The decay-time efficiency function, A, is defined as

$$A(t; a, n, t_0, \beta, \beta_2) = \frac{\left[a(t-t_0)\right]^n}{1+\left[a(t-t_0)\right]^n} \times (1+\beta t+\beta_2 t^2), \tag{4-6}$$

where a, n, t_0, β, β_2 are parameters determined by the fit. An sFit technique[125] is used to fit the decay-time distribution, where B^0 lifetime is constrained to $\tau_{B^0} = 1.520 \pm 0.004$ ps[58]. The fit results of the decay-time efficiency is shown in Fig. 4.15.

A comparison of B^0 decay-time efficiency is given in Fig. 4.16. The flat distribution implies that the simulation can well model the acceptance effect, especially in the low decay-time region. A fit using first-order polynomial is performed on this relation and resulting in a slope of $(0.82 \pm 0.17)\%$ ps^{-1} , which implies that the simulation slightly overestimate the inefficiency in the high decay-time region. Thus the simulated sample is insufficient to describe this inefficiency, and the decay-time efficiency for B^0 data is used instead.

The different final states and kinematics between B^0 and B_s^0 decays resulting in slight differences in their decay-time efficiency. A correction factor, obtained from simulations, is assigned to the decay-time efficiency in the control channel to account for these differences. The decay-time efficiency in simulated samples is calculated as the reconstructed decay-time distribution divided by the theoretical function convoluted with the decay-time resolution. The impact of the resonance structure in B_s^0 data is considered by assigned a per-event weight, extracted using results from a time-integrated amplitude

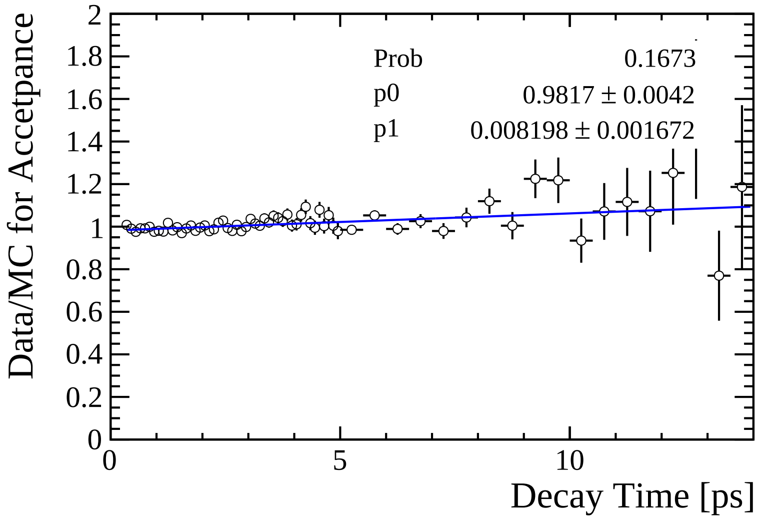

Figure 4.16 Relative efficiency between data and simulation from $B^0 \to J/\psi K^{*0}$. The fit function is $p_0 \cdot (1 + p_1 t)$.

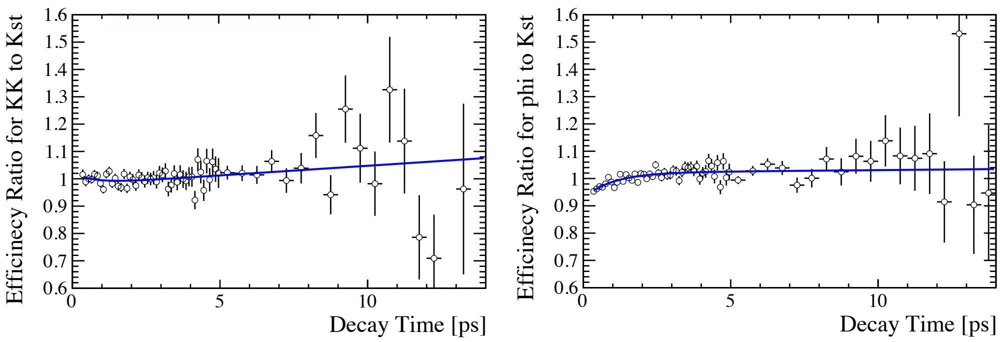

Figure 4.17 Efficiency ratio as a function of decay time between $B_s^0 \to J/\psi K^+K^-$ and $B^0 \to J/\psi K^{*0}$ for $m_{KK} > 1.05$ GeV (left), and for $m_{KK} < 1.05$ GeV (right).

analysis to data, to the phase space $B_s^0 \to J/\psi K^+K^-$ simulated samples. The decay-time efficiency ratios obtained in simulations are shown in Fig. 4.17. The corrections are both small for candidates in $m_{KK} > 1.05$ GeV and $m_{KK} < 1.05$ GeV region. The imperfect prediction of the decay-time efficiency in high decay-time region should be largely cancel. The ratios are described by the function $R \cdot (1 - p_2 e^{-p_1 t}) \cdot (1 + p_3 t)$ with parameters R, p_1, p_2 and p_3 determined by fits. Parameter R is a normalisation constant.

The final decay-time efficiency is determined as the product of the decay-time efficiency $A(a, n, t_0, \beta, \beta_2)$ in $B^0 \to J/\psi K^{*0}$ data and the correction ratio found from

Table 4.9 Parameters for decay-time efficiency.

Par.	High m_{KK}	Low m_{KK}
a [ps^{-1}]	1.589 ± 0.151	
n	1.150 ± 0.180	
t_0 [ps]	0.097 ± 0.044	
β [ps^{-1}]	-0.037 ± 0.016	
β_2 [ps^{-2}]	0.001 ± 0.001	
p_1 [ps^{-1}]	1.51 ± 1.55	1.01 ± 0.41
p_2	-0.048 ± 0.033	0.091 ± 0.014
p_3 [ps^{-1}]	$(7.2 \pm 3.8) \times 10^{-3}$	$(1.0 \pm 3.2) \times 10^{-3}$

simulations, which can be expressed as

$$\mathcal{E}_t(t; a, n, t_0, \beta, \beta_2, p_1, p_2) = \frac{\left[a(t-t_0)\right]^n}{1+\left[a(t-t_0)\right]^n} \times (1+\beta t+\beta_2 t^2) \times (1-p_2 e^{-p_1 t}) \cdot (1+p_3 t). \quad (4\text{-}7)$$

The parameters are given in Table 4.9.

4.6.3 Angular and m_{KK} efficiency

The selection and reconstruction efficiency is not uniform in m_{KK} and three helicity angles. The efficiency is parameterised by a combination of Legendre and spherical harmonic moments, which was used in $\overline{B}_s^0 \to \psi(2S)K^+\pi^-$ amplitude analysis[129], given by

$$\epsilon(m_{KK}, \cos\theta_{KK}, \cos\theta_{J/\psi}, \chi) = \sum_{a,b,c,d} \epsilon^{abcd} P_a(\cos\theta_{KK}) Y_{bc}(\theta_{J/\psi}, \chi) P_d\left(2\frac{m_{KK} - m_{KK}^{\min}}{m_{KK}^{\max} - m_{KK}^{\min}} - 1\right), \quad (4\text{-}8)$$

where P_a and P_d are Legendre polynomials, Y_{bc} are spherical harmonics, and $m_{KK}^{\min} = 2m_{K^+}$ and $m_{KK}^{\max} = m_{\overline{B}_s^0} - m_{J/\psi}$ are minimum and maximum allowed values for m_{KK}, respectively. A requirement of $\epsilon^{abcd} = -\epsilon^{ab(-c)d}$ is set to ensure the efficiency is real number. The efficiency moments are determined by summing over the fully simulated phase-space candidates

$$\epsilon^{abcd} = \frac{1}{\sum_i w_i} \sum_i w_i \frac{2a+1}{2}\frac{2d+1}{2} P_a(\cos\theta_{KK,i}) Y_{bc}^*(\theta_{J/\psi,i}, \chi_i) P_d\left(2\frac{m_{KK,i} - m_{KK}^{\min}}{m_{KK}^{\max} - m_{KK}^{\min}} - 1\right)\frac{1}{g_i}, \quad (4\text{-}9)$$

where $g_i = P_R^i P_B^i$ is the value of the phase-space probability density for event i. The weights w_i account for kaon identification efficiency, corrections of tracking efficiencies of all final states, and p and p_{T} distributions of B_s^0 and kaons. A per-event correction factor (1-0.01$\times$ $\cos^2\theta_{KK}$) is assigned to account for the underestimation of efficiency for large $\cos^2\theta_{KK}$ candidates when ignoring the correlation between K^+ and K^- PID selection efficiency. The coefficients of the efficiency function are obtained with simulation. The overall efficiency of m_{KK} > 1.05 GeV and m_{KK} < 1.05 GeV are shown in Fig. 4.18 and Fig. 4.19, respectively. The model reproduces the simulated data very well. No evident efficiency variation on m_{KK} is observed for m_{KK} < 1.05 GeV candidates.

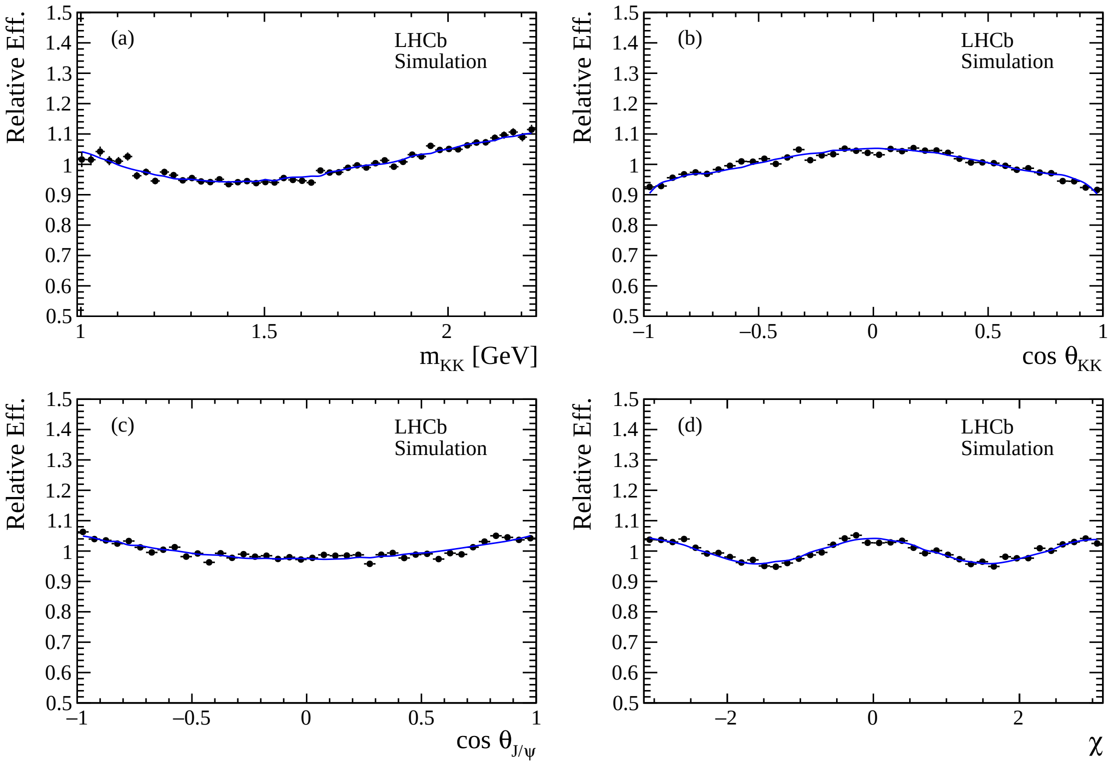

Figure 4.18 Overall efficiency for (a) m_{KK}, (b) $\cos\theta_{KK}$, (c) $\cos\theta_{J/\psi}$ and (d) χ obtained from PHSP $B_s^0 \to J/\psi K^+K^-$ (m_{KK} > 1.05 GeV) simulated sample. The points with error bars are determined from the MC, the curves show the expectation from the efficiency model.

4.7 Fit validation and results

4.7.1 Likelihood construction

The signal decay-time distribution including flavour tagging can be expressed as

$$R(\hat{t}, m_{KK}, \Omega, \mathfrak{q}|\eta) = \frac{1}{1+|\mathfrak{q}|}\left[\left[1+\mathfrak{q}\,(1-2\omega(\eta))\right]\,\Gamma(\hat{t}, m_{KK}, \Omega)\right.$$

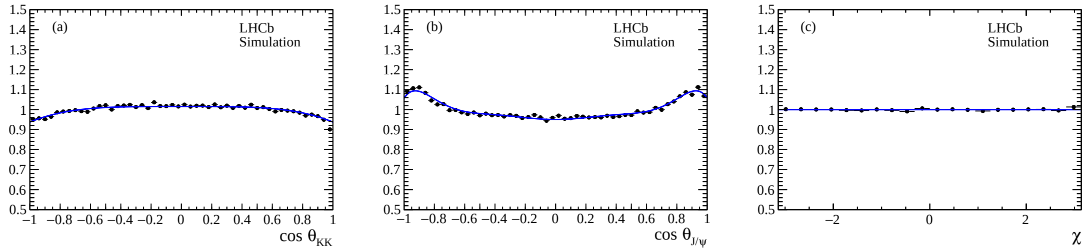

Figure 4.19 Overall efficiency for (a) $\cos\theta_{KK}$, (b) $\cos\theta_{J/\psi}$ and (c) χ obtained from $B_s^0 \to J/\psi K^+K^-$ ($m_{KK} < 1.05$ GeV) MC. The points with error bars are determined from the MC, the curves show the expectation from the efficiency model.

$$+\left[1-\mathfrak{q}\,(1-2\bar{\omega}(\eta))\right]\frac{1+A_P}{1-A_P}\bar{\Gamma}(\hat{t},m_{KK},\Omega)\Bigg], \tag{4-10}$$

where $\hat{t}$ is the true decay time, Γ is defined in Eqs. (1-37) and (1-38), and $A_P = (1.09 \pm 2.69)\%$ is the production asymmetry of B_s^0 mesons at the LHC[130]. The flavour tag $\mathfrak{q}$ takes values of -1, 1, 0, if the signal meson is tagged as $\overline{B}_s^0$,B_s^0, or untagged, respectively.

Considering the decay-time resolution and efficiency, the signal function changes to

$$F(t,m_{KK},\Omega,\mathfrak{q}|\eta,\delta_t) = \left[R(\hat{t},m_{KK},\Omega,\mathfrak{q}|\eta)\otimes T(t-\hat{t}|\delta_t)\right]\cdot\mathcal{E}_t(t)\cdot\varepsilon(m_{KK},\Omega), \tag{4-11}$$

where $\varepsilon(m_{KK},\Omega)$ is the efficiency as a function of K^+K^- mass and angular variables, $T(t-\hat{t};\delta_t)$ is the decay-time resolution function which depends upon the estimated decay-time error δ_t in each event, and $\mathcal{E}_t(t)$ is the decay-time efficiency function.

The normalisation factor is constructed by summing over $\mathfrak{q}$ and integrating over decay time t, m_{KK} and the three angular variables, given the form

$$\mathcal{N}(\delta_t) = 2\int[\Gamma(\hat{t},m_{KK},\Omega)+\frac{1+A_P}{1-A_P}\bar{\Gamma}(\hat{t},m_{KK},\Omega)]\otimes T(t-\hat{t}|\delta_t)\cdot\mathcal{E}_t(t)\cdot\varepsilon(m_{KK},\Omega)\,dm_{KK}\,d\,\Omega\,dt\,, \tag{4-12}$$

where the factor is independent on one of the conditional variables, η. The signal PDF is given by

$$\mathcal{P}(t,m_{KK},\Omega,\mathfrak{q}|\eta,\delta_t) = \frac{1}{\mathcal{N}(\delta_t)}F(t,m_{KK},\Omega,\mathfrak{q}|\eta,\delta_t). \tag{4-13}$$

The *sPlot* technique is used to subtract background components in the fits. A per-event *sWeight* (W_i), determined in the fit to the $m(J/\psi K^+K^-)$ distribution in Sec.4.4, is assigned to each B_s^0 candidates. The log-likelihood in the fit has the expression,

$$-2\ln\mathcal{L} = -2\,s_W\sum_i W_i\ln\mathcal{P}(t,m_{KK},\Omega,\mathfrak{q}|\eta,\delta_t), \tag{4-14}$$

Table 4.10 Comparison between fit results and inputs to full simulated $B_s^0 \to J/\psi\phi$ sample. "Pull" is deviation between fit and inputs, while "Pull data" is calculated by replacing the uncertainty to the overall $\Delta(-2\ln\mathcal{L})$/ndof = 20.0/9.

Parameter	Input	Fit output	Pull	Pull data
Γ_s [ps^{-1}]	0.6653	0.6662 ± 0.0007	1.3	0.3
$\Delta\Gamma_s$ [ps^{-1}]	0.0917	0.0864 ± 0.0022	−2.4	−0.5
$\lvert A_\perp\rvert^2$	0.2490	0.2502 ± 0.0012	1.0	0.2
$\lvert A_0\rvert^2$	0.5213	0.5196 ± 0.0009	−1.9	−0.4
$\delta_\parallel - \delta_0$ [rad]	3.30	3.295 ± 0.009	−0.6	0.0
$\delta_\perp - \delta_0$ [rad]	3.07	3.058 ± 0.009	−1.3	−0.1
Δm_s [ps^{-1}]	17.8	17.802 ± 0.003	0.5	0.0
ϕ_s [rad]	0.07	0.0738 ± 0.0023	1.7	0.1
$\lvert\lambda\rvert$	1.0	0.9981 ± 0.0016	−1.2	−0.1

where $s_W \equiv \sum_i W_i / \sum_i W_i^2$ is a constant factor accounting for the effect of background subtraction on the statistical uncertainty.

4.7.2 Validation of fitter

4.7.2.1 Fit to full simulated $B_s^0 \to J/\psi\phi$ samples

The $B_s^0 \to J/\psi\phi$ simulated samples with $\Delta\Gamma_s = 0$ and $\Delta\Gamma_s \neq 0$ listed in Table 4.2 are used for validation studies. 1.2×10^6 reconstructed signal candidates are obtained for each simulation after applying same selection criteria as in data. The detector effects, including decay-time resolution, decay-time efficiency, m_{KK} and angular efficiency are determined with $\Delta\Gamma_s = 0$ simulated sample. The efficiencies are calculated as the reconstructed distribution divided by a toy sample which is generated using simulated inputs with uniform efficiency. A time-dependent amplitude fit to $\Delta\Gamma_s \neq 0$ simulated sample is performed with detector effects determined from $\Delta\Gamma_s = 0$ sample and tagging information obtained from generator level. No significant bias is found in fit results, as shown in Table 4.10. The correlations between these fit parameters are evaluated with $-2\ln\mathcal{L}$ difference between the minimised fit and the inputs. The $\Delta(-2\ln\mathcal{L})$/ndf= 20.0/9, corresponds to a consistency of 2.3 σ, indicates detector effects determined from $\Delta\Gamma_s = 0$ simulation can be applied to $\Delta\Gamma_s \neq 0$ simulated sample.

Table 4.11 Comparison of fits to ϕ region events from the same 3 fb^{-1} data. This work has 53 000 signal events with $B/S = 1\%$, while the publication[79] has 96 000 signal events with about $B/S = 20\%$.

Parameter	This work	LHCb-PAPER-2014-059
Γ_s [ps^{-1}]	0.6596 ± 0.0032	$0.6603 \pm 0.0027 \pm 0.0015$
$\Delta\Gamma_s$ [ps^{-1}]	0.0697 ± 0.0107	$0.0805 \pm 0.0091 \pm 0.0032$
$\lvert A_\perp\rvert^2$	0.2624 ± 0.0069	$0.2504 \pm 0.0049 \pm 0.0036$
$\lvert A_0\rvert^2$	0.5123 ± 0.0046	$0.5241 \pm 0.0034 \pm 0.0067$
$\delta_\parallel - \delta_0$ [rad]	3.29 ± 0.13	$3.26\,^{+0.10}_{-0.17}\,^{+0.06}_{-0.07}$
$\delta_\perp - \delta_0$ [rad]	3.50 ± 0.19	$3.08\,^{+0.14}_{-0.15} \pm 0.06$
Δm_s [ps^{-1}]	17.800 ± 0.061	$17.711\,^{+0.055}_{-0.057} \pm 0.011$
ϕ_s [rad]	0.010 ± 0.061	$-0.058 \pm 0.049 \pm 0.006$
$\lvert\lambda\rvert$	0.961 ± 0.022	$0.964 \pm 0.019 \pm 0.007$

4.7.2.2 Fit to the data in ϕ region

In comparison with the previous LHCb publication[79], which uses events in ϕ region for determine ϕ_s, a full fit to the $m_{KK} < 1.05$ GeV candidates are performed. Due to different selection criteria, the signal yield extracted in this analysis is 53000 with $B/S = 1\%$ while the yield is 96000 with $B/S = 20\%$ in the publication[79], where S and B are numbers of signal and background, respectively. The publication applied angular analysis with splitting events into six m_{KK} bins while the modelling of m_{KK} distribution is included in this amplitude analysis.

The comparison of fit results in this analysis and the publication is shown in Table 4.11. The statistical uncertainty of ϕ_s, proportional to $\sqrt{S+B}/S$, is expected to be 0.06 rad, and is consistent with the statistical uncertainty 0.061 rad obtained in the fit. The statistical consistency between the two results are checked with toy simulation generated with same numbers of signal and background as observed in the two samples. The consistency for the nine observed parameters are at 1% level.

4.7.3 Fit results

The CP violation for all the transversity states are assumed to be the same in the default fit. Two different sets of fitting parameters $(\phi_s,\ |\lambda|,\ \Gamma_s,\ \Delta\Gamma_s)^{L,H}$ are used for candidates in L and the H regions. According to toy studies, correlations of these parameters between two regions can be totally removed with this configuration. The shared parameters are Δm_s and all amplitudes for the resonances.

A simultaneous fit is performed to candidates in two regions, the CP-violating

Table 4.12 Data fit results for the CP-violating parameters, where fit results are unblinded. The first uncertainties are statistical, and the second when quoted are systematic.

Parameter	ϕ region	Above ϕ region
Δm_s [ps^{-1}]	17.783 ± 0.049	
Γ_s [ps^{-1}]	$0.6592 \pm 0.0032 \pm 0.025$	$0.6501 \pm 0.0055 \pm 0.0043$
$\Delta\Gamma_s$ [ps^{-1}]	$0.067 \pm 0.011 \pm 0.005$	$0.066 \pm 0.018 \pm 0.010$
ϕ_s [rad]	$0.015 \pm 0.060 \pm 0.014$	$0.119 \pm 0.106 \pm 0.034$
$\lvert\lambda\rvert$	$0.951 \pm 0.023 \pm 0.017$	$0.994 \pm 0.018 \pm 0.006$

parameters obtained in the fit are given in Table 4.12. The fit results of the ϕ region candidates are identical to that from the single fit described in Sec.4.7.2.2. The fit fractions and phases are listed in Table 4.13 and Table 4.14. The fit projections are shown in Fig. 4.20 and Fig. 4.21.

Table 4.13 Fit results of the resonant structure.

Component	Fit fraction (%)	Transversity fraction (%) 0	$\parallel$	$\perp$
$\phi(1020)$	$70.5 \pm 0.6 \pm 1.2$	50.9 ± 0.4	23.1 ± 0.5	26.0 ± 0.6
$f_2(1270)$	$1.6 \pm 0.3 \pm 0.2$	76.9 ± 5.5	6.0 ± 4.2	17.1 ± 5.0
$f_2'(1525)$	$10.7 \pm 0.7 \pm 0.9$	46.8 ± 1.9	33.8 ± 2.3	19.4 ± 2.3
$\phi(1680)$	$3.95 \pm 0.3 \pm 0.3$	44.0 ± 3.9	32.7 ± 3.6	23.3 ± 3.6
$f_2(1750)$	$0.59\,^{+0.23}_{-0.16} \pm 0.21$	58.2 ± 13.9	31.7 ± 12.4	$10.1\,^{+16.8}_{-6.1}$
$f_2(1950)$	$0.44\,^{+0.15}_{-0.10} \pm 0.14$	$2.2\,^{+6.7}_{-1.5}$	38.3 ± 13.8	59.5 ± 14.2
S-wave	$10.69 \pm 0.12 \pm 0.57$	100	0	0

A χ^2 test is performed to check the fit quality in the high m_{KK} region, resulting $\chi^2 = 1401$ for 1125 bins of the four dimensional variables m_{KK} and Ω; $\chi^2 = 380$ for 310 bins of the two dimensional variables m_{KK} and $\theta_{J/\psi}$, which indicates data samples are well described by the fits.

As a check, a fit is performed allowing different CP-violating parameters ($\lvert\lambda_i, \phi_s^i\rvert$) for the ϕ transversities states, the K^+K^- S-wave, the $f_2(1270)$, the $f_2'(1525)$, the $\phi(1680)$ and the combination of the $f_2(1750)$ and $f_2(1950)$ resonances. The $-2\ln\mathcal{L}$ is improved for 16 units compared to the default fit since all states have consistent CP-violation within 1.3σ. All $\lvert\lambda\rvert$ are consistent with unity and ϕ_s differences with respect to longitudinal ϕ

Table 4.14 Fitted phase differences. Each phase of a certain CP-state is related to the ϕ transversity amplitude with the same CP-eigenvalue.

Parameter	Value
$\delta f_2^0 - \delta\phi^\perp$	139.5 ± 6.5
$\delta f_2'^0 - \delta\phi^\perp$	-167.9 ± 6.6
$\delta f_2(1750)^0 - \delta\phi^\perp$	-251.5 ± 13.0
$\delta f_2(1950)^0 - \delta\phi^\perp$	-84.1 ± 42.1
$\delta\phi(1680)^0 - \delta\phi^0$	181.5 ± 5.2
$\delta f_2^\perp - \delta\phi^0$	100.5 ± 16.1
$\delta f_2'^\perp - \delta\phi^0$	-145.4 ± 9.2
$\delta f_2(1750)^\perp - \delta\phi^0$	230.2 ± 36.1
$\delta f_2(1950)^\perp - \delta\phi^0$	116.7 ± 17.4
$\delta\phi^\perp - \delta\phi^0$	199.7 ± 7.6
$\delta\phi(1680)^\perp - \delta\phi^\perp$	134.0 ± 7.6
$\delta f_2^\parallel - \delta\phi^\perp$	-140.3 ± 21.4
$\delta f_2'^\parallel - \delta\phi^\perp$	46.2 ± 7.9
$\delta f_2(1750)^\parallel - \delta\phi^\perp$	-27.5 ± 15.9
$\delta f_2(1950)^\parallel - \delta\phi^\perp$	3.8 ± 19.5
$\delta\phi^\parallel - \delta\phi^0$	195.4 ± 3.8
$\delta\phi(1680)^\parallel - \delta\phi^0$	-105.8 ± 8.9

component are consistent with zero, showing no dependence for the states.

4.8 Systematic uncertainties

The sources of systematic uncertainties on the results of the time-dependent amplitude analysis are summarised in Table 4.15. The systematic uncertainties for the fit fractions are summarised in Table 4.16, which are small compared to the statistical uncertainties.

4.8.1 Resonance modelling

The largest systematic uncertainties are from the resonances modelling. Following options are used to evaluate sources of uncertainties:

- Varying the masses and widths of resonances by $\pm 1\sigma$ of their uncertainty listed in Table 5.1. Add all sources in quadrature.
- Doubling the S-wave knot number for the high m_{KK} region.

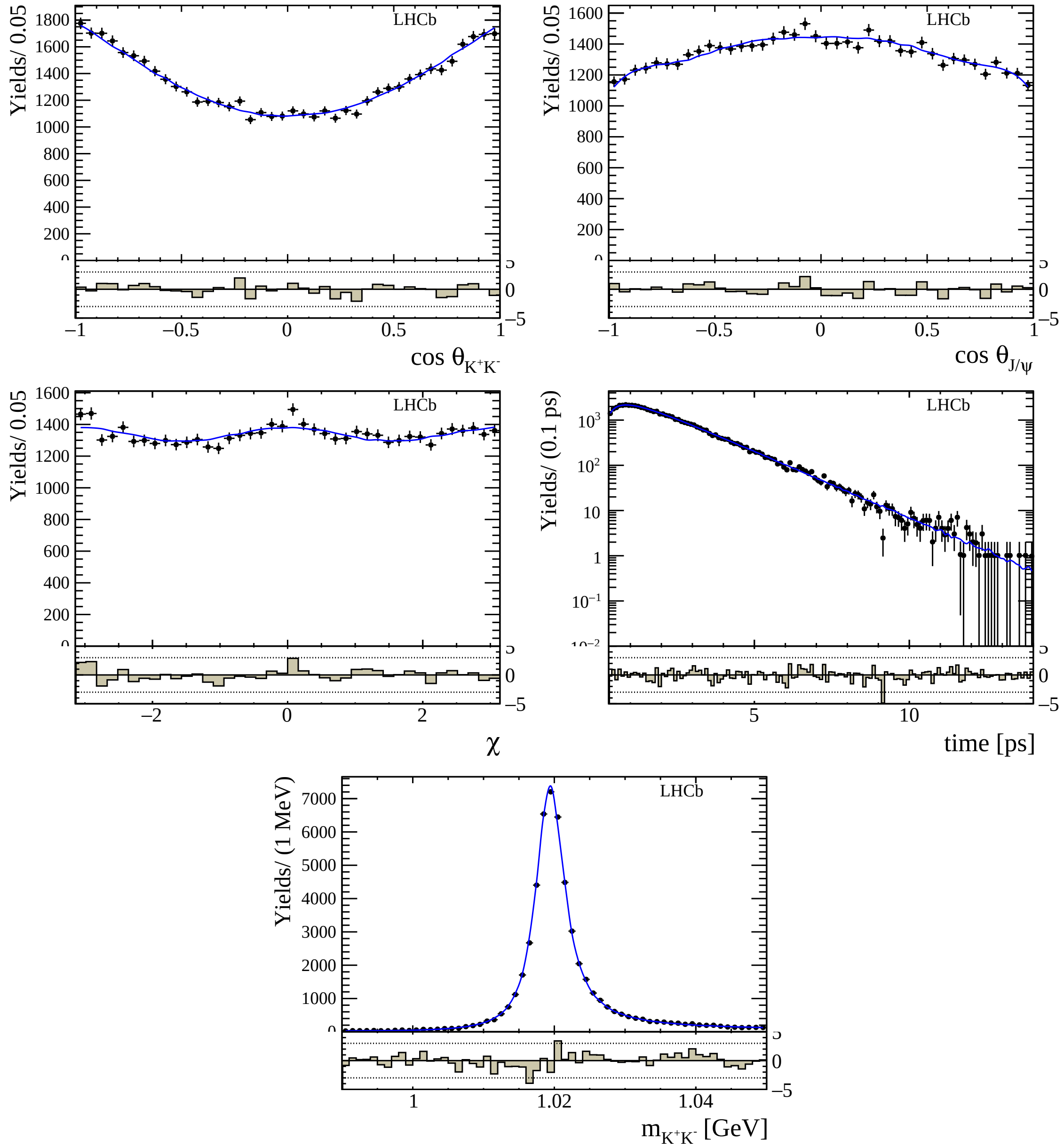

Figure 4.20 Projections of fitting variables in the ϕ region. The χ^2/nbin = 30/40 ($\cos\theta_{KK}$), 30/40 ($\cos\theta_{J/\psi}$), 43/40 (χ), 146/137 (t) and 82/60 (m_{KK}).

- Varying the centrifugal barrier of KK resonances and B_s^0 meson from 0.5–2 times of the default values
- Increasing the default angular momentum L_B for the P and D-wave resonances by 1 or 2. The lowest allowed value for L_B is used for the default fit.

The largest variation among the sources is taken as systematic uncertainty.

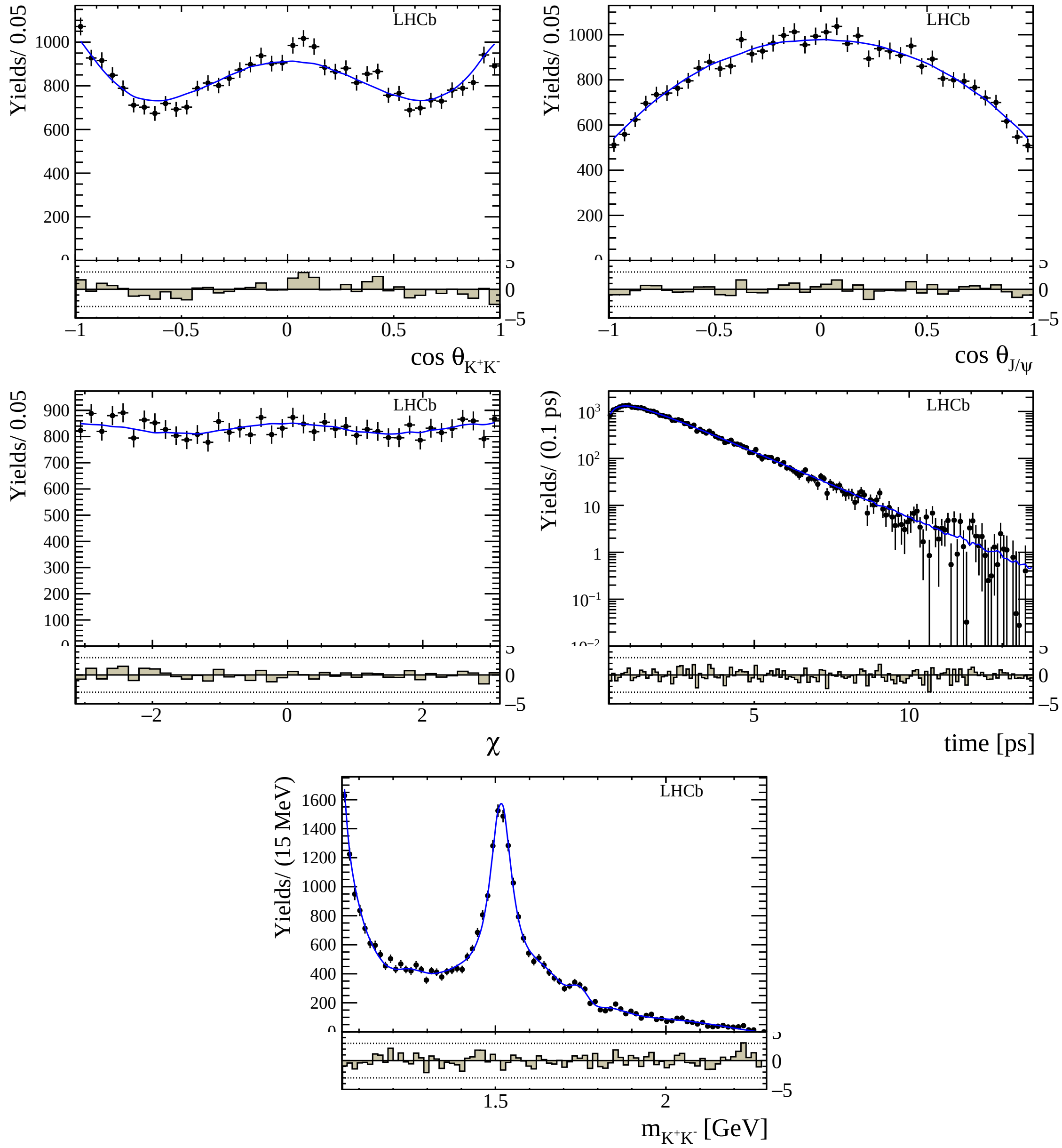

Figure 4.21 Projections of fitting variables above the ϕ region. The χ^2/nbin = 56/40 ($\cos\theta_{KK}$), 26/40 ($\cos\theta_{J/\psi}$), 22/40 (χ), 117/137 (t) and 88/83 (m_{KK}).

4.8.2 Efficiency of m_{KK} and angles

Three sources are considered for the systematic uncertainties of m_{KK} and angles efficiency: statistical uncertainties of simulations, uncertainties from kaon PID selection and the kinematic weights which are used to account for the resonance structures in data. The first one is estimated by repeating the fit to data 100 times with new-efficiency histograms generated each time using Gaussian random to vary the statistical uncertainty in the original histogram. The changes on the physics parameter of interest from the repeated fits with respect to the default one are a Gaussian distribution, whose width

Table 4.15 Sources of absolute systematic uncertainty ($\times 10^3$) versus statistical uncertainty.

Source	$\Delta\Gamma_s{}^L$ [ps^{-1}]	$\Delta\Gamma_s{}^H$ [ps^{-1}]	$\Gamma_s{}^L$ [ps^{-1}]	$\Gamma_s{}^H$ [ps^{-1}]	$\lvert\lambda\rvert^H$	$\lvert\lambda\rvert^L$	M_0 [GeV]	Γ_0 [GeV]	$\phi_s{}^H$ [rad]	$\phi_s{}^L$ [rad]
Resonance modelling	1.6	6.9	0.3	1.9	5.5	16.9	1.1	3.6	23.6	8.8
Efficiency (m_{KK}, Ω)	1.0	3.0	0.2	0.9	0.5	0.3	0.1	0.7	3.4	0.8
Efficiency t	0.5	2.2	1.2	2.8	0.0	1.0	0.0	0.0	0.0	0.0
$\tau_{\bar{B}^0}$	0.6	1.4	2.0	2.0	0.0	1.1	0.0	0.0	0.0	0.0
t resolution	0.1	0.3	0.2	0.2	0.2	0.6	0.0	0.0	1.1	1.2
Fit bias	5.0	5.0	0.6	1.1	-	-	-	-	-	-
A_{CP}^{Prod}	0.0	0.1	0.1	0.3	1.4	1.3	0.0	0.0	4.0	4.0
Tagging	0.0	1.2	0.0	0.3	0.8	2.5	0.0	0.0	11.2	9.1
Backg.	0.3	0.5	0.2	0.8	0.4	0.3	0.1	0.1	1.5	0.8
sWeights	0.4	1.1	0.1	0.1	0.5	2.3	0.1	0.4	21.4	2.4
B_c^+	-	-	0.5	0.5	-	-	-	-	-	-
Total syst.	5.4	9.6	2.5	4.3	5.7	17.4	1.1	3.7	34.2	13.6
Stat.	10.5	17.7	3.2	5.5	18.0	23.4	1.3	3.0	106.6	60.0

Table 4.16 Systematic uncertainty for fit fractions.

Source	$\phi(1020)$	S-wave	$f_2'(1525)$	$\phi(1680)$	$f_2(1270)$	$f_2(1750)$	$f_2(1950)$
Resonance modelling	0.99	0.57	0.73	0.27	0.21	0.21	0.13
Efficiency	0.58	0.06	0.48	0.12	0.04	0.03	0.01
Background	0.06	0.01	0.06	0.02	0.02	0.01	0.00
sWeights	0.11	0.02	0.16	0.05	0.02	0.05	0.04
Total syst.	1.15	0.57	0.89	0.30	0.21	0.21	0.14
Stat.	0.62	0.12	0.67	0.32	0.27	$^{+0.23}_{-0.16}$	$^{+0.15}_{-0.10}$

is taken as systematic uncertainty. Uncertainty of kaon PID selection is estimated by ignoring the $(1-0.01\ \cos^2\theta_{KK})$ correction for the efficiency in the fit. Uncertainty due to the kinematic differences is evaluated with another fit which does not include the weights.

4.8.3 Decay time

Uncertainties due to the correction from simulations and the B^0 lifetime are considered, which are evaluated by adding an additional Gaussian constraint to the correction factor or B^0 lifetime in the ϕ_s fit. The systematic uncertainty is given by the difference in quadrature of the statistical uncertainties for each physics parameter between the nominal fit and the alternative fit. A 5% variation of the width of Gaussian resolution functions and the uncertainty for the mean value are used to estimate the uncertainty due to the decay-time resolution modelling.

4.8.4 Background modelling

Three sources are considered in the background modelling: the lifetime of Λ_b^0, the yields and decay-time distributions in misidentified background. The uncertainty due to Λ_b^0 lifetime is estimated by varying the generated value by $\pm 1\ \sigma$. The uncertainties of yields is estimated by varying 5% of yields to accounting for possible systematic uncertainty in yield extrapolation from sidebands. The uncertainty of decay-time distribution is evaluated by varying the decay time by a factor of $(1+0.0082\times t)$. According to the studies in Sec.4.6.2, simulation overestimates the β factor by 0.0082 ± 0.0017. The systematic uncertainty is given by the difference in quadrature of the statistical uncertainties for each physics parameter between the nominal fit and the alternative fit .

4.8.5 Fit bias

A potential bias of $\Delta\Gamma_s$ of $-0.005\ ps^{-1}$ obtained from the fit to full $J/\psi\phi$ simulation, could be due to the correlation between decay-time and angular acceptance that is introduced by the selection. Similarly, a small bias on Γ_s corresponding to 20% of statistical uncertainty is also found. Both of them are taken as a source of systematic uncertainty.

4.8.6 Flavour tagging and production asymmetry

Same method is used in the determination of systematic uncertainties from flavour tagging calibration parameters and the production asymmetry of B_s^0 and $\overline{B}_s^0$. The systematic uncertainty is given by the difference between the nominal fit and an alternative fit where the parameters are Gaussian constrained by their total uncertainties.

4.8.7 *sWeights*

Two variations are performed to evaluate the uncertainty due to the use of *sPlot* technique. The binning of $|\cos\theta_{J/\psi}|$ is changed from four to five and the decay time is divide to three bins. A *sWeight* is obtained with new fit and the ϕ_s fit result is updated. The larger change on physics parameters of interest is taken as a systematic uncertainty.

4.8.8 B_c^+ contribution

According to previous analysis [79], about 0.8% signal sample is expected from the decays of B_c^+ mesons[131]. Neglecting the B_c^+ contribution leads to a bias of 0.0005 ps^{-1} for Γ_s, which is added as a systematic uncertainty. Other parameters are not affected.

4.9 Results

A time-dependent amplitude analysis is performed using $B_s^0 \to J/\psi K^+K^-$ decays in the $m_{KK} > 1.05$ GeV region, the CP-violating parameters are determined as

$$\begin{aligned} \phi_s &= 0.119 \pm 0.107 \pm 0.034\,\text{rad}, \\ |\lambda| &= 0.994 \pm 0.018 \pm 0.006, \\ \Gamma_s &= 0.650 \pm 0.006 \pm 0.004\,\text{ps}^{-1}, \\ \Delta\Gamma_s &= 0.066 \pm 0.018 \pm 0.010\,\text{ps}^{-1}. \end{aligned}$$

Combined with results from $B_s^0 \to J/\psi K^+K^-$ decays in the ϕ mass region gives

$$\begin{aligned} \phi_s &= -0.025 \pm 0.045 \pm 0.008\,\text{rad}, \\ |\lambda| &= 0.978 \pm 0.013 \pm 0.003, \\ \Gamma_s &= 0.6588 \pm 0.0022 \pm 0.0015\,\text{ps}^{-1}, \\ \Delta\Gamma_s &= 0.0813 \pm 0.0073 \pm 0.0036\,\text{ps}^{-1}. \end{aligned}$$

The two results are consistent within 1.1σ. A further combination is performed by including the ϕ_s and $|\lambda|$ measurements from $B_s^0 \to J/\psi\pi^+\pi^-$ [80], which results in $\phi_s = 0.001 \pm 0.037$ rad and $|\lambda| = 0.973 \pm 0.013$.

Many resonances and a S-wave structure are found in m_{KK} mass spectrum. The $f_2'(1525)$ mass and width are obtained to be $1522.2 \pm 1.3 \pm 1.1$ MeV and $78.0 \pm 3.0 \pm 3.7$ MeV, respectively. The fit fractions of the resonances in $B_s^0 \to J/\psi K^+K^-$ are also determined.

Chapter 5 Measurement of CP-violating phase ϕ_s with $B_s^0 \to J/\psi\, \pi^+\pi^-$

5.1 Introduction

The CP-violating phase $\phi_s \approx -2\beta_s$ in B_s^0 meson is equivalent of -2β for the B^0 meson, which is predicted to be very small $-36.5^{+1.3}_{-1.2}$ mrad[60] in the SM using inputs from other experiments. This phase has been measured in eight analyses: four $B_s^0 \to J/\psi\phi$ analyses from CDF, D0, ATLAS and CMS, and four analyses from LHCb of the decay modes $B_s^0 \to J/\psi K^+K^-$, $B_s^0 \to \psi(2S)\phi$, $B_s^0 \to J/\psi\pi^+\pi^-$ and$B_s^0 \to D_s^+ D_s^+$ using 7 TeV and 8 TeV pp collision data sample. Fig 5.1 shows the summary of ϕ_s measured results comparing with the SM prediction. The combined result is consistent with SM prediction, however there are still room for NP.

The resonance structure in $B_s^0 \to J/\psi\pi^+\pi^-$ decays has been studied with a time-integrated amplitude analysis previously with a data sample of 3 fb^{-1} integrated luminosity[132]. Five interfering $\pi^+\pi^-$ states are required to describe the decay: $f_0(980)$, $f_0(1500)$, $f_0(1790)$, $f_2(1270)$, and $f_2'(1525)$. An alternative solution including these states and adding a non-resonant $J/\psi\pi^+\pi^-$ component also provides a good description of the data. Based on the different transversity components measured for the spin-2 intermediate states, the final state is found to be compatible with being entirely CP-odd, and the CP-even part is found to be $< 2.3\%$ at 95% confidence level[132]. This gives an opportunity to determine the decay width of the heavy B_s^0 mass eigenstate, Γ_H.

5.2 Analysis strategy

In this analysis, the measurement of ϕ_s using $B_s^0 \to J/\psi\pi^+\pi^-$ decays with 13 TeV pp collision data is performed. A time-dependent amplitude analysis is used to determined the CP-violating parameters ϕ_s, $|\lambda|$ and the decay-width difference between B^0 and the heavy mass eigenstate of B_s^0, $\Gamma_H - \Gamma_{B^0}$.

The mass spectrum of $\pi^+\pi^-$ is analysed by considering the resonance contributions listed in Table 5.1. All resonances are described by Breit-Wigner amplitudes, except for the $f_0(980)$ resonance, which is modelled by a Flatté amplitude. The same amplitude description and likelihood construction methods are used as that for analysis discussed

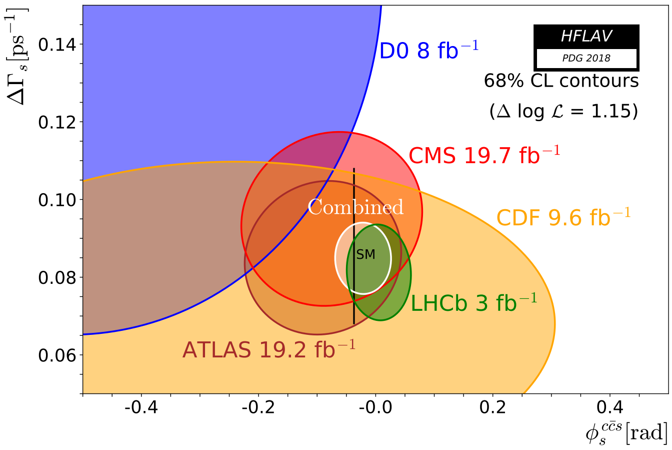

Figure 5.1 Results of ϕ_s from HFLAV.

Table 5.1 Breit-Wigner resonance parameters.

Resonance	Mass (MeV)	Width (MeV)	Source
$f_0(500)$	471 ± 21	534 ± 53	LHCb[133]
$f_0(980)$		Varied in fits	
$f_2(1270)$	1275.5 ± 0.8	$186.7^{+2.2}_{-2.5}$	PDG[58]
$f_0(1500)$		Varied in fits	
$f_2'(1525)$	1522.2 ± 1.7	78.0 ± 4.8	LHCb[134]
$f_0(1710)$	1723^{+6}_{-5}	139 ± 8	PDG[58]
$f_0(1790)$	1790^{+40}_{-30}	270^{+60}_{-30}	BES[135]

in Chap. 4. An unbinned maximum likelihood fit is performed to the decay time t, m_{KK}, and the three helicity angles Ω, along with information on the initial flavour of the decaying hadron, *i.e*. whether it was produced as a B_s^0 or a $\overline{B}_s^0$ meson. The probability density function (PDF) used in the fit consists of only signal component that includes detector resolution and acceptance effects, with the background subtracted statistically with negative weights by the same-sign sample. An event-by-event estimated decay-time error and mistag probability are used in the decay-time resolution model and inclusion of flavour tagging.

The fitting parameters are ϕ_s, $|\lambda|$, $\Gamma_H - \Gamma_{B^0}$, the amplitudes and phases of the resonances. The shape parameters for the $f_0(980)$ and $f_0(1500)$ resonances are allowed to vary. The other parameters, including Δm_s, Γ_L, are fixed to the PDG values.

Table 5.2 Simulated samples used in the analysis.

Decay channel	Production type	Events	Model	Utilisation
$B_s^0 \to J/\psi\pi^+\pi^-$	Full	17.0×10^6	PHSP	Signal study
$\Lambda_b^0 \to J/\psi pK^-$	Full	9.5×10^6	PHSP	Background modelling
$B_s^0 \to J/\psi\eta'$	Full	7.0×10^6	PHSP	Background modelling
$B^0 \to J/\psi K^{*0}$	Full	17.5×10^6	PHSP	Control channel
$B^+ \to J/\psi K^+$	Full	25.6×10^6	PHSP	channel
$B_s^0 \to D_s^+\pi^-$	Full	8.0×10^6	PHSP	Control channel
Inclusive J/ψ	Full	46.0×10^6	PHSP	Control channel

5.3 Dataset and selection requirement

The analysis is performed using 1.9 fb^{-1} pp collision data collected by LHCb at centre-of-mass energies $\sqrt{s}$ = 13 TeV in 2015 and 2016. The simulated samples are generated using the same configuration as for data collection. Table 5.2 lists the simulated samples used in this analysis. The PID variables are not well modelled in the simulation. A data-driven method, implemented in the `PIDCalib` package[108], is used to resample the PID variables in simulation. The correlations between the PID variables are preserved in the resampling process. In order to obtain the correct correlations between the uncertainties on vertex position, particle momenta, flight distance, decay time and invariant mass, the DTF method was applied to B_s^0 candidates. The decay-time related observables are derived from a DTF fit where the position of the primary vertex has been used to constrain the production vertex of the B_s^0 meson. Furthermore, the invariant mass of B_s^0 is determined with both the constrained of primary vertex information and constrain of invariant mass of J/ψ to the central value of the PDG[58].

The event selection consists of four steps: Trigger requirements are made before cut-based selections to reduce various background components. Then, a MVA is used to further suppressed the combinatorial background. Finally, the multiple candidates are studied. Table 5.3 and Table 5.4 gives the trigger lines and selection criteria.

Both $B_s^0 \to J/\psi\pi^+\pi^-$ and $B_s^0 \to J/\psi\pi^\pm\pi^\pm$ candidates are used in this analysis. Signal $B_s^0 \to J/\psi\pi^+\pi^-$ candidates are reconstructed with $J/\psi \to \mu^+\mu^-$ and two opposite-sign tracks (right-sign, RS data) while $B_s^0 \to J/\psi\pi^\pm\pi^\pm$ candidates are reconstructed with $J/\psi \to \mu^+\mu^-$ and two same-sign tracks (wrong-sign, WS data). All tracks are required to have track fit χ^2/ndf less than 3 and the probability that the track is reconstructed from a ghost

Table 5.3 Trigger lines used for selected $B_s^0 \to J/\psi\pi^+\pi^-$ candidates. More details on the trigger lines can be found in Ref.[107].

Trigger level	Trigger line
HLT1	`Jpsi_Hlt1DimuonHighMassDecision_TOS` or `B_Hlt1TrackMuonDecision_TOS` or `B_Hlt1TrackMVADecision_TOS`
HLT2	`Jpsi_Hlt2DimuonDetachedJpsiDecision_TOS`

Table 5.4 Preselection requirements for selected $B_s^0 \to J/\psi\pi^+\pi^-$ candidates.

#	Selection variables	Requirements
1	All tracks χ^2/ndf	< 3
2	Ghost track probability	< 0.2
3	Clone track rejection	$\theta_{\text{two tracks in one candidate}} > 0.5$ mrad
	J/ψ selection	
4	Muon DLL$(\mu - \pi)$	> 0
5	Muon p_{T}	> 500 MeV
6	J/ψ vertex χ^2_{vtx}	< 16
7	$m(\mu^+\mu^-) - m(J/\psi)$	$(-48, +43)$ MeV
	π selection	
8	Pion p_{T}	> 250 MeV
9	Pion χ^2_{IP}	> 4
10	Pion PID	DLL$_{\pi K} > -10$ or `ProbNNk`> 0.05
11	Sum p_{T} of $\pi^+\pi^-$	> 900 MeV
12	$\pi^+\pi^-$ vertex χ^2	< 16
	B_s^0 meson selection	
13	χ^2_{IP}	< 25
14	χ^2_{vtx}/ndf	< 10
15	Next best χ^2_{IP}	> 50
16	Pointing, $\cos\theta_p$	> 0.999
17	Decay time, t	> 0.3 ps
18	Decay-time error, δt	< 0.15 ps
	B^+ veto ($B^+ \to J/\psi K^+ + \pi$ track misID as $B_s^0 \to J/\psi\pi^+\pi^-$)	
19	$m(B^+)$ or `ProbNNk`(π)	$\notin (5243, 5315)$ MeV > 0.1

track (fake track) is less than 0.2. Particles with same charge may share track segments, referred as clone tracks, representing a possible background and may result in a spike in the angular variable χ distributions. The clone tracks are vetoed by requiring the opening angle between any same-charged tracks greater than 0.5 mrad. A comparison of χ distribution before and after this veto is shown in Fig. 5.2. The nonphysical spikes are removed with a signal efficiency of 99.995%. The J/ψ meson is formed by a pair of opposite-sign muon tracks, with transverse momentum p_{T} greater than 500 MeV, χ^2_{IP} larger than 4 and particle identification information $\mathrm{DLL}_{\mu\pi}$ greater than 0. The J/ψ vertex fit χ^2 must satisfy χ^2_{vtx} less than 16 and the invariant mass of di-muon pairs should be in the $(-48, +43)$ MeV mass window around the known J/ψ mass[58]. The pion tracks are required to have p_{T} greater than 250 MeV, χ^2_{IP} larger than 4 and PID requirements $\mathrm{DLL}_{\pi K}$ greater than -10 or `ProbNNk` larger than 0.05. The sum p_{T} of two pion tracks should be greater than 900 MeV and the vertex fit χ^2 less than 16. The B_s^0 meson is formed from a well-reconstructed PV with χ^2_{IP} less than 25, χ^2_{vtx}/ndf less than 10 and χ^2_{IP} of the next best PV greater than 50. The pointing angle are required to satisfy $\cos\theta_p$ larger than 0.999. The decay time of the B_s^0 meson should be greater than 0.3 ps with decay-time error δt less than 0.15 ps. The $B^+ \to J/\psi K^+$ background, arising due to a kaon-pion misidentification followed by a combination of a random π^-, is studied. To check for its contribution, the kaon mass hypothesis is applied in turn to each of the two pions. The invariant mass of the resulting $J/\psi K^+$ system is recalculated and plotted. Such cross-feed background is largely suppressed by vetoing the candidate if one of the pion candidate is consistent with kaon hypothesis (`ProbNNk> 0.1`) and the recalculated $m_{J/\psi K^+}$ is consistent with the known B^+ mass[58] within $\pm 3\sigma = \pm 36$ MeV. A comparison of $m_{J/\psi K^+}$ distribution in data sample with and without this veto is shown in Fig 5.3. This background is rejected with a B_s^0 signal selection efficiency 99.93%.

A fit using Hypatia function and exponential function described signal and background, respectively, is performed on RS data after preselection, as shown in Fig. 5.4. Combinatorial background, consisting of candidates created from random combination of tracks, is further suppressed with a MVA using uBoost BDT algorithm[136] which could ensure a uniform efficiency on the angle variable $\theta_{\pi\pi}$. The signal input to the training stage is the simulated signal sample, while candidates in the upper mass sideband (200,250) MeV above the known B_s^0 mass[58] are used as template for the combinatorial background. The BDT is trained on one half of these samples, the other half being used to test its

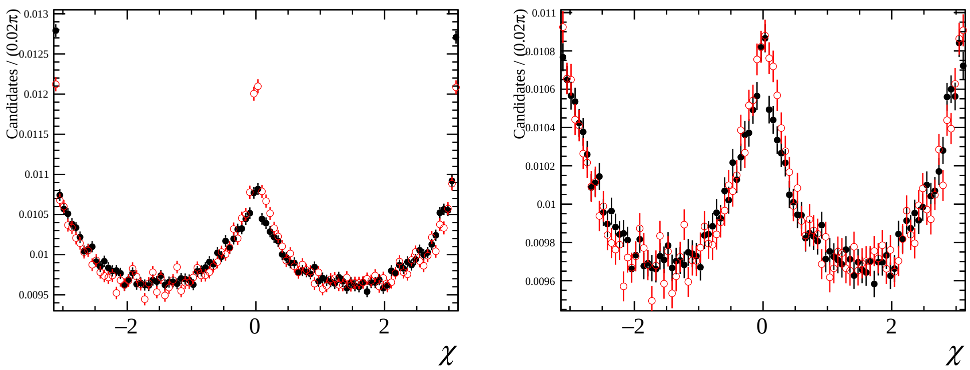

Figure 5.2 Comparison of χ distributions in the RS data (black solid points) and the WS data samples (red open points) before (left) and after (right) the opening angle selection.

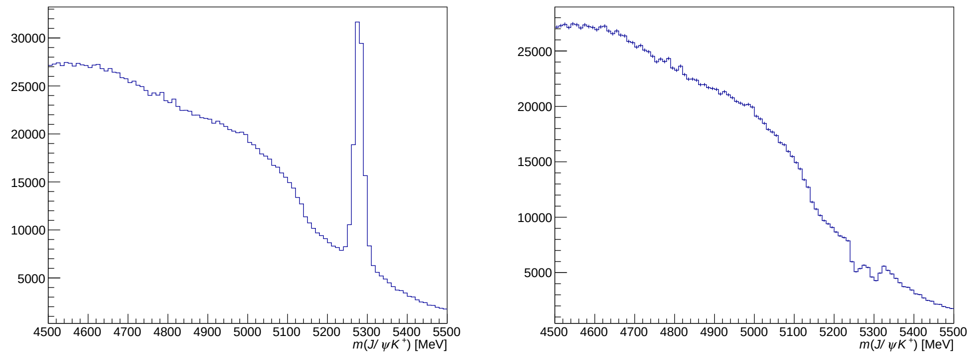

Figure 5.3 Comparison of $m_{J/\psi K^+}$ distributions in RS data sample with (left) and without (right) the veto.

performance. The training variables are: the smaller $\mathrm{DLL}_{\mu\pi}$ of two muons (mmPIDmu); natural logarithm of the smaller χ^2_{IP} of two pions (mmIPCHI2pi); natural logarithm of the larger χ^2_{IP} of two pions (maxIPCHI2pi); natural logarithm of B_s^0 vertex fit χ^2 (LogBCHI2); natural logarithm of B_s^0 DTF fit χ^2 (LogBDTFCHI2); natural logarithm B_s^0 χ^2_{IP} (LogBIPCHI2); p_{T} of B_s^0 (BPT); sum of the p_{T} of two pions (SumPT). The simulated samples are weighted using two-dimension B_s^0 p and p_{T} distributions, as well as smear vertex fit χ^2, to match the distributions in *sWeighted* data with preselection. A comparison of training variables between *sWeighted* data and weighted simulated sample are shown in Fig 5.5. A good consistency is found among them. The BDT output distributions of signal and background training samples are shown in Fig. 5.6. To estimate the best requirement on the output of the BDT classifier, the figure of merit FoM=$S/\sqrt{S+B}$, where $S(B)$ is the number of signal (background) candidates in ± 20 MeV mass window around the known B_s^0 mass, is used. To maximise the signal significance, a cut of BDT$<$ 0.47 is chosen.

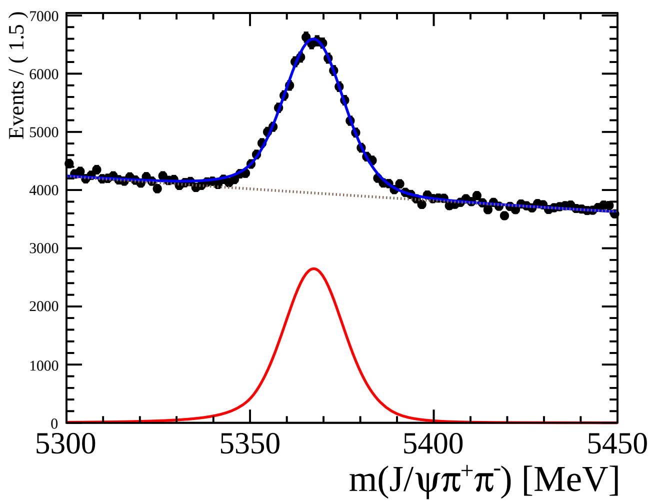

Figure 5.4 The fit of $B_s^0 \to J/\psi\pi^+\pi^-$ mass distribution before BDT selection.

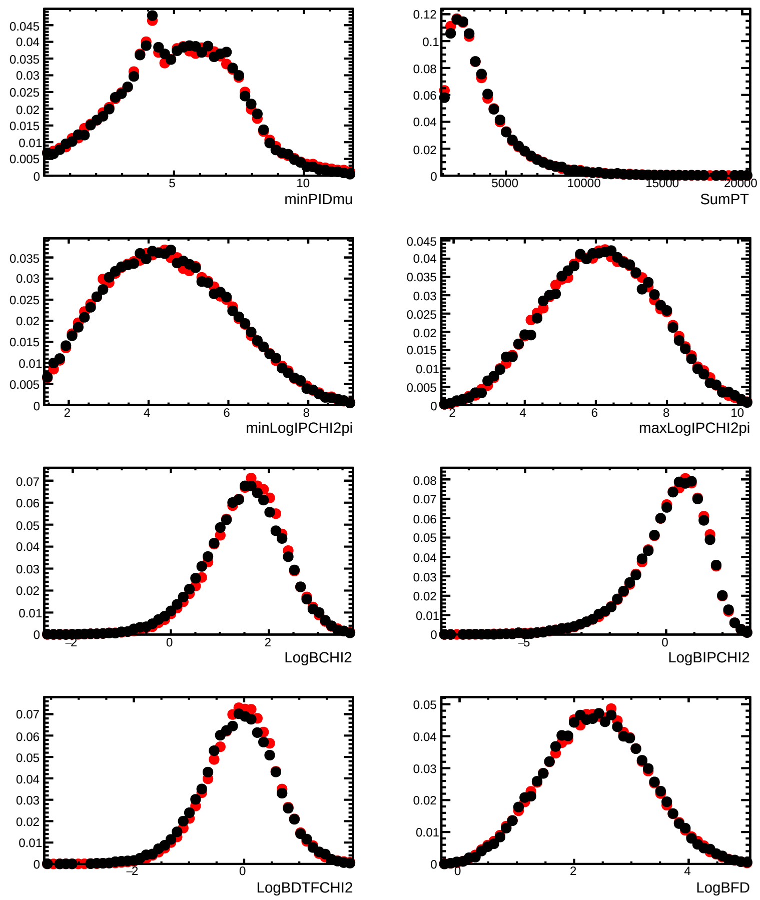

Figure 5.5 Comparison of training variables between *sWeighted* data (black points) and weighted simulation (red points).

After applying full selection to RS data sample, there are 1.4% multiple candidates remained in the mass fit region (5250, 5550) MeV and 0.2% in the ±20 MeV around the

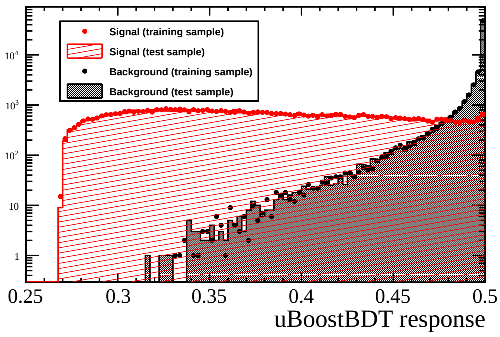

Figure 5.6 uBoost BDT distributions in signal and background training samples.

B_s^0 mass peak. These candidates have a same mass distribution as the combinatorial background, thus are kept in the following procedures.

5.4 Signal yields extraction

5.4.1 Backgrounds

Some physics background candidates that survive the selection chain described in the previous sections are expected. These are $\Lambda_b^0 \to J/\psi p K^-$ with both hadrons misidentified as pion candidates and $B_s^0 \to J/\psi \eta'(\to \rho^0\gamma)$ with γ unreconstructed.

The yield of $\Lambda_b^0 \to J/\psi p K^-$ background is estimated using candidates in $(5250, 5352)$ MeV region of$J/\psi\pi^+\pi^-$ mass of RS data sample. A $J/\psi p K^-$ mass is calculated with mass hypotheses of two pions change to proton and kaon mass hypotheses. The resulting $J/\psi p K^-$ mass is fitted by a Hypatia function for the Λ_b^0 component and an exponential function for the background, as shown in Fig 5.7. The shape parameters of Hypatia function are fixed to Λ_b^0 simulation. The resulting yield is 4222 ± 85 for Λ_b^0, whose central value is used as Λ_b^0 yield in the final $J/\psi\pi^+\pi^-$ mass fit.

The $B_s^0 \to J/\psi \eta'(\to \rho^0\gamma)$ background are studied with simulated samples which indicate that it populates below B_s^0 mass peak in the $J/\psi\pi^+\pi^-$ invariant mass distribution. Thus it is included in the final fit.

Candidates in WS samples are pure combinatorial background which are expected to have same shape as the combinatorial background in RS sample.

5.4.2 Fits to B_s^0 mass distribution

A simultaneous fit to the invariant mass distribution of the selected $J/\psi\pi\pi$ (RS and WS samples) is performed. The B_s^0 signal is parametrised by a Hypatia

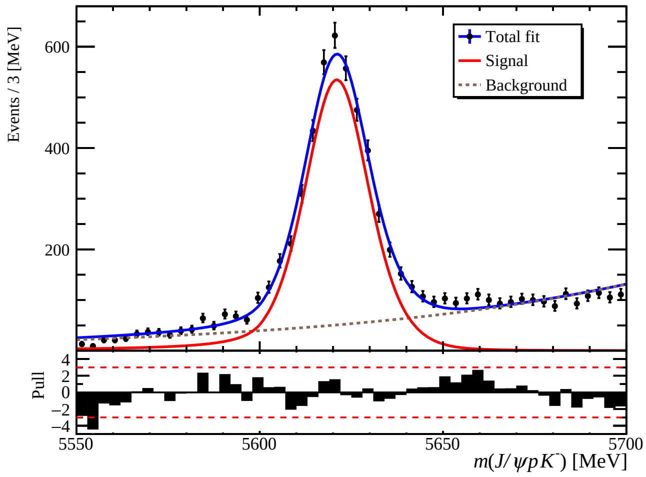

Figure 5.7 Fit to $m(J/\psi p K^-)$ distributions.

Table 5.5 Fitted yields in fit region and ±20 MeV around the known B_s^0 mass[58].

Components	Yields	Yields in ±20 MeV
$B_s^0 \to J/\psi\pi^+\pi^-$	36649 ± 234	33533
$B^0 \to J/\psi\pi^+\pi^-$	23493 ± 256	0
$\Lambda_b^0 \to J/\psi p K^-$	4222 (fixed)	54
$B_s^0 \to J/\psi\eta'$	4309 ± 333	84
Combinatoric	45555 ± 365	6290

function where the signal radiative tail parameters are fixed to values obtained from simulation. The combinatorial backgrounds in RS and WS samples are modelled by an exponential function where their yields are allowed to be different. The two physics backgrounds discussed before are described using shapes from simulation obtained by `RooKeyspdf`[111]. The yield of $B_s^0 \to J/\psi\eta'$ is determined by the fit while the yield of $\Lambda_b^0 \to J/\psi p K^-$ is fixed to 4222. The fit projections of RS and WS candidates are shown in Fig. 5.8. 33533 ± 215 B_s^0 signal candidates are found in ±20 MeV of B_s^0 mass peak with a purity of 84%. Yields of different components in the fits are given in Table 5.5.

5.4.3 Background subtraction

The WS candidates are used to model the combinatorial background with cFit technique in the previous publication[80]. This requires a well-modelled background PDF of variables used in the ϕ_s fit, especially a proper consideration of the correlations between them. To simplify the work, a method, used in the $J/\psi K^+K^-$ analysis[79,134],

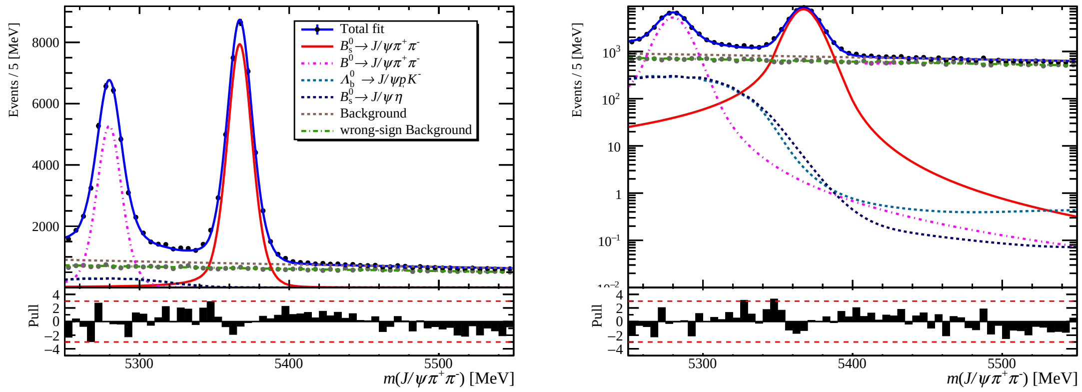

Figure 5.8 The simultaneous fit to the $m(J/\psi\pi\pi)$ distributions right-sign (black points) and wrong-sign (brown points) samples with various fit components. The two physics backgrounds from B_s^0 and Λ_b^0 decays are overlapped each other, and hard to distinguish. The left and right plots show in a linear and logarithm scale, respectively.

with embedding negative weighted events using WS candidates is adopted to subtract the combinatorial background.

A comparison of final fitting parameters in RS and WS samples in upper mass sideband region $(5420, 5550)$ MeV is shown in Fig. 5.9. A good consistency is found for all the variables, except for $m_{\pi\pi}$ and t distributions. The difference in $m_{\pi\pi}$ is due to a $\rho \to \pi^+\pi^-$ component which contribute only to RS sample. The ratio of $m_{\pi\pi}$ distributions between RS and WS candidates is used to weight the WS $m_{\pi\pi}$ distribution. A comparison of final fitting parameters in RS and WS samples in upper mass sideband region $(5420, 5550)$ MeV after the reweighing process is shown in Fig. 5.10. The decay-time differences between RS and WS samples can have sizeable effect on Γ_H determination comparing to the statistical uncertainty. A similar weighting procedure is applied on WS samples to match RS distribution of decay time.

WS candidates with negative weights are added to the RS samples, where the sum of weights in WS sample is set to be equal to the minus yields of the combinatorial background found in the RS sample in the simultaneous fit. In this way the combinatorial background is statistically subtracted by the negative weighted events. Candidates within ± 20 MeV of the B_s^0 mass peak are retained for ϕ_s fit where physics background has a fraction of 0.4% of the total yield and is ignored. Thus the sample can be fit by one signal component. The effect of neglecting such small physics background is evaluated as a systematic uncertainty and discussed in Sec. 5.8.

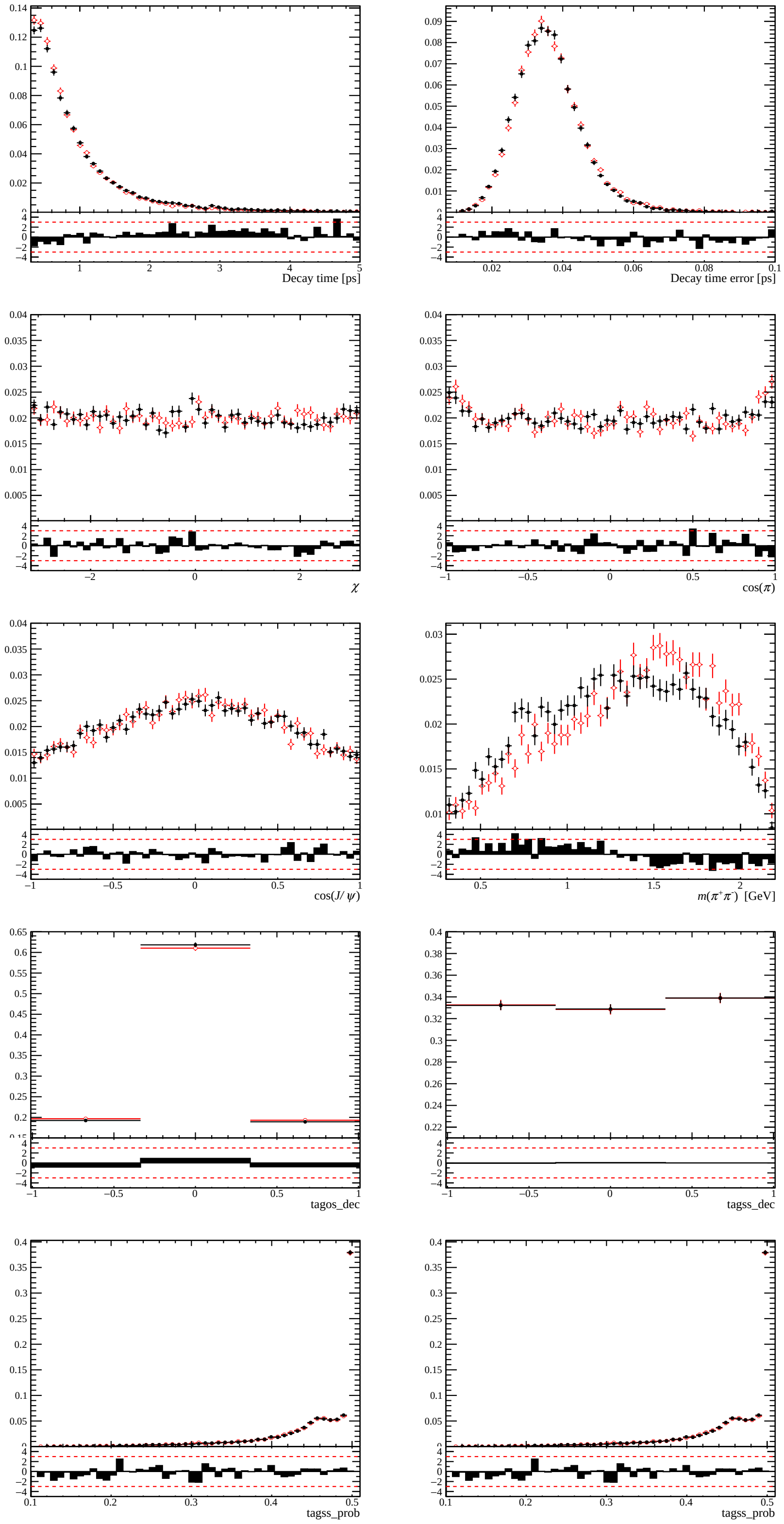

Figure 5.9 Comparison of fitting parameters in the $J/\psi\pi^+\pi^-$ data (black solid points) and the $J/\psi\pi^\pm\pi^\pm$ same-sign data sample (red open points) both from mass sideband region of (5420, 5550) MeV.

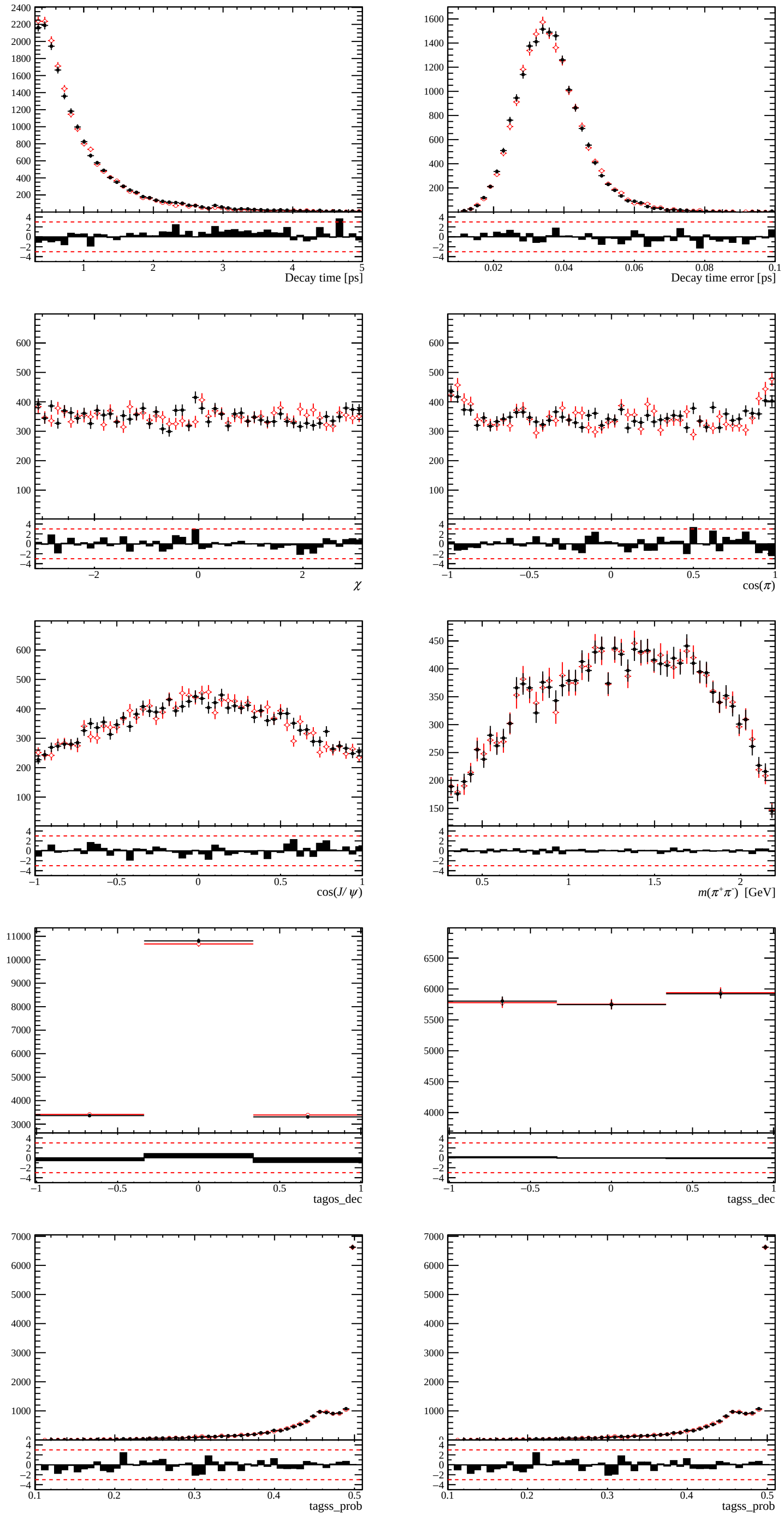

Figure 5.10 Comparison of fitting parameters in the $J/\psi\pi^+\pi^-$ data (black solid points) and the $J/\psi\pi^\pm\pi^\pm$ same-sign data sample (red open points) both from mass sideband region of $(5420, 5550)$ MeV after reweighing m for WS candidates.

Table 5.6 Trigger lines used for selected $B^+ \to J/\psi K^+$ candidates.

Trigger level	Trigger line
HLT1	`Jpsi_Hlt1DimuonHighMassDecision_TOS` or `B_Hlt1TrackMuonDecision_TOS` or `B_Hlt1TwoTrackMVADecision_TOS`
HLT2	`Jpsi_Hlt2DimuonDetachedJpsiDecision_TOS`

5.5 Flavour tagging calibration

As mentioned in Sec.2.3.3, the signal tagging algorithms should be combined and calibrated to improve flavour tagging performance. In this analysis, the combination of the OS-electron, OS-muon, OS-kaon, OS-charm and OS-vertex charge algorithms is used as the nominal OS tagger. The neural network SS kaon tagger is used as the nominal SS tagger. The functional form of the tagging calibrations is studied in control samples of flavour-specific decays properly corrected to resembled the signal decay. The OS tagger is calibrated with $B^+ \to J/\psi K^+$ decay while the SS tagger is calibrated using $B_s^0 \to D_s^+\pi^-$ decay.

5.5.1 Calibration of the OS tagger

5.5.1.1 Data sample

$B^+ \to J/\psi K^+$ candidates are selected with the same trigger requirements and similar selection criteria as the signal channel. The selection criteria is listed on Table. 5.6 and Table. 5.7. A MVA is used to further suppress the combinatorial background using same training variables in data sample if applicable.

A fit to the mass distribution of selected $B^+ \to J/\psi K^+$ candidates is performed to calculate *sWeight*, used in the subsequent steps of the analysis to subtract the background surviving the selection. A Hypatia function and an exponential function are used to described the signal and background components, respectively. The fit result is shown in Fig. 5.11. The B^+ yield is 1623972 ± 1439.

An event-by-event weight is assigned to each $B^+ \to J/\psi K^+$ signal candidate to account for the kinematic differences in p_{T}, rapidity, `nTracks` and `nPV` (numbers of PVs in one events) compared with the $B_s^0 \to J/\psi\pi^+\pi^-$ signal decay. The comparison of distributions of the weighted variables and the mistag probabilities in two samples are shown in Fig. 5.12. Good agreements are found after the reweighing process.

Table 5.7 The selection criteria of $B^+ \to J/\psi K^+$ samples

#	Selection variables	Requirements
1	All tracks χ^2_{track}/ndof	<3
2	All tracks clone distance	> 5000
	J/ψ selection	
4	$-\Delta\log\mathcal{L}(\mu-\pi)$	> 0
5	$\min(p_T(\mu^+), p_T(\mu^-))$	> 0.5 GeV/c
6	χ^2_{vtx}/ndof	< 16
7	$\lvert m(\mu^+\mu^-) - m(J/\psi)\rvert$	$\in [3030,3150]$ MeV/c^2
	K selection	
8	$-\Delta\log\mathcal{L}(K-\pi)$	> 0
9	$p_T(K^+)$	> 0.5 GeV/c
	B selection	
10	$M(B)$	$\in [5200,5550]$ MeV/c^2
11	χ^2_{vtx}/ndof	< 10
12	χ^2_{DTF}/ndof	< 5
13	χ^2_{IP}	<25
14	t	$\in$[0.3,14.0] ps

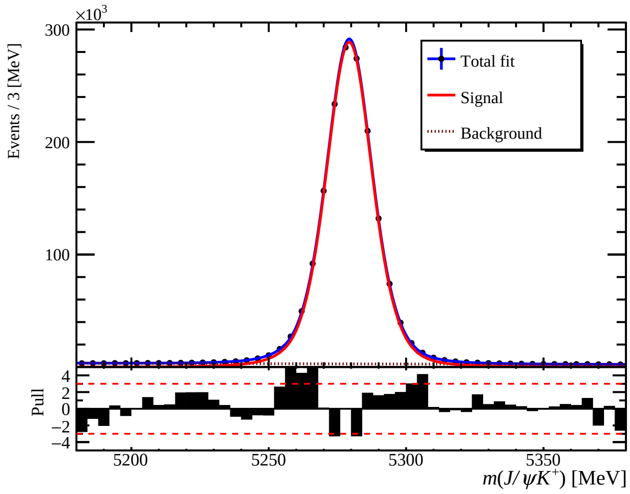

Figure 5.11 Mass fit of $B^+ \to J/\psi K^+$ sample.

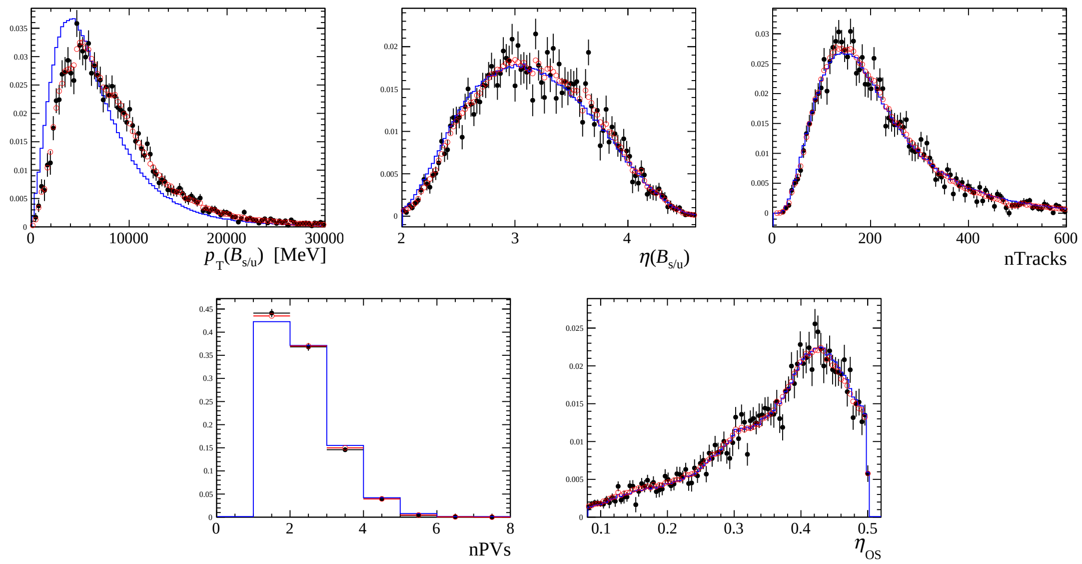

Figure 5.12 Comparison of reweighing parameters and mistag probabilities in $B_s^0 \to J/\psi\pi^+\pi^-$ (black solid points), $B^+ \to J/\psi K^+$ before (blue histogram) and after reweighing (red open points).

5.5.1.2 Calibration

The calibration of the estimates mistag η is performed on the reweighed $B^+ \to J/\psi K^+$ dataset. Five different methods are used to calibrate $\omega^{\mathrm{OS}} - \eta^{\mathrm{OS}}$ relation. Using Eq. (2-14), a binned and an unbinned maximum-likelihood fits are performed on data. To further check the dependence of η^{OS} and ω^{OS}, the binned and unbinned fits assuming quadratic relation between $\omega^{\mathrm{OS}} - \eta^{\mathrm{OS}}$ are also performed. A binned fit without using the weights in kinematic reweighing procedure is also made. The projection of the fitted calibration functions are shown in Fig. 5.13. Good agreements are found for the five methods. The unbinned fit assuming linear relation between ω^{OS} and η^{OS} is taken in the default fit.

The validation of using $B^+ \to J/\psi K^+$ to calibrate OS tagger is checked by applying same selection and calibrated method to the $B^+ \to J/\psi K^+$ and $B_s^0 \to J/\psi\pi^+\pi^-$ simulation samples. The calibrated results are shown in Fig. 5.14. The relative differences on calibrated parameters in B_s^0 and B^+ samples are taken as systematic uncertainties. Systematic uncertainties due to the choice of signal and background models are also considered for the calibration parameters. The signal component is refitted with Double-Sided Crystal Ball function, the background component is refitted using second-order polynomial function. The relative differences in calibrated parameters are taken as a source of systematic uncertainties. The systematics arisen from signal and background model are determined separately and added in quadrature. The systematic

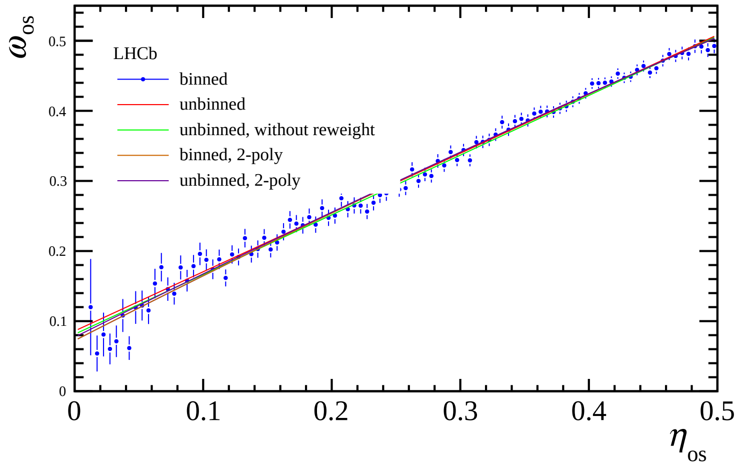

Figure 5.13 ω^{OS} - η^{OS} obtained using the binned and unbinned approaches in $B^+ \to J/\psi K^+$ samples.

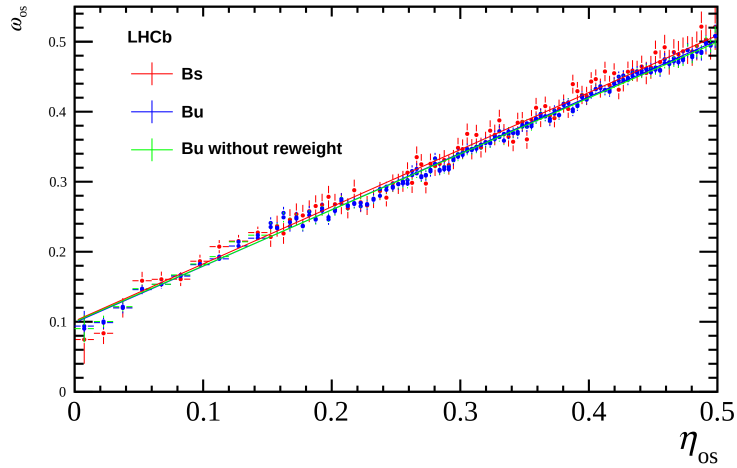

Figure 5.14 ω^{OS} - η^{OS} obtained using the binned and unbinned approaches.

uncertainties on calibrated parameters on listed on Table 5.8.

5.5.2 Calibration of the SS tagger

5.5.2.1 Data sample

$B_s^0 \to D_s^+\pi^-$ candidates are selected with cut-based selection requirements including trigger and some preselection, which are given in Table. 5.9 and Table. 5.10.

The mass distribution of the selected $B_s^0 \to D_s^+\pi^-$ sample is fitted using a Hypatia function for signal, an exponential function for background. Several physics background including $B_s^0 \to D_s K$, $B^0 \to D_s\pi$, $\Lambda_b \to \Lambda_c\pi$, $B_s^0 \to D_s^*\pi$ and $B_s^0 \to D_s\rho$ are described

Table 5.8 Systematic uncertainties for OS tagger calibrated parameters

Item	p_0	p_1
MC portability	0.0055	0.0135
Mass fit model	0.0000	0.0010
Total	0.0055	0.0135

Table 5.9 Trigger lines used for selected $B_s^0 \to D_s^+\pi^-$ candidates.

Trigger level	Trigger line
HLT1	`Bs_Hlt1TrackMVADecision_TOS` or `Bs_Hlt1TwoTrackMVADecision_TOS`
HLT2	`Bs_Hlt2Topo[2||3||4]BodyDecision_TOS`

using shapes from simulated samples. A two-step fit is used to extract the signal yield. First, an unbinned maximum-likelihood fit in the range (5100, 5600) MeV of the invariant mass is performed (Fit A). This allows to control the contamination of various physics backgrounds with $B_s^0 \to D_s^+\pi^-$ candidates. In this fit, the mean and width of the signal components are floated while the tail parameters are taken from simulation. All yields are floating in the fit. After Fit A, an unbinned maximum likelihood fit is performed (Fit B) for which all background components are combined into one single background component and the shapes are fixed to the values found in Fit A. Furthermore, the fit range is reduced to (5300, 5600) MeV to prevent a dilution of the *sWeight*. The background components which are neither combinatorial nor close to the signal are removed. In Fit B, only two parameters are floating: the yield of the signal $B_s^0 \to D_s^+\pi^-$ component and the yield for the combination of all backgrounds. Fig. 5.15 shows the invariant mass fit projection in Fig A and Fit B. 101984 ± 365 B_s^0 candidates are found in the fit.

Same reweighing approach is used for $B_s^0 \to D_s^+\pi^-$ samples as that used for $B^+ \to J/\psi K^+$. The distributions of reweighed kinematic variables and the mistag probabilities are consistent with the distributions in $B_s^0 \to J/\psi\pi^+\pi^-$ samples as illustrated in Fig. 5.16.

5.5.2.2 Calibration

The SS tagger is calibrated by resolving the B_s^0-$\overline{B}_s^0$ flavour oscillation in $B_s^0 \to D_s^+\pi^-$ samples. The decay-time distribution of $B_s^0 \to D_s^+\pi^-$ decay considering this oscillation

Table 5.10 The selection criteria of $B_s^0 \to D_s^+\pi^-$ samples

#	Selection variables	Requirements
	Bachelor π^+ selection	
1	p	> 2000 MeV
2	p_{T}	> 400 MeV
3	χ^2_{IP}	> 36
4	χ^2_{track}/ndf	< 2
5	PIDK	<0
	D_s^- selection	
6	Mass	$\in (1933, 2003)$ MeV
7	χ^2_{IP}	> 4
8	χ^2_{vtx}/ndof	> 2
	π^+ from D_s^- selection	
9	χ^2_{track}/ndof	< 2.5
10	χ^2_{IP}	> 9
11	$\mathrm{DLL}_{K\pi}$	< 8.0
	$K^\pm$ from D_s^- selection	
12	χ^2_{track}/ndof	< 2.5
13	χ^2_{IP}	> 9
14	$\mathrm{DLL}_{K\pi}$	>0
	B_s^0 selection	
15	DIRA	> 0.9999
16	χ^2_{IP}	< 16
17	decay time	> 0.2 ps
18	$M(B_s^0)$	$\in (5000, 6000)$ MeV
	D^0 veto ($D^0 + \pi$ track misID as D_s^+)	
19	$m(KK)$	< 1840 MeV
	$D^\pm$ veto ($D \to KK\pi$ misID as $D_s^+ \to KK\pi$)	
20	$\mathrm{DLL}_{K\pi}$	> 10.0
	or $M(D)$	$\notin (1840, 1900)$ MeV
	Λ_c veto ($\Lambda_c \to p\pi K$ track misID as $D_s^+ \to KK\pi$)	
21	DLL_{Kp}	> 5.0
	or $M(\Lambda_c)$	$\notin (2255, 2315)$ MeV

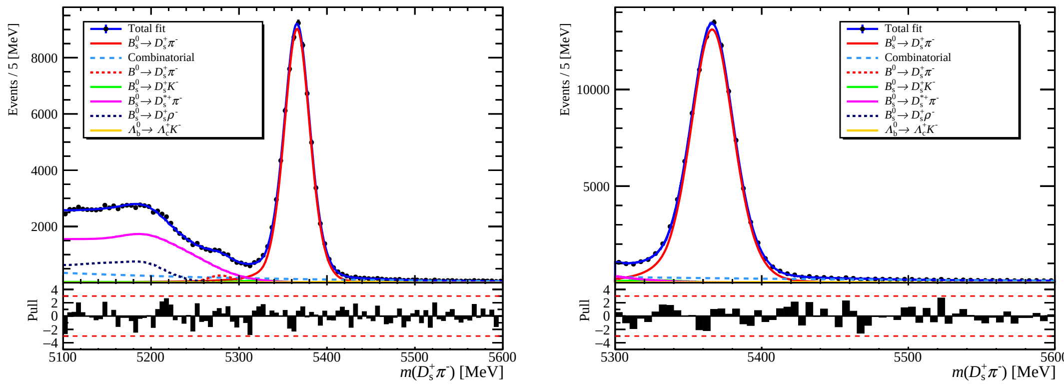

Figure 5.15 Fit projections of $B_s^0 \to D_s^+\pi^-$ invariant mass Fit A (left) and Fit B (right).

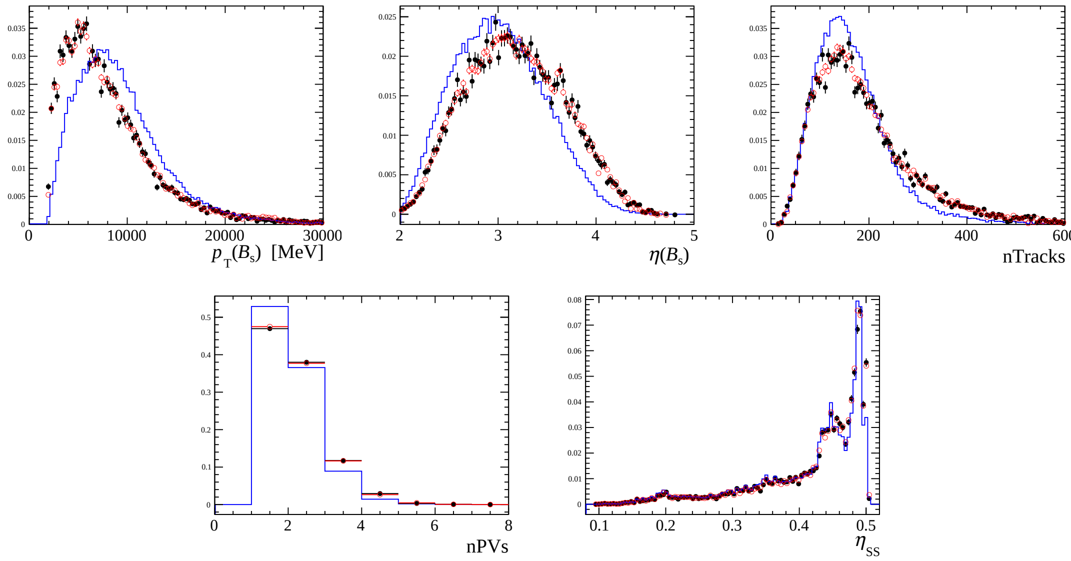

Figure 5.16 Comparison of reweighing parameters and mistag probabilities in $B_s^0 \to J/\psi\pi^+\pi^-$ (black solid points), $B_s^0 \to D_s^-\pi^+$ before (blue histogram) and after reweighing (red open points).

is given by

$$\begin{aligned} \mathcal{P}(t) &= \epsilon(t)\left[\Gamma(t') \otimes R(t,t';\delta t)\right], \\ \Gamma(t) &= \Gamma_s e^{-\Gamma_s t}(\cosh(\Delta\Gamma_s t/2) + q^{mix}(1-2\omega(\eta))\cos(\Delta m_s t)), \end{aligned} \tag{5-1}$$

where $\epsilon(t)$ is the decay-time efficiency function, t and t' are the reconstructed and true decay time, δ_t is the predicted per-event uncertainty of decay time, $R(t,t';\delta t)$ is the decay-time resolution function, $\Gamma(t)$ is the decay rate of $B_s^0 \to D_s^+\pi^-$. The decay-time efficiency is empirically parametrised as $\epsilon(t) = 1 - \frac{1}{1+(at)^n+b}$. Here, $q^{mix} = -1(1)$ if B_s^0 meson has (not) changed flavour between its production and decay, determined by

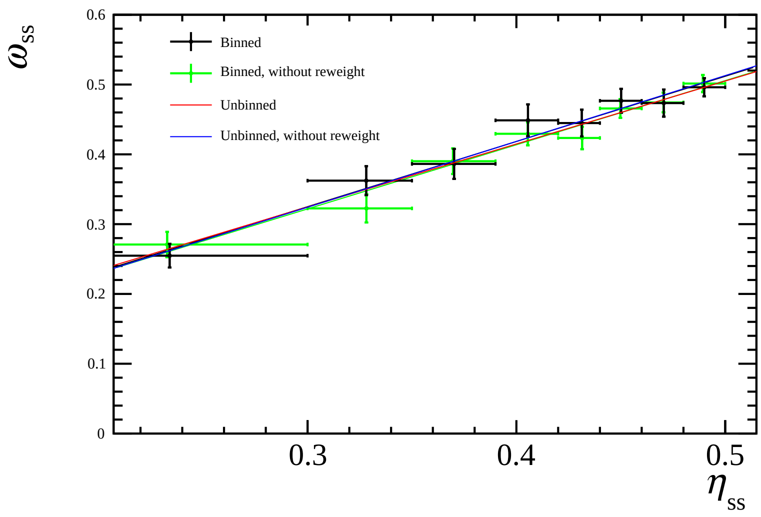

Figure 5.17 ω^{SS} - η^{SS} obtained using the binned and unbinned approaches in $B_s^0 \to D_s^-\pi^+$samples.

comparison of the charge of the bachelor pion and the flavour-tagging decision.

A linear relation between the $\omega^{\rm SS}$ and $\eta^{\rm SS}$ is assumed. Four different methods are used to calibrate this relation.

- An unbinned maximum-likelihood simultaneous fit to decay-time distribution in *sWeighted* data in eight $\eta^{\rm SS}$ bins (Binned method);
- An unbinned maximum-likelihood simultaneous fit to decay-time distribution in *sWeighted* data in eight $\eta^{\rm SS}$ bins without using the weights from kinematic reweighing process (Binned method without reweighing);
- An unbinned maximum-likelihood fit to decay-time distribution in *sWeighted* data (Unbinned method) ;
- An unbinned maximum-likelihood fit to decay-time distribution in *sWeighted* data without using the weights from kinematic reweighing process (Unbinned method without reweighing) ;

The projection of the fitted calibration functions are shown in Fig. 5.17. The results of four methods are in good agreements. The unbinned method is taken in the default fit. Fig. 5.18 shows the projection of decay time by splitting the decay to mixed (flavour changed) and unmixed (flavour not changed) candidates.

Same validation approach is used for SS tagger as that used for OS tagger described in Sec. 5.5.1.2. The calibrated results are shown in Fig. 5.19. The relative differences on calibrated parameters in $B_s^0 \to D_s^+\pi^-$ and $B_s^0 \to J/\psi\pi^+\pi^-$ simulated are taken as a source of systematic uncertainty. Systematic uncertainty due to the choice of mass fit model is

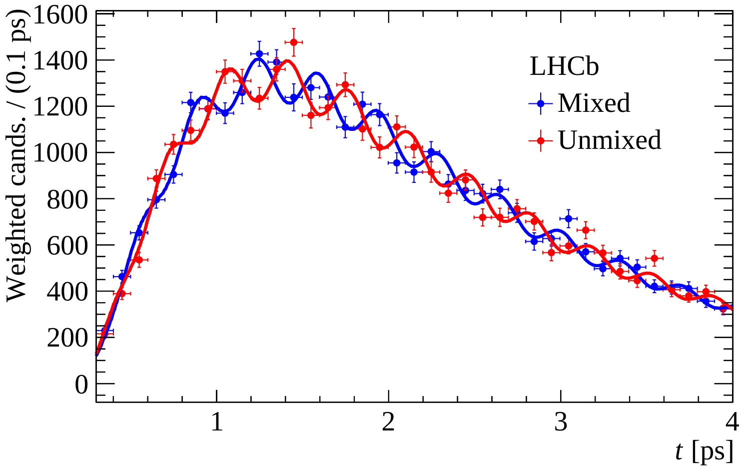

Figure 5.18 Distributions of the decay time for $B_s^0 \to D_s^+\pi^-$ candidates tagged as mixed and unmixed with the projection of the fit result.

Table 5.11 Systematic uncertainties for SS tagger calibrated parameters

Item	p_0	p_1
MC portability	0.0025	0.0461
Mass fit model	0.0008	0.0113
Total	0.0026	0.0475

also considered as discussed in Sec. 5.5.1.2. The resulting systematic uncertainties on calibrated parameters are listed on Table 5.11.

5.5.3 Tagging performance

The calibrated parameters for both OS and SS are summarised in Table 5.12. When events are tagged by both the OS and the SSK algorithms, a combined tag decision, $q^{\mathrm{OS+SSK}}$, and wrong-tag probability, $\omega^{\mathrm{OS+SSK}}$, are given by the algorithm in Table 5.13. The combined wrong-tag probability, $\bar{\omega}^{\mathrm{OS+SSK}}$, for $\overline{B}{}_s^0$ meson is calculated in same way by replacing all ω by $\bar{\omega}$. The detailed tagging information is listed in Table 5.14.

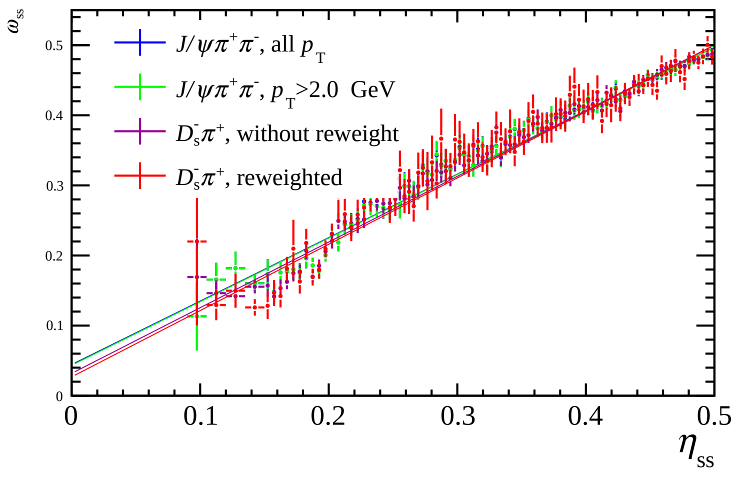

Figure 5.19 ω^{SS} - η^{SS} obtained using the binned and unbinned approaches.

Table 5.12 Flavour tagging calibration parameters.

Parameters	OS	SSK
$\langle\eta\rangle$	0.3580	0.4167
p_0	$0.3885 \pm 0.0007 \pm 0.0055$	$0.4342 \pm 0.0103 \pm 0.0026$
p_1	$0.8449 \pm 0.0063 \pm 0.0135$	$0.9431 \pm 0.1245 \pm 0.0475$
Δp_0	$+0.0080 \pm 0.0014$	0.00 ± 0.02
Δp_1	$+0.0158 \pm 0.0126$	0.00 ± 0.02

Table 5.13 Algorithms to combine both the OS and the SSK tagger. The last two conditions have the same form $(1-2\omega)\cdot q$ which is used in fit function Eq. (4-10), so the two conditions can be combined in the fit code.

combined	decision	Condition
$\frac{\omega^{\mathrm{OS}}\omega^{\mathrm{SSK}}}{\omega^{\mathrm{OS}}\omega^{\mathrm{SSK}}+(1-\omega^{\mathrm{OS}})(1-\omega^{\mathrm{SSK}})}$	q^{OS}	$q^{OS} = q^{SSK}$
$\frac{\omega^{\mathrm{OS}}(1-\omega^{\mathrm{SSK}})}{\omega^{\mathrm{OS}}(1-\omega^{\mathrm{SSK}})+(1-\omega^{\mathrm{OS}})\omega^{\mathrm{SSK}}}$	q^{OS}	$q^{\mathrm{OS}} = -q^{\mathrm{SSK}}$ and $\omega^{\mathrm{OS}} < \omega^{\mathrm{SSK}}$
$\frac{(1-\omega^{\mathrm{OS}})\omega^{\mathrm{SSK}}}{\omega^{\mathrm{OS}}(1-\omega^{\mathrm{SSK}})+(1-\omega^{\mathrm{OS}})\omega^{\mathrm{SSK}}}$	$-q^{\mathrm{OS}}$	$q^{\mathrm{OS}} = -q^{\mathrm{SSK}}$ and $\omega^{\mathrm{OS}} > \omega^{\mathrm{SSK}}$

Table 5.14 Tagging information.

Category	Fraction(%)	ε_{tag} (%)	$\varepsilon_{\text{tag}} D^2$
OS only	14.054	11.035	0.86 ± 0.05
SSK only	54.226	42.579	1.54 ± 0.33
OS and SSK	31.720	24.907	2.66 ± 0.19
Total	100	78.522	5.06 ± 0.38

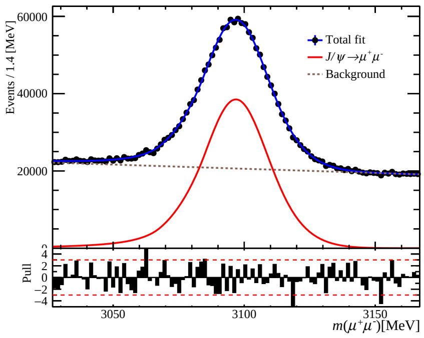

Figure 5.20 The projection plot of the fit to the J/ψ mass spectrum with total fit overlaid. The signal and background components are shown by red solid and (brown) dashed lines, respectively.

5.6 Detector effects

5.6.1 Decay-time resolution

The decay-time resolution is determined on a sample of *fake* B_s^0 candidates formed from a prompt J/ψ candidate with two opposite-sign tracks originating from the PV. These *fake* B_s^0 candidates are expected to have a decay time of zero and therefore the sample is also referred to as prompt sample. The candidates are selected with a similar selection as presented in Table 5.4 except for time-bias selection #9, 13, 15-17, mass veto #19 and BDT. A similar calibrated method validation is performed as that studies in Sec. 4.6.1, which indicates reweighing the DTF fit χ^2 and track multiplicity of the calibration sample to match the data distributions could give a properly estimate decay-time resolution of the signal decay within 3% accuracy. The *sWeight* is determined by a fit to the invariant mass of J/ψ meson in order to examine only signal contribution in the following procedures. The fit projection is shown in Fig. 5.20. 0.9×10^6 J/ψ signal candidates are obtained.

The resolution function is described by a triple-Gaussian function with widths proportional to a quadratic function $\sigma_t \equiv \delta_t + \sigma_t^0 + s_2(\delta_t)^2$, where δ_t is the estimated decay-time error, and σ_t^0 and s_2 are constants to be determined.

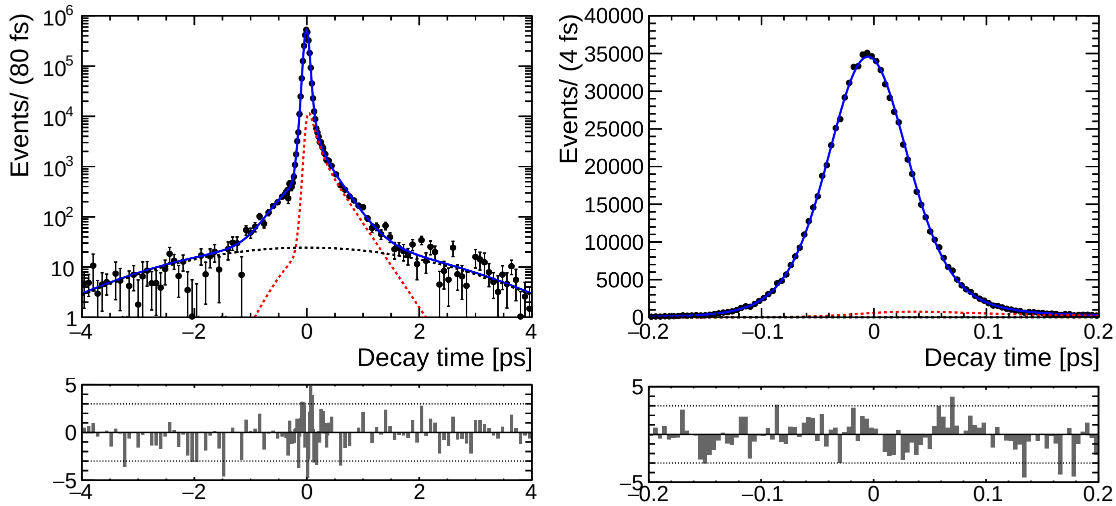

Figure 5.21 Decay-time distribution of $J/\psi\pi^+\pi^-$ calibration sample plotted in (left) whole fit region and (right) central region of $(-0.2, 0.2)$ ps. The solid curve shows the total fit, the red dashed line shows the long-lived background and the black dashed line show the wrong PV component.

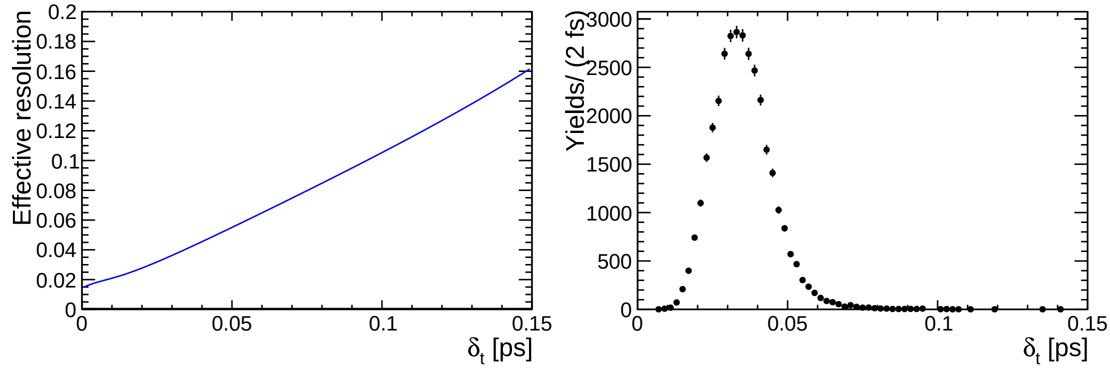

Figure 5.22 Calibrated effective time resolution as a function of the predicted decay-time error (left). Predicted decay-time error distribution from real B_s^0 after subtracting the background. (right)

An unbinned maximum-likelihood fit is performed to the decay-time distribution in the weighted calibration sample using Eq. (4-5). The fit model consists of three components: a delta function convolved with the triple-Gaussian function to describe true prompt J/ψ candidates, a pair of exponential functions convolved with the same triple-Gaussian to describe long-lived backgrounds from b hadrons and a wide Gaussian function to describe backgrounds due to wrongly associated PVs. The fit projection is shown in Fig. 5.21. The relation of effective resolution and the corresponding average decay-time error δ_t is shown in Fig. 5.22. To take into account the δ_t distribution of B_s^0 data sample, shown in Fig. 5.22, the average effective resolution is found to be 41.5 fs.

5.6.2 Decay-time acceptance

Due to the displacement requirements made on hadrons in the offline selection and the inefficiencies in the VELO reconstruction, the detector efficiency is not constant over the B_s^0 decay time. As discussed in Sec.4.6.2, this efficiency is determined with a control channel $B^0 \to J/\psi K^{*0}\,(\to K^+\pi^-)$, which is known to have a purely exponential decay-time distribution with $\tau_{B^0} = 1.520 \pm 0.004$ ps[58]. The signal efficiency is calculated as

$$\varepsilon_{\text{data}}^{B_s^0}(t) = \varepsilon_{\text{data}}^{B^0}(t) \times \frac{\varepsilon_{\text{sim}}^{B_s^0}(t)}{\varepsilon_{\text{sim}}^{B^0}(t)}, \tag{5-2}$$

where $\varepsilon_{\text{data}}^{B^0}(t)$ is the efficiency of the control channel and $\varepsilon_{\text{sim}}^{B_s^0}(t)/\varepsilon_{\text{sim}}^{B^0}(t)$ is the ratio of efficiencies of the simulated signal and control mode after the full trigger and selection chain has been applied. This correction accounts for the small differences in the kinematics between the signal and control mode.

5.6.2.1 $B^0 \to J/\psi K^{*0}$ sample

$B^0 \to J/\psi K^{*0}$ candidates are selected using same preselection and BDT algorithm as that used in B_s^0 sample. Two additional cuts are added to further suppress the combinatorial background, which are `ProbNNk` of the final state kaon track is greater than 0.05 and the invariant mass of $K^+\pi^-$ is in ±100 MeV region of the known K^{*0} mass. Three misidentified physics backgrounds are controlled by veto. $\Lambda_b^0 \to J/\psi p K^-$ contribution, arisen from the proton misidentifies as a pion, is removed by requiring the pion candidates has `ProbNNp`(π) less than 0.2 or the recomputed $J/\psi K^- p$ mass do not consistent with the Λ_b^0 mass hypothesis within $\pm 3\sigma = \pm 22.2$ MeV. $B^0 \to J/\psi K^+\pi^-$ contribution, arisen from a doubly misidentification, is vetoed when the recomputed $J/\psi K^+\pi^-$ mass consistent with the B^0 mass hypothesis within $\pm 3\sigma = \pm 32.7$ MeV and satisfying `ProbNNk`$(\pi) > 0.1$, `ProbNNpi`$(K) > 0.1$ and `ProbNNk`$(\pi) >$ `ProbNNk`(K). $B_s^0 \to J/\psi K^+K^-$ contribution is also vetoed by requiring the recomputed invariant mass m_{KK} less than 1.04 GeV and `ProbNNk`(π) greater than 0.1.

A fit to invariant mass distribution of $J/\psi K^+\pi^-$, using a Hypatia function modelled B^0 signal and an exponential function described combinatorial background, is performed, as shown in Fig. 5.23. The signal yield is $(510 \pm 1.2) \times 10^3$. An event-by-event *sWeight* is generated to subtract the background used in the fit of decay-time distribution.

The PHSP $B^0 \to J/\psi K^{*0}$ simulation is reweighed according to the B^0 p_{T}, rapidity,

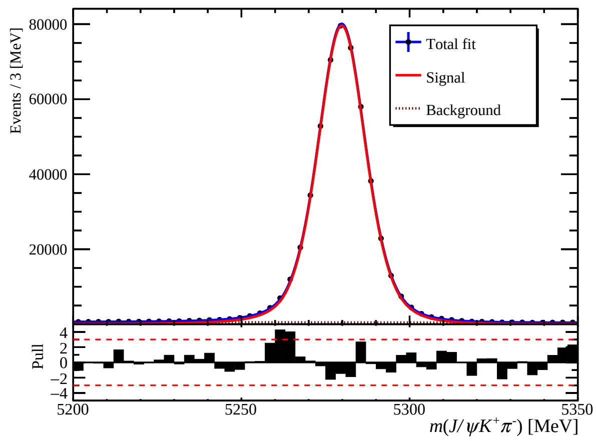

Figure 5.23 Mass distribution of $B^0 \to J/\psi K^{*0}$ candidates in data.

`nTracks`, $m_{K\pi}$ and $\cos\theta_{K\pi}$ distributions in the background subtracted B^0 data sample, to account for the $S-$wave $K\pi$ contribution in data as well as the kinematic difference between MC and data.

5.6.2.2 Determination of decay-time efficiency in B_s^0 data

The decay-time efficiency is parametrised by splines, which are implemented analytically in the decay-time fit as described in Ref.[137]. These splines consist of cubic polynomials defined piecewise in decay time. The efficiency parametrisation is characterised by the limits of the ranges on which the cubic polynomials are defined (also denoted as knots) and associated coefficients. It is optimised in order to find the ideal knot positions giving a good description of the decay time while minimising the number of knots. A good description was found using seven knots at [0.3, 0.58, 0.91, 1.35, 1.96, 3.01, 10.0] ps, where the coefficient as 1.96 ps is set to one to fix the overall normalisation.

The simulations of B_s^0 signal, $B^0 \to J/\psi K^{*0}$ signal and background-subtracted data are fitted simultaneously to determine the parameters for $\varepsilon_{\rm data}^{B_s^0}(t)$. Each sample is fitted by an exponential function convoluted by a decay-time resolution function, and then multiplied by decay-time efficiency. Different decay-time resolution functions are used for data and simulation. Data uses parameters obtained from the prompt J/ψ sample discussed in Sec. 5.6.1 while simulations use the calibration parameters obtained from B_s^0 signal simulated sample. Decay-time error δ_t distribution of each sample is included in the time resolution function. The lifetime is fixed to PDG value 1.520 ps for the B^0 data sample, and the input 1.519 ps for the B^0 simulation. The decay-time distributions

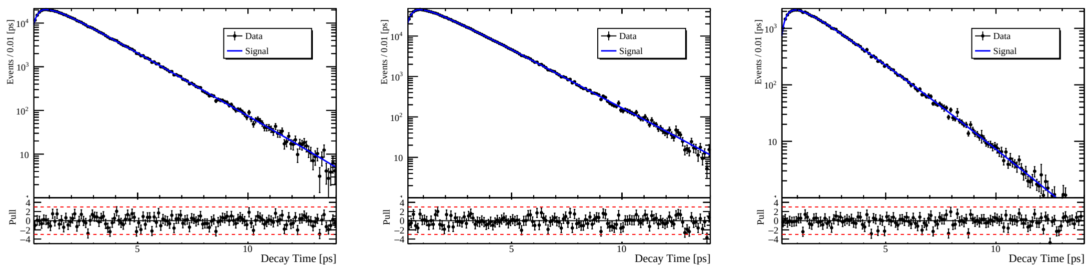

Figure 5.24 The decay-time distributions superimposed with fit functions in blue curves for the samples of B^0 data (left), B^0 simulation (middle) and B_s^0 signal MC (right). The pull distributions are also shown.

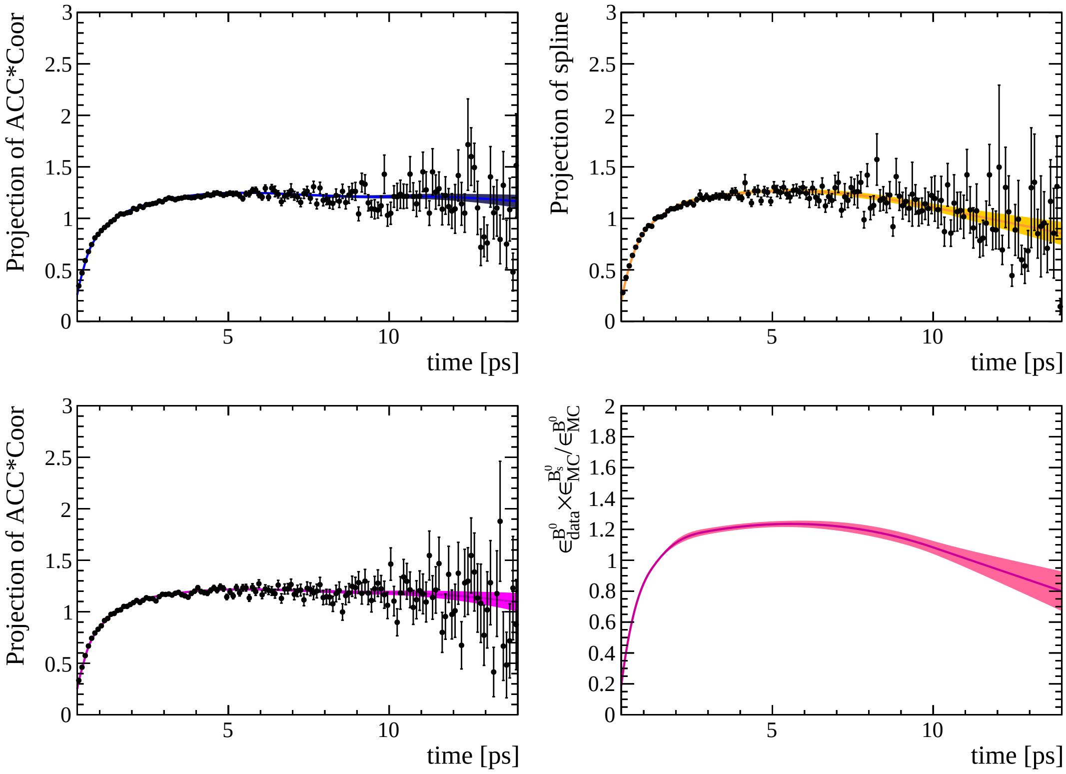

Figure 5.25 The decay-time efficiency for (top left) the B^0 MC, (top right) the B_s^0 MC, (middle left) the B^0 data, (middle right) the decay-time efficiency derived for the B_s^0 data.

and fit curves are shown in Fig. 5.24. Fig. 5.25 shows a graphical representation of the used parametrisation with the coefficients obtained on three samples, the numerical values and correlations of the coefficients are given in Tab. 5.15. Except for very small decay time, the ratio is consistent with unity, as expected. The acceptance in small decay time is sensitive to resonance and angular distributions.

Table 5.15 Decay-time acceptance coefficients and their correlations, where the 5th coefficient is fixed to 1.

	Correlations								Value
Coefficients	1	2	3	4	6	7	8	9	
1	1.00	-0.04	0.13	0.30	0.30	0.05	0.16	0.14	0.185 ± 0.009
2	-0.04	1.00	-0.25	0.49	0.41	0.08	0.22	0.18	0.340 ± 0.012
3	0.13	-0.25	1.00	0.05	0.33	0.04	0.18	0.15	0.596 ± 0.014
4	0.30	0.49	0.05	1.00	0.76	0.16	0.40	0.34	0.850 ± 0.023
6	0.30	0.41	0.33	0.76	1.00	-0.15	0.57	0.40	1.152 ± 0.026
7	0.05	0.08	0.04	0.16	-0.15	1.00	-0.52	-0.08	1.276 ± 0.035
8	0.16	0.22	0.18	0.40	0.57	-0.52	1.00	0.29	1.248 ± 0.059
9	0.14	0.18	0.15	0.34	0.40	-0.08	0.29	1.00	1.083 ± 0.042

5.6.2.3 Verification of decay-time efficiency using $B^+ \to J/\psi K^+$

$B^+ \to J/\psi K^+$ data sample obtained in Sec. 5.5.1 are used for verifying the method of extracting decay-time efficiency using control mode with a correction from simulation. With replacing B_s^0 by B^+ in Eq. (5-2), the decay-time efficiency of B^+ could be determined using B^0 data, B^0 simulation and B^+ simulated samples. The B^+ simulation is reweighed according to the B^+ p_{T}, rapidity and `nTracks` distributions in background subtracted B^+ data sample. The lifetime is fixed to PDG value 1.520 ps for the B^0 data sample, and the inputs of 1.519 ps and 1.639 ps for the B^0 and B^+ simulations, respectively. The decay-time distribution is shown in Fig. 5.26. The obtained efficiency ratio between B^0 and B^+ decays and observed efficiency for B^+ data are shown in Fig. 5.27. The efficiency ratio is not uniform in low decay-time region, since B^+ decay has only one bachelor hadron. The obtained spline parameters is fitted in an unbinned maximum likelihood fit to the *sWeighted* decay-time distribution of B^+ data sample. The fitted decay-width difference between the B^+ and B^0 mesons is $\Gamma_{B^+} - \Gamma_{B^0} = -0.0475 \pm 0.0005(\text{stat})\ \text{ps}^{-1}$, is well consistent with the PDG value of $-0.0474 \pm 0.0023\ \text{ps}^{-1}$ [58]. The decay-width difference and B^+ lifetime are further checked by splitting the data samples in four B meson bin, no bias are found.

5.6.3 Angular and $m_{\pi\pi}$

The selection and reconstruction efficiency is not uniform in $m_{\pi\pi}$ and three helicity angles. Using Eqs. (4-8) and (4-9) described in Sec. 4.6.3 with replacing KK by $\pi\pi$ in the equations, this efficiency is parametrised by a combination of Legendre and spherical

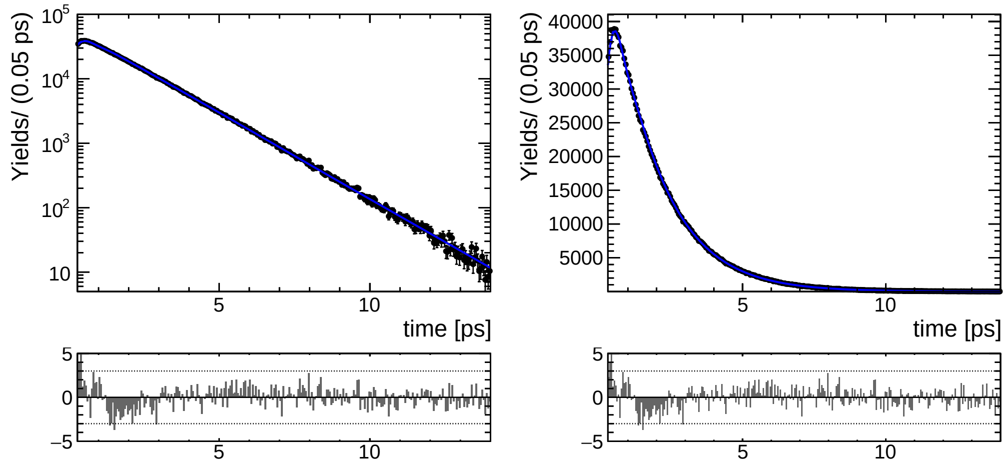

Figure 5.26 Decay-time distributions of B^+ candidate in data (points) and fit curve (blue line) in logarithm (left) and linear (right) scale.

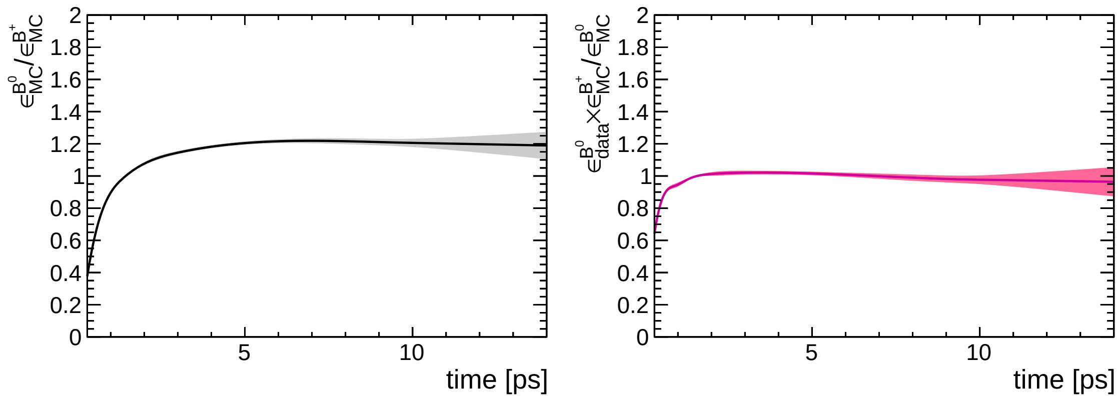

Figure 5.27 Fit results for (left) $\varepsilon_{sim}^{B^0}(t)/\varepsilon_{sim}^{B^+}(t)$, and (right) the decay-time acceptance derived for the B^+ data. The 1σ statistical uncertainty is shown by the area.

harmonic moments fitted with $B_s^0 \to J/\psi\pi^+\pi^-$ simulated sample. Table 5.16 lists the coefficients calculated using Eq. (4-9). The resulting one-dimensional projections are compared with simulated events, which includes phase space factor, as shown in Fig. 5.28. The modelling reproduces the simulated data very well. The efficiency is uniform within 4% for $\theta_{J/\psi}$ and 10% for χ, as shown in Fig 5.29, while $m_{\pi\pi}$ and $\cos\theta_{\pi\pi}$ variables show large efficiency variations and correlation. This loss of efficiency is mainly due to the $\chi^2_{\rm IP}$ requirements on hadrons. Candidates with $\cos\theta_{\pi\pi} = \pm 1$ and $m_{KK} \simeq 0.6 - 0.8$ GeV located at the region with minimum or maximum $m^2_{J/\psi\pi^+}$, as shown in Fig. 5.30. One of the pion in these events has very small momentum in the B_s^0 rest frame, thus the pion points to the PV , resulting in a very small $\chi^2_{\rm IP}$.

Table 5.16 Efficiency coefficients.

a	b	c	d	Coefficient	Error
0	0	0	0	1.000000	0.001603
0	0	0	1	0.139818	0.003476
0	0	0	2	0.152215	0.004666
0	0	0	3	−0.095417	0.005538
0	0	0	6	−0.043625	0.007436
0	0	0	8	−0.026165	0.008325
0	2	0	0	0.010998	0.001650
0	2	0	1	−0.023368	0.003656
0	2	2	0	0.028467	0.001163
0	2	2	1	0.026263	0.002587
0	4	0	0	0.006579	0.001634
0	4	0	1	−0.011402	0.003541
2	0	0	0	−0.275061	0.003519
2	0	0	1	0.308126	0.007975
2	0	0	2	0.145536	0.010994
2	0	0	3	−0.252047	0.013049
2	0	0	4	0.107741	0.014721
2	2	0	1	0.065041	0.008617
2	2	0	2	0.070008	0.012073
2	2	2	0	−0.017077	0.002560
2	2	2	1	−0.027993	0.005988
4	0	0	0	−0.062933	0.004601
4	0	0	1	0.085741	0.010138
4	0	0	3	−0.106464	0.016297
4	0	0	4	0.066716	0.018612
4	2	2	0	−0.010285	0.003165

5.7 Fit validation and results

5.7.1 Toy study

The fit procedure is validated by generating toy experiments according to the PDF used for fit. The dependence of angular acceptance as a function of decay time is checked by determined the angular and $m_{\pi\pi}$ efficiency coefficients in three bins of decay time ([0.3, 1] ps. [1,2] ps and [2,14] ps) in PHSP simulation which are used to generate three toy experiments. Figure. 5.31 shows the projections of obtained efficiency coefficients of two-dimensional $m_{\pi\pi}$ and $\cos\theta_{\pi\pi}$ in three decay-time bins. 500 signal toy experiments

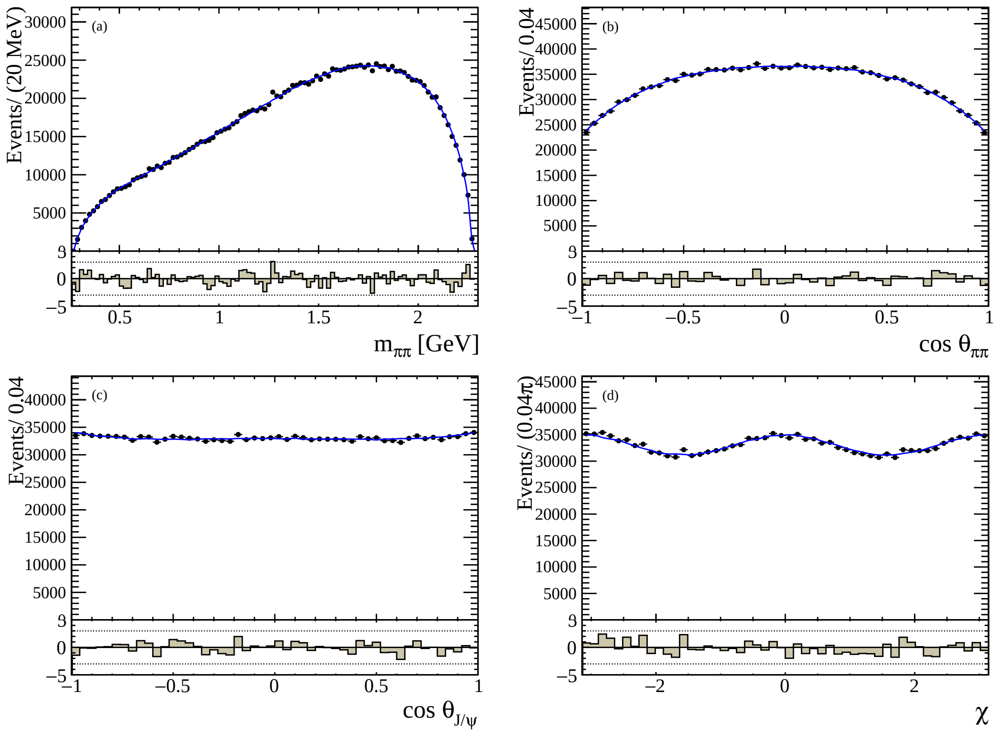

Figure 5.28 Projections of (a) $m_{\pi\pi}$, (b) $\cos\theta_{\pi\pi}$, (c) $\cos\theta_{J/\psi}$ and (d) χ from the phase space $B_s^0 \to J/\psi\pi^+\pi^-$ MC. The points with error bars are $B_s^0 \to J/\psi\pi^+\pi^-$ MC, the curves show the expectation from the efficiency model.

are generated with physics input parameters taken from the data fit results discussed Sec.5.7.3. The efficiencies $\varepsilon(m_{\pi\pi}, \Omega)$ and $\mathcal{E}_t(t)$ are determined using PHSP toy and toy with signal model but assuming $\Gamma_H = \Gamma_L$, respectively, same as that used for data fit. After generation, the samples are fitted with the same strategy as the nominal fit to extract the CP observables. Unbiased fit results on Γ_H, ϕ_s and λ are found, as shown in the pull distributions of toy fits in Fig. 5.32.

5.7.2 Fit to $B_s^0 \to J/\psi\,\pi^+\pi^-$ simulated samples

$B_s^0 \to J/\psi\pi^+\pi^-$ simulated sample is used to validate the fit procedure. The physics parameters obtained in the fit discussed in Sec. 5.7.3 are used to generate CP-violation included simulated sample . Each candidates in the PHSP $B_s^0 \to J/\psi\pi^+\pi^-$ simulation is assigned by a weight corresponding to the PDF ratio between CP-violation generation and the phase-space generation, by

$$r(\hat{t}, m_{KK}, \Omega, \mathfrak{q}) = R(\hat{t}, m_{KK}, \Omega, \mathfrak{q}|\eta = 0)/(P_B P_R(e^{-\hat{t}/\tau_{\rm L,MC}} + e^{-\hat{t}/\tau_{\rm H,MC}})), \tag{5-3}$$

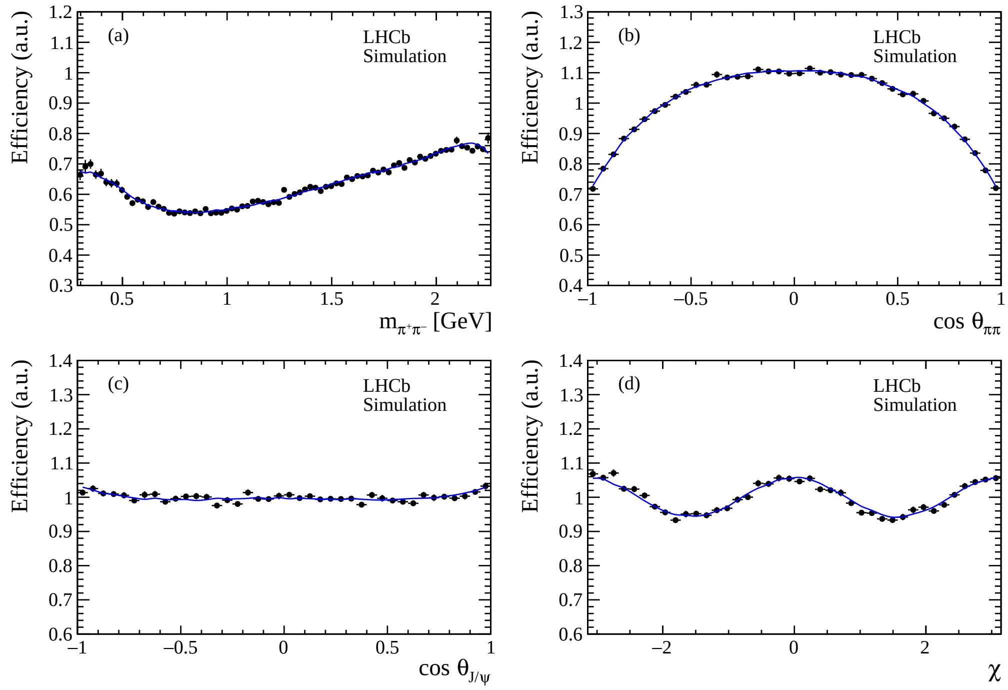

Figure 5.29 Overall efficiency for (a) $m_{\pi\pi}$, (b) $\cos\theta_{\pi\pi}$, (c) $\cos\theta_{J/\psi}$ and (d) χ . The points with error bars are $B_s^0 \to J/\psi\pi^+\pi^-$ MC, the curves show the expectation from the efficiency model.

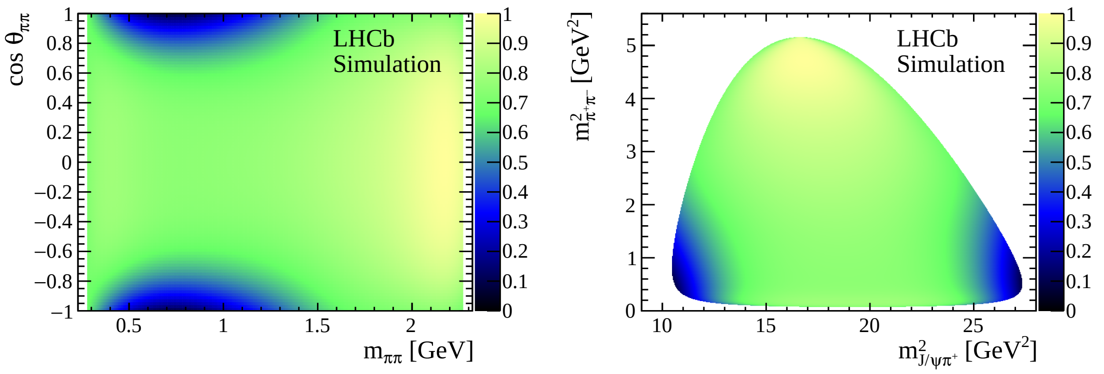

Figure 5.30 Overall efficiency for (left) m_{KK} vs $\cos\theta_{\pi\pi}$ and (right) $m^2_{J/\psi\pi^-}$ vs $m^2_{\pi^+\pi^-}$. The inefficiency is at kinematic boundary of $m^2_{J/\psi\pi^\pm}$.

where R is the PDF defined in Eq. (4-10), with $\hat{t}$ being the true decay time, and $\tau_{\rm L,MC} =$ 1.405 ps and $\tau_{\rm H,MC} = 1.661$ ps being the lifetimes of B_s^0 light and heavy mass eigenstates used in simulation, respectively. The efficiency parameters are obtained with the same procedure as that used for data, expect the reweighing procedure is not applied. The pull and statical uncertainties of the $\Gamma_H - \Gamma_{B^0}$, ϕ_s and $|\lambda|$ in the fits are given in Table 5.17. No obvious bias is seen for these three physics parameters.

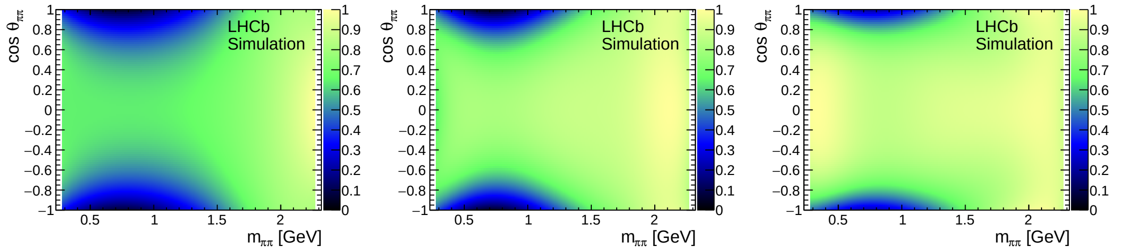

Figure 5.31 Efficiencies as a function of m_{KK} and $\cos\theta_{\pi\pi}$ for events in the decay time $t \in (0.3, 1)\,ps$ (left) $\in (1, 2)\,ps$ (middle) and $\in (2, 14)\,ps$ (right).

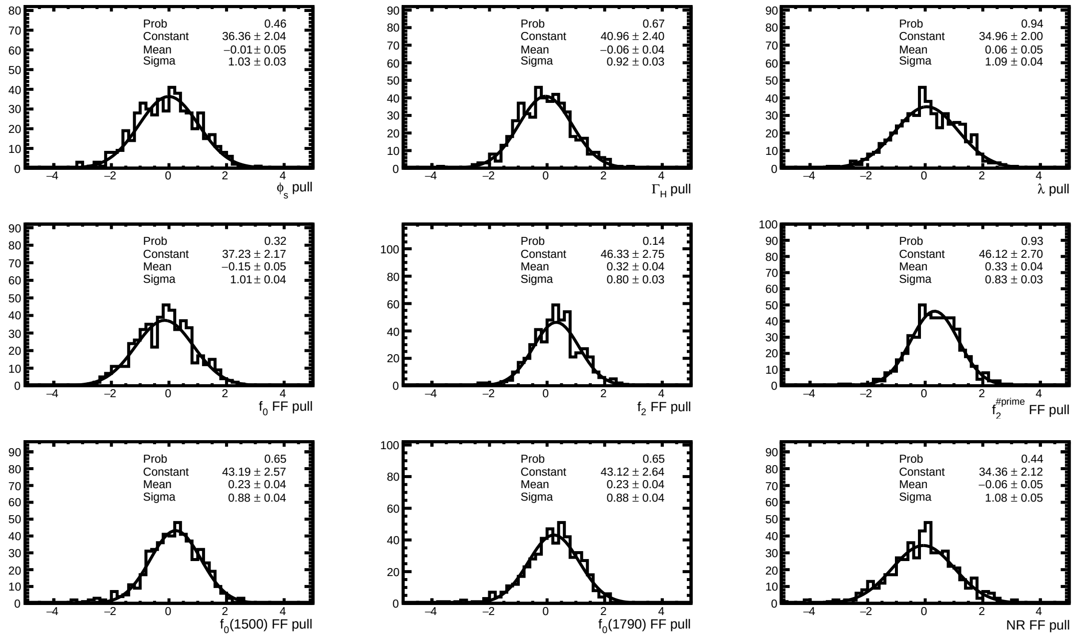

Figure 5.32 Pull distributions of fit variables from the toy samples.

Table 5.17 Pull and statistical uncertainty of the fit to the full MC.

Par.	Pull	σ (stat)
$\Gamma_H - \Gamma_{B^0}$	0.05	$0.0017\,ps^{-1}$
ϕ_s	0.28	0.012 rad
$\lvert\lambda\rvert$	0.69	0.012

5.7.3 Fit results

Five different resonance models are implemented and the one with largest $|-2\ln\mathcal{L}|$ are chosen as the default fit model. First, all the resonant and a non-resonant contributions listed in Table 5.1 are including in the fit model. Including $f_0(500)$ resonance in the fit only gives fit fraction of less than 0.1%, thus it is not included in the default model and considered as a systematic uncertainty in Sec. 5.8.1. The mass and width of most

Table 5.18 Likelihoods of various resonance model fits. Positive or negative interferences (Int) among the contributing resonances are indicated. The Solutions are indicated by #.

#	Resonance content	Int	$-2\ln L$
I	$f_0(980) + f_0(1500) + f_0(1790) + f_2(1270) + f_2'(1525)$+NR	−	−4850
II	$f_0(980) + f_0(1500) + f_0(1710) + f_2(1270) + f_2'(1525)$+NR	+	−4834
III	$f_0(980) + f_0(1500) + f_0(1790) + f_2(1270) + f_2'(1525)$+NR	+	−4830
IV	$f_0(980) + f_0(1500) + f_0(1790) + f_2(1270) + f_2'(1525)$	−	−4828
V	$f_0(980) + f_0(1500) + f_0(1710) + f_2(1270) + f_2'(1525)$	−	−4706

Table 5.19 Fit results for the CP-violating parameters for Solution I. The first uncertainties are statistical, and the second systematic. The last three columns show the statistical correlation coefficients for the three parameters.

	Fit result	Correlation		
Parameter		$\Gamma_H - \Gamma_{B^0}$	$\lvert\lambda\rvert$	ϕ_s
$\Gamma_H - \Gamma_{B^0}$ (ps^{-1})	$-0.050 \pm 0.004 \pm 0.004$	1.000	0.022	0.038
$\lvert\lambda\rvert$	$1.01^{+0.08}_{-0.06} \pm 0.03$	0.022	1.000	0.065
ϕ_s (rad)	$-0.057 \pm 0.060 \pm 0.011$	0.038	0.065	1.000

resonances are fixed to the central values listed in Table 5.1, except for the $f_0(980)$ and $f_0(1500)$ resonances whose parameters are varied in the fits. Comparing the results in Table 5.18, Solution I is taken as default fit model and Solution II is used for systematic studies.

The CP-violation for all the transversity states are assumed to be the same in fit. The central value of the physics parameters Δm_s and Γ_L are fixed to $\Delta m_s = 17.757 \pm 0.021$ ps^{-1} [58] and $\Gamma_L = 0.6995 \pm 0.0047$ ps^{-1} [134]. The resulting CP-violating parameters and their correlations are shown in Table 5.19 from default fit model. The fit fraction of each resonant contribution is listed in Table 5.20, comparing between Solutions I and II. The data is well modelled by the fit, as shown in Fig. 5.33 for the projections from the default fit. Projection of resonant components in $m_{\pi\pi}$ is shown in Fig. 5.34.

5.8 Systematic uncertainties

The systematic uncertainties for the physics parameters are summarised in Table 5.21. They are small compared to the statistical ones for these CP-violating parameters.

Table 5.20 Fit results of the resonant structure for both Solutions I and II. These results do not supersede those in Ref.[132] for the resonant fractions because no systematic uncertainties are quoted. The sum of fit fraction is not necessary 100% due to possible interferences between resonances with the same spin.

Component	Fit fractions (%)	Transversity fractions (%)		
		0	$\parallel$	$\perp$
Solution I				
$f_0(980)$	60.09 ± 1.48	100	–	–
$f_0(1500)$	8.88 ± 0.87	100	–	–
$f_0(1790)$	1.72 ± 0.29	100	–	–
$f_2(1270)$	3.24 ± 0.48	13 ± 3	37 ± 9	50 ± 10
$f_2'(1525)$	1.23 ± 0.86	40 ± 13	31 ± 14	29 ± 25
NR	2.64 ± 0.73	100	–	–
Solution II				
$f_0(980)$	93.05 ± 1.12	100	–	–
$f_0(1500)$	6.47 ± 0.41	100	–	–
$f_0(1710)$	0.74 ± 0.11	100	–	–
$f_2(1270)$	3.22 ± 0.44	17 ± 4	30 ± 8	53 ± 10
$f_2'(1525)$	1.44 ± 0.36	35 ± 8	31 ± 12	34 ± 17
NR	8.13 ± 0.79	100	–	–

5.8.1 Resonances modelling

The largest systematic uncertainty is from the resonances modelling, following options are used to evaluate sources of uncertainties:

- Allow the centrifugal barrier factors of default value 1.5 GeV $^{-1}$ for $\pi\pi$ resonances and 5.0 GeV $^{-1}$ for B_s^0 meson to vary from 0.5–2 times of the default values.
- Increasing the default angular momentum L_B for the D-wave resonances by 1 or 2. The lowest allowed value for L_B is used for the default fit.
- Replacing NR by $f_0(500)$,the difference between Solutions I and II are taken as systematics.
- Adding $\rho(770)$ contribution in the model. $\rho(770)$ fit fraction is found to be $(1.1 \pm 0.3)\%$ which is larger but consistent with the previous reported $(0.7 \pm 0.3)\%$[132]. This gives the largest systematic uncertainty for ϕ_s.

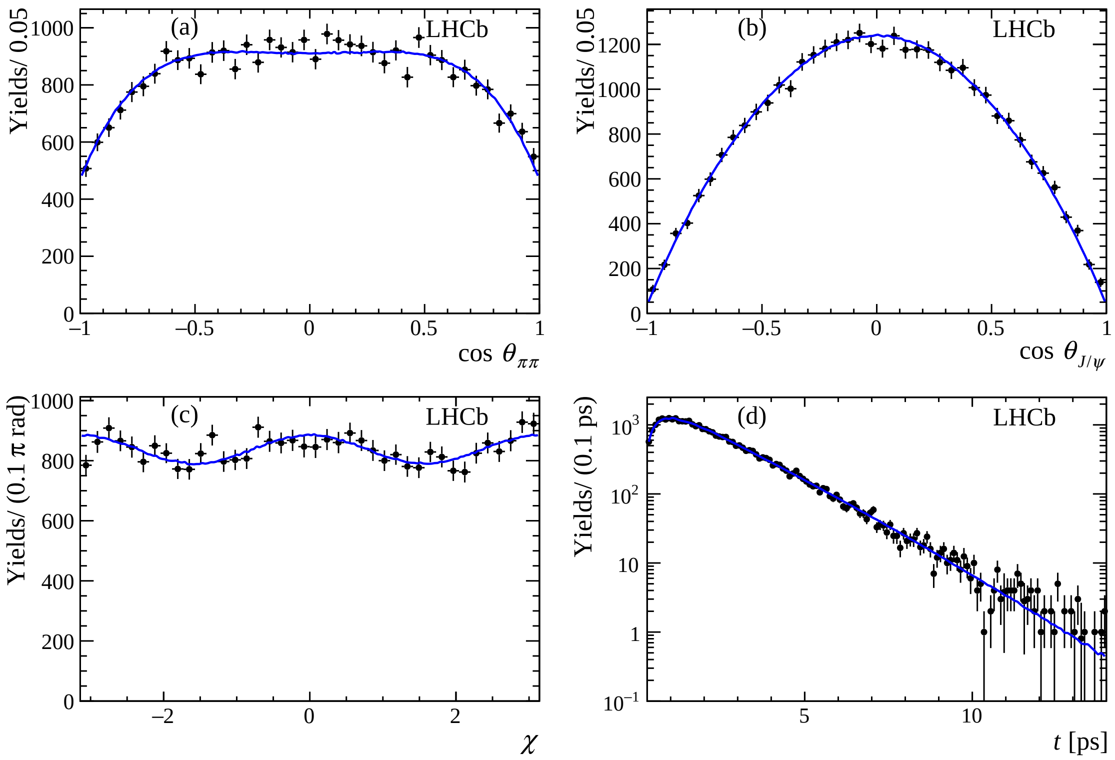

Figure 5.33 Projections of the angular and decay-time variables with the fit result overlaid. The points (black) show the data and the curves (blue) the fits.

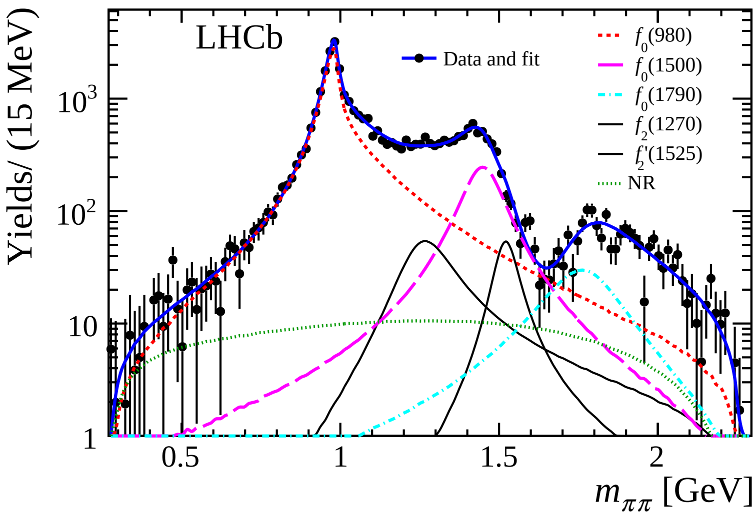

Figure 5.34 Data distribution of m_{KK} with the projection of the Solution I fit result overlaid. The data are described by the points (black) with error bars. The solid (blue) curve shows the overall fit.

The largest variation among the sources is taken as systematic uncertainty.

Table 5.21 Absolute systematic uncertainties for the physics parameters.

Source	$\Gamma_H - \Gamma_{B^0}$ [fs^{-1}]	$\lvert\lambda\rvert$ [$\times 10^{-3}$]	ϕ_s [mrad]
Decay-time acceptance	2.0	0.0	0.3
τ_{B^0}	0.2	0.5	0.0
Efficiency (m_{KK}, Ω)	0.2	0.1	0.0
Decay-time resolution width	0.0	4.3	4.0
Decay-time resolution mean	0.3	1.2	0.3
Background	3.0	2.7	0.6
Flavour tagging	0.0	2.2	2.3
Δm_s	0.3	4.6	2.5
Γ_L	0.3	0.4	0.4
B_c^+	0.5	-	-
Resonance parameters	0.6	1.9	0.8
Resonance modelling	0.5	28.9	9.0
Production asymmetry	0.3	0.6	3.4
Total	3.8	29.9	11.0

5.8.2 Resonant masses and widths

This systematic uncertainty is determined by varying the masses and widths of resonances used by the default model by $\pm 1\sigma$ of their uncertainty listed in Table 5.1 . All the sources are added in quadrature and taken as one uncertainty.

5.8.3 Efficiency of $m_{\pi\pi}$ and angles

Uncertainty due to the modelling of efficiency is estimated by repeating the fit to data sample with 300 times. Using efficiency parameters resampled each time according to the corresponding covariance matrix determined from simulation. The changes on the physics parameters for interest from the repeated fits with respect to the default one are a Gaussian distribution, whose width is taken as a systematic uncertainty.

5.8.4 Decay-time efficiency

Uncertainty due to the decay-time efficiency parametrisation is estimated using the same method in Sec. 5.8.3. The toy studies are used, the width of the Gaussian is take as the uncertainty due to this source, which is the largest contribution to the uncertainty of the decay width difference $\Gamma_H - \Gamma_{B^0}$.

5.8.5 B^0 lifetime

Uncertainty due to the B^0 lifetime is evaluated by varying the lifetime within ± 0.004 ps. The changes of the statistical uncertainties of each physics parameters between the nominal fit and the alternative fit is taken as the systematic uncertainties.

5.8.6 Decay-time resolution

The source includes 3% variation of the widths of Gaussian resolution functions, and varying the uncertainty for the mean value of Gaussians in the time resolution function. The former is obtained by Gaussian constraint on a scale factor for the widths by 1.00 ± 0.03. Since from the simulation study, the means of the resolution model obtained from calibration simulated sample and signal simulation are different by $(3.2\pm0.6)\times10^{-4}$, 5.4σ. Combination with statistical uncertainty, the total uncertainty on the mean is 3.4×10^{-4}, which is varied to to estimate the systematic uncertainty.

5.8.7 Background modelling

Two sources are considered in the background modelling: the decay-time distributions in background and the yield of background. The uncertainty due to the decay-time distribution is estimated by using WS data samples without decay-time difference correction for the background subtraction. The uncertainty of yield is evaluated by varying the background yield by 2.4%, corresponding to total uncertainty of combinatorial background and neglected physics background. The relative differences in the CP observables between alternative fit and default fit of the two sources are added in quadrature and taken as a source of systematic uncertainty.

5.8.8 Calibration of flavour tagging

Uncertainty due to the calibrated parameters are estimated by an alternative fit where the tagging parameters are Gaussian constrained by their total uncertainties. The difference on physics parameter of interest is taken as the systematic uncertainty.

5.8.9 Production asymmetry

The production asymmetry of B_s^0 is measured to be $(-0.65 \pm 2.88 \pm 0.59)\%$ in centre-mass-energy of 7 TeV and $(1.98 \pm 1.90 \pm 0.59)\%$ in 8 TeV, respectively[138]. No updated result for 13 TeV is available yet. In the default fit, $A_P = 0$ is used. An alternative fit with ±2% variation is performed. The difference on physics parameter of interest is taken as the systematic uncertainty.

5.8.10 Fix of Δm_s and Γ_L

The values of Δm_s and Γ_L are fixed in the default fit. An alternative fit with their value constrained by its error is performed. The increase of statistical uncertainty of the physics with respect to the default fit in quadrature is take as the systematic uncertainty.

5.8.11 B_c^+contribution

According to previous analysis[79], about 0.8% signal sample is expected from the decays of B_c^+ mesons. Neglecting the B_c^+ contribution leads to a bias of 0.0005 ps^{-1} for $\Gamma_H - \Gamma_{B^0}$, which is added as a systematic uncertainty. Other parameters are not affected.

5.9 Results

A time-dependent amplitude analysis is performed with $B_s^0 \to J/\psi\pi^+\pi^-$ decay using 1.9 fb^{-1} pp collisions data collected by LHCb in 2015-2016, the CP-violating parameters are determined to be

$$\begin{aligned}
\phi_s &= -0.057 \pm 0.060 \pm 0.011\,\text{rad},\\
|\lambda| &= 1.01^{0.08}_{0.06} \pm 0.03,\\
\Gamma_H - \Gamma_{B^0} &= -0.050 \pm 0.004 \pm 0.004\,\text{ps}^{-1},
\end{aligned}$$

which are consistent with the Run-I results from the same decay channel. The decay width of B_s^0 heavy mass eigenstate is first determined with this channel. Combined with the ϕ_s and $|\lambda|$ results obtained in $B_s^0 \to J/\psi\pi^+\pi^-$ decay using Run-I data gives

$$\begin{aligned}
\phi_s &= 0.002 \pm 0.044 \pm 0.012\,\text{rad},\\
|\lambda| &= 0.949 \pm 0.036 \pm 0.019
\end{aligned}$$

The results still have uncertainties greater than the SM prediction and are slightly more precise than the measurement using $B_s^0 \to J/\psi K^+K^-$ decays, based only on Run-I data, which has a precision of 0.049 rad[79].

Chapter 6 Summary and prospects

With the discovery of Higgs boson in 2012, the last piece of SM is found. However, SM itself is not a final theory, it fails to explain phenomena such as the non-zero masses of neutrinos, the dark matter and the observed matter-antimatter asymmetry in the universe. Verifying predictions based on the SM and searching for new particles beyond the SM will continuously help us improving and perfecting the current theory which is crucial for the development of particle physics.

Since the operation of LHC in 2010, a series of important b- and c-physics results have been reported by the LHCb experiment in $b \to J/\psi X$ decays. Experimentally, $J/\psi \to \mu^+\mu^-$ is often used in the event reconstruction. LHCb detector can efficiently reconstruct and precisely identify muon particles. It also has many stable muon triggers which are important for the J/ψ meson detection. J/ψ has a relatively narrow decay width, thus requiring selections on J/ψ mesons and μ particles will effectively suppressed the background.

In this dissertation, using pp collision data collected by the LHCb experiment, two categories of $b \to J/\psi X$ analyses, including searching for pentaquark states in $\Xi_b^- \to J/\psi \Lambda K^-$ decay and measurements of CP-violating phase ϕ_s in $B_s^0 \to J/\psi K^+K^-$ decays with K^+K^- mass above $\phi(1020)$ mass region and $B_s^0 \to J/\psi \pi^+\pi^-$ decays are performed. These measurements provide tests of the SM and good probes of NP scenarios.

In the first category of analyses, the decay $\Xi_b^- \to J/\psi \Lambda K^-$ is observed for the first time at a significance level of 24 Gaussian standard deviations using 3 fb^{-1} LHCb Run-I data. The data sample yields around 300 $\Xi_b^- \to J/\psi \Lambda K^-$ signal candidates. Taking into account the relative fragmentation fraction between Λ_b^0 and Ξ_b^-, the relative branching fraction of $\Xi_b^- \to J/\psi \Lambda K^-$ relative to $\Lambda_b^0 \to J/\psi \Lambda$ decays is determined as

$$R \equiv \frac{f_{\Xi_b^-}}{f_{\Lambda_b^0}} \frac{B(\Xi_b^- \to J/\psi \Lambda K^-)}{B(\Lambda_b^0 \to J/\psi \Lambda)} = 0.0419 \pm 0.0029(\text{stat.}) \pm 0.0015(\text{syst.}).$$

The mass difference between Λ_b^0 and Ξ_b^- baryons is also measured

$$\delta M = 178.08 \pm 0.47(\text{stat.}) \pm 0.16(\text{syst.}) \text{ MeV},$$

which is one of the best measurements of this parameter in the world.

According to theoretical prediction, a strangeness hidden-charm pentaquark state $udsc\bar{c}$ could be observed in $\Xi_b^- \to J/\psi \Lambda K^-$ decay as a $J/\psi\Lambda$ state. However, with selections that removes $\Xi(1690)$ and $\Xi(1820)$ events applied, only about 55 signal candidates left. The statistics of the sample is too small to perform a dedicate amplitude analysis for the extraction of pentaquark states.

In the second category of analyses, The CP-violating phase ϕ_s is determined with two decay channels. Using 3 fb^{-1} LHCb Run-I data, the phase ϕ_s is first time measured in $B_s^0 \to J/\psi K^+K^-$ decays with $m(K^+K^-)$ above the $\phi(1020)$ mass region. Different from the 'golden channel' $B_s^0 \to J/\psi\phi$, a rich resonance spectrum was found in this sample. Significant contributions from the $f_2^{'}(1525)$ resonance and nonresonant S-wave made the CP violation studies possible . The CP-violating parameters obtained are

$$\begin{aligned}
\phi_s &= 0.119 \pm 0.107(\text{stat.}) \pm 0.034(\text{syst.})\,\text{rad},\\
|\lambda| &= 0.994 \pm 0.018(\text{stat.}) \pm 0.006(\text{syst.}),\\
\Gamma_s &= 0.650 \pm 0.006(\text{stat.}) \pm 0.004(\text{syst.})\,\text{ps}^{-1},\\
\Delta\Gamma_s &= 0.066 \pm 0.018(\text{stat.}) \pm 0.010(\text{syst.})\,\text{ps}^{-1}.
\end{aligned}$$

which are consistent with the results from $B_s^0 \to J/\psi\phi$ decays.

After LHC Run-I data-taking period, a series of measurements of ϕ_s in B_s^0 decays has been performed at LHCb. The combined result is consistent with the SM calculation but there still remains about 10% space for NP contribution. LHCb has collected 1.9 fb^{-1} pp collision data in the first two years of Run-II operation time. Taking advantages of increasing collision energy and B_s^0 production cross-section, the phase ϕ_s has been first determined with 13 TeV dataset in $B_s^0 \to J/\psi\pi^+\pi^-$ decays. The CP-violating parameters obtained are

$$\begin{aligned}
\phi_s &= -0.057 \pm 0.060(\text{stat.}) \pm 0.011(\text{syst.})\,\text{rad},\\
|\lambda| &= 1.01^{+0.08}_{-0.06}(\text{stat.}) \pm 0.03(\text{syst.}),\\
\Gamma_H - \Gamma_{B^0} &= -0.050 \pm 0.004(\text{stat.}) \pm 0.004(\text{syst.})\,\text{ps}^{-1},
\end{aligned}$$

which are consistent with Run-I results in the same decay channel.

These two results are both consistent with the calculation from SM prediction, however it does not exclude the possibility of NP contributions.

LHCb has collected 9 fb^{-1} pp collision data until the end of Run-II data-taking period. With higher collision energy, the production of b-hadrons are expected to increased approximately by a factor two compared to Run-I. After Run-II, a two-year shutdown (2019-2020) of LHC will allow a major upgrade of several LHCb detectors and LHCb will continue data taking and target to achieve an integrated luminosity of at least 50 fb^{-1} by the end of 2029. As a result, both $\Xi_b^- \to J/\psi \Lambda K^-$ analysis and ϕ_s measurements will benefit from it. The signal yields of $\Xi_b^- \to J/\psi \Lambda K^-$ decay might increased by a factor of 40, which provide the chance to perform a full amplitude analysis for new pentaquark states search. Similarly, the statistical error on all the CP-observables in $B_s^0 \to J/\psi K^+ K^-$ and $B_s^0 \to J/\psi \pi^+ \pi^-$ decays could be reduced by a factor of $1/\sqrt{40}$. Moreover, given the good calorimeter performance after LHCb upgrade, channels that has not been exploited could be studied in the future, these includes $B_s^0 \to J/\psi (\to e^+ e^-)\phi$, $B_s^0 \to J/\psi \eta' (\to \rho^0 \gamma, \eta \pi^+ \pi^-, \pi^+ \pi^- \pi^0)$, etc., and these channels can be used to further reduce the uncertainty of the phase ϕ_s.

Bibliography

[1] Salam A. Weak and electromagnetic interactions. Elementary particle theory, 1968, 367.

[2] Weinberg S. A model of leptons. Phys. Rev. Lett., 1967, 19(21):1264.

[3] Glashow S L. Partial Symmetries of Weak Interactions. Nucl. Phys., 1961, 22:579-588.

[4] Glashow S L, Iliopoulos J, Maiani L. Weak Interactions with Lepton-Hadron Symmetry. Phys. Rev., 1970, D2:1285-1292.

[5] Gell-Mann M. A schematic model of baryons and mesons. Physics Letters, 1964, 8(3):214-215.

[6] Zweig G. An SU_3 model for strong interaction symmetry and its breaking; Version 1: number cern-th-401. Geneva: CERN, 1964. https://cds.cern.ch/record/352337.

[7] Branco G C, Lavoura L, Silva J P. CP Violation. Int. Ser. Monogr. Phys., 1999, 103:1-536.

[8] Bigi I I, Sanda A. CP violation. Camb. Monogr. Part. Phys. Nucl. Phys. Cosmol., 2000, 9:1-382.

[9] Chatrchyan S, Khachatryan V, Sirunyan A M, et al. Observation of a new boson at a mass of 125 gev with the cms experiment at the lhc. Phys. Lett., 2012, B716(1):30-61.

[10] Aad G, Abajyan T, Abbott B, et al. Observation of a new particle in the search for the standard model higgs boson with the atlas detector at the lhc. Phys. Lett., 2012, B716(1):1-29.

[11] Gell-Mann M. A Schematic Model of Baryons and Mesons. Phys. Lett., 1964, 8:214-215.

[12] Fritzsch H, Gell-Mann M, Leutwyler H. Advantages of the Color Octet Gluon Picture. Phys. Lett., 1973, B47:365-368.

[13] Gross D J, Wilczek F. Ultraviolet Behavior of Nonabelian Gauge Theories. Phys. Rev. Lett., 1973, 30:1343-1346.

[14] Politzer H D. Reliable Perturbative Results for Strong Interactions? Phys. Rev. Lett., 1973, 30: 1346-1349.

[15] Jaffe R L. Multi-Quark Hadrons. 1. The Phenomenology of (2 Quark 2 anti-Quark) Mesons. Phys. Rev., 1977, D15:267.

[16] Jaffe R L. Multi-Quark Hadrons. 2. Methods. Phys. Rev., 1977, D15:281.

[17] Hogaasen H, Sorba P. The Systematics of Possibly Narrow Quark States with Baryon Number One. Nucl. Phys., 1978, B145:119-140.

[18] Strottman D. Multi - Quark Baryons and the MIT Bag Model. Phys. Rev., 1979, D20:748-767.

[19] He Q, et al. Confirmation of the $Y(4260)$ resonance production in ISR. Phys. Rev., 2006, D74: 091104.

[20] Xiao T, Dobbs S, Tomaradze A, et al. Observation of the Charged Hadron $Z_c^{\pm}(3900)$ and Evidence for the Neutral $Z_c^0(3900)$ in $e^+e^- \to \pi\pi J/\psi$ at $\sqrt{s} = 4170$ MeV. Phys. Lett., 2013, B727:366-370.

[21] Aubert B, et al. Observation of a broad structure in the $\pi^+\pi^- J/\psi$ mass spectrum around 4.26 GeV/c^2. Phys. Rev. Lett., 2005, 95:142001.

[22] Choi S K, et al. Observation of a narrow charmonium - like state in exclusive $B^{\pm} \to K^{\pm}\pi^+\pi^- J/\psi$ decays. Phys. Rev. Lett., 2003, 91:262001.

[23] Acosta D, et al. Observation of the narrow state $X(3872) \to J/\psi\pi^+\pi^-$ in $\bar{p}p$ collisions at $\sqrt{s} = 1.96$ TeV. Phys. Rev. Lett., 2004, 93:072001.

[24] Abazov V M, et al. Observation and properties of the $X(3872)$ decaying to $J/\psi\pi^+\pi^-$ in $p\bar{p}$ collisions at $\sqrt{s} = 1.96$ TeV. Phys. Rev. Lett., 2004, 93:162002.

[25] Aaltonen T, et al. Evidence for a Narrow Near-Threshold Structure in the $J/\psi\phi$ Mass Spectrum in $B^+ \to J/\psi\phi K^+$ Decays. Phys. Rev. Lett., 2009, 102:242002.

[26] Ablikim M, et al. Observation of a charged charmonium like structure in $e^+e^- \to \pi^+\pi^- J/\psi$ at $\sqrt{s}$=4.26 GeV. Phys.Rev.Lett., 2013, 110:252001.

[27] Aaij R, et al. Determination of the $X(3872)$ meson quantum numbers. Phys. Rev. Lett., 2013, 110:222001.

[28] Chatrchyan S, et al. Measurement of the $X(3872)$ Production Cross Section Via Decays to $J/\psi\pi^+\pi^-$ in pp collisions at $\sqrt{s} = 7$ TeV. JHEP, 2013, 04:154.

[29] Chatrchyan S, et al. Observation of a peaking structure in the $J/\psi\phi$ mass spectrum from $B^\pm \to J/\psi\phi K^\pm$ decays. Phys. Lett., 2014, B734:261-281.

[30] Nakano T, et al. Evidence for a narrow S = +1 baryon resonance in photoproduction from the neutron. Phys. Rev. Lett., 2003, 91:012002.

[31] Hicks K H. On the conundrum of the pentaquark. Eur. Phys. J., 2012, H37:1-31.

[32] Aaij R, et al. Observation of $J/\psi\, p$ resonances consistent with pentaquark states in $\Lambda_b^0 \to J/\psi\, pK^-$ decays. Phys. Rev. Lett., 2015, 115:072001.

[33] Aaij R, et al. Study of the productions of Λ_b^0 and $\overline{B}^0$ hadrons in pp collisions and first measurement of the $\Lambda_b^0 \to J/\psi\, pK^-$ branching fraction. Chin. Phys. C, 2016, 40:011001.

[34] Karliner M, Rosner J L. New Exotic Meson and Baryon Resonances from Doubly-Heavy Hadronic Molecules. Phys. Rev. Lett., 2015, 115(12):122001.

[35] Chen R, Liu X, Li X Q, et al. Identifying exotic hidden-charm pentaquarks. Phys. Rev. Lett., 2015, 115(13):132002.

[36] Roca L, Nieves J, Oset E. LHCb pentaquark as a $\bar{D}^*\Sigma_c - \bar{D}^*\Sigma_c^*$ molecular state. Phys. Rev., 2015, D92(9):094003.

[37] He J. $\bar{D}\Sigma_c^*$ and $\bar{D}^*\Sigma_c$ interactions and the LHCb hidden-charmed pentaquarks. Phys. Lett., 2016, B753:547-551.

[38] Meißner U G, Oller J A. Testing the $\chi_{c1}\, p$ composite nature of the $P_c(4450)$. Phys. Lett., 2015, B751:59-62.

[39] Chen H X, Chen W, Liu X, et al. Towards exotic hidden-charm pentaquarks in QCD. Phys. Rev. Lett., 2015, 115(17):172001.

[40] Eides M I, Petrov V Yu, Polyakov M V. Narrow Nucleon-$\psi(2S)$ Bound State and LHCb Pentaquarks. Phys. Rev., 2016, D93(5):054039.

[41] Shimizu Y, Suenaga D, Harada M. Coupled channel analysis of molecule picture of $P_c(4380)$. Phys. Rev., 2016, D93(11):114003.

[42] Ortega P G, Entem D R, Fernández F. LHCb pentaquarks in constituent quark models. Phys. Lett., 2017, B764:207-211.

[43] Chen H X, Cui E L, Chen W, et al. QCD sum rule study of hidden-charm pentaquarks. Eur. Phys. J., 2016, C76(10):572.

[44] Huang H, Deng C, Ping J, et al. Possible pentaquarks with heavy quarks. Eur. Phys. J., 2016, C76(11):624.

[45] Maiani L, Polosa A D, Riquer V. The New Pentaquarks in the Diquark Model. Phys. Lett., 2015, B749:289-291.

[46] Wang Z G, Huang T. Analysis of the $\frac{1}{2}^{\pm}$ pentaquark states in the diquark model with QCD sum rules. Eur. Phys. J., 2016, C76(1):43.

[47] Wang Z G. Analysis of $P_c(4380)$ and $P_c(4450)$ as pentaquark states in the diquark model with QCD sum rules. Eur. Phys. J., 2016, C76(2):70.

[48] Lebed R F. The Pentaquark Candidates in the Dynamical Diquark Picture. Phys. Lett., 2015, B749:454-457.

[49] Lebed R F. Do the P_c^+ pentaquarks have strange siblings? Phys. Rev., 2015, D92(11):114030.

[50] Anisovich V V, Matveev M A, Nyiri J, et al. Nonstrange and strange pentaquarks with hidden charm. Int. J. Mod. Phys., 2015, A30(32):1550190.

[51] Zhu R, Qiao C F. Pentaquark states in a diquark–triquark model. Phys. Lett., 2016, B756: 259-264.

[52] Guo F K, Meißner U G, Wang W, et al. How to reveal the exotic nature of the $\mathrm{P}_c(4450)$. Phys. Rev., 2015, D92(7):071502.

[53] Liu X H, Wang Q, Zhao Q. Understanding the newly observed heavy pentaquark candidates. Phys. Lett., 2016, B757:231-236.

[54] Liu X H, Oka M. Understanding the nature of heavy pentaquarks and searching for them in pion-induced reactions. Nucl. Phys., 2016, A954:352-364.

[55] Aaij R, et al. Observation of a narrow $P_c(4312)^+$ state, and of two-peak structure of the $P_c(4450)^+$. Phys. Rev. Lett., 2019, 122:222001.

[56] Cabibbo N. Unitary Symmetry and Leptonic Decays. Phys. Rev. Lett., 1963, 10:531-533.

[57] Kobayashi M, Maskawa T. *CP* Violation in the renormalizable theory of weak Interaction. Prog.Theor.Phys., 1973, 49:652-657.

[58] Tanabashi M, et al. Review of Particle Physics. Phys. Rev., 2018, D98(3):030001.

[59] Wolfenstein L. Parametrization of the Kobayashi-Maskawa Matrix. Phys. Rev. Lett., 1983, 51: 1945.

[60] Charles J, et al. Current status of the Standard Model CKM fit and constraints on $\Delta F = 2$ new physics. Phys. Rev., 2015, D91:073007.

[61] Jarlskog C. Commutator of the Quark Mass Matrices in the Standard Electroweak Model and a Measure of Maximal CP Violation. Phys. Rev. Lett., 1985, 55:1039.

[62] Sakharov A D. Violation of CP Invariance, C asymmetry, and baryon asymmetry of the universe. Pisma Zh. Eksp. Teor. Fiz., 1967, 5:32-35.

[63] Abe F, et al. Observation of the B_c meson in $p\bar{p}$ collisions at $\sqrt{s} = 1.8\,\mathrm{TeV}$. Phys. Rev. Lett., 1998, 81:2432-2437.

[64] Abe F, et al. Observation of B_c mesons in $p\bar{p}$ collisions at $\sqrt{s} = 1.8$ TeV. Phys. Rev., 1998, D58:112004.

[65] Aubert B, et al. Observation of CP violation in the B^0 meson system. Phys. Rev. Lett., 2001, 87:091801.

[66] Abe K, et al. Observation of large CP violation in the neutral B meson system. Phys. Rev. Lett., 2001, 87:091802.

[67] Aaltonen T, et al. First Flavor-Tagged Determination of Bounds on Mixing-Induced CP Violation in $B_s^0 \to J/\psi\phi$ Decays. Phys. Rev. Lett., 2008, 100:161802.

[68] Abazov V M, et al. Measurement of B_s^0 mixing parameters from the flavor-tagged decay $B_s^0 \to J/\psi\phi$. Phys. Rev. Lett., 2008, 101:241801.

[69] Alves Jr. A A, et al. The LHCb detector at the LHC. JINST, 2008, 3(LHCb-DP-2008-001): S08005.

[70] Alves Jr. A A, et al. Performance of the LHCb muon system. JINST, 2013, 8:P02022.

[71] Aaij R, et al. Measurement of the track reconstruction efficiency at LHCb. JINST, 2015, 10: P02007.

[72] Aaij R, et al. LHCb detector performance. Int. J. Mod. Phys., 2015, A30:1530022.

[73] Aaij R, et al. First observation of the decay $B_c^+ \to J/\psi\pi^+\pi^-\pi^+$. Phys. Rev. Lett., 2012, 108: 251802.

[74] Aaij R, et al. Observation of $B_c^+ \to J/\psi D_s^+$ and $B_c^+ \to J/\psi D_s^{*+}$ decays. Phys. Rev., 2013, D87 (11):112012.

[75] Aaij R, et al. First observation of the decay $B_c^+ \to J/\psi K^+$. JHEP, 2013, 09:075.

[76] Aaij R, et al. Observation of the decay $B_c \to J/\psi K^+K^-\pi^+$. JHEP, 2013, 11:094.

[77] Aaij R, et al. Measurement of CP violation in $B^0 \to J/\psi\ K_S^0$ decays. Phys. Rev. Lett., 2015, 115: 031601.

[78] Aaij R, et al. Measurement of CP violation in $B^0 \to J/\psi\ K_S^0$ and $B^0 \to \psi(2S)K_S^0$ decays. JHEP, 2017, 11:170.

[79] Aaij R, et al. Precision measurement of CP violation in $B_s^0 \to J/\psi\ K^+K^-$ decays. Phys. Rev. Lett., 2015, 114:041801.

[80] Aaij R, et al. Measurement of the CP-violating phase ϕ_s in $\overline{B}_s^0 \to J/\psi\ \pi^+\pi^-$ decays. Phys. Lett., 2014, B736:186.

[81] Alves Jr. A A, et al. The LHCb detector at the LHC. JINST, 2008, 3:S08005.

[82] Evans L, Bryant P. LHC machine. JINST, 2008, 3:S08001.

[83] Aad G, et al. The ATLAS experiment at the CERN large hadron collider. JINST, 2008, 3: S08003.

[84] Chatrchyan S, et al. The CMS experiment at the CERN LHC. JINST, 2008, 3:S08004.

[85] Aamodt K, et al. The ALICE experiment at the CERN LHC. JINST, 2008, 3:S08002.

[86] CERN. The cern accelerator complex. [Accessed October 27, 2019]. http://cds.cern.ch/record /2636343.

[87] collaboration L. Lhcb integrated luminosity. https://lbgroups.cern.ch/online/OperationsPlots/in dex.htm.

[88] Aaij R, et al. Measurement of the b-quark production cross-section in 7 and 13 TeV pp collisions. Phys. Rev. Lett., 2017, 118:052002.

[89] Sjöstrand T, Mrenna S, Skands P. PYTHIA 6.4 physics and manual. JHEP, 2006, 05:026.

[90] Sjöstrand T, Mrenna S, Skands P. A brief introduction to PYTHIA 8.1. Comput.Phys.Commun., 2008, 178:852-867.

[91] Elsässer C. $\bar{b}b$ production angle plots. [2019-05-27]. https://lhcb.web.cern.ch/lhcb/speakersbureau/html/bb_ProductionAngles.html.

[92] Alves Jr. A, et al. The LHCb detector at the LHC. JINST, 2008, 3:S08005.

[93] Aaij R, et al. Performance of the LHCb Vertex Locator. JINST, 2014, 9:P09007.

[94] Arink R, et al. Performance of the LHCb Outer Tracker. JINST, 2014, 9:P01002.

[95] Aaij R, et al. Design and performance of the LHCb trigger and full real-time reconstruction in Run 2 of the LHC. JINST, 2019, 14(04):P04013.

[96] Belyaev I, et al. Handling of the generation of primary events in Gauss, the LHCb simulation framework. J. Phys. Conf. Ser., 2011, 331:032047.

[97] Lange D J. The EvtGen particle decay simulation package. Nucl. Instrum. Meth., 2001, A462: 152-155.

[98] Golonka P, Was Z. PHOTOS Monte Carlo: A precision tool for QED corrections in Z and W decays. Eur.Phys.J., 2006, C45:97-107.

[99] Allison J, Amako K, Apostolakis J, et al. Geant4 developments and applications. IEEE Trans.Nucl.Sci., 2006, 53:270.

[100] Aaij R, et al. Opposite-side flavour tagging of B mesons at the LHCb experiment. Eur. Phys. J., 2012, C72:2022.

[101] Aaij R, et al. A new algorithm for identifying the flavour of B_s^0 mesons at LHCb. JINST, 2016, 11:P05010.

[102] Aaij R, et al. New algorithms for identifying the flavour of B^0 mesons using pions and protons. Eur. Phys. J., 2017, C77:238.

[103] Chen H X, Geng L S, Liang W H, et al. Looking for a hidden-charm pentaquark state with strangeness S=−1 from Ξ_b^- decay into $J/\psi\, K^-\Lambda$. Phys. Rev., 2016, C93:065203.

[104] Breiman L, Friedman J H, Olshen R A, et al. Classification and regression trees. Belmont, California, USA: Wadsworth international group, 1984

[105] Adinolfi M, et al. Performance of the LHCb RICH detector at the LHC. Eur. Phys. J., 2013, C73:2431.

[106] Hulsbergen W D. Decay chain fitting with a Kalman filter. Nucl.Instrum.Meth., 2005, A552: 566-575.

[107] Gligorov V V, Williams M. Efficient, reliable and fast high-level triggering using a bonsai boosted decision tree. JINST, 2013, 8:P02013.

[108] Anderlini L, et al. The pidcalib package: number lhcb-pub-2016-021. [S.l.: s.n.].

[109] Martínez Santos D, Dupertuis F. Mass distributions marginalized over per-event errors. Nucl.Instrum.Meth., 2014, A764:150-155.

[110] Cranmer K S. Kernel estimation in high-energy physics. Comput.Phys.Commun., 2001, 136: 198-207.

[111] Verkerke W, Kirkby D P. The RooFit toolkit for data modeling. eConf, 2003, C0303241: MOLT007.

[112] Skwarnicki T. A study of the radiative cascade transitions between the Upsilon-prime and Upsilon resonances. [S.l.]: Institute of Nuclear Physics, Krakow, 1986.

[113] Correcting for the tracking efficiency in your MC.

[114] Aaij R, et al. Precision measurement of the ratio of the Λ_b^0 to $\overline{B}^0$ lifetimes. Phys. Lett., 2014, B734:122.

[115] Aaij R, et al. Precision measurement of the mass and lifetime of the Ξ_b^- baryon. Phys. Rev. Lett., 2014, 113:242002.

[116] Aaij R, et al. Precision measurement of D meson mass differences. JHEP, 2013, 06:065.

[117] Charles J, Deschamps O, Descotes-Genon S, et al. Predictions of selected flavour observables within the Standard Model. Phys. Rev., 2011, D84:033005.

[118] Buras A. Flavour theory: 2009. PoS EPS-HEP2009, 2009, 024.

[119] Chiang C W, Datta A, Duraisamy M, et al. New Physics in B0(s) —> J/psi phi: A General Analysis. JHEP, 2010, 04:031.

[120] Aaij R, et al. Amplitude analysis and branching fraction measurement of $\overline{B}_s^0 \to J/\psi\, K^+K^-$. Phys. Rev., 2013, D87:072004.

[121] Zhang L, Stone S. Time-dependent Dalitz-plot formalism for $B_q^0 \to J/\psi h^+h^-$. Phys.Lett., 2013, B719:383-387.

[122] Aaij R, et al. Measurement of the CP asymmetry in B_s^0–$\overline{B}_s^0$ mixing. Phys. Rev. Lett., 2016, 117: 061803.

[123] Aaij R, et al. Measurement of CP violation and the B_s^0 meson decay width difference with $B_s^0 \to J/\psi K^+K^-$ and $B_s^0 \to J/\psi\pi^+\pi^-$ decays. Phys.Rev., 2013, D87:112010.

[124] Pivk M, Le Diberder F R. sPlot: A statistical tool to unfold data distributions. Nucl.Instrum.Meth., 2005, A555:356-369.

[125] Xie Y. sfit: a method for background subtraction in maximum likelihood fit. arXiv preprint, 2009.

[126] Shen C P, et al. Observation of the $\phi(1680)$ and the $y(2175)$ in $e^+e^- \to \phi\pi^+\pi^-$. Phys. Rev. D, 2009, 80:031101.

[127] Abe K, et al. Measurement of k+ k- production in two-photon collisions in the resonant-mass region. Eur. Phys. J., 2003, C32(3):323-336.

[128] Aaij R, et al. Measurements of the B^+, B^0, B_s^0 meson and Λ_b^0 baryon lifetimes. JHEP, 2014, 04: 114.

[129] Aaij R, et al. Observation of the decay $\overline{B}_s^0 \to \psi(2S)K^+\pi^-$. Phys. Lett., 2015, B747:484.

[130] Aaij R, et al. Measurement of the $\overline{B}^0$–B^0 and $\overline{B}_s^0$–B_s^0 production asymmetries in pp collisions at $\sqrt{s}$ =7 TeV. Phys. Lett., 2014, B739:218.

[131] Aaij R, et al. Observation of the decay $B_c^+ \to B_s^0\pi^+$. Phys. Rev. Lett., 2013, 111:181801.

[132] Aaij R, et al. Measurement of resonant and CP components in $\overline{B}_s^0 \to J/\psi\,\pi^+\pi^-$ decays. Phys. Rev., 2014, D89:092006.

[133] Aaij R, et al. Analysis of the resonant components in $\overline{B}^0 \to J/\psi\,\pi^+\pi^-$. Phys. Rev., 2013, D87: 052001.

[134] Aaij R, et al. Resonances and CP-violation in B_s^0 and $\overline{B}_s^0 \to J/\psi\, K^+K^-$ decays in the mass region above the $\phi(1020)$. JHEP, 2017, 08:037.

[135] Ablikim M, et al. Resonances in $J/\psi \to \phi\pi^+\pi^-$ and ϕK^+K^-. Phys. Lett., 2005, B607:243.

[136] Stevens J, Williams M. uBoost: A boosting method for producing uniform selection efficiencies from multivariate classifiers. JINST, 2013, 8:P12013.

[137] Karbach T M, Raven G, Schiller M. Decay time integrals in neutral meson mixing and their efficient evaluation. 2014.

[138] Aaij R, et al. Measurement of B^0, B_s^0, B^+ and Λ_b^0 production asymmetries in 7 and 8 TeV proton-proton collisions. Phys. Lett., 2017, B774:139.

Acknowledgments

感谢我的导师陈少敏老师和张黎明老师对我的悉心指导，他们对待工作认真负责，对待生活积极向上的态度，深深地影响了我。尤其需要感谢张黎明老师，在我科研学习遇到困难时，耐心指导帮助我。他们的言传身教将使我终身受益。同时我想要感谢高原宁老师，是他让我有机会，可以开始这段粒子物理的探索旅程。

感谢实验室的杨振伟老师，朱相雷老师，王$\boxed{\mathrm{F}}$老师，续本达老师一直以来对我的关心，指导与热情帮助。以及高能物理研究中心的同学们，和你们一起的学习和讨论的时光，使我的博士生涯变得丰富多彩。

感谢我在巴黎六大 LPNHE 实验室交换期间的指导老师 Eli Ben-Haim 和 Mattew Charles，及 LPNHE 实验室的 ATLAS 和 LHCb 实验的同事，让我在巴黎一年的时光格外精彩。

最后，感谢我的家人一直陪伴在我的身边，你们的支持一直是我前进的动力。

声 明

本人郑重声明：所呈交的学位论文，是本人在导师指导下，独立进行研究工作所取得的成果。尽我所知，除文中已经注明引用的内容外，本学位论文的研究成果不包含任何他人享有著作权的内容。对本论文所涉及的研究工作做出贡献的其他个人和集体，均已在文中以明确方式标明。

签 名：刘宇来 日 期：2019.12.13

Appendix A Time-dependent amplitude analysis

The main idea of this method is to simultaneously measure the *CP*-even and *CP* odd decay amplitude for different h^+h^- (h denotes K or π) resonance regardless of their final state angular momentum in the $B_s^0 \to J/\psi\, h^+h^-$ decays.

The decay amplitude is expressed as a function of the h^+h^- invariant mass m_{hh} and the three angular variables $\Omega \equiv (\cos\theta_h, \cos\theta_l, \chi)$, defined in the helicity basis, as illustrated in Fig. A.1. θ_h is the angle between h^+ direction in the h^+h^- rest frame with respect to the h^+h^- direction in the B_s^0 rest frame, θ_l is the angle between the μ^+ direction in the J/ψ rest frame with respect to the J/ψ direction in the B_s^0 rest frame and χ is the angle between the J/ψ and h^+h^- decay planes in the B_s^0 rest frame. (These definitions are the same for B_s^0 and $\overline{B}_s^0$, namely, using μ^+ and h^+ to define the angles for both B_s^0 and $\overline{B}_s^0$ decays.)

For decays of B_s^0-$\overline{B}_s^0$, the time-dependent decay rates can be expressed as Eq. (1-37) and Eq. (1-38). The time-independent decay rate of B_s^0 is

$$|A_f(m_{hh}, \theta_{\pi\pi}, \theta_{J/\psi}, \chi)|^2 = \sum_{\alpha=\pm1} \left| \sum_{\lambda,J}^{|\lambda|\leqslant J} \sqrt{\frac{2J+1}{4\pi}} H_\lambda^J(m_{hh}) e^{i\lambda\chi} d^1_{\lambda,\alpha}(\theta_{J/\psi}) d^J_{-\lambda,0}(\theta_{\pi\pi}) \right|^2, \tag{A-1}$$

where $\lambda = 0, \pm1$ is the J/ψ helicity, $\alpha = \pm1$ is the helicity difference between the two muons, J is the spin of the h^+h^- intermediate state, and $H_\lambda^J(m_{hh})$ is a helicity amplitude depending on m_{hh} that could be expressed using a formalism similar to that in a Dalitz-plot analyses. $\theta_{\pi\pi}$ is θ_h and $\theta_{J/\psi}$ is θl. Using the definition:

$$H_\lambda(m_{hh}, \theta_{\pi\pi}) = \sum_J \sqrt{\frac{2J+1}{4\pi}} H_\lambda^J(m_{hh}) d^J_{-\lambda,0}(\theta_{\pi\pi}). \tag{A-2}$$

The Eq. (A-1) changes to

$$\begin{aligned}
|A_f(m_{hh}, \theta_{\pi\pi}, \theta_{J/\psi}, \chi)|^2 &= \sum_{\alpha=\pm1} \left| \sum_\lambda e^{i\lambda\chi} d^1_{\lambda,\alpha}(\theta_{J/\psi}) H_\lambda(m_{hh}, \theta_{\pi\pi}) \right|^2 \\
&= \sum_{\alpha=\pm1} \left[\left(\sum_{\lambda'} e^{i\lambda'\chi} d^1_{\lambda',\alpha}(\theta_{J/\psi}) H_{\lambda'}(m_{hh}, \theta_{\pi\pi}) \right)^* \left(\sum_\lambda e^{i\lambda\chi} d^1_{\lambda,\alpha}(\theta_{J/\psi}) H_\lambda(m_{hh}, \theta_{\pi\pi}) \right) \right]
\end{aligned}$$

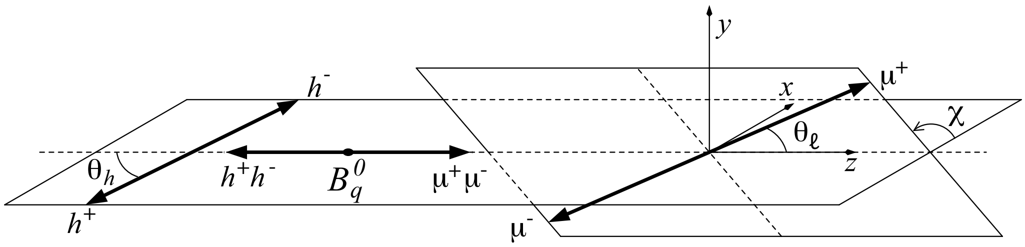

Figure A.1 Definition of helicity angles.

Table A.1 Functional forms of $\Theta_{\lambda'\lambda}(\theta)$ defined in Eq. (A-4) for different values of λ and λ'.

λ	λ'	$\Theta_{\lambda'\lambda}(\theta)$
0	0	$\sin^2\theta$
0	1	$\frac{1}{\sqrt{2}}\sin\theta\cos\theta$
0	−1	$-\frac{1}{\sqrt{2}}\sin\theta\cos\theta$
1	0	$\frac{1}{\sqrt{2}}\sin\theta\cos\theta$
1	1	$\frac{1}{2}(1+\cos^2\theta)$
1	−1	$\frac{1}{2}\sin^2\theta$
−1	0	$-\frac{1}{\sqrt{2}}\sin\theta\cos\theta$
−1	1	$\frac{1}{2}\sin^2\theta$
−1	−1	$\frac{1}{2}(1+\cos^2\theta)$

$$= \sum_{\lambda',\lambda}\left(\sum_{\alpha=\pm1} d^1_{\lambda',\alpha}(\theta_{J/\psi})d^1_{\lambda,\alpha}(\theta_{J/\psi})\right) H^*_{\lambda'}(m_{hh},\theta_{\pi\pi})H_\lambda(m_{hh},\theta_{\pi\pi})\, e^{i(\lambda-\lambda')\chi}. \tag{A-3}$$

Defining

$$\Theta_{\lambda'\lambda}(\theta_{J/\psi}) \equiv \sum_{\alpha=\pm1} d^1_{\lambda',\alpha}(\theta_{J/\psi})d^1_{\lambda,\alpha}(\theta_{J/\psi}), \tag{A-4}$$

results in

$$|A_f(m_{hh},\theta_{\pi\pi},\theta_{J/\psi},\chi)|^2 = \sum_{\lambda',\lambda} H_\lambda(m_{hh},\theta_{\pi\pi})H^*_{\lambda'}(m_{hh},\theta_{\pi\pi})\, e^{i(\lambda-\lambda')\chi}\Theta_{\lambda'\lambda}(\theta_{J/\psi}). \tag{A-5}$$

The functional form of $\Theta_{\lambda'\lambda}(\theta_{J/\psi})$ is listed in Table A.1. They are invariant under the interchange of λ and $\lambda^{'}$ and transform with respect to a change of the sign of λ and $\lambda^{'}$.

Using Eq. (A-5), the amplitude becomes

$$\begin{aligned}|A_f(m_{hh},\theta_{\pi\pi},\theta_{J/\psi},\chi)|^2 =&|H_0(m_{hh},\theta_{\pi\pi})|^2\sin^2\theta_{J/\psi} + \frac{1}{2}\left(|H_+(m_{hh},\theta_{\pi\pi})|^2 + |H_-(m_{hh},\theta_{\pi\pi})|^2\right)\\ &\times(1+\cos^2\theta_{J/\psi}) + \mathcal{R}e\left[H_+(m_{hh},\theta_{\pi\pi})H^*_-(m_{hh},\theta_{\pi\pi})e^{2i\chi}\right]\sin^2\theta_{J/\psi}\end{aligned}$$

$$+\sqrt{2}\mathcal{R}e\left[\left(H_0(m_{hh},\theta_{\pi\pi})H_+^*(m_{hh},\theta_{\pi\pi})-H_0^*(m_{hh},\theta_{\pi\pi})H_-(m_{hh},\theta_{\pi\pi})\right)e^{-i\chi}\right]$$
$$\times\sin\theta_{J/\psi}\cos\theta_{J/\psi}, \tag{A-6}$$

where we denote H_λ by 0, +, and −, rather than 0, +1 and −1.

Similarly, the time-independent part of the $\overline{B}_s^0$ decays is

$$\begin{aligned}|\overline{A}_f(m_{hh},\theta_{\pi\pi},\theta_{J/\psi},\chi)|^2 =&|\overline{H}_0(m_{hh},\theta_{\pi\pi})|^2\sin^2\theta_{J/\psi}+\frac{1}{2}\left(|\overline{H}_+(m_{hh},\theta_{\pi\pi})|^2+|\overline{H}_-(m_{hh},\theta_{\pi\pi})|^2\right)\\ &\times(1+\cos^2\theta_{J/\psi})+\mathcal{R}e\left[\overline{H}_+(m_{hh},\theta_{\pi\pi})\overline{H}_-^*(m_{hh},\theta_{\pi\pi})e^{2i\chi}\right]\sin^2\theta_{J/\psi}\\ &+\sqrt{2}\mathcal{R}e\left[\left(\overline{H}_0(m_{hh},\theta_{\pi\pi})\overline{H}_+^*(m_{hh},\theta_{\pi\pi})-\overline{H}_0^*(m_{hh},\theta_{\pi\pi})\overline{H}_-(m_{hh},\theta_{\pi\pi})\right)e^{-i\chi}\right]\\ &\times\sin\theta_{J/\psi}\cos\theta_{J/\psi}\ .\end{aligned} \tag{A-7}$$

The interference term of the two amplitude are:

$$\begin{aligned}&A_f^*(m_{hh},\theta_{\pi\pi},\theta_{J/\psi},\chi)\overline{A}_f(m_{hh},\theta_{\pi\pi},\theta_{J/\psi},\chi)=\\ &\sum_{\alpha=\pm1}\left[\left(\sum_{\lambda'}e^{i\lambda'\chi}d^1_{\lambda',\alpha}(\theta_{J/\psi})H_{\lambda'}(m_{hh},\theta_{\pi\pi})\right)^*\left(\sum_{\lambda}e^{i\lambda\chi}d^1_{\lambda,\alpha}(\theta_{J/\psi})\overline{H}_{\lambda}(m_{hh},\theta_{\pi\pi})\right)\right]\\ &=\sum_{\lambda',\lambda}\overline{H}_\lambda(m_{hh},\theta_{\pi\pi})H_{\lambda'}^*(m_{hh},\theta_{\pi\pi})\,e^{i(\lambda-\lambda')\chi}\Theta_{\lambda'\lambda}(\theta_{J/\psi}).\end{aligned} \tag{A-8}$$

Replacing the explicit terms leads to

$$\begin{aligned}A_f^*(m_{hh},\theta_{\pi\pi},\theta_{J/\psi},\chi)\overline{A}_f(m_{hh},\theta_{\pi\pi},\theta_{J/\psi},\chi)=&\,\overline{H}_0(m_{hh},\theta_{\pi\pi})H_0^*(m_{hh},\theta_{\pi\pi})\sin^2\theta_{J/\psi}\\ &+\frac{1}{2}\left(\overline{H}_+(m_{hh},\theta_{\pi\pi})H_+^*(m_{hh},\theta_{\pi\pi})+\overline{H}_-(m_{hh},\theta_{\pi\pi})H_-^*(m_{hh},\theta_{\pi\pi})\right)(1+\cos^2\theta_{J/\psi})\\ &+\frac{1}{2}\left(\overline{H}_+(m_{hh},\theta_{\pi\pi})H_-^*(m_{hh},\theta_{\pi\pi})e^{2i\chi}+\overline{H}_-(m_{hh},\theta_{\pi\pi})H_+^*(m_{hh},\theta_{\pi\pi})e^{-2i\chi}\right)\sin^2\theta_{J/\psi}\\ &+\frac{1}{\sqrt{2}}\left(\overline{H}_0(m_{hh},\theta_{\pi\pi})H_+^*(m_{hh},\theta_{\pi\pi})e^{-i\chi}-\overline{H}_0(m_{hh},\theta_{\pi\pi})H_-^*(m_{hh},\theta_{\pi\pi})e^{i\chi}\right.\\ &\left.+\overline{H}_+(m_{hh},\theta_{\pi\pi})H_0^*(m_{hh},\theta_{\pi\pi})e^{i\chi}-\overline{H}_-(m_{hh},\theta_{\pi\pi})H_0^*(m_{hh},\theta_{\pi\pi})e^{-i\chi}\right)\sin\theta_{J/\psi}\cos\theta_{J/\psi}.\end{aligned} \tag{A-9}$$

Assuming $|p/q|=1$, the differential decay rates in Eq. (1-37) and Eq. (1-38) can be expressed as a function of five variables $t, m_{hh}, \theta_l, \theta_h$ and χ as

$$\begin{aligned}\frac{d^5\Gamma}{dtdm_{hh}d\cos\theta_{J/\psi}d\cos\theta_{\pi\pi}d\chi}\propto e^{-\Gamma t}&\left\{\frac{|A_f|^2+|\overline{A}_f|^2}{2}\cosh\frac{\Delta\Gamma_s t}{2}+\frac{|A_f|^2-|\overline{A}_f|^2}{2}\cos(\Delta m_s t)\right.\\ &\left.-\mathcal{R}e\left(\frac{q}{p}A_f^*\overline{A}_f\right)\sinh\frac{\Delta\Gamma_s t}{2}-\mathcal{I}m\left(\frac{q}{p}A_f^*\overline{A}_f\right)\sin(\Delta m_s t)\right\},\end{aligned} \tag{A-10}$$

$$\frac{d^5\overline{\Gamma}}{dtdm_{hh}d\cos\theta_{J/\psi}d\cos\theta_{\pi\pi}d\chi} \propto e^{-\Gamma t}\left\{\frac{|A_f|^2+|\overline{A}_f|^2}{2}\cosh\frac{\Delta\Gamma_s t}{2}-\frac{|A_f|^2-|\overline{A}_f|^2}{2}\cos(\Delta m_s t)\right.$$
$$\left.-\mathcal{R}e\left(\frac{q}{p}A_f^*\overline{A}_f\right)\sinh\frac{\Delta\Gamma_s t}{2}+\mathcal{I}m\left(\frac{q}{p}A_f^*\overline{A}_f\right)\sin(\Delta m_s t)\right\} \quad \text{(A-11)}$$

The functions $|A_f|^2$, $|\overline{A}_f|^2$ and $A_f^*\overline{A}_f$ are defined in Eqs. (A-6), (A-7) and (A-9) respectively.

The function $H_\lambda(m_{hh},\theta_{\pi\pi})$ defined in Eq. (A-2) is expressed using the Dalitz-plot variables m_{hh} and θ_h, which gives:

$$H_\lambda(m_{hh},\theta_{\pi\pi}) = \sum_R h_\lambda^R\sqrt{2J_R+1}\sqrt{P_RP_B}F_B^{(L_B)}F_R^{(L_R)}A_R(m_{hh})\left(\frac{P_B}{m_B}\right)^{L_B}\left(\frac{P_R}{m_{hh}}\right)^{L_R}d^{J_R}_{-\lambda,0}(\theta_{\pi\pi}), \quad \text{(A-12)}$$

where R represents the intermediate state with different spins; $F_B^{(L_B)}$ and $F_R^{(L_R)}$ are the B_s^0 and R decay form factors; $P_B(P_R)$ is the J/ψ (either of the R resonance daughter's) momentum in the B_s^0 (R) rest frame;m_B is the B_s^0 mass; J_R is spin of R; $L_B(L_R)$ is the orbital angular momentum between the B_s^0 meson (R resonance) 's daughters; $A_R(m_{KK})$ is the amplitude used to describe the mass line-shape of the resonance R. And $\overline{H}_\lambda$ is summed over all h^+h^-.

The helicity complex coefficients $\overline{h}^R$ is replaced using the transversity complex coefficients $\overline{a}^R$ using their relations

$$\begin{aligned}
\mathbf{a}_0^R &= \mathbf{h}_0^R,\\
\mathbf{a}_\parallel^R &= \frac{1}{\sqrt{2}}(\mathbf{h}_+^R+\mathbf{h}_-^R),\\
\mathbf{a}_\perp^R &= \frac{1}{\sqrt{2}}(\mathbf{h}_+^R-\mathbf{h}_-^R).
\end{aligned} \quad \text{(A-13)}$$

where $\mathbf{a}_0^R$ corresponds to longitudinal polarization of the J/ψ meson, $\mathbf{a}_\parallel^R$ for parallel polarization of the J/ψ and h^+h^- and $\mathbf{a}_\perp^R$ for their perpendicular polarization.

If we only consider tree level contribution in the B_s^0 decay, the CKM weak phase only appears as $\frac{q}{p} = e^{-2i\beta}$. The $\bar{\mathbf{a}}_i$ amplitudes only contain strong phases, $\bar{\mathbf{a}}_i = \eta_i^R\mathbf{a}_i^r$, where η_i^R is CP eigenvalue of the ith transversity component for the intermediate state R. (Here $i = 0, \ \parallel, \ \perp$.)

Considering the contribution from direct CP violation, the complex coefficients can be parameterized as

$$a_i^R = c_i^R(1+b_i^R)e^{i(\delta_i^R+\phi_i^R)}, \quad \bar{\mathbf{a}}_i^R = \eta_i^Rc_i^R(1-b_i^R)e^{i(\delta_i^R-\phi_i^R)}, \quad \text{(A-14)}$$

where c_i^R, b_i^R, δ_i^R and ϕ_i^R are real numbers that can be determined in the experiment. b_i^R and ϕ_i^R are CP violating, while c_i^R and δ_i^R are CP conserving. So the direct CP asymmetry for each resonance R with tranversity i component is

$$A_{CP}(R)_i \equiv \frac{|\bar{\mathbf{a}}_i^R|^2 - |a_i^R|^2}{|\bar{\mathbf{a}}_i^R|^2 + |a_i^R|^2} = \frac{-2b_i^R}{1 + (b_i^R)^2}. \tag{A-15}$$

Experimentally, the measured CP observable includes both the contribution from mixing and decay, given by

$$\phi_s^{eff}(R)_i = \phi_s + 2\phi_i^R, \ or \ 2\beta^{eff}(R)_i = 2\beta + 2\phi_i^R. \tag{A-16}$$

To implement this procedure, the probability density functions (PDFs) given in Eqs. (A-10) and (A-11) are used. The normalization can be computed by first integrating over t, $\theta_{J/\psi}$ and χ analytically, following by using numerical integration for the remaining variables. If the data is flavour tagged, the two PDFs should be average.

Resume and publications

Resume

- Apr. 1992, born in Beijing, China.
- Sep. 2010 - Jul. 2014, B.S. in Physics.
  College of Physics, Sichuan University, Sichuan, China
- Sep. 2014 - present, Ph.D. candidate in Nuclear Science and Technology.
  Department of Engineering Physics, Tsinghua University, Beijing, China

Publications

[1] LHCb Collaboration, R. Aaij *et al.*, (corresponding author Xuesong Liu) *Observation of the* $\Xi_b^- \to J/\psi \Lambda K^-$ *decay*, Phys. Lett. B772 (2017) 265.

[2] LHCb Collaboration, R. Aaij *et al.*, *Resonances and CP violation in* B_s^0 *and* $\overline{B}_s^0 \to J/\psi K^+K^-$ *decays in the mass region above the* $\phi(1020)$, JHEP 08 (2017) 037.

[3] LHCb Collaboration, R. Aaij *et al.*, (corresponding author Xuesong Liu) *Measurement of CP-violating phase* ϕ_s *from* $B_s^0 \to J/\psi\pi^+\pi^-$ *decays in 13 TeV pp collisions*, Phys. Lett. B797 (2019) 134789

[4] Xuesong Liu (on behalf of the LHCb Collaboration) R. Aaij *et al.*, (corresponding author Xuesong Liu) *Mixing and CP-violation results in b-hadron decays at LHCb*, CERN-LHCb-PROC-2017-032.